Application of Oxidation Protective Coatings on Diboride Based Ultra-High Temperature Ceramics: Fundamental Studies on the Oxidation Behavior

Zur Erlangung des akademischen Grades eines

DOKTORS DER INGENIEURWISSENSCHAFTEN (Dr.-Ing.)

von der KIT-Fakultät für Maschinenbau des
Karlsruher Instituts für Technologie (KIT)
angenommene

DISSERTATION

von

M.Sc. Jan Erik Förster

Tag der mündlichen Prüfung:	28.11.2024
Hauptreferentin:	Prof. Dr.-Ing. habil. Bronislava Gorr
Korreferent:	Prof. Dr.-Ing. Günter Schell

„Ma, all'incontro, essendo la natura inesorabile ed immutabile, e mai non trascendente i termini delle leggi impostegli, come quella che nulla cura che le sue recondite ragioni e modi d'operare sieno o non sieno esposti alla capacità degli uomini.“

“But Nature, on the other hand, is inexorable and immutable; she never transgresses the laws imposed upon her, or cares a whit whether her abstruse reasons and methods of operation are understandable to men.”

Galileo Galilei,

Letter to Madame Christina of Lorraine, Grand Duchess of Tuscany,

December 21, 1615

Dedicated to my father (†January 1, 2023) and to my mother.

Acknowledgements

This work was funded by the German Aerospace Center (DLR), Cologne.

First of all, I would like to thank my supervisor and "Guru", Dr. Ravisankar Naraparaju. His fundamental idea of adding oxidation protection coatings on diboride-based Ultra-High Temperature Ceramics (UHTCs), was the first milestone for this manuscript. Even though I am a mechanical engineer, Naraparaju kept trust and faith in me, introducing me to this entirely challenging research fields of materials science, coatings, high temperature oxidation, and Ultra-High Temperature Ceramics. The first lesson of many Naraparaju taught me:

"Always keep in your mind, you can not force or even beat the nature".

This has been my inspiration for the last 4 years and it will continue to be my inspiration for the rest of my life. I took care about the "relationship between me and nature" by accepting what I got (chances, restrictions, results), and try to do the best out of it, even in desperate times. Naraparaju has always supported me, observed my work, motivated me in (very) hard times, and guided me to perform as best as possible. Finally, I was able to complete this important stage of my life. Thank you for your commitment and your trust in me and my work.

I want to thank Prof. Dr.-Ing. habil. Bronislava Gorr as my supervisor at Karlsruhe Institute of Technology (KIT) for her commitment in the last year of my PhD. Prof. Gorr supported me as an external student and managed, that I can finish my PhD as fast as possible. She gave me appropriate recommendations and corrections, in order to push the performance of this work at its limit. Thank you for your support to make my PhD possible.

Furthermore, I would also like to thank Prof. Dr. William Fahrenholtz and Prof. Dr. Gregory Hilmas from the Missouri University of Science and Technology (MS&T). Both are luminaries in the research field of UHTCs, provided the needed UHTC materials for this work. Moreover, both welcomed me for several weeks in their lab in Rolla, MO, United States of America, to introduce me in the fundamental production of ZrB_2 powder and monolithic bulk material. Their support and input as co-authors in the publications and presentations at several conferences pushed the visibility of this project. Thank you very much for the steady support.

Finally, I want to thank several people for their exceptional support during my PhD.

Dr. Klemens Kelm, Alexander Franke, and Frederik Kreps. (Specialists in metallography, microscope, XRD analysis, TEM lamella preparation, and crystallographic analysis). All three supported me during my PhD phase by giving me important advises and assisted me in several task, facing analytics.

Dr. Peter Mechnich (Specialists in ceramics, minerals, and high-temperature synthesis and oxidation). He introduced me to high-temperature tube furnaces and assisted me in my first sets of experiments. Furthermore, his contributions were always very helpful and brought new perspectives to various discussions.

My colleagues of the department of high-temperature and functional coatings of the institute of materials research at DLR cologne, who brought me a wonderful time and accompanied me through the highs and lows of my PhD (Department leader Dr. Uwe Schulz, Dr. Bilge Saruhan-Brings, Dr. Apurba Ray, Dr. Svitlana Krüger, Andrea Ebach-Stahl, Dr. Nadine Laska, Dr. Ronja Anton, Dr. Peter Bauer, Oliver Helle, Christop Mikulla and Cynthia Yanel Guijosa Garcia)

Special thanks go to our technicians Andreas Handwerk, Jörg Brien, Daniel Peters, Ramin Nodeh-Farahani and Matthias Rossmeier. Without their technical advises, support, and pro-active commitment in tasks of coating development and deposition as well as in the conceptualization and construction of needed facilities and equipment, this work would not be done.

Dr. Antonio Vinci and Dr. Diletta Sciti are famous for their detailed studies in the field of Ultra-High Temperature Ceramic Matrix Composites (UHTCMCs). During our cooperation, both supported me and gave me very useful feedback and advices. Further, Vinci helped me in the thermodynamic calculations of the proposed reactions. I want to thank you for your support.

Finally, I want to thank my friends Ray Donald Dewald, Ricky Rix, Markus Lankenau, and Janik Evert. All took their time to read this work carefully and gave me constructive feedback.

Last, but not least, I would like to thank my oldest friend, Nadine Lütjohann. We know each other since elementary school (26 years already) and she motivated me all my life, always read my theses (Bachelor's, Master's, ...) and supported me right up to the last minute during my PhD. Thank you very much for your contribution.

Eigenständigkeitserklärung

Ich, Jan Erik Förster, erkläre hiermit, die vorliegende Arbeit selbstständig angefertigt und keine anderen als die angegebenen Quellen und Hilfsmittel benutzt zu haben. Wörtlich oder inhaltlich übernommene Stellen wurden als solche kenntlich gemacht. Die Satzung des Karlsruher Instituts für Technologie (KIT) zur Sicherung guter wissenschaftlicher Praxis wurde beachtet.

Hiermit erkläre ich, dass für mich Promotionsverfahren außerhalb der Fakultät für Maschinenbau des Karlsruher Instituts für Technologie (KIT) weder anhängig sind noch erfolglos abgeschlossen wurden.

Köln, den 27.10.2024

Jan Erik Förster

Kurzfassung

Die Raumfahrtindustrie erlebt derzeit eine Renaissance aufgrund von Zukunftsvisionen bezüglich Weltraumtourismus oder der Besiedelung des Mars. Infolgedessen steigt die Nachfrage nach Hochleistungswerkstoffen für extreme Temperaturen stetig an. Der Wiedereintritt eines Raumfahrzeugs oder der Flug eines Hyperschallflugkörpers innerhalb der Erdatmosphäre führt zu extremen thermischen Belastungen bestimmter Bauteile wie den Leitkanten oder den Hitzekacheln eines thermischen Schutzsystems. Aus heutigem Stand ist kein Material für die hohen thermischen und mechanischen Anforderungen geeignet, um die Wiederverwendbarkeit jener Komponenten zu gewährleisten, was angesichts der enormen wirtschaftlichen Kosten unabdingbar ist.

Potentielle Materialien für derartige wiederverwendbare Komponenten stellt die Gruppe der Ultrahochtemperaturkeramiken dar. Jene Materialien vereinen eine hohe Wärmeleitfähigkeit κ_T, eine hohe Oxidationsbeständigkeit bis ~1200°C durch Selbst-Passivierung, eine geringe Dichte und einen extrem hohen Schmelzpunkt (T_M>3000°C). Insbesondere ZrB_2 besitzt aufgrund seiner geringen Dichte (~6.085 g/cm³) ein hohes Potential für entsprechende Anwendungen in Hyperschallflugkörpern. Leider führt die unzureichende Oxidationsbeständigkeit zur Bildung einer porösen Oxidschicht aus ZrO_2 sowie einem leicht verdampfenden B_2O_3 Glases bei Temperaturen zwischen 1500°C bis 1700°C. Dies verhindert derzeit den kommerziellen Einsatz von ZrB_2 für entsprechende Anwendung.

Aus diesem Grund wird in dieser Arbeit ein neuartiger Ansatz zur Verbesserung der Oxidationsbeständigkeit Diborid-basierter UHTCs vorgestellt und eingehend untersucht. Zum ersten Mal konnte gezeigt werden, dass schützende Beschichtungen unterschiedlichster Materialklassen (Metallisch, Keramisch) auf ZrB_2 mittels (reaktiven) Magnetron Sputtern abgeschieden werden können. Die Oxidationsexperimente haben eindeutig gezeigt, dass die abgeschiedenen Schichten eine Temperaturwechselbeständigkeit von bis zu 1700°C überstehen können und die Oxidationseigenschaften des ZrB_2 Grundmaterials verbessern konnten. Der Schutz des Substrates mittels Beschichtung konnte der dichten und fehlerfreien Mikrostruktur der abgeschiedenen Beschichtungen, der Bildung eines schützenden Flüssigkeitsfilm auf der Oberfläche (Glasstabilisator), sowie der Versinterung bzw. Verdichtung der sich ausbildenden Oxidschicht (Sinterwerkstoff) zugeschrieben werden. Die untersuchten Beschichtungen auf ZrB_2 umfassten unteranderem Gadolinium-Oxid Beschichtungen (GdO), metallische Niob Beschichtungen, und Hafnium Oxid Beschichtungen (HfO_2).

Im Vergleich zu unbeschichteten kommerziellen ZrB_2 haben besonders die GdO Beschichtungen zu einer signifikanten Minderung der Oxidschichtbildung beigetragen und die Oxidschichtdicke nach einer Belastung von 30 min bei 1700°C um ca. -60% reduziert. Der Schutzmechanismus basiert auf der Bildung eines schützenden Flüssigkeitsfilm (Gd,B)O auf der Probenoberfläche. Dieser mindert die Durchlässigkeit für Sauerstoffmoleküle zum darunterliegenden ZrB_2 Grundmaterial. Zur gleichen Zeit führt der Flüssigkeitsfilm aufgrund von Flüssigphasensinterung zur Verdichtung der obersten Lage der ausgebildeten Oxidschicht. Die Verdichtung mindert die Knudsen Diffusion von Sauerstoffmolekülen entlang der Oxidschichtdicke zum Grundmaterial.

Ähnliche Schutzmechanismen wurden für die metallischen Niob Beschichtungen identifiziert. Die Beschichtungen führten zur Reduktion der Oxidschichtdicke um ca. -55% nach 30 min bei 1700°C. Die metallischen Niob Beschichtungen zeigten eine geringere Schutzwirkung als die getesteten GdO Beschichtungen. Dies wurde auf die leicht verdampfende Flüssigkeitsmischung (Nb,B)O zurückgeführt. Die Verdampfung limitiert die Verdichtung der Oxidschicht mittels Flüssigphasensinterung und führt zu einer unvollständig verdichteten Oxidschicht. Jedoch genügte der Grad der Verdichtung, um die Kondensation von sekundären ZrO_2 (gelöst im flüssigen B_2O_3) an der Oberfläche zu ermöglichen. Aufgrund der stetigen Verdampfung der B_2O_3 Flüssigkeit ergab sich eine nachträgliche Verdichtung oder Oxidschicht bei der Oxidation um 1700°C oder verlängerten Belastungszeiten von 60 min.

Im Gegensatz zu den Glasstabilisatoren (GdO, Nb) basiert der Schutzmechanismus der hochschmelzenden HfO_2 Beschichtung auf der dichten und fehlerfreien Mikrostruktur der Schicht. Aufgrund der dichten Beschichtung konnte die Knudsen Diffusion von Sauerstoffmolekülen zum Grundmaterial zeitlich limitiert werden. Resultierend führte die Beschichtung zu einer Minderung der Oxidschichtdicke von ca. -48% nach 60 min bei 1700°C. Die unvermeidbare Bildung von flüssigem B_2O_3 unterhalb der dichten HfO_2 Beschichtung hat zur Abplatzung der Schutzschicht und zur Erzeugung mehrerer Risse entlang der Schichtdicke geführt. Ab diesem Zeitpunkt bestand kein weiterer Schutz gegenüber der Oxidation des Grundmaterials. In Hinblick auf die Temperatur und der Belastungszeit führte die Kondensation von sekundären ZrO_2 aufgrund stetiger B_2O_3-Verdampfung zu Verdichtung der aufgerissenen HfO_2 Beschichtung und stellte die schützende Wirkung der dichten Mikrostruktur zum Teil wieder her. Jener Effekt ist bei Temperaturen um 1700°C oder sehr langen Belastungszeiten von bis zu 240 min zu erkennen.

Der direkte Vergleich des unbeschichteten ZrB_2 gegenüber dem beschichteten ZrB_2 zeigt eine eindeutige Verbesserung der Oxidationsbeständigkeit des Grundmaterials und beweist damit die Funktionsfähigkeit von oxidationsschützenden Beschichtungen auf Diborid-basierten UHTCs. Der vorgestellte Lösungsansatz stellt ein neues und vielversprechendes Forschungsgebiet dar, welches das Potential besitzt, sich in der UHTC-Gemeinschaft zu etablieren.

Abstract

The aerospace industry is currently undergoing a renaissance due to visions such as space tourism or the colonization of Mars. As a result, the demand for high-performance materials for extreme temperatures is ever-increasing. The re-entry operation of a spacecraft or a hypersonic flight within the Earth's atmosphere induces extreme thermal loads on certain components such as leading edges or tiles of the thermal protective system. No current state-of-the-art material is suitable to face these harsh environmental requirements and to ensure the reusability of such kind of components, which is mandatory to accommodate the huge economic costs.

Potential candidates for such kind of reusable components are the group of ultra-high temperature ceramics, in particular diboride-based transition metals. These materials combine a high thermal conductivity κ_T, high oxidation resistance up to ~1200°C through self-passivation, low density, and extremely high melting points (T_M >3000°C). Especially ZrB_2 offers a high potential for corresponding applications in hypersonic missiles due to its low density (~6,085 g/cm³). Unfortunately, the insufficient oxidation resistance at the desired temperatures between 1500°C and 1700°C is the current bottleneck for ZrB_2, forming a porous oxide scale of ZrO_2 and volatile B_2O_3 glass at the surface.

For this reason, a novel approach to improve the oxidation resistance of diboride-based UHTCs is proposed in this study and is investigated extensively. In a first attempt, it has been shown that protective overlay coatings of different material classes (metallic, ceramic) can be deposited on ZrB_2 surfaces by means of (reactive) magnetron sputtering. The oxidation experiments have clearly shown, that the applied coatings are thermal shock resistant up to 1700°C and improve the oxidation resistance of the ZrB_2 substrate. Protective mechanisms were found to be the dense microstructure of the applied solid coating, the formation of a protective liquid layer at the surface (glass stabilizer), or the densification of the uppermost section of the formed oxide scale (solid scale densifier). Tested coatings including gadolinium-based oxide coatings (GdO), metallic niobium coatings, and ceramic hafnia coatings (HfO_2).

Compared to uncoated baseline ZrB_2, the GdO coatings, in particular, have contributed a significant reduction in the oxide scale formation and reduced the scale thickness by approximately -60% after an exposure for 30 min at 1700°C. The protection mechanism is based on the formation of a protective liquid layer (Gd,B)O at the surface, which provoked the permeation of oxygen molecules to the oxidation front of the underlying ZrB_2 substrate. Simultaneously, the protective liquid induced the densification of the uppermost section of the oxide scale by liquid phase sintering. The densification reduced the Knudsen diffusion of oxygen molecules to the oxidation front of the ZrB_2.

Similar protection mechanisms were found for metallic Nb coatings. The coating reduced the oxide scale thickness by -55% after 30 min at 1700°C. The metallic Nb coatings were found to be less protective than the GdO coatings due to the more volatile nature of the formed (Nb,B)O liquid solution. However, the densification of the scale was found to be sufficient to ensure the precipitation of secondary ZrO_2 (dissolved in liquid B_2O_3) at the surface during the evaporation of the protective liquid B_2O_3. A subsequent densification of the oxide scale was observed at 1700°C or extended exposure times of 60 min.

In contrast to the glass stabilizing coatings, the dense and solid HfO_2 coating protected the substrate and induced the reduction of the Knudsen diffusion of oxygen molecules to the oxidation front of ZrB_2. As a result, the protective coating reduced the oxide scale thickness by ~48% after 60 min at 1700°C. The inevitable formation of liquid B_2O_3 beneath the dense HfO_2 coating detached the coating from the formed oxide scale and induced the formation of cracks across the coating thickness. .The ruptured coating has been densified due to the precipitation of secondary ZrO_2 at the surface and improved the oxidation resistance at 1700°C or extended exposure times of 240 min.

The comparison of the performance of uncoated ZrB_2 with coated ZrB_2 proved the oxidation protection of the substrate and validated the approach of the application of protective overlay coatings on diboride-based UHTCs. The solution to improve the oxidation behavior of UHTCs by overlay coatings represents a new and highly promising research field, which has the potential to be established in the UHTC community.

Table of Contents

List of Figures

List of Tables

List of Abbreviations

Abbreviation	Meaning
AC	As-coated, the condition after coating deposition procedure
AlSint^{TM}	Gastight aluminum oxide with extreme high purity, Trademark
APS	Atmospheric plasma spray
at.%	Atomic percentage
BSE	Backscattered electron
CIRA	Centro Italiano Ricerche Aerospaziali
CFD	Computational fluid dynamics
CMC	Ceramic matrix composites
COD	Crystallography open database
CTE	Coefficient of thermal expansion
DC	Direct current
e.g.	Exempli gratia, Latin term for “for example”
EB-PVD	Electron beam physical vapor disposition
EDM	Electrical discharge machining
EDS	Energy dispersive X-ray spectroscopy
et al.	Et al.ia, Latin term for “and other”
FIB	Focused ion beam
GDOES	Glow discharge optical emission spectroscopy
HE-UHTCs	High entropy ultra-high temperature ceramics
HF	High frequence
HIP	Hot isostatic pressing
HP	Hot pressing
i.e.	Id est, Latin term for “that is”
ICDD	International center for diffraction data
LM	Light microscope
NASA	National Aeronautics and Space Administration
o.i.	Own illustration (based on references if indicated)
PVD	Physical vapor deposition
P/Q	Pushing and quenching of specimens (Rapid oxidation, Thermal shock)
r.a.	Round about
R/C	Ramping and cooling of specimens (Ramped oxidation)
SA	Synthetic air
SAED	Selective area electron diffraction
SEM	Scanning electron microscope

Abbreviation	Meaning
SPS	Spark plasma sintering
STEM-EDS	Scanning transmission electron microscopy – EDS
TM	Transition metal
TEM	Transmission electron microscope
TMB_2	Transition metal diboride
TPS	Thermal protective system
UHP	Ultra-high purity
UHTCMC	Ultra-high temperature ceramic matrix composites
UHTCs	Ultra-high temperature ceramics
US	United states
VPS	Vacuum plasma spray
WDS	Wavelength dispersive X-ray spectroscopy
XRD	X-ray diffraction
VA	Vacuum-annealed, the condition of specimens after annealing procedure
VISR	Model of hypersonic missile by Hypersonix
vol%	Volume percentage
wt%	Weight percentage

List of Symbols

Latin Symbols (Capital letters)

Symbol	Meaning	Unit
A_t	Surface target	mm²
A_s	Surface substrate	mm²
$BK_{\alpha 1}$	Characteristic energy line for boron (183.3 keV)	keV
$CK_{\alpha 1}$	Characteristic energy line for carbon (277 keV)	keV
$CoK_{\alpha 1}$	Characteristic X-rays for Cobalt radiation source	nm
D	Diffusion coefficient	cm²/s
D50	Cumulative average particle size, 50% of all particles	%
D90	Cumulative average particle size, 90% of all particles	%
$D_{K,\ Pore}$	Knudsen diffusion in a pore	m²/s
$D_{K,\ Medium}$	Knudsen diffusion in porous medium	m²/s
E	Young´s modulus	GPa
E_A	Activation energy	kJ/mol ∨ cal/mol
F_g	Molecular distribution factor for reactive gas	Molecules/m³·s
F_m	Sputtered metal atoms per unit time	sccm
Fc	Sputtered compound molecules per unite time	sccm
ΔG	Gibbs free energy	kJ
ΔG^O	Standard free energy	kcal/mol
$\Delta G_{t\rightarrow m}$	Total Gibbs free energy during phase transition	kJ
ΔG_{ch}	Chemical free energy	kJ
ΔG_{Strain}	Strain energy	kJ
$\Delta G_{Surface}$	Surface energy at interfaces	kJ
ΔH	Enthalpy	kJ
I	Current	A
J	Current density	A/m²
J_A	Intrinsic diffusion flux of material A	mol/m²·s
$J_{\square A}$	Intrinsic vacancy flux of material A	
K	Bulk modulus	GPa
K_{Pi}	Parabolic oxidation rate constant	µm²/min ∨ kg²/m⁴·s
L_h	Tube length with homogeneous temperature	mm
M	Molar mass	g/mol
$OK_{\alpha 1}$	Characteristic energy line for oxygen (524 keV)	keV
P	Power	W
Q_t	Consumption of oxygen per unit time	sccm

Symbol	Meaning	Unit
R	Ideal gas constant	J/K·mol ∨ cal/K·mol
S	Transformation area for martensitic transformation	m²
T	Temperature	K ∨ °C
T_∞	Temperature of freestream condition	K
T_e	Temperature at boundary layer edge	K
T_W	Temperature at the surface	K
ΔT	Temperature difference	K
T_i	Temperature in segment i	K ∨ °C
T_D	Dew-point	°C
T_S	Processing temperature for sputtering	°C
T_M	Melting point	°C
U	Voltage	V
V	Transformation volume for martensitic transformation	m³
V_m	Molar volume	cm³/mol
Y_m	Sputter yield of metallic atoms	$Atom_{Ar}/Atom_{Metal}$
Y_c	Sputter yield of compound molecules	$Atom_{Ar}/Molecule_{Ceramic}$
Z	Atomic number	-

Latin Symbols

Symbol	Meaning	Unit
a	Lattice parameter: Axial length	Å
b	Lattice parameter: Axial length	Å
c	Lattice parameter: Axial length	Å
c_p	Specific heat capacity	J/g·K
d	Inner tube diameter of the high-temperature furnace	mm
d_{Pore}	Pore diameter	m
f	Frequence factor for diffusion of oxygen in niobium	cm^2/s
g	Gravitational acceleration (9.81 m/s^2)	m/s^2
h	Parameter in Equ.6.1 and Fig.6.1	-
i	Parameter in Equ.6.16 and Fig.6.9	-
k	Parameter in Equ.6.1 and Fig.6.1	-
l	Tube length of the high-temperature furnace	mm
m	Mass for the gas molecules (reactive gas)	kg
n	Stochiometry factor for oxides (number of gas atoms)	-
p_v	Vacuum	mbar
p_m	Pressure (hot embedding)	bar
p	Pressure	mbar ∨ Pa
p_s	Pressure (Spark plasma sintering)	MPa
p_{Ar}	Argon, partial pressure	mbar ∨ Pa
$p_{(x)}$	Partial pressure of gaseous component	mbar
p_{O2}	Partial pressure of oxygen	mbar ∨ Pa
q	Elementary electronic charge	eV
$\dot{q}_{conv}$	Heat flux due to convection	W/m^2
$\dot{q}_{chem}$	Heat flux due to chemical reactions	W/m^2
$\dot{q}_{rad}$	Heat flux due to radiation	W/m^2
$\dot{q}_{cond}$	Heat flux due to conduction	W/m^2
$\dot{q}_{surface}$	Heat flux at the surface	W/m^2
t	Time	min
t_i	Time segment	min
x_i	Measured oxide scale thickness	µm
x	Parameter in Equ.6.1 and Fig.6.1	-
y	Parameter in Equ.6.2 and Fig.6.1	-
z	Surface depth	m

Greek Symbols

Symbol	Meaning	Unit
α	Lattice parameter: Angle in crystal	°
α_v	Coefficient of thermal expansion	1/K
β	Lattice parameter: Angle in crystal	°
γ	Lattice parameter: Angle in crystal	°
ε	Porosity	-
Θ	Angle between incident X-ray beam / diffraction beam	°
κ_E	Electrical conductivity	S/cm ∨ µS/cm
κ_T	Thermal conductivity	W/m·K
λ_{Co}	Wavelength of $CoK_{\alpha 1}$ X-rays	Å
ξ_t	Fraction of metallic target surface, covered by oxides	-
π	Pi-bonding	-
ρ	Density	g/cm³
σ	Sigmar-bonding	-
τ	Tortuosity	-
ϕ_{Ar}	Gas flow of Argon	Atoms/s ∨ sccm
ϕ_{SA}	Gas flow of synthetic air (SA)	l/min
ϕ_{O2}	Gas flow of oxygen	Atoms/s ∨ sccm
ϕ	Gas flow	Atoms/s ∨ sccm
ψ	Sticking coefficient of oxygen gas molecules	-

1 Introduction

Advanced materials have driven the development of new aerospace vehicles ever since they were introduced during the last decades. Historical milestones of aerospace vehicles are presented in Fig. 1.1, beginning with Titanium alloys for the SR-71 reconnaissance aircraft (Lockheed Corporation; up to ~Mach3.2) to Nickel-based superalloys (Inconel®) for the construction of supersonic missiles such as the X-15 (North American; up to ~Mach6.7) to modern ceramics for thermal protection systems (TPS) of Orbiters.

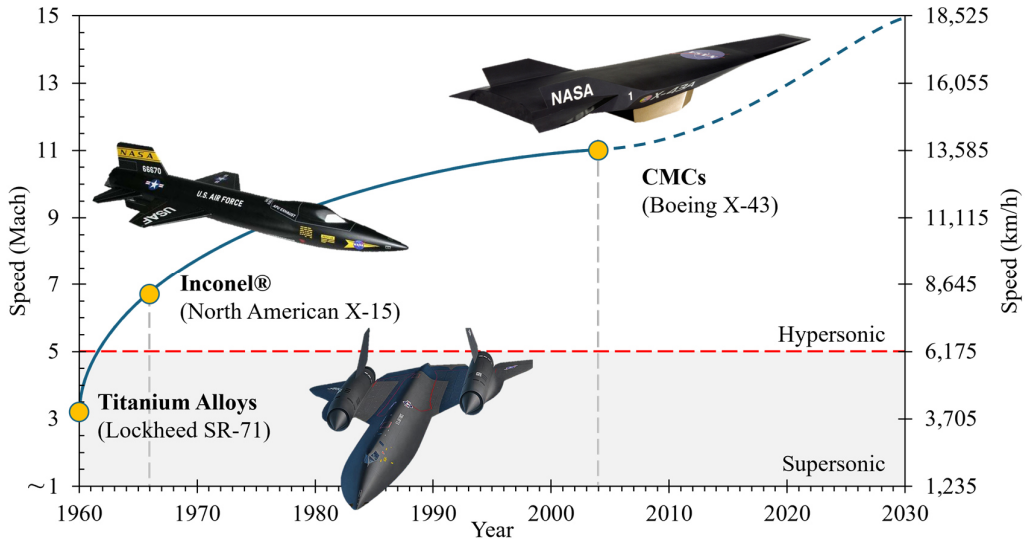

Fig. 1.1: Historical milestones in the development of modern hypersonic vehicles (o.i.) [1-4]

Currently, the focus is on developing reusable hypersonic vehicles such as the X-43 (NASA, Boing; up to ~Mach9.6) and agile space shuttles for the atmospheric re-entry of short to medium flying operations (<30 min). Key solution for hypersonic missiles are leading edges of several mm in thickness (radii at tip ~2 mm). Chemical and physical mechanisms are inducing particularly extreme thermal loads of up to 2200°C and ~120W/cm². No state-of-the-art alloying system or ceramic can be used at these temperatures rather than withstand these harsh environmental conditions for extended exposure times up to 30 min. Therefore, a relatively new group of material is needed to be considered to face and sustain these harsh environments. A potential candidate is the class of Ultra-High Temperature Ceramics (UHTCs).

Unfortunately, the oxidation behavior of UHTCs at elevated temperatures up to 1700°C draws back the commercial usage of the materials in nowadays aerospace industry. Several alloying solutions were carried out to improve the oxidation resistance of UHTCs with appropriate success. However, a new approach of protective overlay coatings on diboride-based UHTCs to extend its operational lifetime further than ever before at temperatures up to 1700°C will be proposed in this study, which has never been done before.

2 State-of-the-Art

2.1 Hypersonic Spacecrafts and Re-entry Vehicles

The motivation for exploring the space and visions such as the colonization of Mars has been growing in the last two decades. The global space industry is recording a steady increase in turnover from ~217 billion US dollars in 2009 to ~546 billion US dollars in 2022. State-of-the-art systems allow the reuse of individual rocket components to make launches more cost-efficient for the open market. As a result, the number of rocket launches per year has been increasing continuously [5, 6].

Early-stage modules such as the Mercury space capsule for transporting a single person (1953-1963) changed to more efficient space shuttles to transport several people and goods (1981-2011) [7]. Next-generation systems such as the Dream Chaser space glider (Sierra Nevada Corporation) are ready to ensure the safe transportation of goods and people into orbit and back to Earth [8].

Besides re-entry vehicles for human transportation, modern hypersonic missiles were developed to operate specifically in the earth's atmosphere for a payload of up to 50 kg. An example of a modern multi-mission hypersonic flyer is the VISR, developed by Hypersonix Launch Systems Ltd. This vehicle can accelerate from ~Mach5 (~1.7 km/s) to ~Mach10 (~3.4 km/s) for a limited range of 2500 km (<25 min of operation). A concept of the vehicle is presented in Fig. 2.1 [9].

The high speed of a hypersonic missile can be achieved by using a modern ramjet/scramjet engine. This type of engine bridges the gap between rotating gas turbines for modern airplanes and rocket engines. The innovative design of the static scramjet engine (no rotating parts) channels air into the engine and induces compression of the incoming air stream at supersonic velocity, followed by combustion and exhaust. A minimal velocity at supersonic speeds is needed for the functionality of the scramjet. This technique relies on a second system to accelerate the vehicle in the beginning [6, 9].[10]

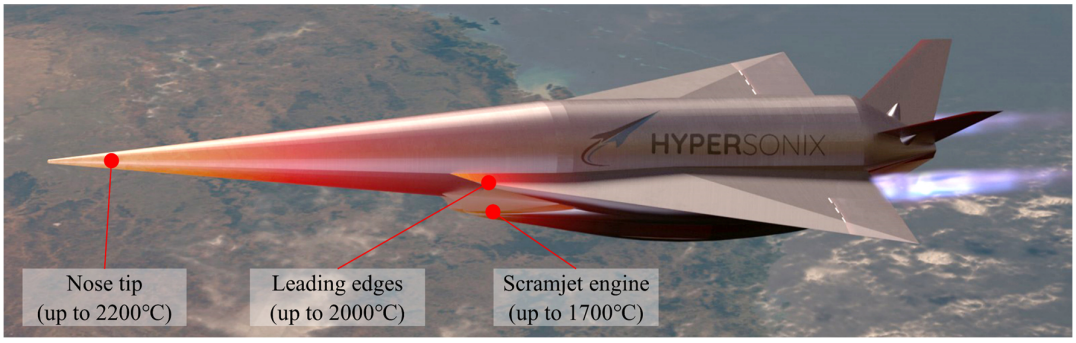

Fig. 2.1: Concept of a hypersonic missile with estimated temperatures during flight operation of up to Mach10, Model VISR, Operating product by Hypersonix Launch Systems Ltd. (o.i.) [9]

Hypersonic missiles need thin and sharp leading edges with a radius of ~1 mm and a wedge angle of ~10°, stabilizing the vehicle during flying operation and preventing turbulent fluxes and drag. The Breguet equation describes the effect of sharp leading edges during hypersonic flight

operations, considering the lift/drag relation. The thinner the leading edge, the higher the lift and the lower the drag, which results in more efficient flight conditions in case of fuel consumption to traveled distance [11]. Due to the speed between Mach5 to Mach10, the sharp leading edges will experience temperatures up to 2200°C [12]. Currently, engineers need to face various challenges to enable hypersonic flights. The extraordinarily harsh environmental conditions during re-entry (up to 8 km/s) or hypersonic flight (up to 3.4 km/s) induce extreme thermal loads and mechanical stresses [3, 11, 13].

2.2 Re-entry Strategies and Hypersonic Flights

Engineers must face enormous challenges regarding aerodynamics, thermodynamics, and materials science to ensure reliable and reusable vehicles for hypersonic flight operations. One of the current bottlenecks is heat-resistant materials that can withstand high thermal loads during hypersonic flights and re-entry [12, 14-16]. Right now, ablation shields are used to withstand harsh environmental loads during the service, which can give protection for up to several minutes [17]. Even the spacecraft Orion (upcoming Artemis missions of NASA) will be equipped with an ablation shield. Tiles of the ablative material "AVcoat 5026-39" cover the next-generation construction. The tiles consist of an epoxy novolac resin with fiberglass in a honeycomb matrix for increased mechanical stability [18]. The ablator will burn off during re-entry and transfer the heat away from the spacecraft. Since the environmental conditions are extremely harsh, the ablation shield vanishes into the air during re-entry and can not be reused for a second time [17]. Therefore, multiple re-entry missions to Mars and back to Earth are not possible yet since the heat shield might already be destroyed by the re-entry to Mars [3].

The re-entry follows two fundamental strategies. Each has its distinct influence on the temperature, speed, and landing procedure of the vehicle. Schematics for both strategies namely, ballistic re-entry, and aerodynamic lifting re-entry, are presented in Fig. 2.2. Information about the deceleration loads, the expected temperatures, and the exposure time at these temperatures are added to the figure [17]. The ballistic re-entry (red) uses a steep re-entry angle. The vehicle falls directly into the denser areas of the atmosphere with a velocity of up to 15 km/s. A g-force of 6g to 12g can be expected during the re-entry. Due to the steep trajectory and the increased velocity, the capsule modulus will experience extensive temperatures up to 2200°C at the flight-controlling surfaces with a high heat flux of >120 W/cm² [12, 19, 20]. However, the re-entry time takes <10 min and limits the exposure time at these extremely high temperatures. Finally, the vehicle gets decelerated by multiple parachutes, reducing its velocity for the vertical spot landing, generally in irrigated regions [17].

Aerodynamic lifting re-entry, also known as aerodynamic breaking, follows the principle of keeping up the vehicle for an extended period at an increased altitude. The flat re-entry angle (yellow) leads to an aerodynamic lift of the vehicles and stops the module from falling into the denser parts of the atmosphere. Since the rate of deceleration is a function of the speed of the vehicle and the density of the atmosphere, the reduced velocity of ~6-8 km/s during the lifting re-entry limits the g-forces to ~2g [17]. This strategy was used in the Apollo missions (1961-1972) to reduce the thermal heat loads on the surfaces of the capsule modules or space shuttles [19]. Due to this technique, the temperatures at flight critical components will be limited to <1700°C with a reduced

heat flux <20W/cm². The extended flight period increases the exposure time at elevated temperatures up to ~20 min [12, 21, 22]. Considering multiple re-entries, a cumulated exposure time of up to ~60 min (3 times of use) can be expected.

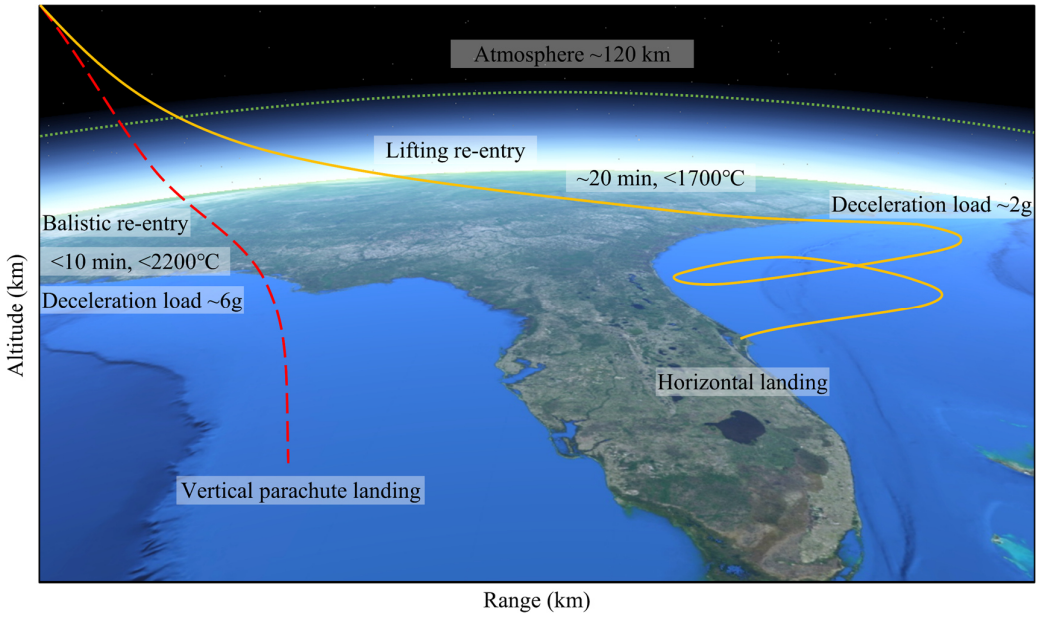

Fig. 2.2: Trajectories for ballistic re-entry (red) and aerodynamic lifting re-entry (yellow) (o.i.) [17]

Modern simulations of hypersonic aerothermodynamic environments, i.e. Computational Fluid Dynamics (CFD), enable the prediction of the thermal conditions during hypersonic flights and reveal surface temperatures of around 2200°C for sharp leading edges [12, 15, 23]. Tests in plasma wind tunnels („Scirocco“, Italian Aerospace Research Center (CIRA)) were performed to verify the calculated values (~120 W/cm², ~1860°C after 78 seconds) [13]. The thermal load at the leading edge can be attributed to the gas molecules in the atmosphere. As presented in Fig. 2.3a, a shock wave forms in front of the leading edge due to the elevated velocities [15]. The shock wave consists of a compressed atmosphere, containing gaseous components such as N_2, and O_2. The increased enthalpy of the compressed gas molecules inside the shock wave induces the dissociation and the formation of a high-temperature plasma with highly reactive radicals. The exothermic recombination of the single atoms inside the boundary layer near the surface of the leading edge results in a significant thermal load. The energy balancing in the boundary layer of a leading edge is shown in Fig. 2.3b [13, 15, 24, 25].

The static energy balancing at the surface of a leading edge considers four different energy fluxes: the convection of thermal energy from the boundary layer to the surface $\dot{q}_{conv}$, the chemical heat energy due to the reaction of the radicals at the surface $\dot{q}_{chem,}$ the emission of thermal energy into the environment due to radiation $\dot{q}_{rad}$ and the conduction of thermal energy from the surface to the inner parts of the leading edge $\dot{q}_{cond}$.

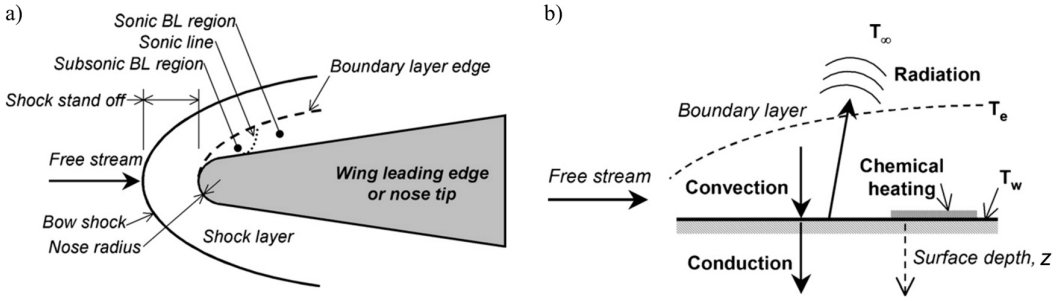

Fig. 2.3: a) Hypersonic flow conditions at a leading edge of a hypersonic vehicle; b) Energy balance at a surface for hypersonic applications [15]

According to Equ. 2.1 to Equ. 2.3, the balancing of the energy fluxes at the surface enables the determination of the cumulated energy flux $\dot{q}_{surface}$ and the temperature difference at the surface for a leading edge during hypersonic flight operation, considering the wall temperature T_W, the surrounding temperature of the freestream condition T_∞ and the Temperature T_e at the boundary layer edge. [15, 26].

$$\dot{q}_{surface} = \sum(\dot{q}_{in}) - \sum(\dot{q}_{out}) \qquad \text{Equ. 2.1}$$

$$\dot{q}_{surface} = (\dot{q}_{conv} + \dot{q}_{chem}) - (\dot{q}_{rad} + \dot{q}_{cond}) \qquad \text{Equ. 2.2}$$

$$\dot{q}_{surface} = \frac{\kappa_T \cdot \Delta T}{z} \qquad \text{Equ. 2.3}$$

With κ_T for thermal conductivity (W/m·K), ΔT for the temperature difference (K), z for surface depth (m). With respect to the CFD simulations and the plasma wind tunnel tests, a requirement list of thermal properties for leading edge materials can be derived. The most important thermal properties are an extremely high melting point, a high specific heat capacity, and a high thermal conductivity to ensure the distribution of the thermal energy along the leading edge, avoiding thermal peaks at the surface. Further, the thermal shock resistance is a particularly important property, as the leading edges will be exposed to extreme temperature fluctuations [15, 24, 26].

2.3 Ultra-High Temperature Ceramics

The Space race from 1955 to 1975 spurred the development of materials that could withstand the harsh and extreme environmental conditions in rocket propulsion systems, leading edges, and tiles of the thermal protective systems (TPS). Undoubtfully, it was already declared that materials with an extremely high melting point are needed to withstand the temperatures during re-entry [27]. Refractory metals such as tungsten (W), rhenium (Re), or tantalum (Ta) reveal melting points >3000°C. However, the density of those metals is too high for such kind of applications (requirements of lightweight constructions). Alternative classes are the borides, nitrides, and carbides of early transition metals. These materials exhibit elevated melting points as shown in Fig. 2.4 and

might be potential candidates for leading edges or thermal protection systems (TPS) for next-generation hypersonic vehicles [27].

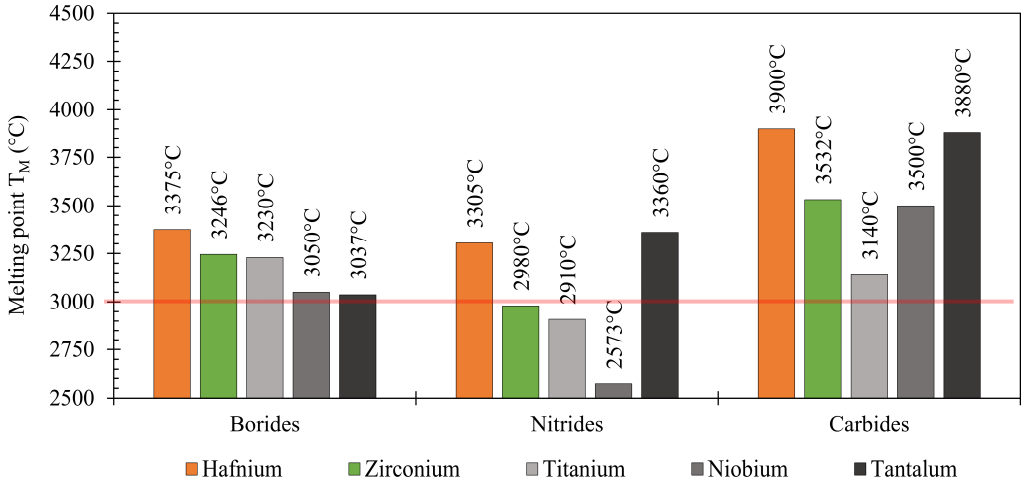

Fig. 2.4: Ultra-High Temperature Ceramics (UHTCs) with the reported melting temperatures, grouped into distinct material families (borides, nitrides, and carbides) (o.i.) [22]

Documents and recordings from the early 1950s labeled these materials as hard metals, cermets, ceramals, refractory ceramics, or oxidation-resistant ceramics. There was no standardized definition. The term "Ultra-High Temperature Ceramics" (UHTCs) appeared in the mid-1960s and is commonly used today for this class of materials [22]. UHTCs define materials with an extreme melting point >3000°C, which can be used in oxidative atmospheres at temperatures of ~1600°C and might be usable for hypersonic applications. Stupendous research on UHTCs with respect to their processing capability, oxidation behavior, mechanical properties, etc. has proposed two most promising candidates namely HfB_2 (orange) and ZrB_2 (green) for applications as reusable leading edges or TPS of hypersonic vehicles. [16, 22, 27, 28].

2.3.1 Transition Metal Diborides

Transition metal diborides (TMB_2) such as ZrB_2 or HfB_2 belong to the most promising UHTCs and consist of a hexagonal crystal lattice with the crystal space group P6/mmm as presented in Fig. 2.5. The Wykoff position for the metal atoms (yellow) is 1a (0,0,0) and the boron atoms (black) is 2d (⅓, ⅔, ½) [16].

The crystal lattice of TMB_2 contains individual layers of metal and boron atoms (Fig. 2.5a-b). The metal atoms are bonded via metallic bonds, revealing delocalized electrons. The boron atoms form a graphite-like ring structure (Fig. 2.5c) with covalent σ and π bonds. Ionic bonding between the individual layers of the metal- and boron atoms leads to the stability of the crystal. Further, covalent π bonds appear between the boron and metal layers due to the hybridization of the 4d orbital of the metal atoms and the 2p orbital of the boron atoms. Therefore, an ionic-covalent bonding prevails between the single layers [16]. The bonding and the hexagonal structure derive the material properties of TMB_2, such as the high hardness (~23 GPa), the high melting point (>3000°C), the low coefficient of thermal expansion, and the high thermal conductivity (κ_T = >65 W/m K). These and other properties depend on the bond strength, the bond type, and

the bonding partners inside the crystal. Table 2.1 summarizes some specific material properties for the predestined candidates ZrB_2 and HfB_2 [16, 29].

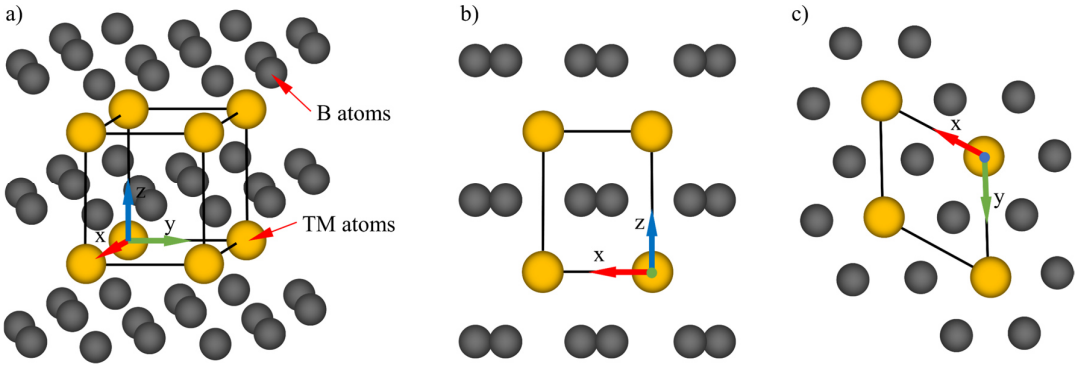

Fig. 2.5: Hexagonal crystal structure of transition metal diborides (TMB_2) with P6/mmm space group in three different perspectives: a) 3D-perspective; b) Perspective in the x-z plane; c) Perspective in the x-y plane (o.i) [16, 30]

Table 2.1: Material properties of ZrB_2 and HfB_2 [11, 13, 16, 27, 29, 30, 31, 32]

Property	ZrB_2	HfB_2	Unit
Crystal system	Hexagonal (AlB_2)	Hexagonal (AlB_2)	-
Prototype structure	P6/mmm (No.191)	P6/mmm (No.191)	-
a = b	3.17	3.14	Å
c	3.55	3.47	Å
α = β	90	90	°
γ	120	120	°
Density ρ	6.07	11.24	g/cm³
Meting point T_M	3245	3380	°C
Young´s modulus E	489	480	GPa
Bulk modulus K	215	212	GPa
Hardness	23	28	GPa
Coefficient of thermal expansion α_v	$5.9*10^{-6}$	$6.3*10^{-6}$	1/K
Specific heat capacity c_P	48.2	49.5	J/g·K
Thermal conductivity κ_T (at 1400°C)	67	104	W/m·K

The superior mechanical, physical, and thermal properties of ZrB_2 and HfB_2 make them suitable materials for their usability for applications such as leading edges, rocket noses, or TPS of hypersonic missiles [11, 13]. As provided in Table 2.1, both ceramics are similar in most of the properties. HfB_2 has a higher thermal conductivity κ_T and a slightly higher specific heat capacity c_p. Furthermore, HfB_2 reveals better oxidation resistance up to temperatures of 1790°C compared to ZrB_2, which will be described in detail (see Chapter 3.2). However, ZrB_2 has a lower density

compared to HfB_2 by r.a. ~47%. The high density of HfB_2 (ρ~11 g/cm³) is more comparable to high refractory metals such as tungsten (ρ~19 g/cm³) or tantalum (ρ~16 g/cm³) and is too high to follow the requirements of light-weight constructions in the space and aerospace industry. Therefore, ZrB_2 is the first choice to be considered by most research groups and companies over the world [27, 31, 32].

2.3.2 Processing of Zirconium Diboride Bulk Material

Theoretically, ZrB_2 consists of ~33 at.% zirconium and ~66 at.% boron. Various reaction processes can be used to produce ZrB_2. The process of carbon/borothermal reduction is particularly common, in which powder of zirconium dioxide (ZrO_2) is used as the transition metal source and powder of boron carbide (B_4C) as the boron source. Powders are ball-milled for several hours to produce a homogenous powder mixture with a specific average grain size. After milling, the powder mixture will be synthesized. An excess of C is added to the powder mixture as a reaction aid for the reaction described in Equ. 2.4. The reaction leads to an increase in the enthalpy of ΔH = 1175 kJ or a free enthalpy of ΔG = 961 kJ [30, 33, 34].

$$2ZrO_2 + B_4C + 3C \rightarrow 2ZrB_2 + 4CO \uparrow \qquad \text{Equ. 2.4}$$

$$ZrO_2 + \frac{5}{6}B_4C \rightarrow ZrB_2 + \frac{5}{6}C + \frac{2}{3}B_2O_3 \uparrow \qquad \text{Equ. 2.5}$$

$$ZrO_2 + B_2O_3 + 5C \rightarrow ZrB_2 + 5CO \uparrow \qquad \text{Equ. 2.6}$$

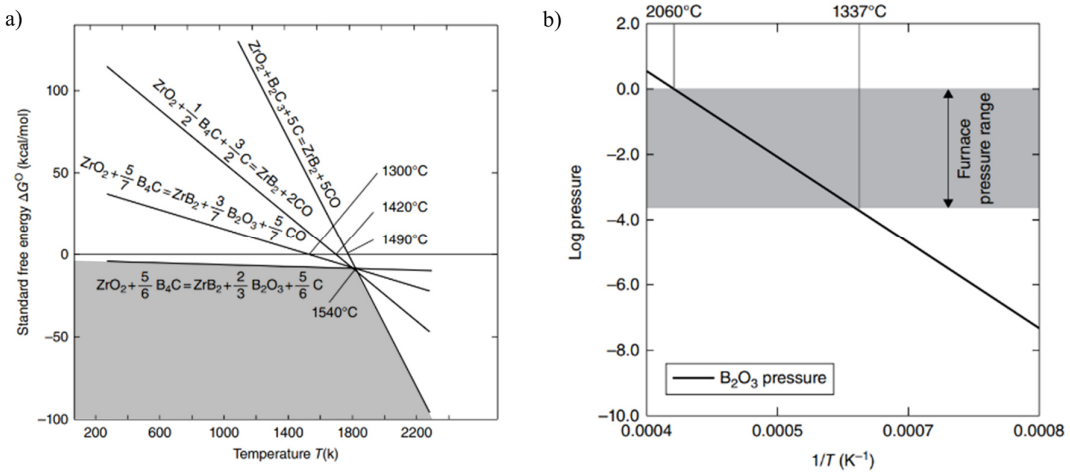

Fig. 2.6: a) Standard free energy ΔG^O of various possible ZrB_2 reactions as a function of temperature; b) Calculated vapor pressure of B_2O_3 as a function of temperature in the pressure range maintained during sintering [34]

The endothermic reaction takes place at temperatures >1300°C. Several reports have confirmed intermediate reactions according to Equ. 2.5 and Equ. 2.6. The results of thermodynamic calculations for the reactions are shown in Fig. 2.6a. The reaction of Equ. 2.5 is the favorable reaction

at temperatures <1540°C and leads to an incomplete reaction by forming boron Trioxide (B_2O_3). Then again, at temperatures >1540°C, reaction Equ. 2.6 is favored and induces the reaction between ZrO_2 and B_2O_3 to ZrB_2. The vapor pressure of B_2O_3 increases with the temperature and leads to evaporation >1250°C (see Fig. 2.6b). Several publications proved the negative influence of the loss of B_2O_3 during the synthesis process [30, 34].

According to Equ. 2.7, the deficit in B_2O_3 might lead to the formation of zirconium carbide (ZrC). To avoid the formation of ZrC, a surplus of approximately 20-25 wt.% B_4C is added to the powder mixture to compensate the loss of B_2O_3. As a result, the synthesis follows Equ. 2.8 [34].

$$ZrO_2 + 3C \rightarrow ZrC + 2CO \uparrow \qquad \text{Equ. 2.7}$$

$$ZrC + B_2O_3 + 2C \rightarrow ZrB_2 + 3CO \uparrow \qquad \text{Equ. 2.8}$$

For the next step, the synthesized ZrB_2 will be ball-milled and sieved to a uniform grain size. Subsequently, the ZrB_2 powder can be processed to a dense monolithic body using sintering processes such as spark plasma sintering (SPS) or hot-pressing methods (HP, HIP, …) [35, 36]. The powder sinters to a monolithic bulk under high pressure of up to 30 MPa and temperatures >1900°C The addition of sintering aids such as carbon improves the sintering process to achieve a bulk density of >95%. Depending on the amount of sintering aid, an excess of C can accumulate at grain boundaries. Adequate sintering parameters are well-studied. Several parameters such as the grain size, the temperature, the pressure, the dwell times, as well as the heating/cooling rates have a dramatic effect on the sintering process and the material properties of the produced materials. Neuman et al. investigated the hot-pressing process of ZrB_2 in detail and performed several experiments. The results are described in detail in literature [33].

2.3.3 Oxidation Behavior of Zirconium Diboride

The oxidation and degradation of materials under hypersonic flight conditions is a limiting factor for components of hypersonic vehicles, especially for leading edges or rocket noses. Therefore, the characterization of the oxidation behavior and optimization of the oxidation resistance is in research focus worldwide. The oxidation behavior of TMB_2 has been analyzed under a wide variety of test methods/test facilities (thermogravimetry, isothermal oxidation, oxidation under various atmospheres/box furnaces, tube furnaces, plasma wind tunnels, torch testing, …). Most oxidation experiments have been tested in atmospheric furnaces with electrical resistance heaters. However, it is extremely difficult to simulate the near hypersonic conditions in a laboratory setup. Parameters such as the energy flux, the temperature, the static and dynamic pressure changes, the velocity of the atmosphere at the surface, the structural vibrations, moisture in the air, and more factors can not be considered in most cases [13, 20, 37-41]. However, the laboratory tests enable to understand the fundamental mechanisms.

Based on the extensive amount of literature over the last 60 years in the research field of UHTC oxidation, the mechanisms, the oxidation products, as well as the oxidation kinetics of ZrB_2 and other TMB_2 are well understood and are described in the following.

2.3.4 Oxidation Products of Zirconium Diboride

Following Equ. 2.9, thermal exposure of ZrB_2 in an oxygen-rich atmosphere leads to the oxidation of the material and the formation of ZrO_2 and B_2O_3 [28, 42-44].

$$ZrB_2 + \frac{5}{2}O_2 \rightarrow ZrO_2 + B_2O_3 \qquad \text{Equ. 2.9}$$

2.3.4.1 Zirconium Dioxide

The high refractory oxide ZrO_2 shows a monoclinic crystal structure at room temperature with the space group P21/c. According to the chemical composition, the oxide consists of ~33 at% Zr and 66 at% O. Temperature-depending phase transitions of ZrO_2 from monoclinic (m-ZrO_2) to tetragonal (t-ZrO_2) and to cubic structure (c-ZrO_2) occurs, following Equ. 2.10. Properties of the crystal modifications are provided in Table 2.2 [42, 43, 45, 46].

$$m - ZrO_2 \underset{950°C}{\overset{1120°C}{\rightleftarrows}} t - ZrO_2 \underset{2370°C}{\overset{2370°C}{\rightleftarrows}} c - ZrO_2 \underset{2680°C}{\overset{2680°C}{\rightleftarrows}} liquid \qquad \text{Equ. 2.10}$$

Table 2.2: Properties of ZrO_2 modifications [47-50]

Property	m-ZrO_2	t-ZrO_2	c-ZrO_2
Crystal system	Monoclinic	Tetragonal	Cubic
Space group	$P2_1/c$, (No.14)	$P4_2/nmc$ (No.137)	Fm-3m (No.225)
Density ρ (g/cm³)	5.817	5.861	7.195
Unit cell volume (Å³)	146.81	68.56	131.87
Wyckoff position (Zr)	2a, 2d	2a	4a
Volume per Zr-atom	36.70	34.28	32.97
Volume contraction (vol%)	-	-6.59	-9.17

The phase transition from m-ZrO_2 to t-ZrO_2 at~1120°C leads to a volume reduction of ~6.6 vol% (considering the Wykoff position of the zirconium atoms and the volume of the elementary cell). Since the temperature range of interest is focused <2370°C, the transformation to the cubic ZrO_2 modification will not be discussed [50].

A detailed investigation of the phase transition of m-ZrO_2↔t-ZrO_2 was carried out, describing the martensitic transformation of ZrO_2 grains due to the volume expansion during t-ZrO_2→m-ZrO_2 phase transition. The martensitic transformation is well known for metallic alloys, very well known for steel with a carbon content of 0.22-0.6 % [51]. This phenomenon is also observed in ceramic materials. Martensitic transformation is defined as a crystal modification in a solid state, that is athermal, diffusionless, and requires a significant volume change such that strain energy affects the kinetics and morphology of the crystal during transformation [46, 51-56].

The induced volume expansion for the t-ZrO_2→m-ZrO_2 phase transition was calculated to be ~6.6 vol% (calculated by Wykoff position of Zr Atoms in the unit cells, compare Table 2.2). Values of ~5 vol% are mentioned in the literature. However, the diffusionless and abrupt phase transition leads to stresses inside the m-ZrO_2, increasing the strain energy in the system. To induce the martensitic transformation, the free energy barrier needs to be overcome according to Equ. 2.11 [46, 54].

$$\Delta G_{t\rightarrow m} = V \cdot (-\Delta G_{ch} + \Delta G_{Strain}) + S \cdot \Delta G_{Surface} \qquad \text{Equ. 2.11}$$

with $\Delta G_{t\rightarrow m}$ for the change in total Gibbs free energy (kJ), V for the volume of the transformed volume (m^3), ΔG_{ch} for the chemical free energy change (kJ), ΔG_{Strain} for the strain energy (including shear and dilatation energy) (kJ), S for the transformation area (m^2) and $\Delta G_{Surface}$ for the surface energy at the interface between the martensite and the former phase (including twinning energy and micro-cracking energy) (kJ) [46].

The martensite is characterized by twinning and several twin variants as described in numerous investigations for the martensitic t-ZrO_2→m-ZrO_2 phase transition. After extensive research, Kelly and Rose assigned the twinning in the ZrO_2 as the mechanism to reduce the overall shear strain in the crystals. Detailed information about the twinning planes and crystal orientations of ZrO_2 are described in literature [46, 52-55]. The schematic in Fig. 2.7 illustrates a stepwise transformation of a spherical t-ZrO_2 grain to the self-accommodating m-ZrO_2 variant with marked shear stresses in the untransformed regions of the grain. The shear forces induce the continuous growth of transformed variants by twinning, forming regular structures, sometimes described as „herringbone“ structures [52, 54].

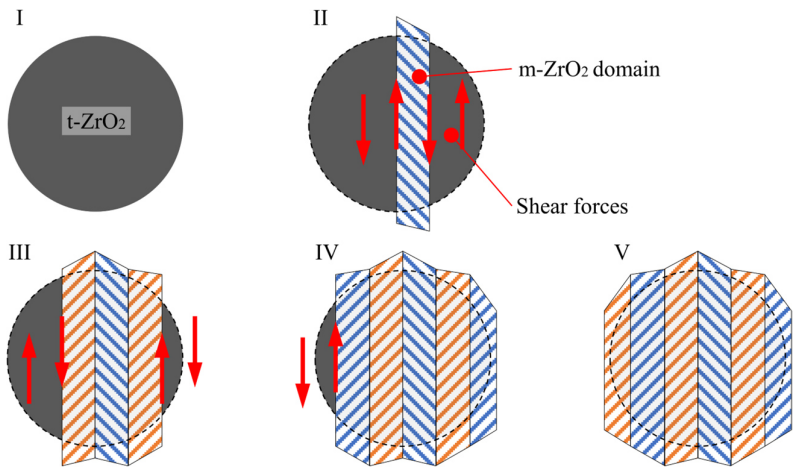

Fig. 2.7: Stepwise schematic of martensitic transformation of t-ZrO_2 to self-accommodating m-ZrO_2 variants (twins), starting from I to V (o.i.) [54]

A second mechanism was observed for ZrO_2, which induces twinning. Hereby, twins form in tetragonal stabilized ZrO_2 with additives such as Ceria (CeO_2) or Yttria (Y_2O_3). The mechanism is called ferroelastic transformation and occurs in case of external mechanical stresses. Similar to the martensitic transformation, twinning planes form in the ZrO_2, causing tetragonal polydomains

(t‘-ZrO_2). Instead of a phase transition, that induces volume contraction (martensitic transformation), the phase and volume remain stable during ferroelastic transformation.

In both cases, martensitic or ferroelastic transformation, the mechanical properties such as the toughness of the ZrO_2 increase due to the transformation. The stressed grains in the transformed areas inhibit the progression of cracking through the material by changing the transformation zone at the tips of cracks. The transformation lowers the peak strain and inhibits crack propagation. This well-known mechanism to increase the toughness of ZrO_2 is used for biomedical applications such as implantates [52-54].

2.3.4.2 Boron Trioxide

Boron Trioxide (B_2O_3), also commonly known as boria, is the second oxidation product from the oxidation of ZrB_2 (see Equ. 2.9). Crystalline and white B_2O_3 powder reveals a hexagonal crystal structure with the space group P31. The production of crystalline B_2O_3 is complex and time-consuming due to its very low crystallization rate [57]. Rapid cooling/quenching usually exhibits the amorphous nature of B_2O_3 with glass-like properties and a whitish-transparent appearance. B_2O_3 glass has a melting point of ~450°C and forms a viscous liquid [58]. At elevated temperatures >1250°C, the liquid starts to evaporate and forms gaseous products such as BO, BO_2, or B_2O_3 [58, 59]. The vaporization rate of B_2O_3 increases with respect to the oxidation temperature and/or in the presence of moisture, inducing the formation of volatile components such as HBO_2 [39]. Various properties of B_2O_3 such as its solubility in water, the low-weight elements, and its amorphous nature due to the extremely slow crystallization rate pose various challenges in the identification of the glass. Its amorphous state disables the detection via diffraction techniques such as X-ray diffraction (XRD) or electron diffraction. The elemental analysis via energy-dispersive X-ray spectroscopy (EDS) is not a reliable measuring method for the differentiation of light elements such as boron, carbon, and oxygen ($Z < 11$) [60, 61]. Finally, the water-solubility of B_2O_3 does not allow the preparation of polished cross sections with intact glassy layers and won't provide any information regarding the B_2O_3. Appropriate alternatives to detect B_2O_3 in a more reliable way would be wavelength-dispersive X-ray spectroscopy (WDS), Raman spectroscopy, or Glow Discharge Optical Emission Spectroscopy (GDOES) [39, 60].

2.3.5 Oxidation Mechanisms of Zirconium Diboride

The oxidation behavior of ZrB_2 is complex and is affected by environmental conditions such as the oxidation temperature, composition of the atmosphere, the energy flux, the velocity and sheer force of the oxidizing atmosphere to the surface, and more. A fundamental oxidation model for ZrB_2 and other diboride-based UHTCs was developed and described by Parthasarathy et al. The model based on the results of several publications over the years. The oxidation model by Parthasarathy et al. for three distinct temperature regimes is illustrated in Fig. 2.8, considering normal lab air in a static oxidizing atmosphere [42, 43].

Oxidation temperatures <1000°C are defined as the low-temperature regime (formation rate of $B_2O_3 \geq$ evaporation rate of B_2O_3) (Fig. 2.8a). The oxidation in this temperature regime leads to the formation of a liquid B_2O_3 layer at the surface and a porous ZrO_2 scale with elongated grains. Gaps between the single ZrO_2 grains are filled with the liquid B_2O_3 [42]. According to the model of Parthasarathy, the porous ZrO_2 is impermeable to oxygen. It is concluded that the low electrical

conductivity (κ_E = ~2x10^{-6} S/cm) for ZrO_2 does not guarantee ambipolar diffusion of positively charged oxygen vacancies and negatively charged electrons as described in Wagner´s model of oxidation [43, 62]. The porosity inside the ZrO_2 oxide scale is assumed to be a continuous network, which enables the mobility of oxygen through the porous oxide scale to the oxidation front of the ZrB_2 substrate, controlled by Knudsen diffusion [43]. However, the liquid layer of B_2O_3 at the surface acts as a protective layer and inhibits the mobility of oxygen to the substrate. Oxygen must permeate through the liquid scale, which reduces the mobility of oxygen molecules through the oxide scale to the oxidation front of the underlying ZrB_2 substrate. Correspondingly, the B_2O_3 glass reduces the oxidation progression [42, 43, 63-66].

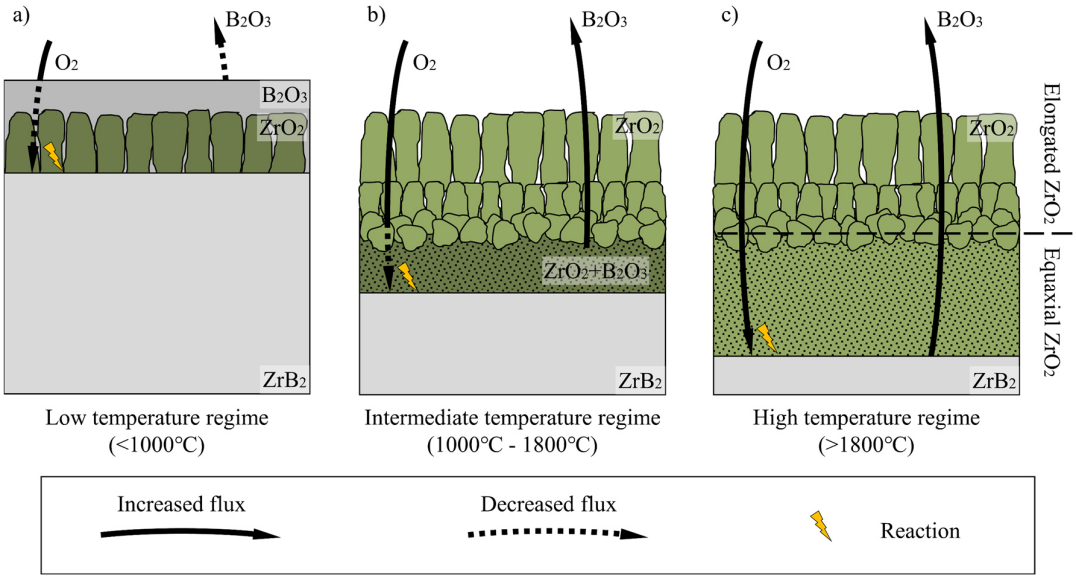

Fig. 2.8: The model of oxidation for ZrB_2 at different temperature regimes by Parthasarathy et al.: a) Low-temperature regime <1000°C; b) Intermediate temperature regime between 1000°C to 1800°C; c) High-temperature regime >1800°C (o.i.) [42, 43]

The oxidation studies of Opeka et al. carried out a temperature-related equilibrium between the condensation and the evaporation of the protective B_2O_3 in the low-temperature regime. This ensures the coverage of the surface with protective B_2O_3 glass for long-term periods [12, 23, 67]. Fahrenholtz et al. continued this work and developed a volatility diagram for ZrB_2 as presented in Fig. 2.9. The work provides a comprehensive view of the thermodynamic behavior of ZrB_2. The black lines in the diagram show the partial pressure $p_{(x)}$ of the most favorable boron-based gaseous composition for isothermal oxidation at different partial pressures of oxygen. Gaseous species such as B, BO, or B_2O_2 might form, considering crystalline ZrB_2 as the primary condensed phase in oxygen-reduced atmospheres (i.e. low vacuum conditions or different gas mixtures). Gaseous components such as B_2O_3, or BO_2 will form involving ZrO_2 and B_2O_3 as the primary condensed phases at normal or oxygen-rich atmospheres [32, 58, 59, 68]. As the thermodynamic calculations demonstrate, the partial pressure of gaseous boron-based species increases with the oxidation temperature and indicates enhanced evaporation of the B_2O_3 glass during oxidation. This aligns with the observations of Rizzo et al. Parabolic oxidation rates were observed for the oxidation of boron for temperatures up to ~1000°C, whereas the evaporation of the protective

B_2O_3 glass at higher temperatures revealed a rate-limiting step in the oxidation of kinetics [58]. Regarding to the results of Opeka, Fahrenholtz, and Rizzo, the evaporation of the protective B_2O_3 glass induces the recession of the protective liquid layer at the surface. Since the rate-controlling mechanism belongs to the liquid layer, the recession of the glass must cause a transition of the oxidation mechanisms of ZrB_2 at temperatures >1000°C [12, 23, 32, 59].

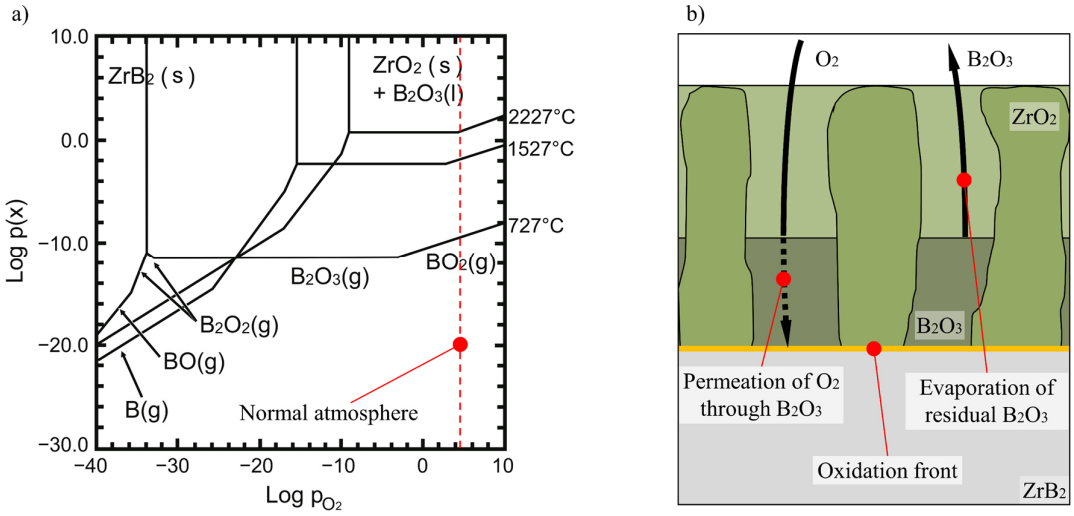

Fig. 2.9: *a) . The volatility diagram of ZrB_2 at 727°C, 1527°C, and 2227 °C [59]; b) Mechanistic steps at the oxidation front of ZrB_2 in the intermediate temperature regime (1000°C to 1800°C) (o.i.) [42, 43]*

Temperatures between 1000°C to 1800°C are defined as the intermediate temperature regime (formation rate of $B_2O_3 \leq$ evaporation rate of B_2O_3). The increased exposure temperature induces rapid evaporation of B_2O_3 and the formation of gaseous components such as B_2O_3 or BO_2 according to Equ. 2.12 and Equ. 2.13 [32, 59].

$$B_2O_3 \rightarrow B_2O_3 \uparrow \qquad \text{Equ. 2.12}$$

$$B_2O_3 + \frac{1}{2}O_2 \rightarrow 2BO_2 \uparrow \qquad \text{Equ. 2.13}$$

As illustrated in Fig. 2.8b, once the protective B_2O_3 evaporates during oxidation and leaves behind a dry and unprotective porous ZrO_2 scale with residual B_2O_3 liquid inside the porous oxide scale. The Fig. 2.9b presents a model for the oxidation mechanisms inside the porous ZrO_2 scale during oxidation at the intermediate temperature regime. Oxygen molecules trespass the oxide scale through the dry pores to the residual B_2O_3 liquid, following the Knudsen diffusion of porous materials. Subsequently, the oxygen molecules get inhibited in their mobility at the B_2O_3 surface and must diffuse/permeate through the boria-filled pores to the oxidation front of ZrB_2. Simultaneously, the residual B_2O_3 liquid in the porous network evaporates with a distinct evaporation rate and leaves the oxide scale [43, 69].

Finally, oxidation at temperatures >1800°C is defined as the high-temperature regime (formation rate of $B_2O_3 <<$ evaporation rate of B_2O_3). As implied in Fig. 2.8c, the increased evaporation rate

of B_2O_3 prevents the formation of a protective liquid layer and leads to the instantaneous evaporation of B_2O_3 at the oxidation front of ZrB_2. Consequently, the formed oxide scale on ZrB_2 consists of porous ZrO_2 with a dry pore network, which does not prevent the oxygen mobility to the oxidation front of ZrB_2 [42, 43]. As already mentioned, the temperature affects the formation rate and evaporation rate of B_2O_3. It can be concluded, that as long as the formation rate is ≥ the evaporation rate, the system undergoes passive oxidation by liquid B_2O_3 layer [58].

2.3.6 Oxidation Kinetics of Zirconium Diboride

Several publications address the oxidation kinetics for ZrB_2 and other TMB_2. As mentioned above, the various parameters affect the oxidation mechanisms and, consequently, change the oxidation kinetics. Therefore, deviations in the results are possible. However, it is understood that ZrB_2 exhibits parabolic oxidation with increasing oxidation rate constant with enhancing temperature and time. Parabolic oxidation kinetics can be determined by measuring the oxide scale growth, the recession of the substrate, or the mass change with respect to time. Considering extended exposure time for several minutes, Deal and Grove´s differential equation for linear-parabolic oxidation kinetics can be applied by measuring the oxide scale thickness, following Equ. 2.14 [70-72].

$$K_{P\,i} = \frac{x_i^2}{t_i} \qquad \text{Equ. 2.14}$$

with K_{Pi} (µm²/min) for the parabolic oxidation rate constant and x_i (µm) for the measured oxide scale thickness at time t_i (min). The effect of boria and its evaporation, concerning the temperature and time, won't be considered in the calculations [70]. The Fig. 2.10a presents linear and parabolic oxide growth in a graph of thickness x_i vs. time t_i, whereas Fig. 2.10b presents the plots of linear and parabolic oxide growth in a graph of thickness squared x_i^2 vs. time t_i. As visible, parabolic oxidation is related to a linear plot progression (yellow plot) and indicates the parabolic oxidation rate constant K_{Pi}, corresponding with the slope of the plot as marked in the figure [72].

Further, an Arrhenius plot can be used to visualize the effect of the temperature on the oxidation kinetics for a prescribed exposure time t_i. The slope of the Arrhenius plot corresponds to the activation energy E_A/R as marked in Fig. 2.10c [28, 71]. The relation between the parabolic rate constants, the oxidation temperatures, and the activation energy for the oxidation process of a prescribed exposure time can be described by Equ. 2.15 [71, 72].

$$ln\left(\frac{K_{P_1}}{K_{P_{ref}}}\right) = \frac{E_A}{\mathrm{R}} \cdot \left(\frac{1}{T_{ref}} - \frac{1}{T_1}\right) \qquad \text{Equ. 2.15}$$

with E_A (kJ/mol) for the activation energy, R for the ideal gas constant (8.314 J/mol·K), K_{Pi} (µm²/min) for the parabolic oxidation rate constant, and T_i (K) for the temperatures.

A steeper slope of the Arrhenius plot corresponds with increased activation energy for the oxidation and an increased sensitivity of the oxidation process to temperature changes. A fluctuating progression of the plot can be interpreted as the modification of the oxidation mechanisms and/or the change of the oxidation kinetics (i.e. phase transitions, loss of a protective coating/scale, change in oxidation reaction, …) [71, 72].

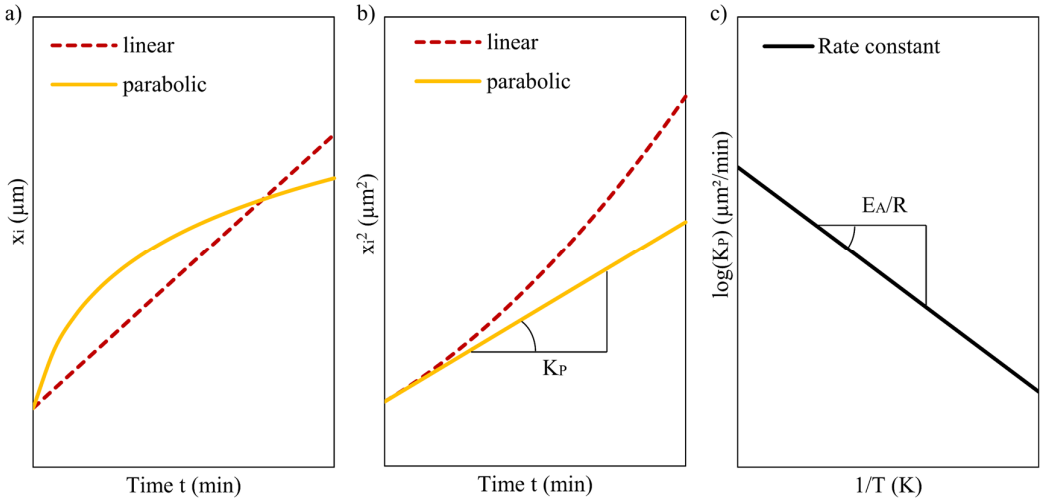

Fig. 2.10: *a) Oxide scale thickness x_i vs. Time; b) Oxide scale thickness squared x_i^2 vs. Time; c) Logarithmized oxidation rate constants K_P vs. inverse Temperature (1/T) (compare Equ. 2.14 and Equ. 2.15) (o.i.) [71, 72]*

The Arrhenius plot of ZrB_2 is an adequate example of a discontinuous progression of oxidation and the transition of the oxidation mechanisms with respect to the oxidation temperature. The Arrhenius plot for ZrB_2 is presented in Fig. 2.11, showing the logarithmized oxidation rate constants vs. the inverted temperature. A constant increase of the oxidation rate constants can be observed in the temperature range of ~1000°C to ~1120°C. The phase transition from m-ZrO_2 to t-ZrO_2 at ~1120°C leads to a volume reduction of ~6.6 vol%. The volume reduction induces the formation of cracks along the pores, forming a comprehensive porous network inside the porous oxide scale. As per the observations and calculations are concerned, the mobility of oxygen molecules through the porous oxide scale to the oxidation front of ZrB_2 increases abruptly, leading to a steep increase of the oxidation rate constant and significantly high activation energy (~1400K to ~1430K). Further increase of the oxidation temperature enforces the evaporation of the protective B_2O_3. In combination, the porous network and the evaporation of B_2O_3 induce an increase in activation energy and oxidation kinetics [43].

According to the observations of Parthasarathy et al., a more dominant influence to improve the oxidation resistance was found in the reduction of the porous ZrO_2 oxide scale rather than the protection of the system by liquid B_2O_3. Most of the protective liquid will be blown away during hypersonic flight operation and won't remain at the surface to provide protection [42, 43].

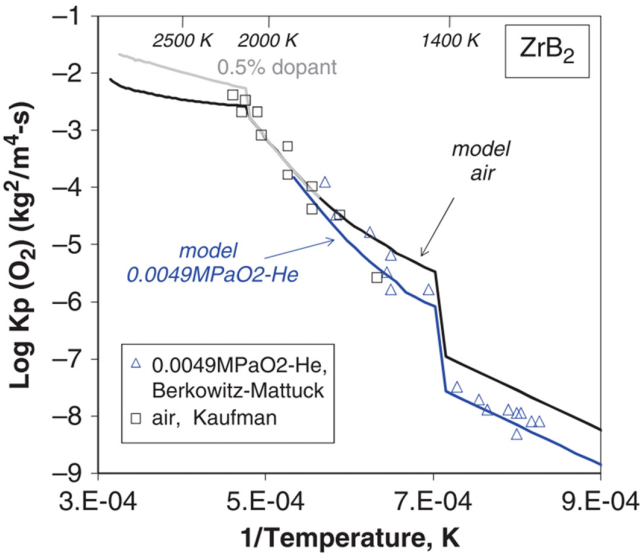

Fig. 2.11: Arrhenius plot of the parabolic rate constant of ZrB_2: Discontinuous plot indicates a transition of the oxidation behavior and aligns with the phase transitions of ZrO_2 [43]

As mentioned above, the oxygen mobility through a porous ZrO_2 scale can be described with Knudsen diffusion, which based on Fick´s laws of diffusion. The equations for the Knudsen diffusion coefficient $D_{K,\,Pore}$ (m^2/s) for an ideal gas through a pore as well as a diffusion coefficient through a porous network $D_{K,\,Medium}$ (m^2/s) with a specific porosity ε and tortuosity τ are presented in Equ. 2.16 and Equ. 2.17 [42, 43, 63, 65, 73, 74].

$$D_{K,\ Pore} = \frac{d_{Pore}}{3} \cdot \sqrt{\frac{8}{\pi} \cdot \frac{R \cdot T}{M}} \qquad \text{Equ. 2.16}$$

$$D_{K,\ Medium} = \frac{\epsilon}{\tau} \cdot D_{K,\ Pore} \qquad \text{Equ. 2.17}$$

with d_{Pore} for the pore diameter (m), M for the molar mass of the diffusing gas (kg/mol), ε for the porosity in the solid medium (no unit), and τ for the tortuosity (no unit) [74]. The results of the parametric sensitivity study of Parthasarathy et al. are presented in Fig. 2.12, considering the porosity ε and the average pore diameter d_{Pore}. The tortuosity τ was neglected for the study [43].

As illustrated in Fig. 2.12a, the pore diameter d_{Pore} influences the oxidation behavior for diameters ≤3 µm. A significant reduction of the oxidation rate constant can be observed with decreasing pore diameter. Considering the Knudsen diffusion through a pore (Equ. 2.16), the mobility of the oxygen molecules will be reduced with the pore diameter and oxygen molecules will take more time to pass the pores in the solid oxide. The reducing effect of the pore diameter on the rate constants becomes more significant for temperatures >1400°C. This can be explained by the enhanced evaporation of the protective B_2O_3, leaving the dry and porous ZrO_2 scale. Consequently, a strong effect of the pore diameter can be seen at high temperatures of ~2100°C since there is no formation of a protective B_2O_3 liquid [42, 43].

An increase in the pore diameter comes with increased oxygen mobility through the pore. As a result, more oxygen molecules will be able to pass the pore for a prescribed time and will increase the amount of reactive oxygen molecules at the oxidation front of the ZrB_2 substrate. Subsequently, the parabolic oxidation rate constants increase, which is accompanied by increased kinetics [42, 43].

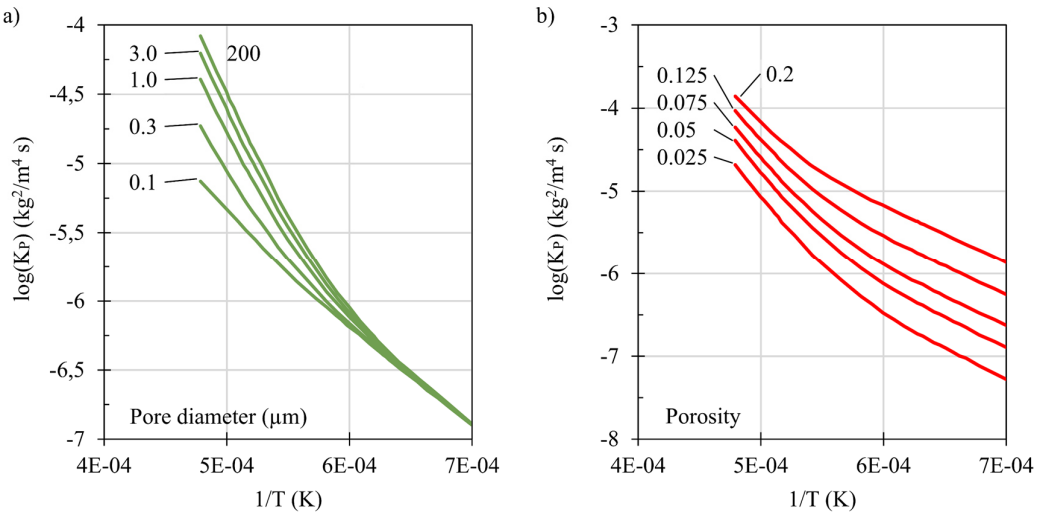

Fig. 2.12 : a) The effect of pore diameter (Knudsen effect) on the parabolic rate constant of ZrB_2 (o.i.) [42]; b) The effect of pore fraction/porosity on the parabolic rate constant of ZrB_2 (o.i.) [42]

The porosity affects the oxidation mechanisms differently than the pore diameter as visible in Fig. 2.12b. An increase of the pore fraction from ~2.5 10^{-2} to 2 10^{-1} results in an increase of approximately one order of magnitude for the logarhitmized oxidation rate constant. The effect of the increase is nearly linear in the temperature range of 1400°C to 2100°C, shifting the oxidation rate constants to lower values with decreasing porosity. The increasing porosity will enable multiple oxygen molecules simultaneously to pass the porous oxide scale in a prescribed time. As a result, more oxygen molecules in the magnitude of the number of pores will pass the porous oxide scale to the oxidation front of ZrB_2 and induce the oxidation of the substrate (increased oxidation kinetics) [42, 43].

2.3.7 Solutions to Improve the Oxidation Resistance of Zirconium Diboride

2.3.7.1 Addition of Silicon Carbide to Zirconium Diboride

Several approaches were considered to improve the oxidation resistance of ZrB_2 for the intermediate temperature regime >1500°C. The most common and partially successful approach is to alloy UHTCs with additives such as Silicon carbide (SiC). Shugart et al. studied the effect of SiC addition to ZrB_2 extensively by adding a distinct amount of SiC from 5 vol% up to 30 vol%, described the oxidation mechanisms, and determined the oxidation kinetics for different test conditions. Shugart observed that the addition of 30 vol% SiC revealed the best protection mechanisms [38, 44, 63, 68, 75-77].

This can be explained by the oxidation mechanisms of ZrB_2-SiC compounds. While ZrB_2 oxidizes to ZrO_2 and liquid B_2O_3, the addition of SiC causes the formation of SiO_2 and gaseous CO, following Equ. 2.18. Finally, B_2O_3 and SiO_2 will form a liquid solution at the surface (Si,B)O, forming a more protective Borosilicate glass following Equ. 2.19 [38, 44, 63, 68, 75-77].

$$ZrB_2 + SiC + 4O_2 \rightarrow ZrO_2 + B_2O_3 + SiO_2 + CO \uparrow \quad \text{Equ. 2.18}$$

$$xSiO_2 + yB_2O_3 \rightarrow xSiO_2 \cdot yB_2O_3 \quad \text{Equ. 2.19}$$

Compared to B_2O_3 liquid, the Borosilicate glass (Si,B)O revealed an increased viscosity and a reduced evaporation rate at elevated temperatures. As a result, the Borosilicate glass accumulates at the surface and forms a protective liquid layer for extended exposure times and enhanced oxidation temperatures (formation rate of (Si,B)O > evaporation rate of (Si,B)O) [77]. A schematic in Fig. 2.13a describes the oxidation mechanisms in the initial time for up to 30 seconds between 1450°C to 1650°C. Borosilicate glass and chunks of ZrO_2 form at the surface of the ZrB_2-SiC substrate after ~10 seconds already. Gaseous components such as CO form during the oxidation of SiC and accumulate at the oxidation front, leading to gas-filled bubbles. Once the bubbles burst, ZrO_2 grains and unoxidized substrate material are exposed (~30 seconds). The top-view micrograph in Fig. 2.13b shows ZrB_2-30 vol% SiC after the oxidation for 30 seconds at 1500°C. The surface revealed several burst bubbles at the surface, exposing ZrO_2 grains and unoxidized material to the oxidizing atmosphere [38, 44, 63, 68, 75-77].

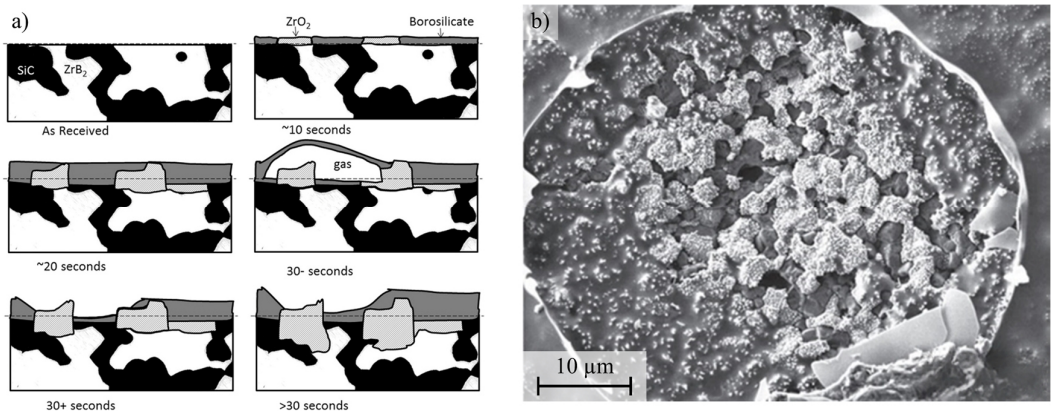

Fig. 2.13: a) Proposed oxidation mechanism of ZrB_2-SiC composites for short term oxidation in a temperature regime of 1450°C-1650°C [38]; b) Burst bubble at ZrB_2-30 vol% SiC composites after oxidation for 30 seconds at 1500°C [76]

The proposed oxidation mechanisms of ZrB_2-SiC by Karlsdottir et al. during long-term oxidation up to 120 min at ≥1550°C is illustrated in Fig. 2.14 . A four-layer oxide scale was observed. The uppermost section was found to be a continuous layer of Borosilicate glass, covering a ZrO_2 oxide scale with SiO_2. An intermediate layer of a SiC-depleted ZrB_2 separates the unaffected ZrB_2-SiC from the residual oxide scale [68].

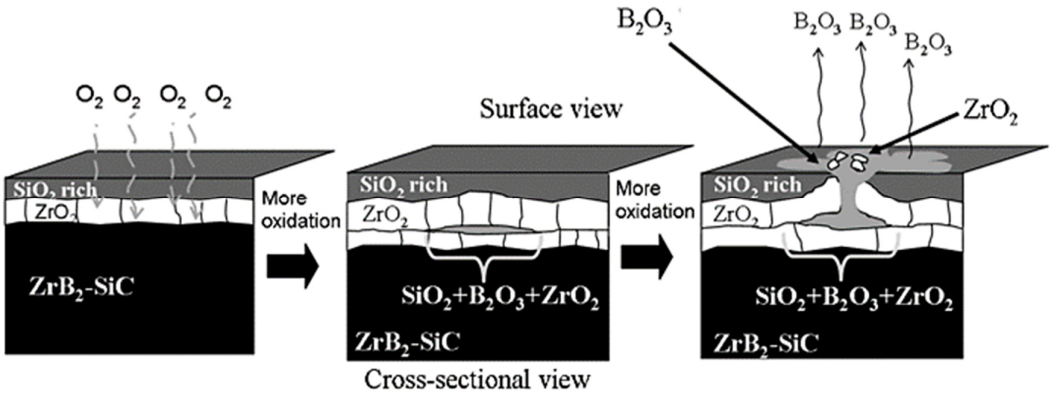

Fig. 2.14: Proposed oxidation mechanism of ZrB_2-SiC for long-term oxidation up to 120 min at 1550°C, showing the formation of convection cells through the ZrO_2 and the SiO_2 layer [78]

The oxidation at temperatures ≥1550°C induces the evaporation of the liquid B_2O_3 and the formation of a SiO_2-rich layer at the surface. This layer prevents the oxygen mobility to the substrate. Considering an increase of the molar volume of SiC (V_m = 12.43 cm³/mol) to SiO_2 (V_m = 27.43 cm³/mol) as well as for ZrB_2 (V_m = 18.54 cm³/mol) to B_2O_3 (V_m = 55.2 cm³/mol) and ZrO_2 (V_m = 20.92 cm³/mol), the Borosilicate glass will lead to an increase of the volume by approximately ~380 % [78].

Further oxidation of the ZrB_2-SiC substrate leads to the formation of reservoirs inside the oxide scale, filled with liquid Borosilicate and dissolved ZrO_2. The liquid-filled reservoirs were defined as convection cells (third picture in Fig. 2.14). The volume expansion due to the formation of liquid Borosilicate glass induces pressure inside the reservoirs, which will lead to the breakthrough of the liquid through the ZrO_2 oxide scale to the surface. The volatile B_2O_3 evaporates at the surface and enforces the precipitation of the dissolved ZrO_2, forming particles with a size of 0.5-2 µm at the surface. The Fig. 2.15a shows a top-view micrograph of ZrB_2-15 vol% SiC after the oxidation at 1550°C for 120 min. Several convection cells inside the SiO_2 scale with precipitated ZrO_2 particles and residual B_2O_3 pools can be found. A cross-sectional micrograph of a convection cell, formed on ZrB_2-15 vol% SiC 1550°C is presented Fig. 2.15b [35, 68].

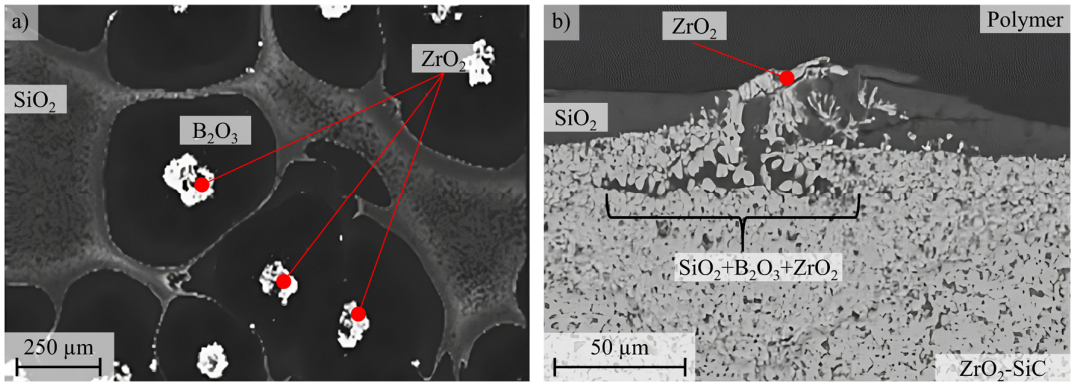

Fig. 2.15 : a) Top-view of convection cells after oxidation of ZrB_2-15 vol% SiC at 1550°C for 120 min [78]; b) Cross-sectional micro-graph through a convection cell after oxidation of ZrB_2-15 vol% SiC at 1550°C for 240 min [78]

Shugart et al. performed oxidation experiments with ZrB_2-30 vol% SiC for a discrete time of 10 min at various oxidation temperatures. The logarithmized parabolic oxidation rate constants ($\log(K_P)$) for the tested specimens (ZrB^2-30vol% SiC) are visualized in an Arrhenius plot in Fig. 2.16a. A protective nature can be observed for temperatures between 1300°C to 1500°C with low oxidation rate constants and significantly reduced activation energies, indicating passive oxidation by the protective Borosilicate glass and/or SiO_2 layer at the surface [75].

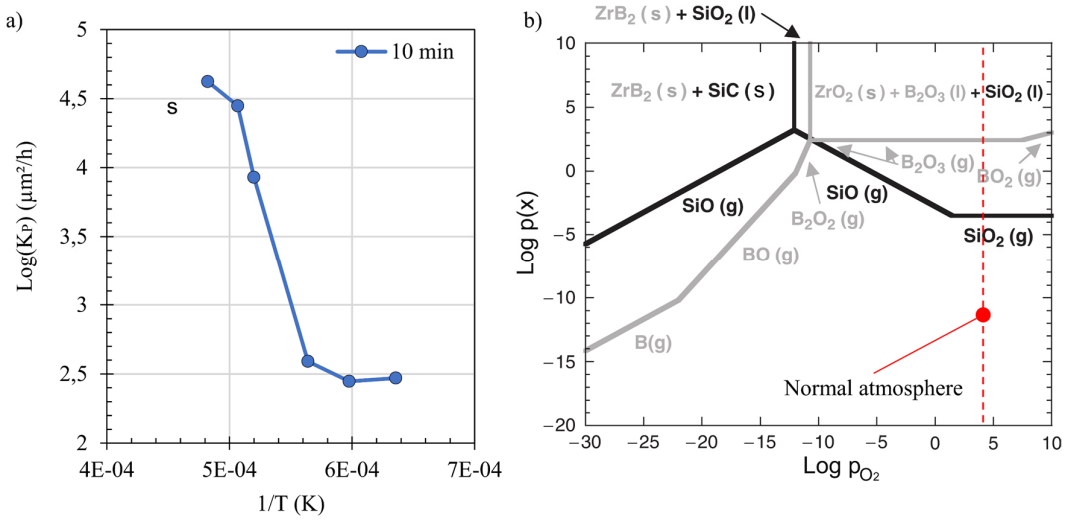

Fig. 2.16: a) Arrhenius plot of the parabolic oxidation rate constants for ZrB_2 with 30 vol% SiC for an exposure of 10 min (o.i.) [75]; b) Volatility Diagram of ZrB_2-SiC for the oxidation at 1500°C [68]

An abrupt change of the oxidation rate constant for the tested ZrB_2-SiC specimens for 10 min appears at ~1627°C. This temperature is a tipping point for the oxidation progression of ZrB_2-SiC materials by changing the oxidation mechanism of SiC. As can be seen in the calculated volatility diagram for SiC and ZrB_2 in Fig. 2.16b, the exposure at temperature ≥1627°C leads to the active oxidation of SiC, forming gaseous components such as SiO and CO, at atmospheric pressure ($\log(pO_2) \sim 4.3$). The active oxidation at >1627°C follows Equ. 2.20 [63, 68, 75].

$$ZrB_2 + SiC + \frac{7}{2}O_2 \rightarrow ZrO_2 + B_2O_3 \uparrow + SiO \uparrow + CO \uparrow \qquad \text{Equ. 2.20}$$

As a result, the loss of the protective SiO_2 layer at the surface at temperatures >1627°C reduces the oxidation resistance of the ZrB_2-SiC significantly. The direct evaporation of SiC leaves a ZrO_2 scale with enlarged pores. Consequently, the oxide scale can not prevent the mobility of oxygen and leads to a dramatic increase in the oxidation kinetics [68, 75].

2.3.7.2 Addition of Transition Metals to Zirconium Diboride

The addition of transition metals such as Nb, Ta, or W to ZrB_2 induced a change in the oxidation mechanisms of ZrB_2, resulting in interesting phenomena. Dehdashti et al. performed a screening of different metallic additives for baseline ZrB_2. The addition of ~6 wt.% metallic Nb led to the oxidation of the ZrB_2 and the metallic Nb forming the oxidation pro-ducts Nb_2O_5, ZrO_2, and B_2O_3. After oxidation at 1500°C for 180 min, a two-layer oxide scale formed on top of the ZrB_2-Nb

compound. A scale of a liquid solution with a thickness of ~37 µm covered a porous ZrO_2 oxide scale with a thickness of ~45 µm. In comparison, the baseline ZrB_2 formed a dry and porous ZrO_2 scale of ~73 µm in thickness. It can be seen that the Nb addition reduced the formation of a porous ZrO_2 scale by ~38%. This is attributed to the liquid solution formation and the accumulation of the liquid at the surface, which provokes the permeation of oxygen molecules through the oxide scale to the oxidation front of ZrB_2 [37, 79].

Considering the phase diagram of Nb_2O_5-B_2O_3 system, it was assumed that the Nb_2O_5 will melt at 1500°C and mix with the liquid B_2O_3, forming a more stable liquid solution of (Nb,B)O at the surface [80]. The formation rate of the protective liquid solution was found to be faster than the evaporation rate (formation rate of (Nb,B)O ≥ evaporation of (Nb,B)O). This led to the accumulation of the protective liquid solution at the surface of the oxide scale with respect to time and the formation of a ~37 µm thick liquid layer. Since there will be a continuous supply of Nb_2O_5 and B_2O_3 (homogenous distribution of ZrB_2 and metallic Nb in the compound expected), the liquid solution that is formed at the surface is more stable. Therefore, it can be expected, that the liquid layer will be stable or even increase in thickness even for longer exposure time at 1500°C. The behavior might change at temperatures >1500°C [37, 79].

In the same time, the phase diagram of Nb_2O_5-ZrO_2 system revealed the solid solution formation of both oxides, forming a mixed oxide $Nb_2Zr_6O_{17}$ [81]. Sparsely distributed areas of the mixed oxide phase were found in the porous ZrO_2 scale. However, most of the porous oxide scale contained ZrO_2 with dissolved Nb_2O_5 and did not induce densification of the oxide scale. The lack of dense $Nb_2Zr_6O_{17}$ can be explained with the limited addition of 6 wt.% metallic Nb. According to the chemical composition of the mixed oxide phase $Nb_2Zr_6O_{17}$, 1mol of Nb_2O_5 (corresponds to 2mol of metallic Nb) and 6mol of ZrB_2 are needed to form the mixed oxide phase. Considering the molar mass (ZrB_2 = 112.85 g/mol; Nb = 92.9 g/mol), an addition of ~22 wt.% metallic Nb is needed to form a dense scale of $Nb_2Zr_6O_{17}$. Consequently, no significant densification of the porous oxide scale was observed, which would reduce the porosity and pore diameter in the porous ZrO_2 scale, causing improved oxidation resistance [37, 79, 82].

Similar results were observed for the addition of metallic tungsten (W) (~8 mol%) and tungsten carbide (WC) (~4-10 mol%). Up to 1300°C, a steady increase in liquid layer thickness was observed at the surface for an exposure of 5 min. Above 1300°C, the liquid layer thickness was reduced significantly, leaving a dry surface at temperatures ≥1500°C. The oxidation at 1500°C for 60 min led to the formation of a porous ZrO_2 scale with a thickness of ~25 µm compared to baseline ZrB_2 with a total oxide scale of ~73 µm. Globular grains of ZrO_2 with traces of W were found in the uppermost section of the oxide scale. The gaps between the grains were found to be filled with WO_3, containing traces of ZrO_2. It is expected that the WC as well as the metallic W oxidizes to WO_3. Simultaneously, ZrB_2 will form ZrO_2 and B_2O_3. Due to the melting point of WO_3 (T_M ~1435°C), WO_3 will melt and form a liquid with dissolved ZrO_2. This liquid solution might promote the formation of globular ZrO_2 grains with traces of W due to liquid phase sintering. The calculation of the partial pressure of WO_3 species in equilibrium with liquid WO_3 revealed the fact that WO_3 volatilizes heavily at temperatures >1300°C. Finally, it was assumed that the liquid solution protected the system against oxidation as long as it was present on the surface. Furthermore, liquid phase sintering of ZrO_2 grains in the WO_3-based liquid was expected,

which induced the densification of the ZrO_2 oxide scale. In the case of intense evaporation of the liquid, the complete densification of the oxide scale was not possible [83, 84].

On the other hand, it was concluded that the dissolution of WO_3 into the liquid B_2O_3 led to a boria-based liquid solution (W,B)O at the surface. However, the volatile liquid solution was not stabilized for temperatures >1300°C and evaporated already after 5 min. Therefore, the liquid boria-based solution was not found to protect the oxide scale at elevated temperatures >1300°C for longer exposure times. [83-85].

A novel approach to improve the oxidation resistance of ZrB_2 is the formation of high entropy Ultra-High Temperature ceramics (HE-UHTCs). The equi-atomic multi-component solid solutions exhibit exceptional mechanical properties and phase stability at elevated temperatures. However, the fabrication, scale-up, and simulation of HE-UHTCs are very complex. Further, the oxidation mechanisms of each of the components will be different and lead to superimpositions of mechanisms. Further information about HE-UHTCs can be found in the literature [37, 67, 86-88].

2.4 Coatings

2.4.1 Protective Overlay Coatings

The oxidation resistance of metals or alloy systems can be attributed to the formed oxide scale at the surface. The formed oxide scales act as a barrier against oxygen since electrons and ions of oxygen and metal need to be transported through the oxide scale, following the oxidation model of Wagner [64]. Well-known oxides, which provide passive oxidation even at elevated temperatures are chromia (Cr_2O_3 (Eskolaite)) and alumina (α-Al_2O_3 (Corundum)) due to their low thermal and electrical conductivity κ_T and κ_E [89].

Chromia-forming protection can be seen in stainless steels with a chromium content of at least 10.5 wt%. Due to the preferred reaction of oxygen with chromium Cr rather than iron, a thin and comprehensive layer of Cr_2O_3 forms at the surface during oxidation. The protective Cr_2O_3 layer prevents further oxidation for temperatures up to ~1000°C. Extensive spallation of the chromium oxide layer and the evaporation of chromia by forming volatile CrO_3 lead to the loss of oxidation protection at higher temperatures [62, 90]. Chromia-forming coatings were developed for the automotive industry and aerospace industry to protect specific components against oxidation and corrosion. Engine valves in automotive vehicles for example will experience temperatures up to 900°C, several thermal shocks, and will be exposed to aggressive combustion atmospheres. Therefore, chromium coatings were developed for materials such as X33CrNiMn23-8 or X55CrMnNiN20-8 to improve the protection of the alloys. The formation of protective Cr_2O_3 and $FeCr_2O_4$ spinels at the surface decreases the degradation of the coated materials and improves the lifetime significantly [89].

Whereas chromia formers are limited in temperature due to the volatilization of the protective Cr_2O_3 scale at temperatures >1000°C, alumina formers can be exposed to higher temperatures due to the more stable α-Al_2O_3 phase. For this reason, alumina formers can be found in many high-temperature aerospace applications with temperatures up to 1400°C [62]. A well-known example for α-Al_2O_3-forming coatings are turbine blades, made by Ni-based superalloys. The

components have to withstand temperatures of up to 1350°C for longer lifetimes >1000 h. Therefore, coatings of Me-Cr-Al-Y (Me=Ni, Co) are a common solution to provide oxidation protection. At high temperatures >1100°C, oxygen molecules migrate along the grain boundaries of the coating and induce the oxidation of the coating. At the same time, aluminum cations and already formed Al_2O_3 migrate to the surface and form a dense α-Al_2O_3 layer at the surface (protective thermally grown oxide layer (TGO) of α-Al_2O_3) [91-93].

Another example of alumina formers as an oxidation protective overlay coating can be found for γ-Titanium Aluminides (50 at% Ti, 50 at% Al). The substitution of Ni-based components in the Gas turbine by γ-Titanium aluminides would lead to weight savings of up to 50%. An aluminum content of 60-70 at% for the Titanium Aluminides (no γ-configuration) promotes the formation of a protective α-Al_2O_3 layer at the surface. However, the increased Al content is accompanied by the formation of brittle $TiAl_2$, which forms cracks within and does not ensure reliable protection. A lower aluminum content induces the formation of a mixed oxide layer of Titanium and aluminum, which does not provide sufficient oxidation protection. Therefore, an oxidation protective coating of Ti-Al-Cr has been developed at DLR by means of magnetron sputtering. The applied coating protects the γ-Titanium aluminides against oxidation at temperatures up to 1050°C. The oxidation of the coating leads to the formation of a comprehensive layer of Ti(Cr-Al)$_2$ and a TGO of protective α-Al_2O_3, at the surface [94].

Besides chromia and alumina formers, silica formers revealed similar protective behavior against oxidation. As an example, the oxidation of SiC in dry air leads to the formation of CO and SiO_2. The solid SiO_2 oxide scale contains bubbles and other defects due to the gaseous CO formation and can not provide adequate passive oxidation. Therefore, a metallic Si coating can be applied on SiC (Si bond coat). The oxidation of the coating induces the formation of a comprehensive SiO_2 layer at the surface and provides passive oxidation. However, the presence of water vapor causes the active oxidation of the metallic Si coating and the SiC substrate, forming gaseous components such as SiO (compare Chapter 2.3.7.1). As a result, no protective SiO_2 layer is formed at the surface. An environmental barrier coating (EBC) of rare-earth silicates (Yttrium and/or Ytterbium), containing a layer of Disilicates and Monosilicates, was developed at DLR. The coating prevents the evaporation of the protective SiO_2 scale and ensures passive oxidation of the SiC material even in the presence of water vapor [95].

As already described above (Chapter 2.3.4), TMB_2 forms a protective layer of liquid boria at temperatures <1800°C. Therefore, these materials can be classified as boria formers. The formation of liquid B_2O_3 (T_M ~450°C) leads to a reduction of the oxygen mobility to the underlying substrate. Passive oxidation occurs <1000°C and protects the substrate. The increasing evaporation rate of B_2O_3 >1000°C results in the recession of the protective B_2O_3 layer and active oxidation of the substrate. As presented, several coating solutions were developed for a variety of materials in the last decades by DLR, improving the oxidation resistance of the materials. However, as of today, there have been no approaches for oxidation protective coatings of diboride-based transition metals, which might improve the oxidation behavior at temperatures >1500°C [12, 59].

2.4.2 Physical Vapor Deposition (PVD): Magnetron Sputtering

Sputtering is an established coating process to apply thin metallic or ceramic coatings on top of various materials. The process belongs to the group of Physical Vapor Deposition (PVD), in detail, to the field of thin-film technology with a coating thickness of up to ~20 µm [96, 97]. The principle of sputtering is based on the atomization of material by ionized gas (primarily Argon), the transportation of the sputtered atoms to the substrate surface, and the subsequent deposition/condensation as a layer on the substrate surface. A fundamental sputter facility requires a reaction chamber with the capability to achieve a vacuum of up to 10^{-4} mbar, a negatively charged electrode (cathode), and high-purity argon. Emitted electrons from the cathode induce the ionization of the Argon atoms. A plasma forms around the cathode. The positively charged Argon ions are attracted to the cathode and knock out neutral atoms and clusters of the cathode due to the impact. The sputtered atoms from the cathode migrate into the chamber and condensate as a thin coating on surfaces [96-102].

Modern sputtering facilities are equipped with a magnetron as shown in Fig. 2.17. The magnetron contains a metallic target disc of the coating material (negatively charged cathode), a target holder (usually copper + water cooled), a plasma shield (positively charged anode), and a ring magnet behind the target holder with a yoke for increased magnetic effects [96]. The power supply of the magnetron leads to an electron field (E-field) from the anode to the cathode (inverted direction of electron transport). A permanent ring magnet behind the target holder creates a magnetic field (B-field) parallel to the target surface. The B-field brings the emitted electrons into a spiral trajectory in front of the cathode. This enhances the ionization of Argon atoms, stabilizes the plasma, and increases the sputter yield. The sputtered metal atoms move through the vacuum chamber to the substrate and get adsorbed (physisorption). Surface diffusion induces the mobility of sputtered atoms to energetically most favorable positions at the surface, forming a dense and comprehensive coating at the surface of the substrate with respect to time [96-106].

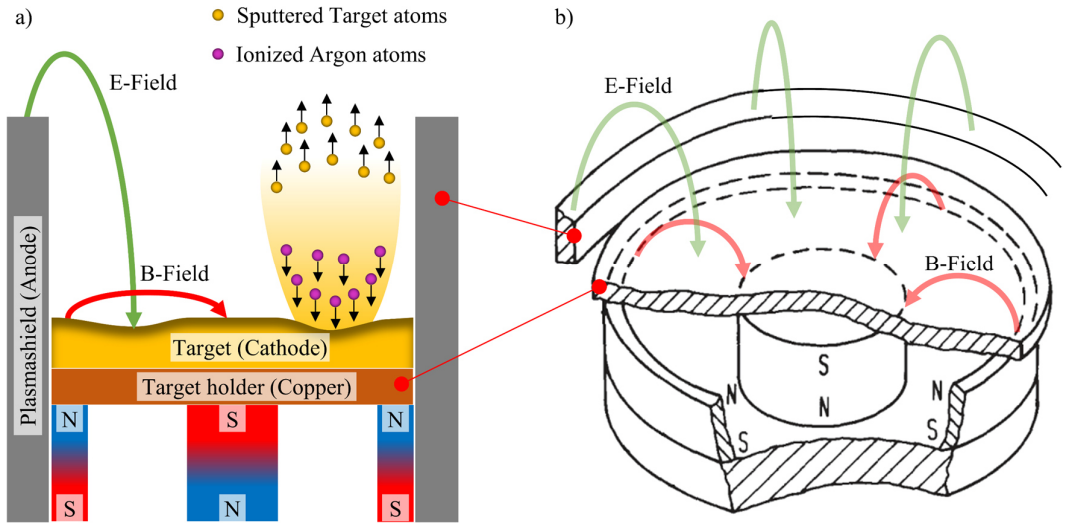

Fig. 2.17: a) Schematic of a general magnetron sputtering mechanism with a metallic target (o.i.) [95]; b) 3D-Schematic of a planar magnetron with circular geometry and marked E-field (green) and B-field (red) (o.i.)[96]

The microstructure and morphology of the coating are influenced by a wide variety of parameters such as the surface roughness of the substrate, the substrate temperature during processing, and the weight of the sputtered atoms (material-depending). An increased roughness of the substrate surface induces the formation of internal stresses inside the applied coating, which might lead to spallation. On the other hand, roughness can increase the adhesion of the applied coating to the substrate surface due to physical anchoring. The effect of the surface roughness depends on the combination of the target material/substrate and needs to be varied for optimal results. Elevated processing temperature increases the surface diffusion and the mobility of the adsorbed atoms at the surface. The adsorbed atoms are moving to the most energetic positions, which enhances the adhesion and density of the coating [96, 106, 107].

2.4.3 Reactive Magnetron Sputtering

Ceramic target materials such as Y_2O_3, HfO_2, or ZrO_2 can be used to apply thin ceramic coatings on substrates via magnetron sputtering. In general, the sputtering rates of ceramic targets are much lower compared to metallic targets. The kinetic energy of the Argon ions does not overcome the needed activation energy to induce sputtering. Instead, the kinetic energy converts into thermal energy and leads to a thermal load at the target surface [102-104].

An alternative to magnetron sputtering with ceramic coatings can be found in reactive magnetron sputtering. Berg et al. have gas causes the reaction with the metallic target, the sputtered metal atoms, and the adsorbed metal atoms on the substrate surface, forming a ceramic compound. The formation of a ceramic compound at the target surface has a strong influence on the reactive sputtering process and will be described in detail [102-104].

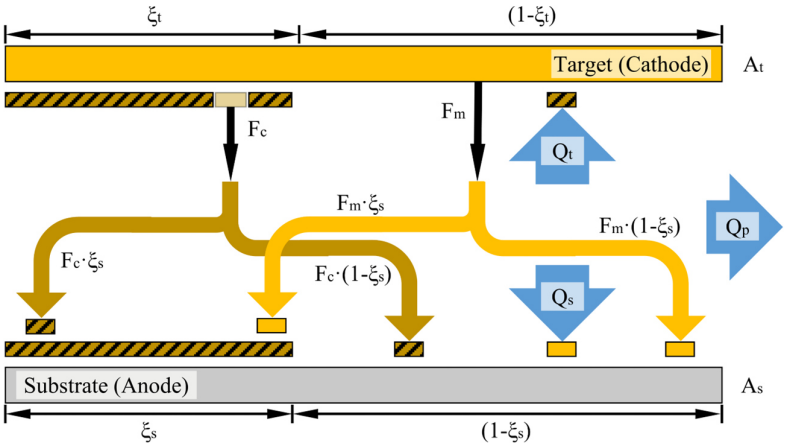

Fig. 2.18: Schematic of a reactive sputtering process with fluxes of sputtered materials (metallic oxidic products) and its deposition of uncoated substrate and coated substrate (o.i.) [104]

Bergs model requires a constant partial pressure p_{O2} for the reaction gas oxygen (other gases such as nitrogen also possible) with a uniform distribution of molecules per area and time in the reaction chamber. The relation between the partial pressure and the molecular distribution factor is shown in Equ. 2.21 [103, 104].

$$F_g = \frac{p_{O2}}{\sqrt{2 \cdot k_B \cdot T \cdot \pi \cdot m}} \quad \text{Equ. 2.21}$$

with the molecular distribution factor F_g (molecules/m³·s), the oxygen partial pressure p_{O2} (mbar), the Boltzmann constant k_B ($1.380649 \cdot 10^{-23}$ J/K), the temperature T (K), and the mass m for the gas molecules (kg) [103, 104]. The target surface during reactive sputtering can be divided into two discrete areas as shown in Fig. 2.18. A specific fraction of the target surface ξ_t is covered with a ceramic compound due to the reaction of the target surface with the reactive gas. The residual target surface ($1-\xi_t$) consists of the metallic target material. The number of sputtered metal atoms per time on the non-reacted target surface can be calculated by Equ. 2.22 [102-104]

$$F_m = \frac{J}{q} \cdot Y_m \cdot A_t \cdot (1 - \xi_t) \quad \text{Equ. 2.22}$$

with F_m for the sputtered metal atoms per unit time (sccm), J for the ion current density (A/m²), q for the elementary electronic charge, Y_m for the sputter yield of Argon atoms by sputtered metal atoms, A_t for the target surface (m²), and ($1-\xi_t$) for the non-reacted fraction of the target surface [102-104]. On the other hand, sputtered ceramic molecules per time from the reacted target surface can be calculated using Equ. 2.23

$$F_c = \frac{J}{q} \cdot Y_c \cdot A_t \cdot \xi_t \quad \text{Equ. 2.23}$$

with F_c for the sputtered ceramic molecules per time (sccm), Y_c for the sputter yield of Argon atoms by sputtered ceramic molecules, and ξ_t for the fraction of reacted target surface. The model by Berg specifies that the sputtering of the ceramic compound at the target surface increases the fraction of metallic target surface. Accordingly, the consumption of the reactive gas by the metallic target surface can be determined by Equ. 2.24 [102-104].

$$Q_t = \psi \cdot n \cdot F_g \cdot (1 - \xi_t) \cdot A_t \quad \text{Equ. 2.24}$$

with Q_t for the consumption of gas molecules per time by the non-reacted target surface (sccm), ψ for the probability factor to form ceramic molecules, n for the stochiometric compounds of dioxides (such as HfO_n, ZrO_n, …), Regarding the Equ. 2.21, an increase of the partial pressure p_{O2} of oxygen will induce increased consumption of oxygen by the metallic target surface and enhances the formation of ceramic compounds. Based on Equ. 2.23 and Equ. 2.24, a steady-state equation can be established by, balancing the sputter kinetic of ceramic molecules and the reaction kinetics of the metallic target surface, following Equ. 2.25 and Equ. 2.26 [102-104].

$$F_c = Q_t \quad \text{Equ. 2.25}$$

$$\frac{J}{q} \cdot Y_c \cdot \xi_t = \psi \cdot n \cdot F_g \cdot (1 - \xi_t) \quad \text{Equ. 2.26}$$

A surplus of the reaction gas (increased partial pressure p_{O2}) provokes a dominant reaction of the target surface, forming a comprehensive ceramic layer at the target surface ($Q_t > F_c$). As mentioned above, the sputter yield for metallic targets is higher than for ceramic targets ($Y_m >> Y_c$). Consequently, the growth of the comprehensive ceramic layer at the target surface ($Q_t > F_c$) will reduce the sputter yield of the target and the deposition rate (µm/time) at the substrate. This effect is defined as "poisoning" of the target.

The poisoning effect for a metallic target during reactive sputtering is presented in Fig. 2.19a, with the voltage, plotted over the gas flow ϕ_{O2}. Target poisoning manifests in high target temperatures, reduced voltage values, and/or an increased current (oxidic sputter conditions). Optimal reactive sputtering conditions would be in the transition area between the metallic and oxidic sputtering conditions (high saturation with reaction gas by high deposition rate in the same time). Unfortunately, processing in the transition area is nearly impossible by controlling the gas flow since different partial pressures may occur for steady gas flows ϕ_{O2} as presented in Fig. 2.19b (P_1, P_2, and P_3 for a steady gas flow ϕ_{O2}). Therefore, the partial pressure p_{O2} at the target must be controlled to ensure reliable and reproducible sputtering conditions for reactive sputtering operations (compare Equ. 2.21) [95, 102-104].

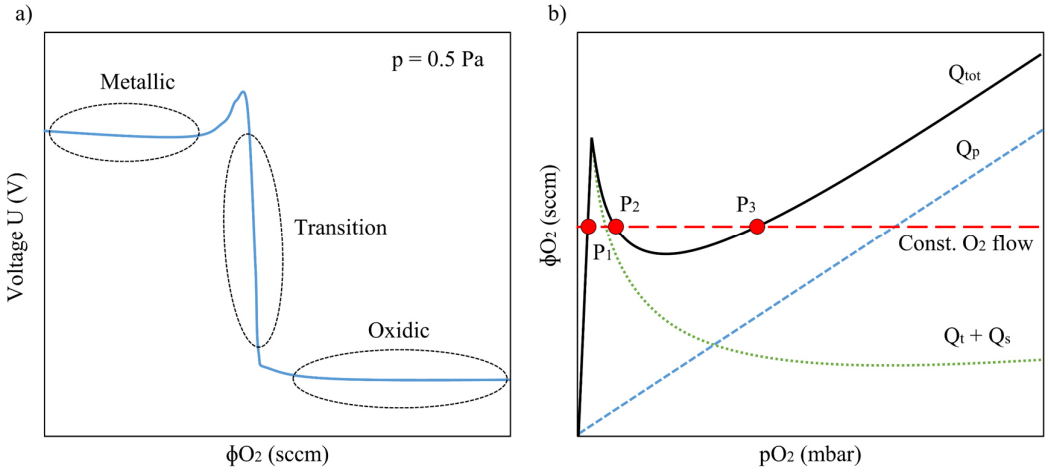

Fig. 2.19: a) Plotted voltage vs. oxygen gas flow to present the poisoning effect (a drop of voltage) of a metallic target during reactive sputtering (o.i.) [95]; b) Calculated consumption of reactive gas during reactive sputtering (o.i.) [105]

3 Motivation and Approach

3.1 Oxidation Protective Overlay Coatings for ZrB_2

Boron-based UHTCs are potential candidates for applications in hypersonic missiles, thermal protection systems of re-entry vehicles, and more as discussed in the previous Chapter. One of the current bottlenecks for their implementation is the poor oxidation resistance at elevated temperatures for long-term exposure >60 min. A novel approach is proposed in this work to improve the oxidation performance of ZrB_2 by applying protective overlay coatings. The coatings must be tailored to obtain chemical and physical compatibility with the UHTC substrate.

This study aims to understand the fundamental oxidation mechanisms of protective overlay coatings on ZrB_2, concerning the interaction of the coating/substrate and the oxidation products of the coating and substrate during oxidation. The objective is to improve the oxidation behavior for at least 30 min up to 1700°C. Alloying UHTCs with elements such as SiC, Nb, or WC will change the overall composition of ZrB_2 and in turn will affect the desired thermal and mechanical properties of the base material. Protective overlay coatings behave in a completely different way compared to the conventional approach of alloying. Coatings generate a high chemical potential due to the abrupt concentration gradient at the coating/substrate interface zone. This might modify the formation of mixed oxidation products just at the surface and might lead to protection by different mechanisms. Considering the well-known oxidation mechanisms of diboride-based UHTCs, three approaches for protective overlay coatings were proposed to adjust the oxidation mechanisms and improve the oxidation resistance of baseline ZrB_2:

Approach 1: Dense Coatings – Deposition of a dense coating on top of ZrB_2

This approach aims to reduce the mobility of oxygen to the underlying ZrB_2 by applying a dense and pore-free coating. A major requirement for the approach is a coating material, which must have a low oxygen diffusivity. This implies a lower electrical conductivity κ_E and/or a low amount of oxygen vacancies. A dense and defect-free coating will inhibit oxygen mobility. As a result, surface diffusion along the grain boundaries or lattice diffusion through the dense scale will be the only possible way for diffusion, which assures diffusion-controlled oxidation kinetics with significantly reduced oxidation rate constants.

Approach 2: Metal oxide scale densifier – Reaction between the applied coating and the ZrO_2

Since the porosity and the phase transition from m-ZrO_2 to t-ZrO_2 were found to have a dramatic effect on the oxidation behavior of ZrB_2, this approach aims to minimize the defects inside the oxide scale by forming a densified and thermally stabilized mixed oxide scale. The densification of the porous oxide scale can be achieved by liquid phase sintering as observed in the case of several additives such as WC. A requirement for liquid phase sintering of the porous oxide scale is the liquefication of the coating during oxidation, high solubility of ZrO_2 in the liquid, further infiltration of the liquid solution into the porous scale, and the precipitation of ZrO_2 or mixed oxides to form grains. As a result, a dense scale of ZrO_2 or a solid solution with increased thermal

phase stability should form at the uppermost section, which might reduce the Knudsen diffusion of oxygen molecules through the formed oxide scale and provoke diffusion-controlled kinetics.

Approach 3: Liquid Glass stabilizer – Reaction between the applied coating and the B_2O_3

The protective nature of the B_2O_3 glass on diboride-based UHTCs is undisputed and irrefutably proven by various experiments. Passive oxidation will occur due to the boria formation, forcing the permeation of oxygen molecules through the liquid layer. The increasing evaporation rate of B_2O_3 liquid at temperatures >1000°C retards the passivating properties of diboride-based UHTCs in the intended temperature range >1500°C. Therefore, an overlay coating can be applied on the surface of ZrB_2, which reacts with the liquid B_2O_3 during oxidation. The reaction should stabilize the liquid at the surface and reduce the evaporation rate at elevated temperatures. Similar effects were already observed for metallic additions such as Nb or W. The reaction of the coating with the liquid B_2O_3 glass might form a liquid and/or solid solution at the surface, which seals the surface and reduces the open porosity inside the oxide scale. The inhibition of the oxygen molecule mobility through the oxide scale will lead to diffusion-controlled oxidation kinetics as long as the liquid remains at the surface.

Essential requirements that are needed to be considered for the deposition of coatings on diboride-based UHTCs by PVD sputter technology, are the following:

- Processability using PVD (reactive) magnetron sputtering or other PVD processes
- Suitable substrate surface to ensure adequate adhesion of the coating after deposition
- CTE match of the coating and the substrate to ensure adhesion during oxidation
- Thermo-shock resistance of the applied coating
- Phase stability during vacuum-annealing to induce crystallization and interdiffusion

PVD (reactive) magnetron sputtering has been chosen to deposit thin and dense overlay coatings on baseline ZrB_2 with a thickness between 7-13 µm. The high feasibility and flexibility of magnetron sputtering to apply dense coatings with near stoichiometric chemical compositions and thicknesses open a large process window to generate specific coatings. Whereas magnetron sputtering will be used to deposit thin metallic coatings such as niobium, reactive sputtering will be used to deposit oxygen-saturated ceramic coatings such as HfO_2 or GdO on baseline ZrB_2. In the following, three promising coatings will be described, which will be tested in this study as an oxidation protective overlay coating, according to the proposed approaches.

3.2 Approach of HfO_2 Coatings on ZrB_2

ZrB_2 and HfB_2 have shown to have the best oxidation resistance among all TMB_2. Parthasarathy et al. compared the oxidation behavior of both Zr- and Hf diborides. Both exhibit an abrupt increase in their oxidation rate constant as shown in Fig. 3.1a. The results prove better oxidation resistance for HfB_2 than for ZrB_2 in the intermediate temperature regime of 1000°C to 1700°C. However, both UHTCs reveal an abrupt increase of the parabolic oxidation rate constant at a discrete temperature (~1155°C for ZrB_2, ~1725°C for HfB_2). The oxidation of HfB_2 and ZrB_2 leads to the formation of B_2O_3 glass and HfO_2 or ZrO_2, following Equ. 3.1 and Equ. 2.9. [31, 44, 108].

$$HfB_2 + \frac{5}{2}O_2 \rightarrow HfO_2 + B_2O_3 \qquad \text{Equ. 3.1}$$

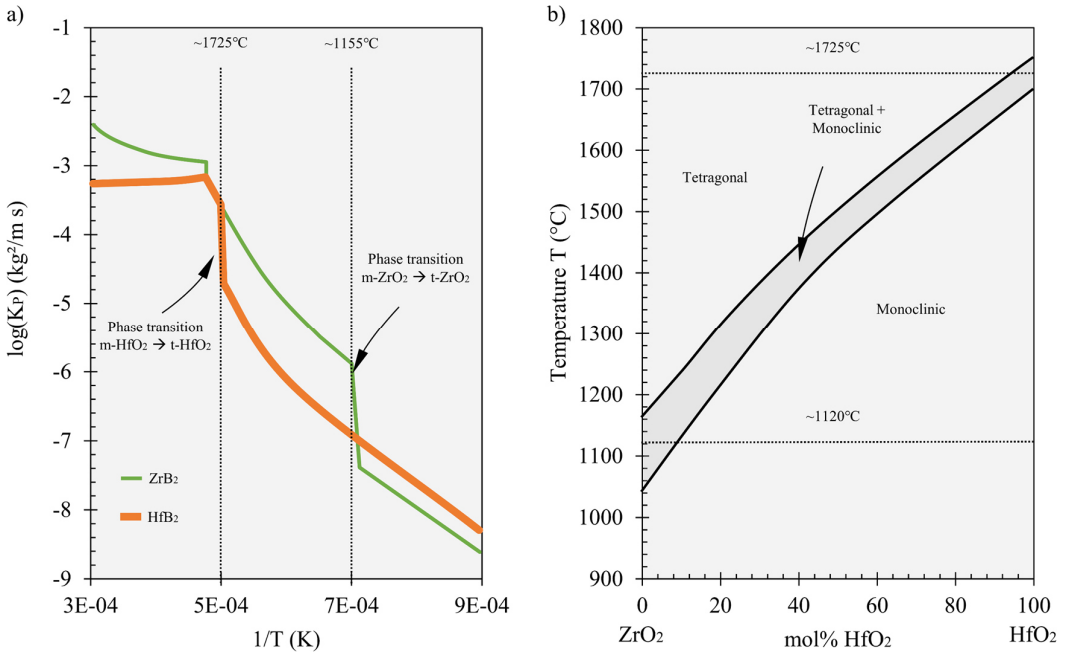

Fig. 3.1: a) Oxidation kinetics of ZrB_2 and HfB_2 (o.i.) [43]; b) Phase diagram of the system HfO_2-ZrO_2 (o.i) [109]

The liquid B_2O_3 at the surfaces protects the system, as long as it covers the surface and/or the pores in the underlying oxide scale. According to the volatility diagrams for ZrB_2 and HfB_2, the conditions of protective glassy B_2O_3 formation and evaporation are similar and do not induce the improved oxidation resistance of HfB_2 compared to ZrB_2 [32]. The formed oxides HfO_2 and ZrO_2 have similar crystal systems, space groups, and unit cell parameters. Information about both crystals are provided in Table 2.2 and Table 3.1. Further, both oxides experience a phase transition from monoclinic to tetragonal structure, following Equ. 2.10 and Equ. 3.2 (ZrO_2 ~1120°C, HfO_2 ~1725°C) [31], [110].

$$m - HfO_2 \underset{1670°C}{\overset{1725°C}{\rightleftarrows}} t - HfO_2 \underset{2200°C}{\overset{2200°C}{\rightleftarrows}} c - HfO_2 \underset{2810°C}{\overset{2810°C}{\rightleftarrows}} liquid \qquad \text{Equ. 3.2}$$

Table 3.1: Properties of m-HfO_2, t-HfO_2, m-ZrO_2, and t-ZrO_2 [49, 50, 110, 111]

Properties	m-HfO_2	t-HfO_2	m-ZrO_2	t-ZrO_2
Crystal system	Monoclinic	Tetragonal	Monoclinic	Tetragonal
Space group	P21/a (No.14)	P42/nmc (No.137)	P21/a (No.14)	P42/nmc (No.137)
Density ρ (g/cm³)	10.1	10.5	5.9	5.17
Unit cell volume (Å³)	141.02	66.55	146.81	68.56
Wyckoff position ™	4e	2a	2a, 2d	2a
Atomic density (Å³/TM)	35.26	33.28	36.70	34.28
Expansion (vol%)	-	-5.6 vol%	-	-6.6 vol%

As can be seen in Fig. 3.1a, the transition temperature of the oxide correlates with the abrupt increase in the parabolic oxidation rate constant for the diboride. In both cases, the phase transition induces a volume reduction for the oxide scale and provokes the formation of cracks. Consequently, the Knudsen diffusion through the porous oxide scale increases. It was concluded that the enhanced oxidation resistance of HfB_2 is attributed to the increased phase transition temperature of HfO_2 compared to ZrO_2, exhibiting a denser oxide scale for temperatures up to 1725°C [42, 43]. Considering the improved oxidation behavior of HfB_2 due to the more stable HfO_2 in a temperature range of 1000°C to 1725°C, a dense coating of m-HfO_2 on ZrB_2 might be beneficial to inhibit the oxygen mobility to the underlying substrate for a distinct time. Further, a dense m-HfO_2 coating might inhibit the evaporation of the protective B_2O_3 glass. The accumulation of the glass beneath the dense HfO_2 coating and in the underlying porous ZrO_2 scale would force the permeation of oxygen molecules through the B_2O_3 filled porous ZrO_2 scale.

The phase diagram of the HfO_2-ZrO_2 system is presented in Fig. 3.1b. As shown, both oxides form a solid solution (Hf,Zr)O_2 and are completely soluble. The solid solution (Hf,Zr)O_2 induces an increase in the transition temperature of ZrO_2 with increasing content of HfO_2. Once the porous ZrO_2 formed beneath the dense HfO_2 coating, the reaction of both oxides to a solid solution might induce the formation of a reaction layer with an increased transition temperature compared to baseline ZrO_2. As a result, the dense monoclinic-stabilized reaction scale might reduce the oxygen mobility to the oxidation front of ZrB_2 for an expanded temperature regime >1120°C. A scheme of the proposed behavior of dense m-HfO_2 coatings on ZrB_2 during high-temperature oxidation >1500°C is presented in Fig. 3.2, following Approach 1 – a dense coating on ZrB_2.

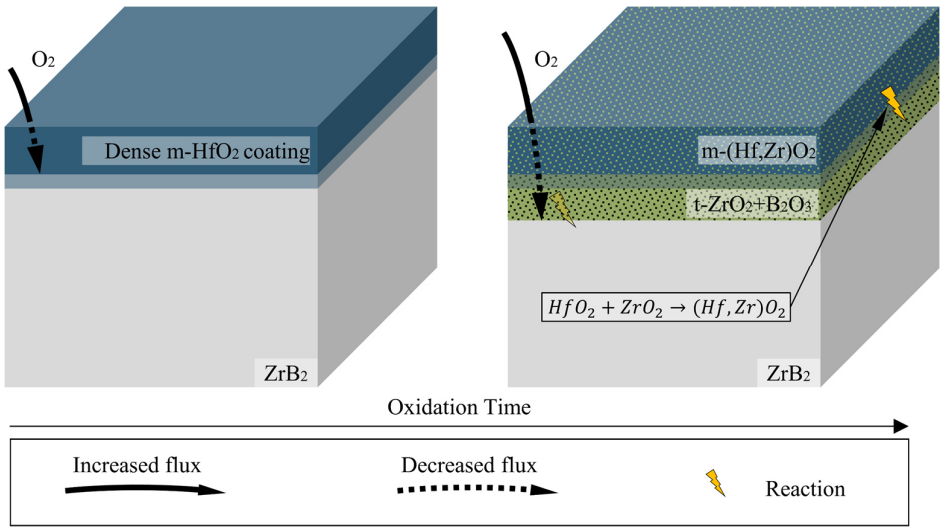

Fig. 3.2: Proposed oxidation mechanism of dense HfO_2 coating on ZrB_2 during oxidation at temperatures ≥1500°C after initial oxidation (first seconds) and after >15 min of oxidation

3.3 Approach of Nb Coatings on ZrB_2

Metallic niobium has been extensively studied in the last decades due to its high technological importance as a superconducting material [112]. Several publications focused on the oxidation behavior and the oxidation mechanisms at different temperatures [80-82, 112-122].

Metallic Nb has a density of ρ~8.57 g/cm³ and appears in a body-centered cubic structure (bcc). The refractory metal (T_M~2469°C) reveals a high chemical potential to react with nitrogen, carbon, or oxygen (solubility of O in Nb up to 4 at% at 1915°C). Oxygen diffusion were analysed in various studies. The diffusion coefficient of oxygen in metallic niobium can be calculated by the expression of Powers et al., following Equ. 3.3 [112] [114].

$$D(T) = f \cdot e^{\left(-\frac{E_A}{R \cdot T}\right)} = 0.0212 \cdot e^{\left(-\frac{26910}{1.987 \cdot T}\right)} \qquad \text{Equ. 3.3}$$

with f for the frequency factor (cm²/s), E_A for the activation energy (cal/mol), and R for the ideal gas constant (cal/K·mol). The diffusion of oxygen in metallic Nb is equal to ~10 µm at 420°C for 60 min. Therefore, a ~10 µm thick coating of metallic Nb will not prevent oxygen mobility at elevated temperatures >1000°C [112].

Oxidation of metallic Nb at temperatures >500°C induces the formation of stable and metastable oxidation products such as NbO, NbO_2, and Nb_2O_5. A three-layer/core-shell oxidation was found for metallic Nb, forming distinct sections in the oxide scale. Table 3.2 provides the crystal parameters of the single Niobia products [112-114, 118].

The oxidation from metallic Nb to Nb_2O_5 leads to a volume expansion of ~170 vol%, considering the unit cell volume and the Wyckoff position of Nb atoms. According to thermodynamics, Nb_2O_5 is the most stable state in the Nb-O system and exhibits several polymorphs (orthorhombic [T],

monoclinic [B, H, N, Z, R], tetragonal [M, P], or pseudohexagonal/monoclinic [TT]). The oxidation of metallic Nb or lower stoichiometry oxide such as NbO or NbO_2 provokes the formation of H-Nb_2O_5 at temperatures >1000°C [114]. Heat treatments of Nb_2O_5 and lower stochiometric niobia under oxygen-reduced atmospheres such as vacuum can enforce the decomposition of the niobia. (Reduction of a ~20 Å thick layer of Nb_2O_5 to NbO after 30 min at 300°C in vacuum) [112, 114, 117, 120, 122].

Table 3.2: Properties of metallic Nb and its oxidation products NbO, NbO_2, and Nb_2O_5 [112, 114]

Properties	Nb	NbO	NbO_2	Nb_2O_5
Crystal system	Cubic	Cubic	Tetragonal	Monoclinic
Space group	Im-3m (No.229)	Pm-3m (No.221)	I41/a (No.88)	P2 (No.3)
Density ρ (g/cm³)	8.57	7.26	5.9	5.17
Meting point T_M (°C)	2468	1945	1915	1510
Unit cell volume (Å³)	36.05	74.67	1121.02	1360.55
Wyckoff position (Nb)	2a	3c	2 16f	7 2m, 6 2n, 1g, 0.5 2i
Atomic density (Å³/Nb)	18.02	24.89	35.01	48.59
Expansion (vol%)	0	+38 vol%	+94	+170 vol%

Phase diagrams of the systems Nb_2O_5-B_2O_3 and Nb_2O_5-ZrO_2 are presented in Fig. 3.3 and reveal the reactivity of the oxides, forming different solid- and liquid solutions. The reaction of Nb_2O_5-B_2O_3 might lead to the formation of a Nb_2O_5 solid solution (T_M ~1352°C), inducing a liquid solution with increased thermal stability compared to B_2O_3 (Fig. 3.3a). The phase diagram Nb_2O_5-ZrO_2 shows the mixed oxide $Nb_2Zr_6O_{17}$ (>10 mol% Nb_2O_5) with a melting point of ~1670°C, a Nb_2O_5 based liquid solution, as well as a ZrO_2 based solid solution (Fig. 3.3b). The orthorhombic mixed oxide phase $Nb_2Zr_6O_{17}$ with the space group Ima2 reveals a commensurable complex lattice of different polyhedral-based structures [81, 119, 123].

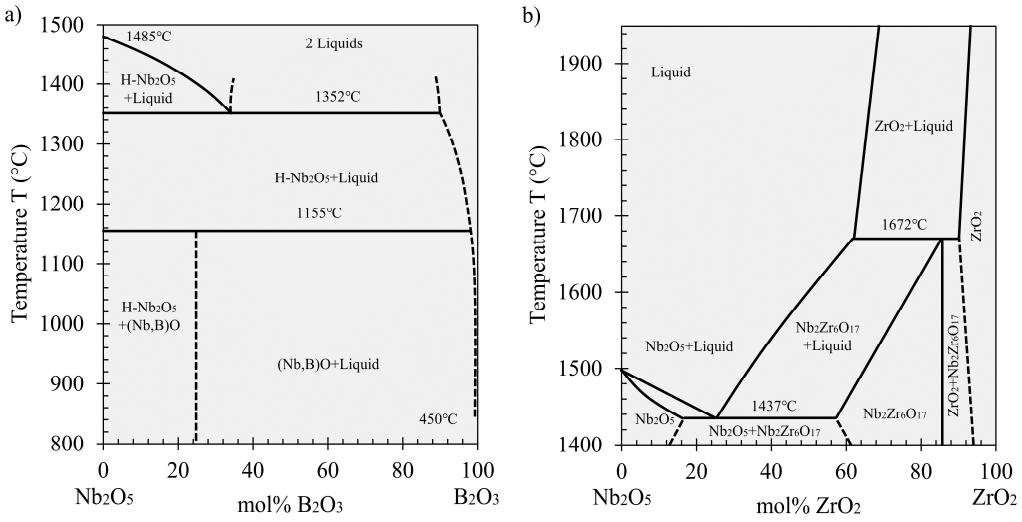

Fig. 3.3: a) Phase Diagram for the System Nb_2O_5-B_2O_3 (o.i.) [82]; b) Phase Diagram of the system Nb_2O_5-ZrO_2 (o.i.) [80, 119, 123]

The modification of the B_2O_3 liquid by Nb_2O_5 can be expected, forming a liquid solution (Nb,B)O at the surface (Approach 3). Further, the formation of a (Nb,Zr)O liquid solution might induce liquid phase sintering of the porous ZrO_2 solid solution at the uppermost section of the oxide scale and the formation of the mixed oxide phase $Nb_2Zr_6O_{17}$ (Approach 2). The proposed protection mechanisms of metallic Nb coatings on ZrB_2 are presented in Fig. 3.4.

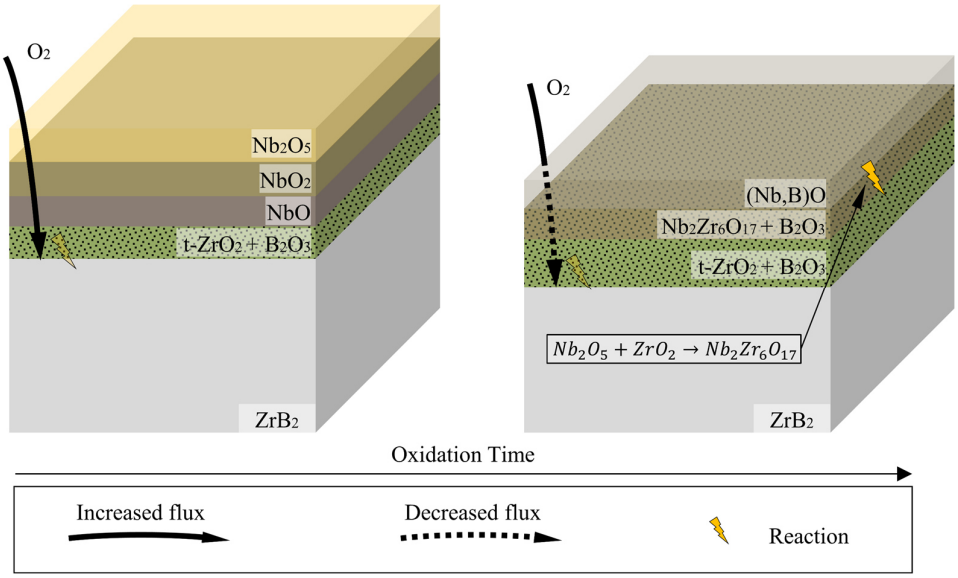

Fig. 3.4: Proposed oxidation mechanism of metallic Nb coating on ZrB_2 during oxidation at temperatures ≥1500°C after initial oxidation (first seconds) and after >15 min of oxidation

3.4 Approach of GdO Coatings on ZrB_2

Gadolinium is one of the most widely used rare-earth elements for various applications due to its unique properties (light emitter, catalyzer, neutron absorber, cement additive). Metallic gadolinium appears in a hexagonal crystal structure and has a low melting point (T_M ~1312°C) compared to other materials in this study. The favorable oxidation of Gd leads to the sesquioxide Gd_2O_3, which is one of the polymorphic crystal structures of the rare-earth oxides. It appears in three different crystal modifications, which are formed depending on the temperature. At room temperature, the Gd_2O_3 can appear in monoclinic, cubic, or hexagonal crystal structures (multiple temperature-related phase transformations). At annealing temperatures below 500°C, a monoclinic crystal structure is formed. In contrast, annealing above 500°C leads to the formation of a cubic structure, following Equ. 3.4 (stable up to 1620°C). The comparison of the Wycoff positions and the unit cell volume indicates a volume expansion during oxidation by ~17 vol% Further information about metallic Gd, m-Gd_2O_3, c-Gd_2O_3, and the metastable condition GdO are provided in Table 3.3.

$$p - Gd_2O_3 \xrightarrow{>500°C} c - Gd_2O_3 \qquad \text{Equ. 3.4}$$

Metallic Gd oxidizes to cubic Gd_2O_3 at temperature >500°C according to Equ. 3.4 and Equ. 3.5. In the presence of water, gadolinium reacts to hydroxides (high water solubility), following Equ. 3.6 [124].

Table 3.3: Properties of metallic Gd and its oxidation products GdO, m-Gd_2O_3, and c-Gd_2O_3 [125-128]

Properties	Gd	GdO	m- Gd_2O_3	c- Gd_2O_3
Crystal system	hexagonal	monoclinic	monoclinic	cubic
Space group	$P6_3/mmc$ (No.194)	F4-3m (No.216)	C2/m (No.12)	Ia-3(No.206)
Density ρ (g/cm³)	7.7	7.34	8.31	7.63
Meting point T_M (°C)	1312	-	2420	2420
Unit cell volume (Å³)	67.79	156.79	434.50	1261.82
Wyckoff position (Gd)	2c	4a	3 4i	8b, 24d
Atomic density (Å³/Gd)	33.89	39.20	36.21	39.41
Expansion (vol%)	-	+15.66 vol%	6.85	+16.28 vol%

$$4Gd + 3O_2 \rightarrow 2Gd_2O_3 \qquad \text{Equ. 3.5}$$

$$2Gd + 6H_2O \rightarrow 2Gd(OH)_3 + 3H_2 \uparrow \qquad \text{Equ. 3.6}$$

The phase diagram of the system Gd_2O_3-ZrO_2 is presented in Fig. 3.5a. The reaction of both oxides leads to a temperature-stabilized mixed oxide phase $Gd_2Zr_2O_7$ with fluorite crystal structure up to the elevated temperatures >2500°C, a Gd_2O_3 solid solution, and a ZrO_2 solid solution. The phase diagram of the system Gd_2O_3-B_2O_3 is illustrated in Fig. 3.5b and indicates the formation of different gadolinium borates (Gd_3BO_6, $GdBO_3$, GdB_3O_6). The melting point of (Gd,B)O decreases with increasing B_2O_3 content from ~1590°C for Gd_3BO_6 to <985°C for GdB_3O_6 [129-132].

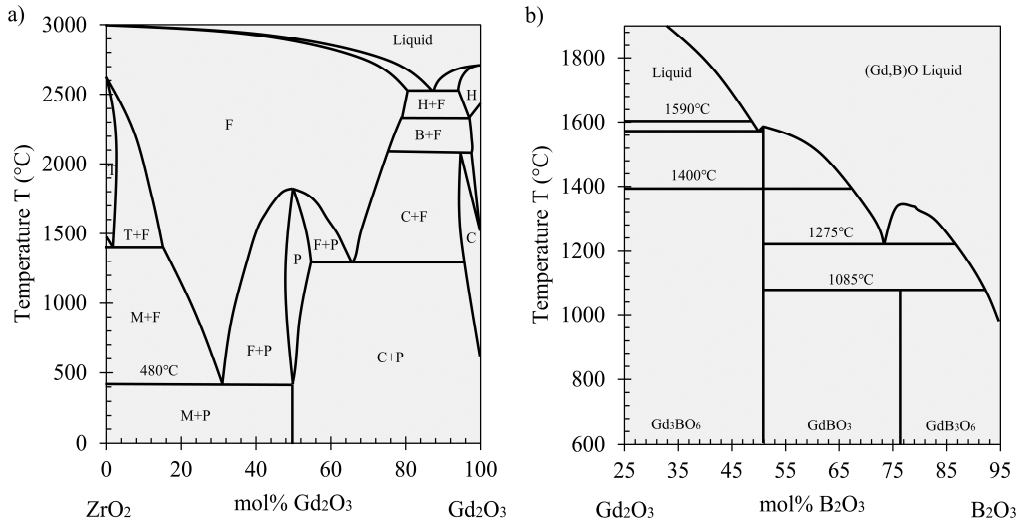

Fig. 3.5: *a) Phase diagram of the system ZrO_2-Gd_2O_3 (o.i.) [130]; b) Phase diagram of the system Gd_2O_3-B_2O_3 (o.i.) [131]*

Considering the potential reactions of Gd_2O_3 with B_2O_3 and ZrO_2, a Gd-based overlay coating might induce multiple reactions on ZrB_2 during oxidation as presented in Fig. 3.6. The reaction of Gd_2O_3 and ZrO_2 could lead to dense mixed oxide scale of $Gd_2Zr_2O_7$. The increased phase stability of the fluorite phase up to 2500°C would ensure the dense microstructure. On the other hand, the reaction of liquid B_2O_3 and Gd_2O_3 might result in the formation of solid/liquid (Gd,B)O, which might reduce the oxygen mobility to the oxidation front and induce passive oxidation.

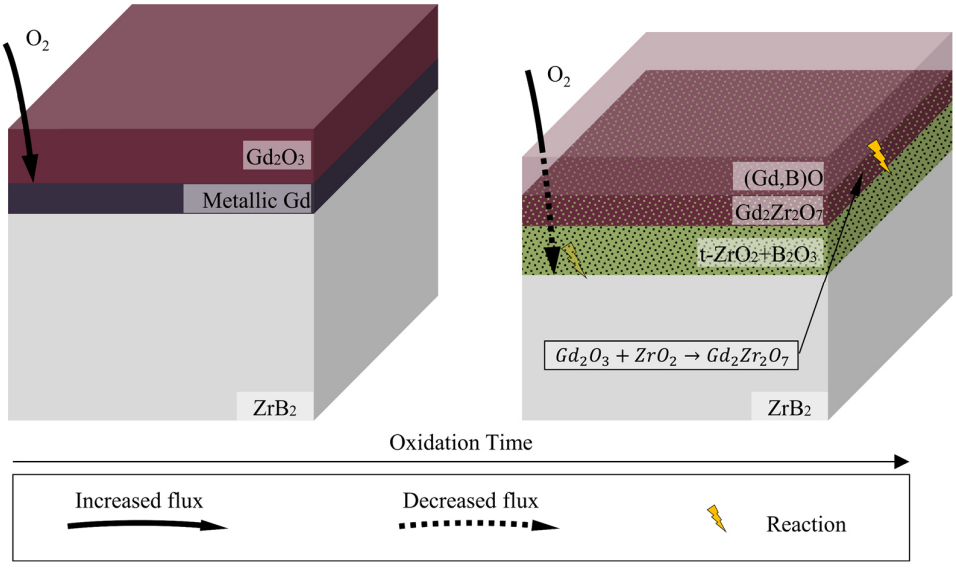

Fig. 3.6: *Proposed oxidation mechanism of metallic Gd coating on ZrB_2 during oxidation at temperatures ≥1500°C after initial oxidation (first seconds) and after >15 min of oxidation*

4 Experimental Method

4.1 Substrates

4.1.1 Zirconium Diboride Substrates

Baseline ZrB_2 specimens were produced by uniaxial hot pressing (Model HP-3060, Thermal Technology, Santa Rosa, CA). Commercially available ZrB_2 powder (Grade B; HC Starck, grain size ≤3 µm, D50) was hot-pressed at 2100°C for 45 min. Detailed process parameters for the hot-pressing process are presented in Fig. 4.1, showing the temperature (blue) and the pressure (orange, dashed) vs. the processing time with marked heating and cooling rates. The powder was compressed with ~2 MPa and heated at 20°C/min to 1450°C in vacuum. After a dwell time of 120 min at 1450°C, the system was heated at 20°C/min to 1650°C and held for 60 min. Isothermal holds at 1450°C and 1650°C are needed to remove surface oxides from the powder particles. Subsequently, the system was flushed with ultra-high-purity Helium (UHP-He). The powder was loaded with 32 MPa, heated at 50°C/min to 2100°C and held for ~60 min. Finally, the system was cooled at 40°C/min to room temperature. The pressure was unloaded at temperatures below 1600°C [30, 33, 79].

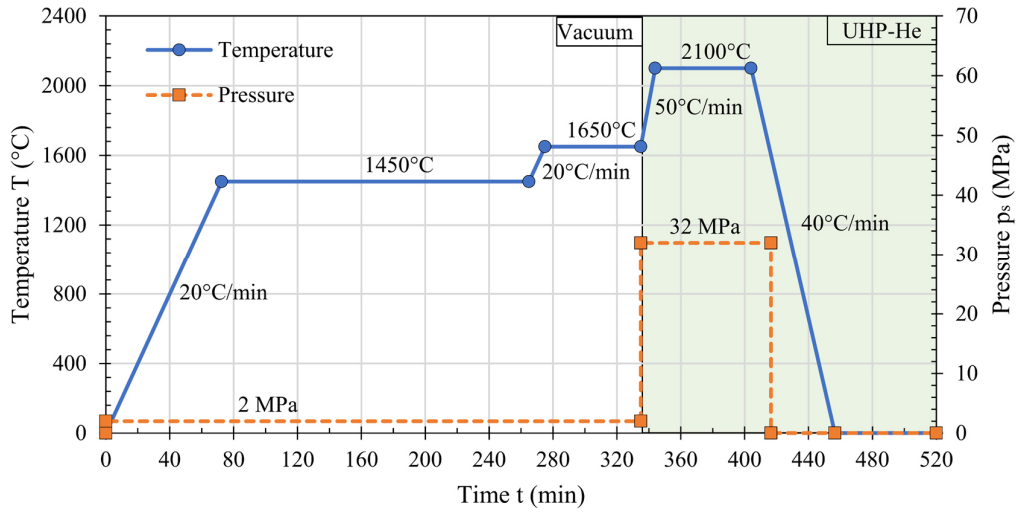

Fig. 4.1: Parameters for the uniaxial hot-pressing process for the baseline ZrB_2 specimens (o.i.) [30, 33]

Two cuboids in two charges were produced, each with a geometry of 30 mm by 20 mm by 10 mm. The cuboids were cut into specimens by means of electrical discharge machining (EDM) (AGIECUT 150 HSS; Agie, Germany). A copper wire with a diameter of 0.3 mm was used for the cutting operation. To differentiate the two charges of ZrB_2 specimens, the cuboids were cut into rectangles of 13 mm by 7 mm by 3 mm or in squares of 9 mm by 9 mm by 3 mm. Afterward, all six sides of the ZrB_2 specimens were ground with 10 µm grit size to avoid potential contamination by copper during the EDM cutting. The relative density of the specimens was determined at ~95%.

A BSE cross-sectional micrograph and the X-ray diffraction pattern of the baseline ZrB_2 substrate are presented in Fig. 4.2. The average grain size was measured for ~16 µm. EDS analysis revealed a chemical composition for ~72 at.% B, ~25 at.% Zr, ~0.3 at.% Hf, ~0.3 at.% W, and~2 at.% O. The diffractogram was assigned to ZrB_2 (PDF00-034-0423).

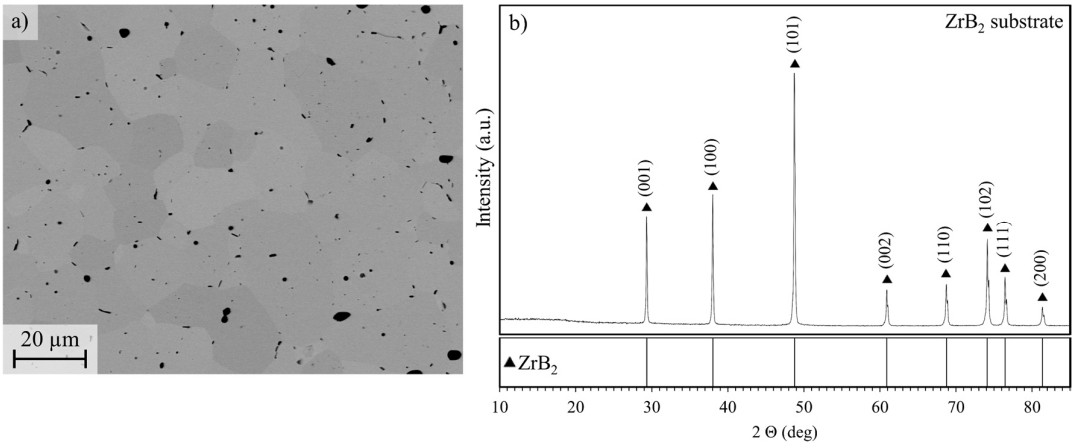

Fig. 4.2: a) BSE cross-sectional micrograph of the baseline ZrB_2 substrates; b) X-ray diffraction pattern of the baseline ZrB_2 substrates

4.1.2 α-Aluminum Dioxide Substrates

Coating trails to optimize the coating thickness, the chemical composition, and the microstructure were performed with α-Al_2O_3 substrates (99.6% purity) since there was no limitation in the quantity of these substrates. The Al_2O_3 substrates had a geometry of 20 mm by 30 mm by 1 mm with an average grain size of ~1 µm (ALO-100x40x1-99, Quick-Ohm Küpper & Co. GmbH, Wuppertal, Germany). A BSE cross-sectional micrograph and the X-ray diffraction pattern for the Al_2O_3 substrate are presented in Fig. 4.3. The diffractogram can be assigned to crystalline Al_2O_3 (PDF00-046-1212). EDS analysis revealed a chemical composition of ~38 at.% Al and ~62 at.% O.

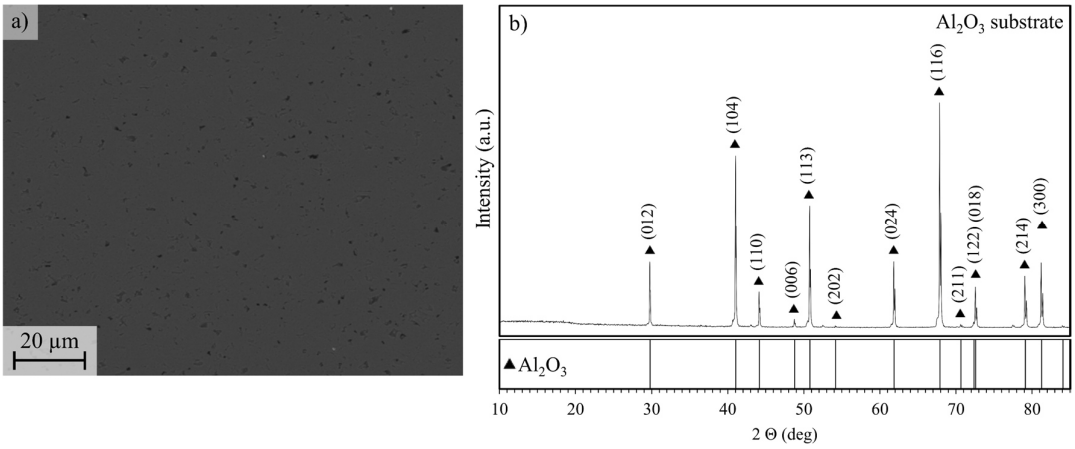

Fig. 4.3: a) BSE cross-sectional micrograph of the Al_2O_3 substrates; b) X-ray diffraction pattern of the Al_2O_3 substrates

4.1.3 Preparation of Specimens

ZrB_2 and Al_2O_3 substrates were mirror polished with a 3 µm grit size. Before coating deposition, specimens were cleaned using a four-staged ultrasonic cleaning facility of industrial standards (Xtra 250 HI; Elma Schmidbauer GmbH, Singen, Germany). Deionized water with an electrical conductivity κ_E of ~0.1 µS/cm was used for all four cleaning steps. A cleaning agent (SC 103-0; Sonitec GmbH, Neuendorf, Germany) was added during the first cleaning step to remove organic contamination.

4.2 Coating Deposition

4.2.1 Magnetron Sputtering Facility: Z400

A magnetron sputtering system of industrial standards was used to deposit PVD coatings on substrates (Z400 2Z/RF; Systec Vacuum Coating Systems GmbH, Karlstadt, Germany). Detailed information about the used magnetron sputtering facility is listed in Table 4.1. A schematic of the reaction chamber of the sputtering facility Z400 is presented in Fig. 4.4

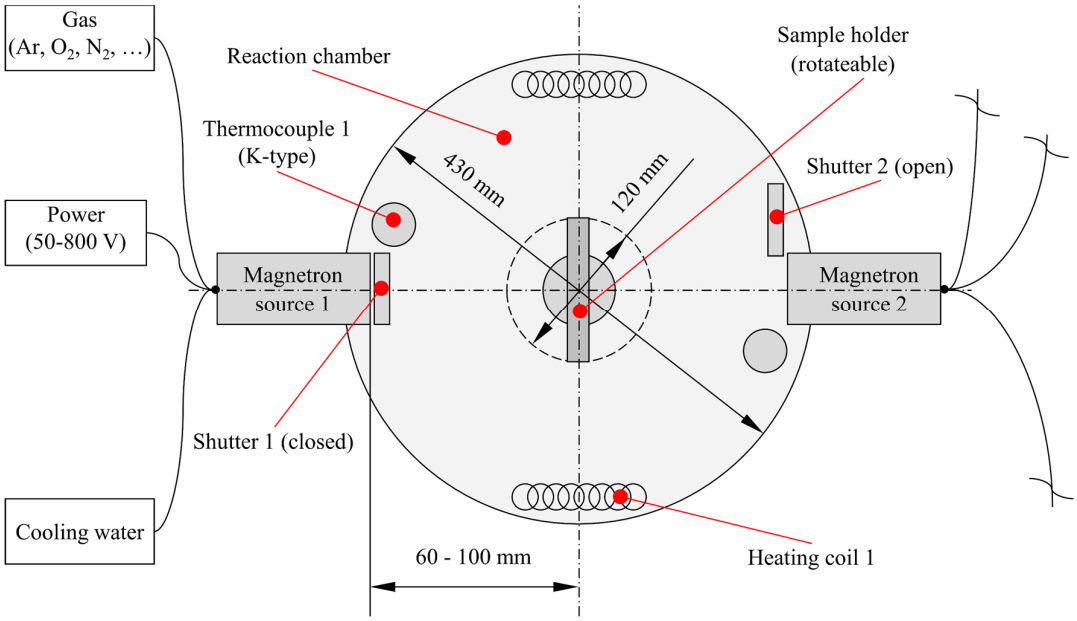

Fig. 4.4: Schematic of the magnetron sputtering facility Z400

An overview photograph of the reaction chamber is presented in Fig. 4.5a. A close-up of the magnetron with an open shutter and used target is presented in Fig. 4.5b. The rainbow-coloration inside the chamber can be attributed to the refraction of light through multiple thin layers/scales of sputtered material. The used target shows increased aging, forming a ring-shaped trench.

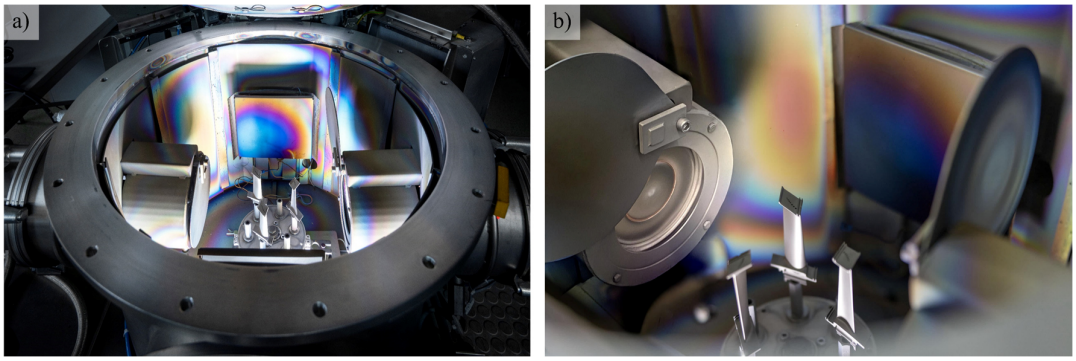

Fig. 4.5: Photographs of the reaction chamber of the magnetron sputtering facility Z400: a) Overview of reaction chamber; b) Close-Up of a magnetron with open shutter and used sputter target

Table 4.1: Operational parameter window for the magnetron sputter facility Z400

Properties	Value	Unit
Width	2500	mm
Depth	2900	mm
Height	2200	mm
Argon gas flow ϕ_{Ar}	≤50	sccm
Gas flow ϕ (Nitrogen, Oxygen, Methane)	≤20	sccm
Vacuum	$\leq 10^{-6}$	mbar
Voltage U (Magnetrons)	≤800	V
Current I (Magnetrons)	≤5	A
Power P (Magnetrons)	≤2000	W

4.2.2 Sputter Targets

Planar magnetrons with circular geometry were used for the PVD magnetron sputtering facility. The target discs (96 mm in diameter by 6 mm) were soldered on a copper plate (100 mm in diameter by 6 mm) for mounting in the water-cooled magnetron (Sindlhauser Materials GmbH, Kempten, Germany). Table 4.2 lists all sputtering targets used for PVD coatings in this study.

Table 4.2: Metallic sputtering targets for the Z400 [133]

Target	Material	Symbol	Atomic No.	Purity (%)	Density (g/cm^3)	T_M (°C)
T1	Hafnium	Hf	72	99.9	13.31	2227
T2	Niobium	Nb	41	99.9	8.57	2477
T3	Gadolinium	Gd	64	99.9	7.9	1312

4.2.3 Processing Gases and Vacuum Condition

Coatings were produced in a high vacuum of ~10^{-4} mbar. High purity Argon was used as processing gas for the sputtering process (Argon5.0, purity of 99.999%; Linde GmbH, Germany). High purity oxygen was used as a reactive gas for reactive magnetron sputtering, producing oxygen-saturated/ceramic coatings (Oxygen5.0, purity of 99.999%; Linde GmbH).

4.3 Vacuum-annealing

Vacuum-annealing of various coated specimens was carried out in a graphite furnace (3060-FP20, Thermal Technology, Santa Rosa, CA). Parameters of the annealing process are presented in Fig. 4.6. Chosen parameters are based on preliminary tests and experiences of the facility operator [134].

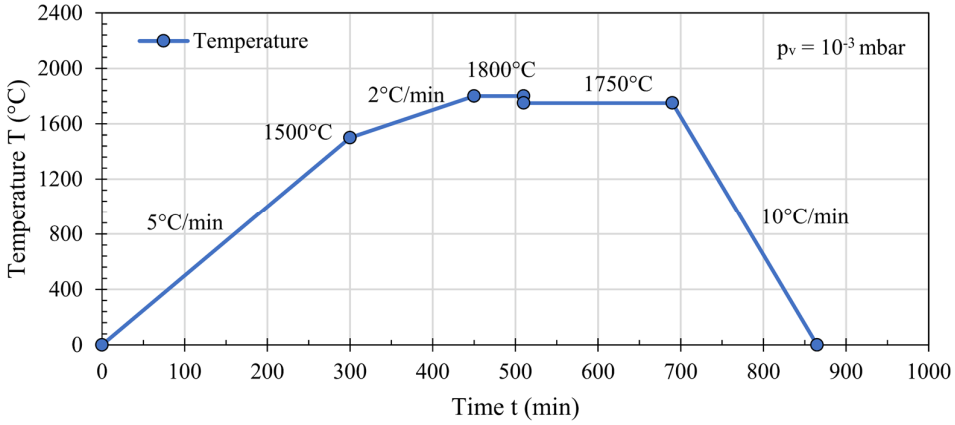

Fig. 4.6: Vacuum annealing process for coated ZrB_2 specimens in a vacuum graphite furnace

The furnace was evacuated until ~10^{-3} mbar. Specimens were heated at the rate of 5°C/min to a temperature of 1500°C. Subsequently, the heating rate was reduced to 2°C/min to prevent spallation of the coating during heat treatment. At 1800°C, specimens were exposed for 60 min, dropped to 1750°C instantly, and held for 180 min[1]. Finally, the system was cooled at 10°C/min to room temperature and exposed to normal atmosphere.

4.4 High-Temperature Oxidation Tests

A horizontal tube furnace for temperatures between 1200°C to 1700°C, (RHTH 120/300/16; Carbolite Gero, Great Britain) was used to investigate the oxidation properties of UHTCs. The tube furnace was equipped with metal/ceramic $MoSi_2$ heating elements and a gastight Al_2O_3 muffle tube (AlSint^{TM}). The tube had an inner diameter of 65 mm with a wall-thickness of 5 mm and a length of 1150 mm. The ends of the tube were mounted in metal flanges with quick locks, which

[1] The drop in temperature from 1800°C to 1750°C was attributed to a defective thermocouple in the first annealing run. The process was reproduced for all vacuum-annealing processes to ensure comparability for all coating systems.

enabled loading and quenching at elevated temperatures. Water-cooled flanges ensured gas tightness during operation and prevented atmosphere contamination inside the tube. The furnace had three gas inlets for synthetic air (SA) (20% O_2, 80% N_2; Linde GmbH, Pullach, Germany), Argon (Argon 5.0, purity 99.999 %; Linde GmbH), and pressed air (dried and cleaned). The gas outlet was equipped with an overpressure valve, which ensured pressure no more than 40 mbar inside the tube during operation. A vacuum pump station enables the evacuation of the system and the operation at 1500°C with a steady vacuum of up to 10^{-5} mbar.

Separately, a water vapor system was developed and equipped to the tube furnace to enable oxidation experiments in distinct humidified atmospheres. Steam (100 m% water) is produced by a water boiler and mixed with air (1 l/min). The humidified air gets cooled to a defined dew point temperature T_D, provoking the precipitation of a specific amount of water. Finally, the tube is flushed by the humid air with a distinct amount of water, which can be controlled and adjusted by T_D, providing steady conditions with up to ~45 m% water in the air.

Further technical information about the tube furnace is provided in Table 4.3. Pictures of the set-up are presented in Fig. 4.7 and Fig. 4.8, showing an overview of the test facility and a close-up of the loading flange.

Table 4.3: Properties of the used high-temperature tube furnace

Properties	Value	Unit
Width	570	mm
Depth	590	mm
Height	670	mm
Tube diameter d	65	mm
Tube length l	1150	mm
Power P	≤8000	W
Recommended heating rate	≤10	°C/min
Temperature range	1200–1700	°C
Cooling water supply	≤10	l/h
Vacuum (at 1500°C)	$\leq 10^{-5}$	mbar
Leakage rate	-	-
Gas supply (SA, Ar, dry pressed air)	≤ 4	l/min
Water vapor content (in relation to dry air)	~45	$m\%_{water}$

Fig. 4.7: High-temperature tube furnace for elevated temperatures, overview

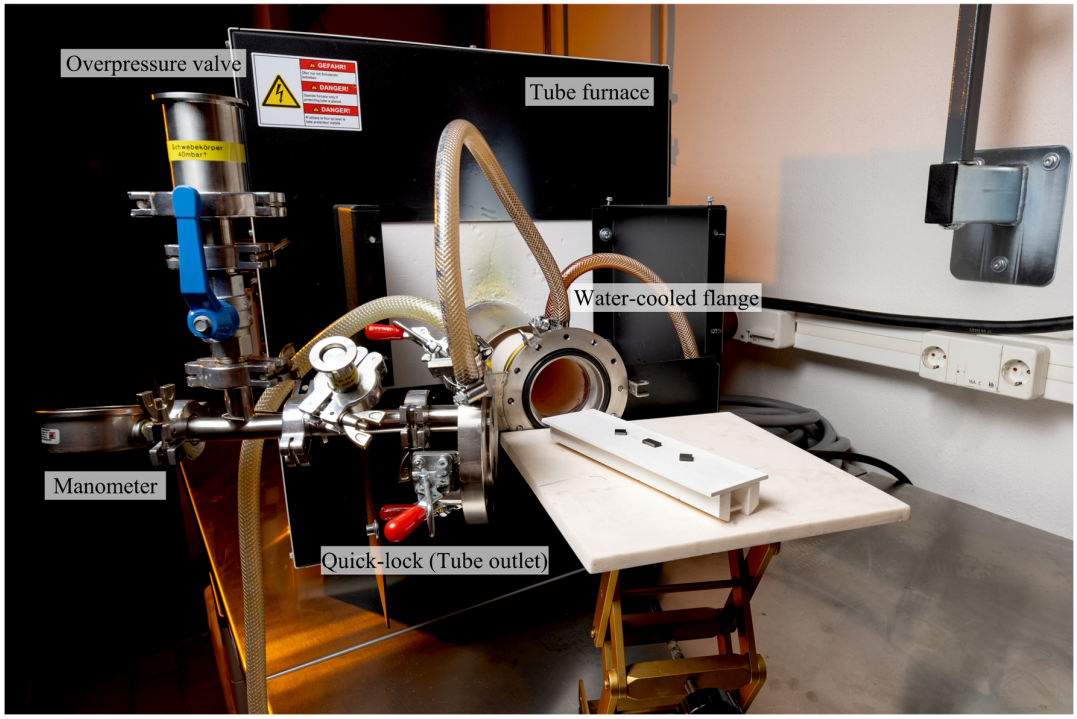

Fig. 4.8: High-temperature tube furnace for elevated temperatures, Tube outlet with quick-lock, water-cooled flanges, and overpressure valve for 40 mbar

Desired temperatures were set by the controller of the furnace. To ensure the correct temperature for the specimens inside the Al_2O_3 tube, a B-type thermocouple with an Al_2O_3 cap was used to calibrate the inner tube temperature along the tube length. A schematic with temperature profiles along the tube length for 1500°C, 1600°C, and 1700°C is presented in Fig. 4.9. The tube had a discrete length with a homogeneous peak temperature ($\Delta T \leq 5°C$). The length of the homogeneous temperature zone L_h (mm) decreased with increasing temperature. E.g. the length of the homogeneous temperature zone was ~150 mm at 1500°C, decreased to ~100 mm at 1600°C, and to ~60 mm at 1700°C. Specimens were always positioned in the homogeneous temperature zone to ensure comparable oxidation conditions.

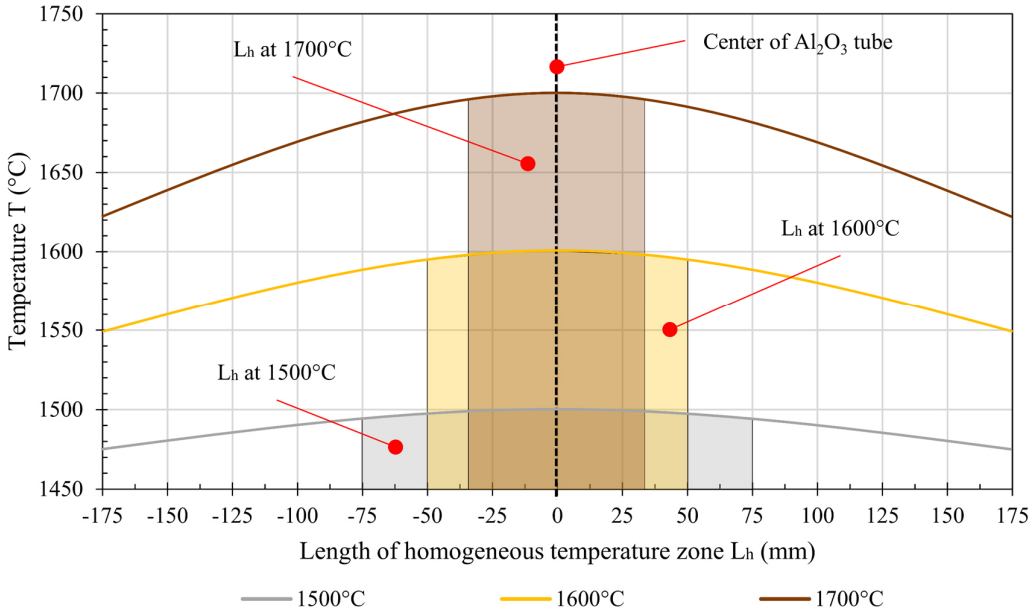

Fig. 4.9: Schematic of the temperature gradient inside the Al_2O_3 tube for different oxidation temperatures T with marked homogen temperature zones ($\Delta T \leq 5°C$)

Fine alumina powder (Nabolax No. 625-31, grain size 4.7 µm, d90) was poured into an alumina crucible (AlSint™) till it reached the wall height. Specimens were kept on top of the alumina powder to avoid sticking to the crucible. Considering the homogeneous temperature zone of ~60 mm at 1700°C, crucibles had a geometry of 70 mm by 10 mm by 9 mm. Two types of oxidation experiments were performed in this study:

- Ramped oxidation experiments (R/C): Specimens were put in the homogeneous temperature zone of the cold furnace, ramped up to a prescribed temperature with the ramp rate of 10°C/min, and held for a specific dwell time at peak temperature. Afterward, the furnace cooled down with the specimens by 10°C/min to ~790°C, then slower to room temperature (self-cooling).

- Rapid oxidation experiments (P/Q): Specimens were pushed into the homogeneous temperature zone of the pre-heated furnace (thermal shock), held for a prescribed dwell time at a calibrated temperature, and subsequently quenched to room temperature.

Detailed process parameters of the oxidation experiments, ramped (blue dashed) and rapid (yellow), are presented in Fig. 4.10 for an oxidation of 60 min at 1500°C.

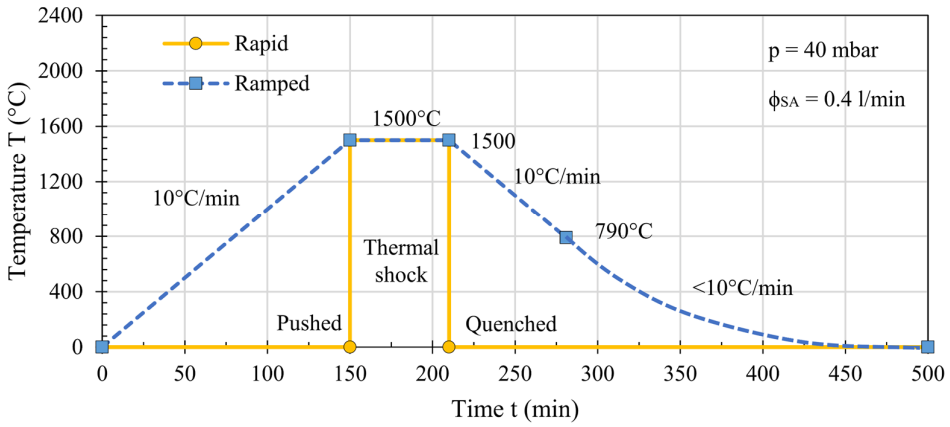

Fig. 4.10: Oxidation of specimens at 1500°C for 60 min via ramped (R/C) and rapid (P/Q) oxidation

The Al_2O_3 tube was initially flushed with dry synthetic air (SA) to remove moisture inside the tube. Afterward, a constant gas flow of ϕ_{SA} = 0.4 l/min was set to create constant atmosphere conditions (to remove gases such as B_2O_3 during oxidation for steady atmospheric conditions). The flow rate of SA was calculated as ~0.25 m/min, considering the inner tube diameter and the flow rate.

4.5 Characterization and Analysis

4.5.1 Light Microscope

Light Microscope (LM) images were taken before and after each process step (coating, annealing, oxidation). The bright field/dark field function of the light microscope (VHX-1000D; Keyence Corporation, Osaka, Japan) enabled the examination of cracks, open pores, and other defects at the surface.

4.5.2 X-ray Diffraction

X-ray Diffraction (XRD) was used to detect crystalline phases at the surface of the specimens after each process step (coating, annealing, oxidation). An XRD machine (D8 Advanced; Bruker Corporation, USA) was used for the analysis, equipped with a cobalt source, that emitted $CoK_{\alpha 1}$ X-rays (λ_{Co}=1.78897 Å). The measurements were performed by the Bragg-Brentano method (angle-dependent penetration depth of the X-rays) with 2000 steps for 1041 seconds at an angle between 10° to 100°. The diffraction patterns were analyzed using the associated software (Diffrac. EVA 6.0; Bruker Corporation, USA) in combination with the ICDD PDF-2 database 2022.

4.5.3 Metallography

A preparation method for diboride-based UHTCs was developed to investigate the water-soluble components of the oxide layer such as B_2O_3 glass. Fractured cross-sections were prepared for this purpose. The preparation method is presented in Fig. 4.11, illustrating the four mandatory steps.

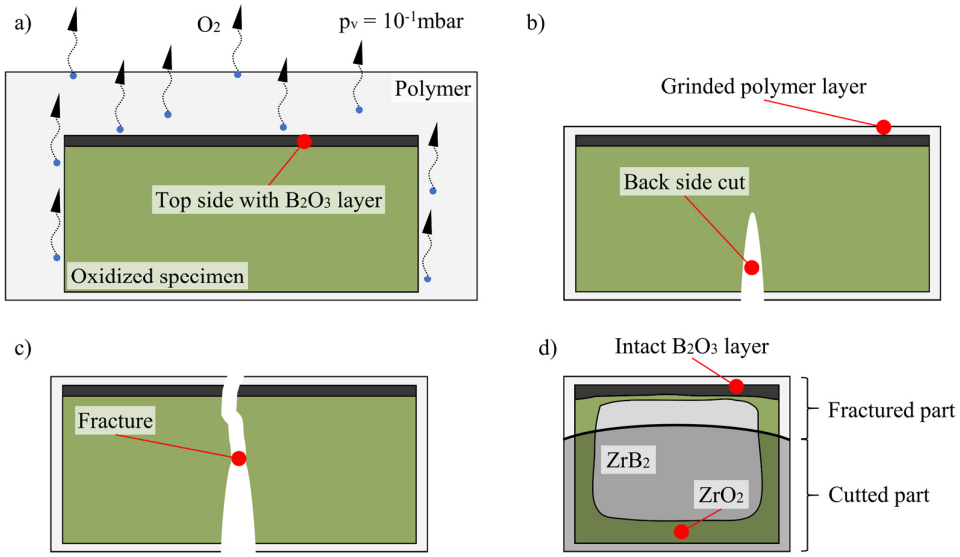

Fig. 4.11: a) Vacuum infiltration of oxidized ZrB_2 specimen in transparent plastic (Epofix™); b) Grinding of exess polymer and back side cutting with a diamond saw; c) Fracturing of the specimen; d) Fractured cross-section of oxidized ZrB_2 with intact B_2O_3 layer

Oxidized specimens were covered in transparent cold embedding medium (Epofix; Struers, Copenhagen, Denmark) [135, 136]. Vacuum infiltration was used to increase the penetration of the low-viscose polymer resin in the porous oxide scale to improve the stability of the oxide scale on the ZrB_2 (Fig. 4.11a). After curing, the excess resin was removed through grinding/polishing. Cold-embedded specimens were cut from the backside till ~2/3rd of the specimen thickness using a saw cutting machine (Accutom5, Struers, Copenhagen, Denmark).

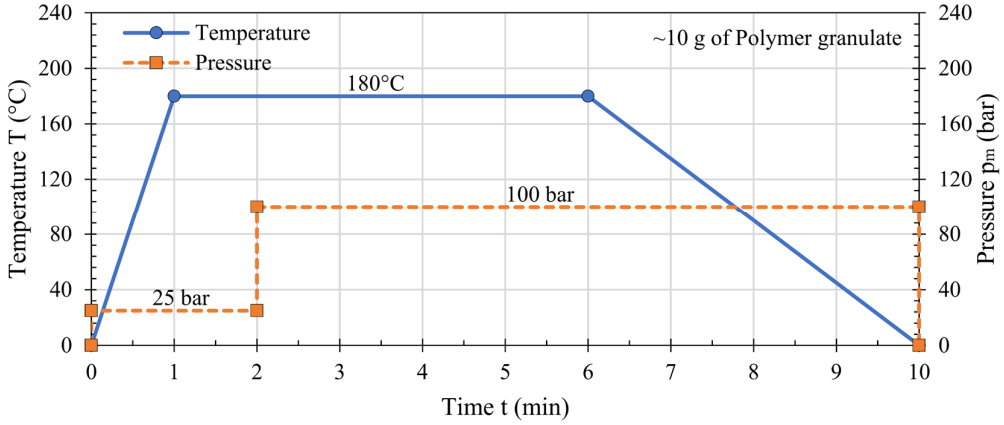

Fig. 4.12: Process parameters for hot embedding of tested specimens

The machine was equipped with a diamond blade (0.6 mm diamond blade; Schmitz Metallography, Herzognrath, Germany) (Fig. 4.11b). Specimens were fractured into two pieces (Fig. 4.11c). One part was analyzed as it is (fractured surface) (Fig. 4.11d), whereas the other part was mounted in conductive plastic and prepared by general metallographic procedure. A hot embedding machine (Citopress-21; Struers, Copenhagen, Denmark) was used to embed the specimens in conductive plastic (PolyFast; Struers, Copenhagen, Denmark). Process parameters for the hot embedding procedure are presented in Fig. 4.12.

Embedded specimens were polished using a polishing machine (Saphier550 Rubin520 Grinding-Polishing combination; ATM Qness GmbH, Mammelzen, Germany). The recipe for the grinding, polishing, and cleaning procedure is listed chronologically in Table 4.4. All polished specimens were ultrasonically cleaned in deionized water for 1 minute. Finally, the cleaned specimens were dried in an exicator at room temperature for 24 hours.

Table 4.4: Grinding and polishing recipe for UHTC materials

Step	Pressure (bar)	Grit (µm)	Abrasive tool	Duration (min)	Head (1/min)	Base (1/min)
I	15	20	Diamond disk	5	150	150
II	15	8	Diamond disk	5	150	150
III	15	3	Diamond disk	5	150	150
IV	15	1	Slurry + Silk cloth	15	30	50
V	15	0.25	Slurry + Silk cloth	15	30	50
VI	15	-	Deionized water	5	30	50

The combination of fractured and polished cross-sections ensured a detailed analysis of the formed oxide scales via microscopy. Whereas fractured cross-sections provided information about the boria glass coverage, polished cross-sections enabled a detailed and reliable analysis of the chemical compositions of the oxide scale.

4.5.4 Scanning Electron Microscope

A Scanning Electron Microscope (SEM) (DSM Ultra 55; Zeiss, Oberkochen, Germany) was used to acquire high-resolution micrographs of the oxidized surface (top-view) as well as of the fractured and polished cross-section, obtaining different information such as microstructure, porosity, and oxide layer thickness. The SEM was equipped with an Angle Selective Backscatter detector (AsB) for Back-Scatter Electron micrographs (BSE). Contrast information of the BSE micrographs can be attributed to different chemical compositions, where phases containing elements with low atomic numbers such as boron, carbon, or oxygen appear darker than phases with elements of high atomic numbers such as zirconium, hafnium, or tungsten. Therefore, the contrast information enables better characterization of the observed scales. Micrographs were taken with an acceleration voltage of 15 kV or 30 kV, depending on the coating material (see Energy Dispersive X-ray Spectroscopy). All specimens were sputtered with Platinum to increase the conductivity of the oxidized specimens, using a sputtering machine (Bal-Tec SCD 500, Baltec, Vaduz, Lichtenstein).

4.5.5 Energy Dispersive X-ray Spectroscopy

Energy Dispersive X-ray Spectroscopy (EDS) (Ultim Max 100, precision ±5 rel%; Oxford Instruments Abingdon, UK) was used with the corresponding software (AzTec, Oxford Instruments Abingdon, UK) to evaluate the chemical composition in the formed scale. Depending on the material, an acceleration voltage of 15 kV (HfO_2, Gd_2O_3) or 30 kV (Nb_2O_5) was selected to ensure a clear and distinct quantification of the elements. Elements with low atomic numbers such as boron and carbon were only qualitatively differentiated since the characteristic energy lines are overlapping ($BK_{\alpha 1}$ = 183.3 keV and $CK_{\alpha 1}$ = 277 keV). Only oxygen was quantified since the characteristic energy line does not overlap with boron, carbon, or other used elements such as aluminum, zirconium, niobium, gadolinium, or hafnium ($OK_{\alpha 1}$ = 524 keV).

4.5.6 Transmission Electron Microscope

A Transmission Electron Microscopy (TEM) (Tecnai F30; Thermo Fisher Scientific, USA) was used to characterize the coatings and oxide scales in high-angle annular dark-field mode (HAADF). Scanning Transmission Electron Microscope (STEM), Selected Area Electron Diffraction (SAED), and Debey-Scherrer Diffraction enabled the analysis of the elemental composition and the crystal structure. Thus, phase fields were assigned to a distinct phase using software (Digital Micrograph; Gatan Inc., Pleasanton, USA). A dual-beam microscopy system (Helios Nanolab; Thermo Fisher Scientific, USA) was used to cut the lamellas for the TEM analysis. A focused ion beam of Gallium (FIB) in combination with an electron beam (SEM function) was used to prepare the lamellas. FIB lamellas with a length of up to 75 µm were prepared. To maintain the internal stability of the lamellas, windows were cut into the lamella (≤100 nm thick).

4.5.7 Oxide Scale Thickness Measurements

Oxide scale thicknesses were measured via SEM cross-sectional micrographs at multiple spots, using ImageJ software (Version 1.52; National Institutes of Health, USA). The average scale thickness and the standard deviation of the scales were calculated by the measured values. An example of the measurement technique is presented in Fig. 4.13a. The measuring spots had a defined distance of ~140 µm from each other (specimen length of ~9 mm, ~65 measurement spots). 80% of the measured values were considered mainly at the center of the specimen. Oxidation phenomena at the edges of the specimen were removed from the calculation. Further, the considered values were divided into a protected area with residual coating and/or reacted oxide scale and an area with spalled coating as shown in the schematic in Fig. 4.13b. However, only the protective areas were thoroughly analyzed by techniques such as EDS, SEM, and TEM.

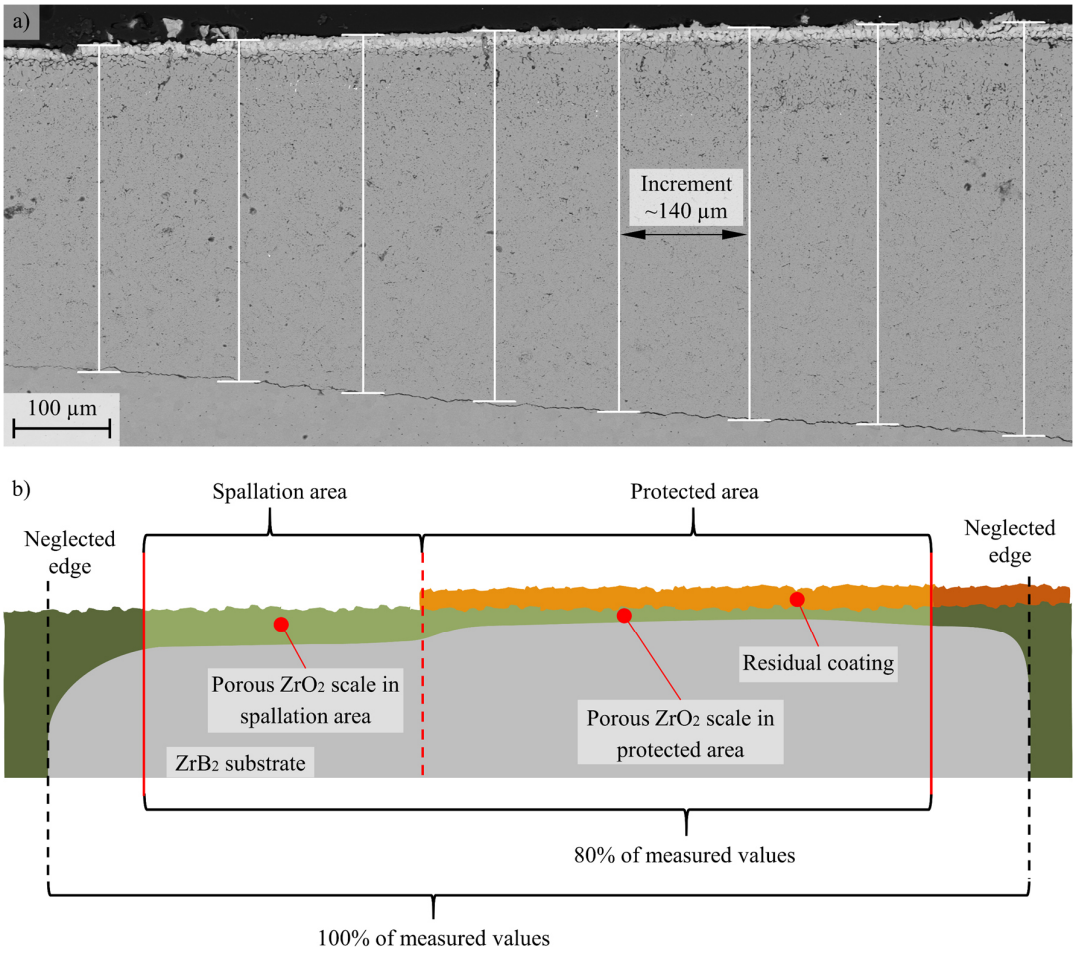

Fig. 4.13: *a) Measurement technique for oxide scales of coated ZrB_2 material; b) Schematic of the technique to measure and calculate the average oxide scale thickness of the protected area*

5 Results

5.1 Baseline ZrB_2

The oxidation behavior of baseline ZrB_2 has been a topic for the research community and was thoroughly studied in detail. Therefore, this chapter gives a short overview of the behavior of baseline ZrB_2, oxidized in similar conditions as the coated ZrB_2. This enables the comparison and discussion of the results one by one under exact experimental conditions (Fig. 4.7, Fig. 4.10).

5.1.1 Ramped Oxidation Experiments of Baseline ZrB_2

Tested baseline ZrB_2 specimen after 60 min at 1500°C using ramped oxidation (R/C) condition (compare Fig. 4.10) is presented in Fig. 5.1. Most of the surface is covered with ZrO_2, giving its white-yellowish surface coloration. Sparsely distributed pools of residual B_2O_3 can also be found at the surface as documented in the literature [39]. The X-ray diffraction pattern of the tested specimen is presented in Fig. 5.1b. m-ZrO_2 (PDF00-037-1484) was indicated for the detected reflections.

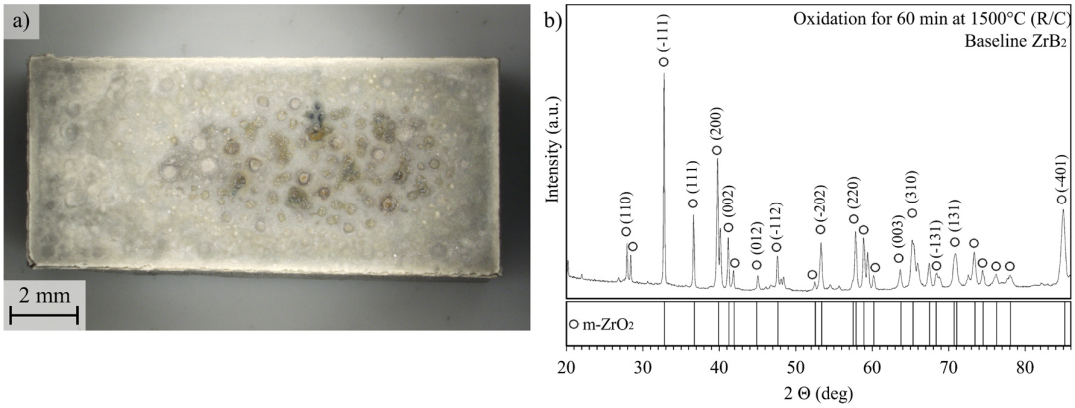

Fig. 5.1: Baseline ZrB_2 after ramped oxidation (R/C) for 60 min at 1500°C: a) Top-view photograph; b) X-ray diffraction pattern with assigned Miller indices for m-ZrO_2

A BSE micrographs of the oxidized surface after 60 min at 1500°C (R/C) is presented in Fig. 5.2. As visible in the micrographs, the surface is covered by ZrO_2 grains with an average size of ~7 µm. Residual B_2O_3 can be found at the surface, beside the ZrO_2 grains (Fig. 5.2b). The polished cross-section of the tested specimen revealed the formation of a porous ZrO_2 scale with a thickness of ~176 µm (Fig. 5.2c, Table 5.1). Brighter particles inside the porous oxide scale (BSE contrast information) were identified as WO_3 and could be present as a result of WC contamination during powder preparation (WC ball-milling media during preparation, compare Chapter 2.5). At the uppermost section, elongated ZrO_2 with a thickness of ~6 µm formed (Table 5.2d, Fig. 2.9b). Gaps between the elongated grains enabled the migration of the B_2O_3 liquid to the surface. As it can be seen, neither a dense Zirconia nor a comprehensive thick layer of boria has formed on the surface.

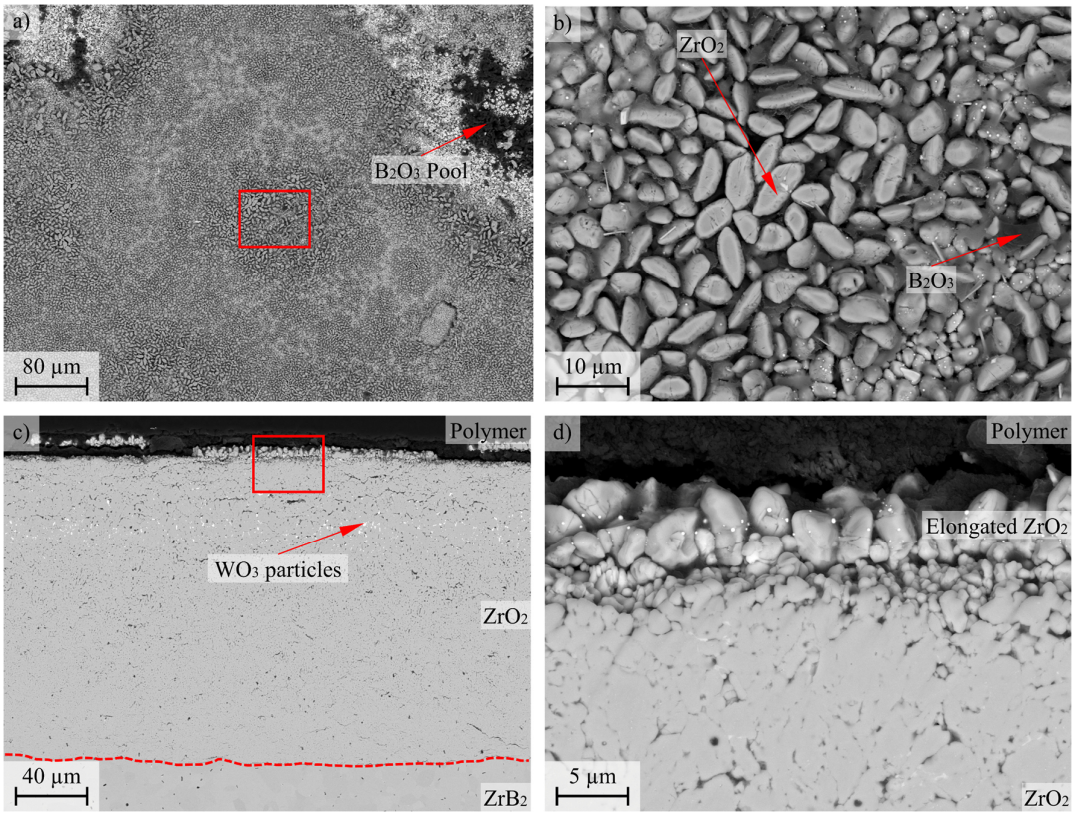

Fig. 5.2: *BSE micrographs of baseline ZrB_2 after ramped oxidation (R/C) for 60 min at 1500°C: a) Overview of oxidized surface; b) High magnification of the ZrO_2 grains at the surface; c) Polished cross-section with holistic ZrO_2 oxide scale, d) High magnification*

5.1.2 Rapid Oxidation Experiments of Baseline ZrB_2

Photographs of the rapidly oxidized specimens of baseline ZrB_2 are presented in Fig. 5.3. The loss of the protective boria liquid can be seen after 30 min at 1500°C, 15 min at 1600°C, and 15 min at 1700°C, forming white-yellowish oxides at the surface. Table 5.1 provides the measurements of oxide scale thickness from both R/C and P/Q conditions as well as the calculated parabolic oxidation rate constants for the porous oxide scales. The oxide scale thicknesses squared over the exposure time for isothermal oxidation at 1500°C, 1600°C, and 1700°C are presented in Fig. 5.4a. The Arrhenius plots for the tested specimens are presented in Fig. 5.4b, depicting the parabolic rate constants vs. the oxidation temperature. Further, the activation energies for the temperature regime 1500°C to 1600°C and 1600°C to 1700°C were calculated and provided in Table 5.2. The constant activation energies for both temperature regimes (similar slope for the Arrhenius plots) indicate steady oxidation mechanisms between 1500°C to 1700°C. Consequently, the oxidation kinetics increase with the temperature and lead to enhanced parabolic oxidation rate constants. The limiting factor for the oxidation is the reaction kinetic of between oxygen an ZrB_2. The porous ZrO_2 scale does not prevent the oxygen mobility to the oxidation front of the underlying substrate. No protection against oxidation can be observed.

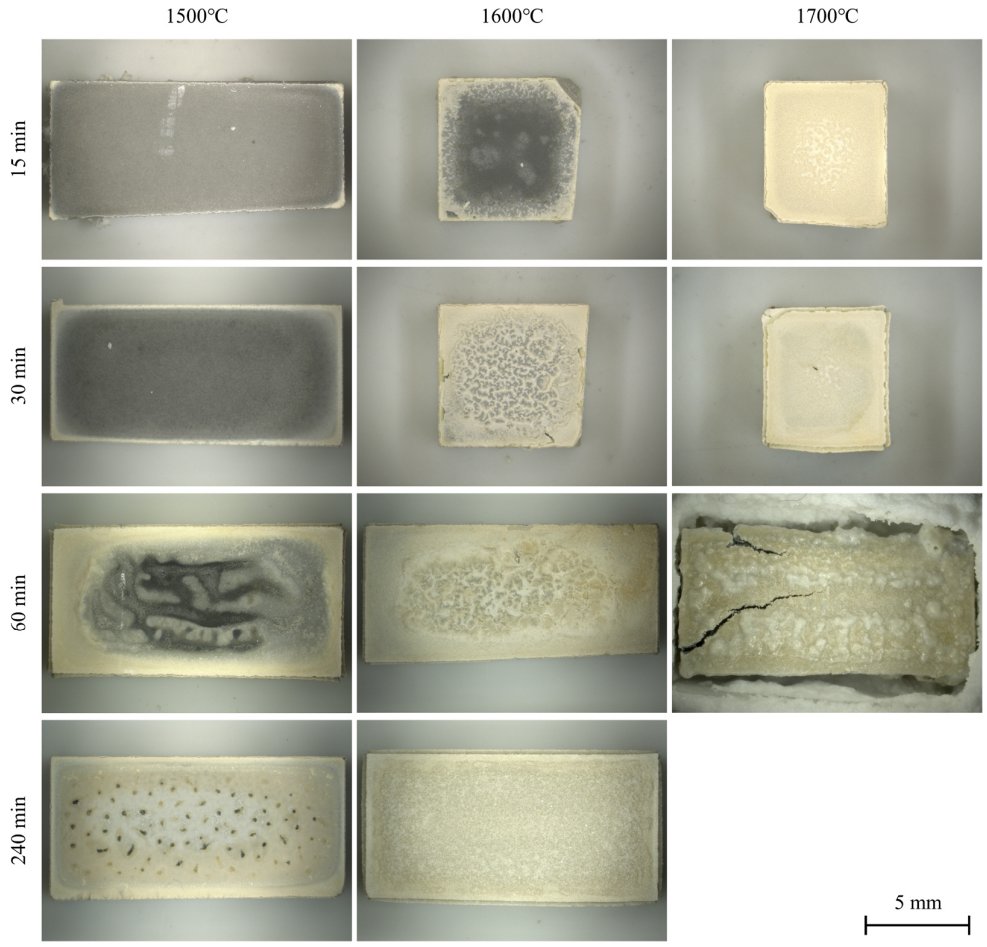

Fig. 5.3: Top-view photographs of tested baseline ZrB_2 at different temperatures and exposure times (P/Q)

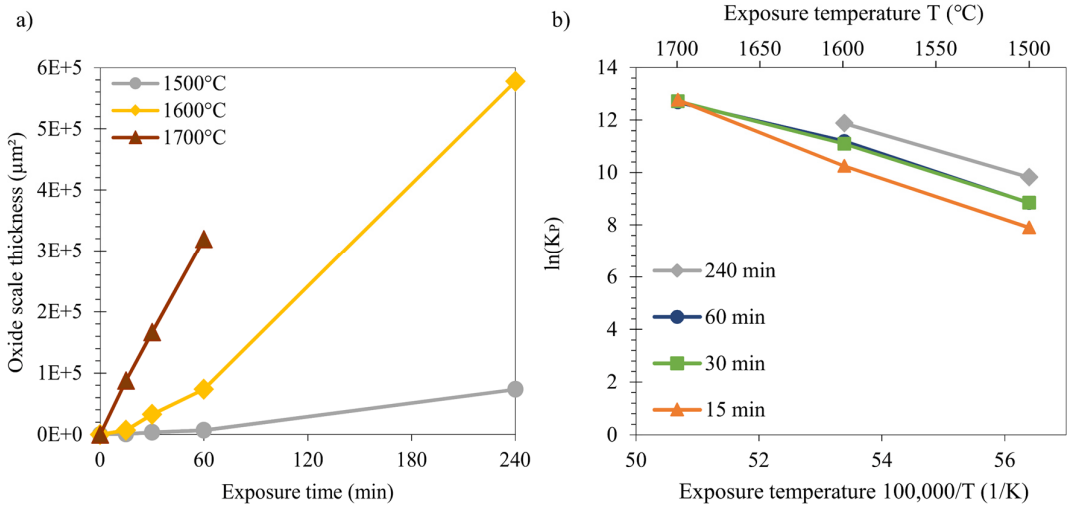

Fig. 5.4: Oxidation kinetics of baseline ZrB_2: a) Thickness of the porous oxide scale (PS) squared vs. exposure time; b) Arrhenius plot with parabolic oxidation rate constants vs. exposure temperature

Table 5.1: Oxide scale thickness of the porous oxide scale as well as the calculated parabolic oxidation rate constants for the porous ZrO_2 scale of baseline ZrB_2 after ramped (R/C) and rapid oxidation (P/Q)

Condition	Temperature	Time (min)	RS (µm)	PS (µm)	TS (µm)	PS/TS (%)	$\ln(K_{P(PS)})$
Baseline ZrB_2 R/C	1500°C	60	-	176	176	100	10.3
Baseline ZrB_2 P/Q	1500°C	15	-	26	26	100	7.9
		30	-	59	59	100	8.9
		60	-	83	83	100	8.8
		240	-	271	271	100	9.8
	1600°C	15	-	84	84	100	10.2
		30	-	181	181	100	11.1
		60	-	271	271	100	11.2
		240	-	760	760	100	11.9
	1700°C	15	-	296	296	100	12.8
		30	-	408	408	100	12.7
		60	-	565	565	100	12.7

Table 5.2: Calculated activation energies for the formation of porous ZrO_2 scales on baseline ZrB_2 for rapid oxidation (P/Q) in a temperature range between 1500°C to 1600°C and 1600°C to 1700°C

Condition	Exposure Time (min)	$E_{A1500-1600}$ (kJ/mol)	$E_{A1600-1700}$ (kJ/mol)
Baseline ZrB_2	15	647	774
	30	619	500
	60	653	451
	240	570	

5.2 Hafnium Oxide Coatings on ZrB_2

5.2.1 Development of HfO_2 Coatings on ZrB_2

This section is based on the published paper "Hafnium oxide coating to improve the oxidation behavior of zirconium diboride" (https://doi.org/10.1016/j.jeurceramsoc.2024.116774) by Förster et al. Content and texts may differ in part from the publication [137].

Oxygen-doped HfO_x coatings (HfO_x; $[x \in \mathbb{R} \mid 0 \leq x \leq 2]$) were deposited by means of reactive magnetron sputtering, using a metallic Hf target (Table 4.2, Target T1) and high-purity oxygen. Appropriate parameters for the reactive sputtering process were carried out with a multilayer coating experiment. Different oxygen gas flows were tested for similar processing conditions to analyze the effect on the deposition rate and chemical composition. The fractured cross-section of the coating experiment on Al_2O_3 substrate is presented in Fig. 5.5 . Details are provided in Table 5.3.

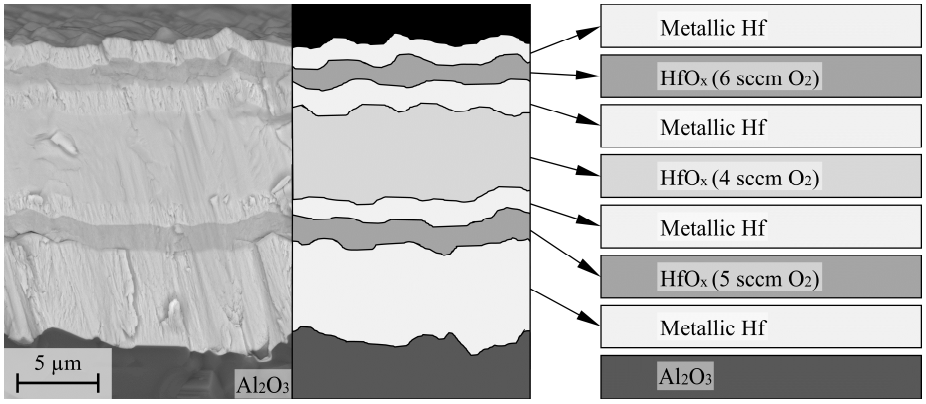

Fig. 5.5: BSE micrograph of fractured cross-section of multilayer parameter study for HfO_x coatings (Run1) with an appropriate schematic of the single layers and used process parameters (sccm O_2)

Table 5.3: Parameters for reactive magnetron sputtering of HfO_x coatings on ZrB_2 with metallic Hf target

Run	Time (min)	Power (W)	Voltage (V)	Argon (sccm)	Oxygen (sccm)	Thickness (µm)	Deposition (µm/h)	Oxygen in scale (at.%)
	90	500	615	20	0	7.3	4.86	15.7
	60	500	498	20	5.0	2.0	2.00	64.9
	15	500	540	20	0	1.5	6.13	14.6
Run1	60	500	621	20	4.0	7.1	7.07	32.9
	15	500	613	20	0	2.1	8.48	17.2
	60	500	523	20	6.0	1.7	1.69	67.6
	15	500	518	20	0	1.6	6.44	13.6
Run2	220	500	501	20	5.0	7.2	1.96	67.1
Run3	240	500	498	20	5.0	-	-	-
Run4	240	500	496	20	5.0	8.3	1.99	68.8

Metallic Hf layers were sputtered below and above each oxygen-doped HfO_x layer. Stopping the oxygen flow for a distinct period "cleans" the target surface from ceramic products (target poisoning during reactive sputtering) and ensures similar starting conditions for each test run (compare Fig. 2.18, Equ. 2.26). The effect of the oxygen flow on the deposition rate of a HfO_x coating and the chemical composition is presented in Fig. 5.6. The data indicates a transition from metallic Hf sputter conditions (≤4 sccm oxygen) to oxidic HfO_2 sputter conditions (≥5 sccm oxygen). It should be emphasized that there are not enough experimental results for a detailed analysis of the deposition behavior of HfO_x coatings in the transition zone. Furthermore, controlling a reactive sputtering process with the gas flow is inaccurate (see Fig. 2.19b). Measuring the partial pressures during the process for more reliable coating processes was not possible.

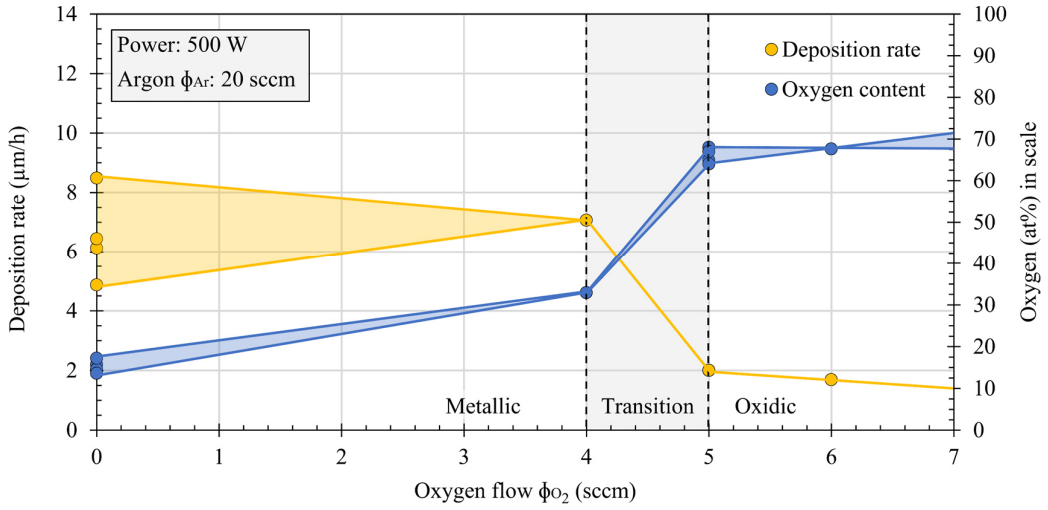

Fig. 5.6: Deposition rate of HfO_x coatings during reactive sputtering as a function of the oxygen gas flow

Considering the results, appropriate coating parameters were found to be with 5 sccm oxygen, providing the chemical composition for HfO_2 with the lowest needed oxygen flow. The deposition rate of ~2 µm/h was found to be high enough for the deposition of a coating of ~9 µm in thickness. Al_2O_3 substrates were coated with Run2 to verify the coating thickness and chemical composition. Subsequently, specimens of ZrB_2 were coated with Run3 and Run4 (compare Table 5.3).

Coatings were applied on ZrB_2 specimens with polished (3 µm grit size, Run3) and ground surfaces (10 µm grit size, Run4). Coatings on polished surfaces spalled directly after exposure to the atmosphere, whereas no spallation was observed for ground specimens. Therefore, all ZrB_2 specimens were ground using a 10 µm grit size before coating deposition [137]. The X-ray diffraction pattern of HfO_2 coated ZrB_2 (AC) is presented in Fig. 5.7a and indicates peaks for HfO_2 (PDF 00-034-0104) and ZrB_2 (PDF 00-034-0423). The widened peaks for the reflections of HfO_2 may indicate a partial amorphous nature for the coating. The Fig. 5.7b shows a BSE cross-sectional micrograph of the fractured Al_2O_3 test substrate with HfO_2 coating (AC, Run4). Analysis of the fractured cross-section revealed a coating thickness of ~8±1 µm. No pores were found in the deposited coating, proving its dense microstructure. The chemical composition was found to be ~31 at.% Hf and ~69 at.% O (Spec.B01). Detailed EDS results are provided in Table 5.4 [137].

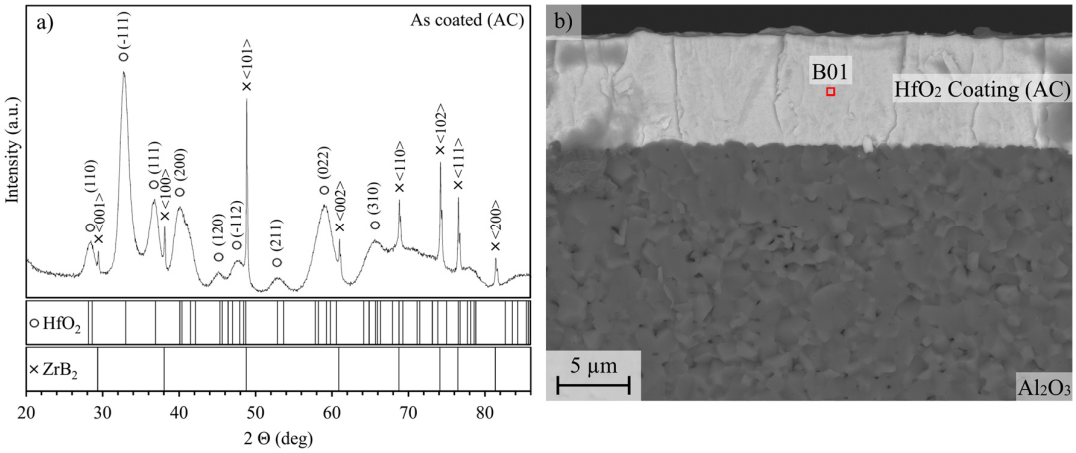

Fig. 5.7: *a) X-ray diffraction pattern of HfO_2 coated ZrB_2 substrate [137]; b) BSE micrograph of the fractured cross-section of HfO_2 coated Al_2O_3 substrate [137]*

To induce crystallization of the applied HfO_2 coating and to improve the adhesion to the ZrB_2 substrate, coated specimens were vacuum-annealed in a graphite furnace (compare Fig. 4.6). Top-view photographs of HfO_2 coated ZrB_2 (AC and VA) are presented in Fig. 5.8. Due to the vacuum-annealing procedure, the coloration of the deposited coating changed from a light brownish hue to a more grey shade. No defects were observed on the annealed surfaces except on one specimen. A chunk of the coating spalled as marked in Fig. 5.8b.

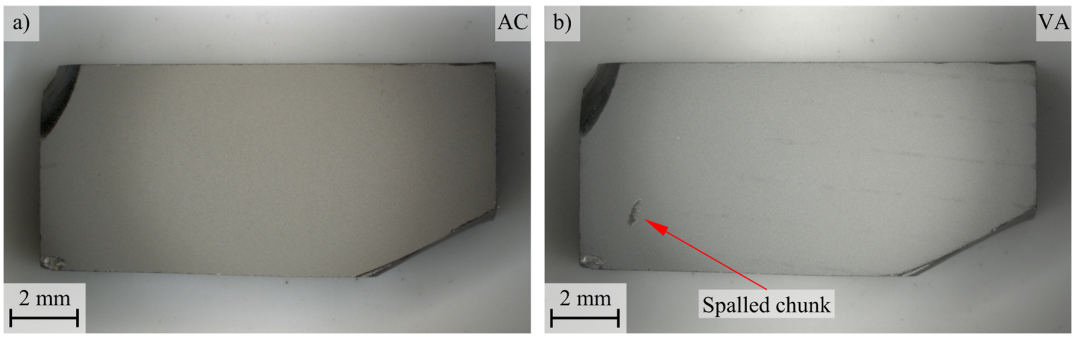

Fig. 5.8: *Top-view photographs of HfO_2 coated ZrB_2 substrate: a) As coated (AC); b) Vacuum-annealed (VA)*

The X-ray diffraction pattern of HfO_2 coated ZrB_2 (VA) is shown in Fig. 5.9a, which represents the crystalline nature of the annealed coating with sharp reflections. Peaks of HfB_2 (PDF 00-038-1398), $(Hf_{0.5}Zr_{0.5})B_2$ (PDF 01-074-5449), and $Hf(C_{0.84}O_{0.16})$ (PDF 01-085-4285) were identified. The associated Miller indices of the crystal lattice planes are marked in the diffraction pattern. A BSE cross-sectional micrograph of HfO_2 coated ZrB_2 (VA) is presented in Fig. 5.9b. Sparsely distributed pores with a diameter <1 µm can be found inside the annealed coating. However, no cracks or spallation were observed. The thickness of the annealed coating was measured as ~7.5±2 µm. Contrast information in the BSE micrograph indicated the formation of different phases inside the coating [137].

EDS spot analysis revealed different chemical compositions for the various phase fields inside the annealed coating. Detailed results of the EDS measurements are provided in Table 5.4. The chemical composition of the coating varied throughout the thickness, showing the content of Hf in the range of ~33-49 at.%, Zr in the range of ~4-24 at.% Zr, and C in the range of ~36-55 at.% (Spec.B02-B05) [137].

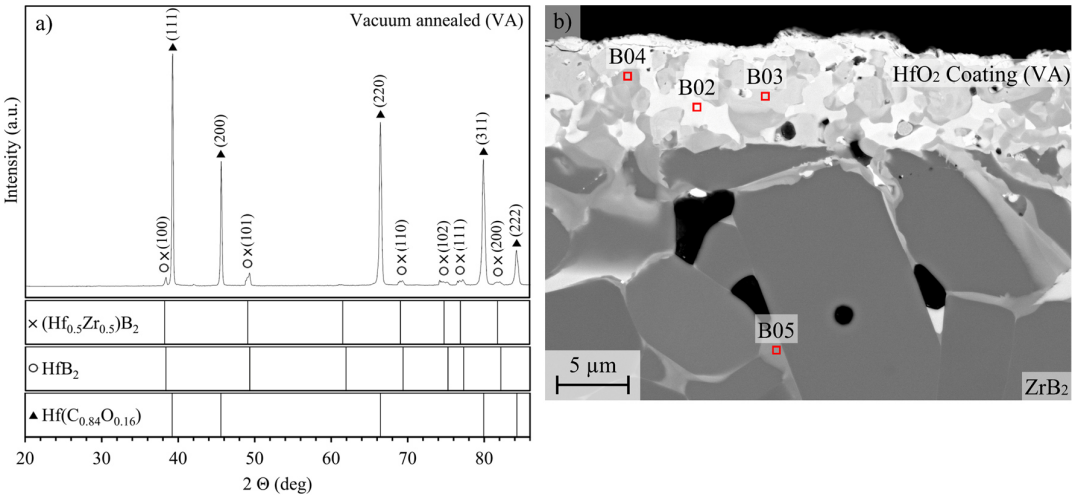

Fig. 5.9: HfO_2 coated ZrB_2 (VA): a) X-ray diffraction pattern [137]; b) BSE cross-sectional micrograph [137]

The low oxygen content of ~5 at.% should be emphasized. Furthermore, Hf cations diffused into the ZrB_2 ceramic along the grain boundaries (Spec.B05). The average diffusion depth was measured as ~21 µm.

Table 5.4: EDS analysis of HfO_2 coatings on ZrB_2 (compare Fig. 5.7 and Fig. 5.9) [137]

Condition	Spec.	O (at.%)	C (at.%)	Hf (at.%)	W (at.%)	Zr (at.%)	Zr/Hf	Phase (Estimated)
AC	B01	68.8	-	31.2	0	0	0	HfO_2
VA	B02	4.7	45.5	45.1	0.8	3.9	7.9	HfC
	B03	4.6	41.6	45.5	0.4	7.9	14.8	HfC
	B04	5.8	36.0	33.5	0.8	23.9	41.6	(Hf,Zr)C
	B05	5.3	70.1	14.2	1.0	9.4	39.8	$(Hf,Zr)B_2$

5.2.2 Ramped Oxidation Experiments of HfO_2 Coated ZrB_2

HfO_2 coated ZrB_2 (AC and VA) specimens were oxidized in a tube furnace at 1500°C for 60 min using ramped oxidation (R/C) (compare Fig. 4.10). The top-view photograph of the tested specimen (AC) as well as the corresponding X-ray diffraction pattern are presented in Fig. 5.10. The oxidized specimen showed a white-yellowish surface coloration with darker areas in the center of the specimen. ZrO_2 and HfO_2 have a similar crystal structure (Table 3.1). A clear differentiation of both oxides is not possible using X-ray diffraction or electron diffraction since both oxides have a quite

similar crystal structure. Therefore, the reflections in the diffraction pattern can be assigned to both oxide phases, m-ZrO_2 (PDF00-037-1484) and/or m-HfO_2 (PDF00-034-0104). Reflections for HfC were not observed. Associated Miller indices of the crystal lattice planes of the oxides are marked in the diffraction pattern [49, 137].

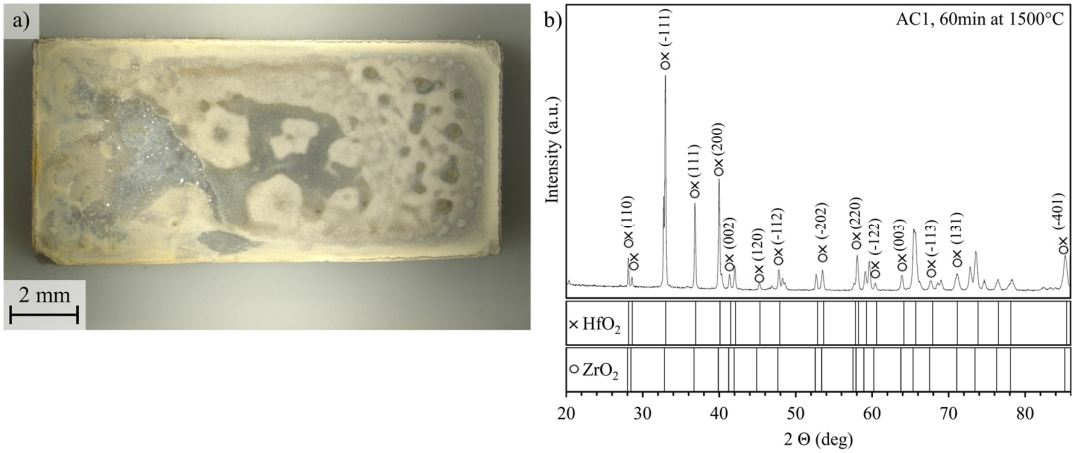

Fig. 5.10: HfO_2 coated ZrB_2 (AC) after ramped oxidation (R/C) for 60 min at 1500°C: a) Top-view photograph [137]; b) X-ray diffraction pattern with assigned Miller indices for m-HfO_2 and m-ZrO_2 [137]

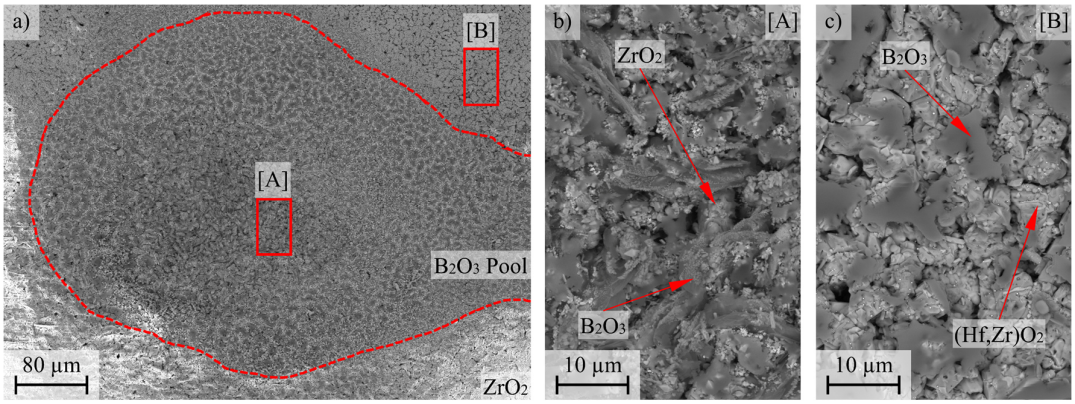

Fig. 5.11: BSE top-view micrographs of HfO_2 coated ZrB_2 (AC) after ramped oxidation (R/C) for 60 min at 1500°C: a) Over-view with marked B_2O_3 pool; b) High magnification of B_2O_3 pool center (area [A]); c) High magnification of the edge of the B_2O_3 pool (area [B])

BSE top-view micrographs are presented in Fig. 5.11 and prove the coverage with residual B_2O_3 glass, forming pools at the surface. The chemical composition of the B_2O_3-filled pools was measured as ~5 at.% Zr, ~1 at.% Hf, and ~94 at.% O. The residual surface is covered with oxide grains. The grains in the center of the B_2O_3 pools revealed a chemical composition of ~1 at.% Hf, ~32 at.% Zr, and ~67 at.% O (area A). The residual dry areas of the oxidized surface revealed grains with a chemical composition of ~19 at.% Hf, ~20 at.% Zr, and ~61 at.% O (area B).

The polished cross-section of the tested specimen is presented in Fig. 5.12. As visible in the BSE micrograph, the oxide scale consists of an uppermost reaction scale, containing (Hf,Zr)O_2. The chemical composition was measured as ~19 at.% Hf, ~20 at.% Zr, and ~61 at.% O (Spec.B06).

Porous ZrO_2 was found beneath the reaction scale (Spec.B07). Detailed EDS results are provided in Table 5.5. The microstructure of the applied coating was strongly influenced by the oxidation. The former dense HfO_2 coating transformed into a layer of single globular grains with an average diameter of ~2.7 µm. Partial spallation of the uppermost section was also observed [137].

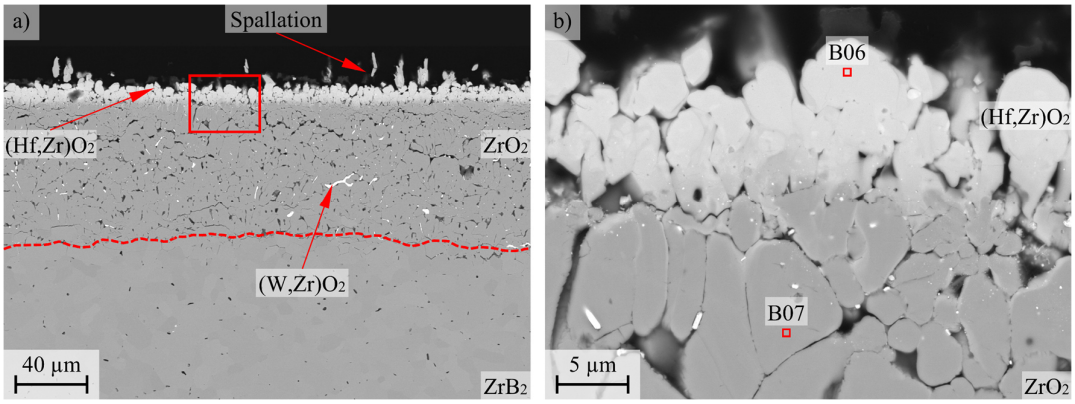

Fig. 5.12: BSE micrographs of HfO_2 coated ZrB_2 (AC) after ramped oxidation (R/C) for 60 min at 1500°C: a) Holistic oxide scale; b) High magnification of the uppermost reaction scale [137]

The BSE contrast information indicated a concentration gradient of Zr/Hf across the scale thickness from the uppermost section of the reaction scale to the underlying porous ZrO_2. An EDS line scan was used to identify the chemical gradient of Zr/Hf at the transition zone of the reaction scale to the porous ZrO_2. The results are presented in Fig. 5.13 and revealed a significant enrichment of the reaction scale by Zr (red marked area). The Zr content (red line) varies in a range of ~20-40 at.%, whereas the Hf content (grey line) decreased from 20 at.% to 0 at.% for porous ZrO_2. The oxygen content (blue line) was found to be constant at ~62 at.% [137].

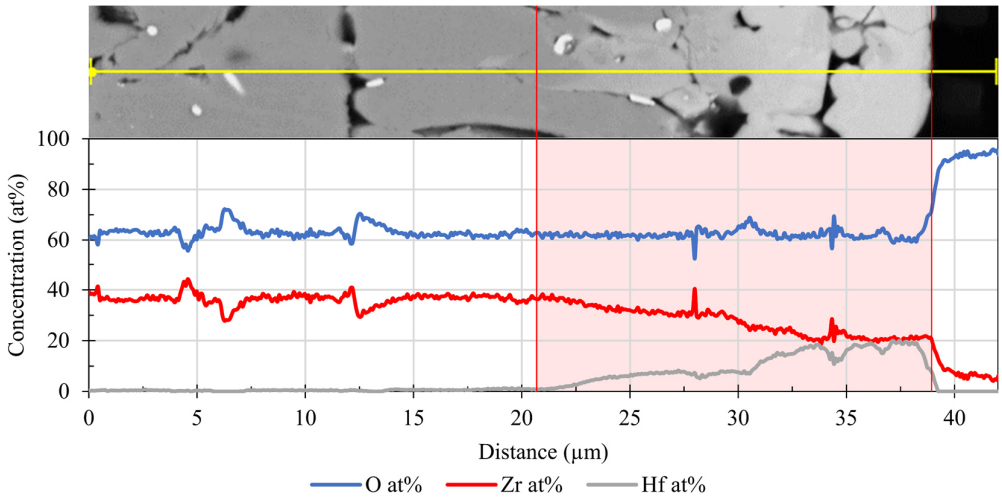

Fig. 5.13: EDS line scan of HfO_2 coated ZrB_2 (AC) after rapid oxidation (R/C) at 1500°C for 60 min

In contrast, HfO_2 coated ZrB_2 (VA) revealed different behavior for similar test conditions. The top-view photograph and X-ray diffractogram with assigned phases are presented in Fig. 5.14. As visible in the top-view photograph, the surface of HfO_2 coated ZrB_2 (VA) revealed a homogeneous distribution of B_2O_3 all over the surface, whereas the outer edges of the specimen were dry and covered with white-yellowish oxide (Fig. 5.14a). Crystalline ZrO_2 (PDF 00-037-1484) and HfO_2 (PDF 00-034-0104) were assigned to the diffraction pattern of the oxidized specimen (Fig. 5.14b).

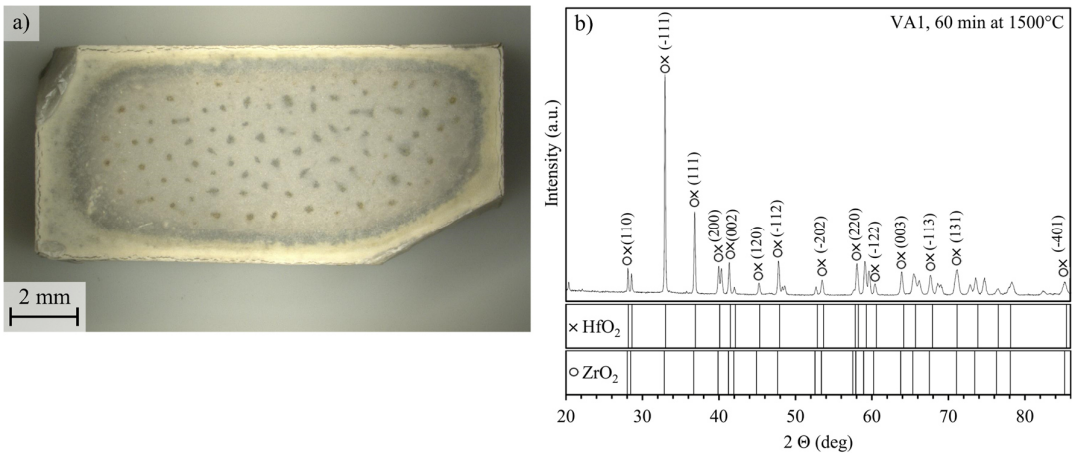

Fig. 5.14: HfO_2 coated ZrB_2 (VA) after ramped oxidation (R/C) for 60 min at 1500°C: a) Top-view photograph [137]; b) X-ray diffraction pattern with assigned Miller indices for m-HfO_2 and m-ZrO_2 [137]

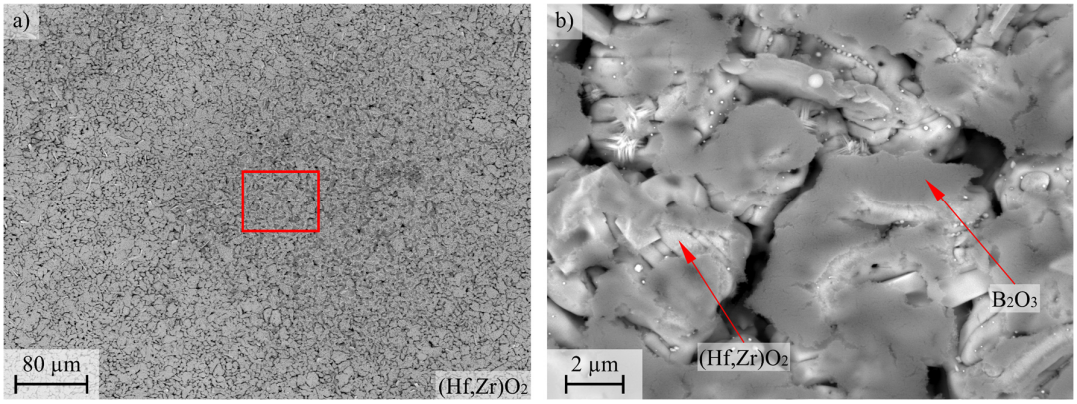

Fig. 5.15: BSE top-view micrographs of HfO_2 coated ZrB_2 after ramped oxidation (R/C) for 60 min at 1500°C: a) Overview of oxidized surface; b) High magnification of the surface grains at the surface

BSE top-view micrographs of the oxidized surface are presented in Fig. 5.15. The micrographs revealed the presence of B_2O_3 on the surface and inside the oxide scale. Arbitrary-shaped grains with an average size of ~9 µm were found at the oxidized surface. The grains were engraved and revealed a chemical composition of ~20 at.% Hf, ~19 at.% Zr, and ~61 at.% O.

BSE micrographs of the polished cross-section of HfO_2 coated ZrB_2 (VA) are presented in Fig. 5.16. The cross-section revealed an oxide scale, containing an overlaying reaction scale of $(Hf,Zr)O_2$ with irregularly shaped grains and an average diameter of 4.9±2 µm. Several gaps with a diameter of ~1 µm appeared between the single grains. The chemical composition for the grains was

measured as ~18 at.% Hf, ~19 at.% Zr, and ~63 at.% O (Spec.B08). Detailed results of the EDS spot analysis are provided in Table 5.5. Spallation of the coating was not observed, leading to an average thickness of the reaction scale of ~11 µm. The underlying porous ZrO_2 consists of ~35 at.% Zr and ~65 at.% O (Spec.B109). BSE contrast information indicated a distinct transition of the reaction scale to the underlying ZrO_2 scale [137].

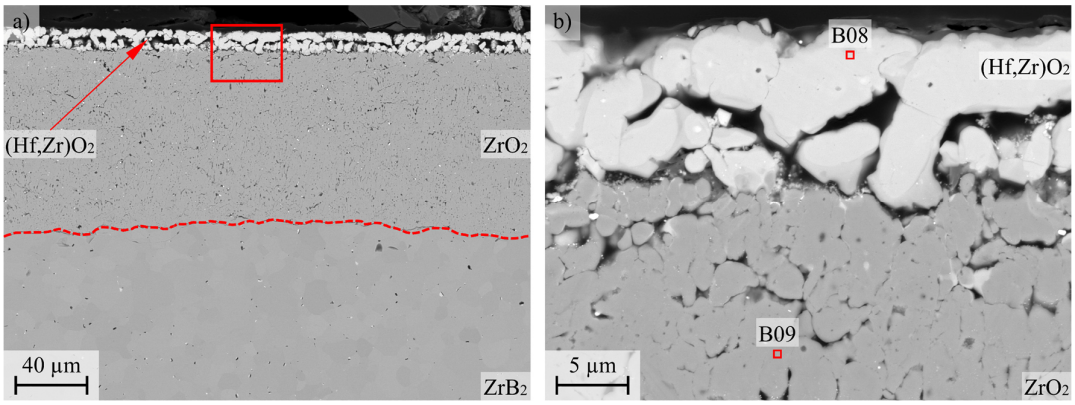

Fig. 5.16: BSE micrographs of HfO_2 coated ZrB_2 (VA) after ramped oxidation (R/C) for 60 min at 1500°C: a) Holistic oxide scale; b) High magnification of the uppermost reaction scale [137]

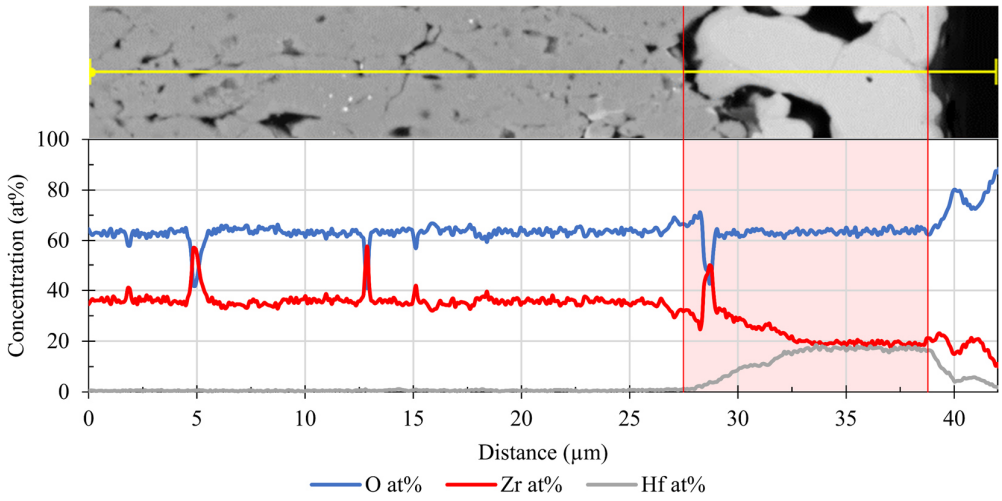

Fig. 5.17: EDS line scan HfO_2 coated ZrB_2 (VA) after ramped oxidation (R/C) at 1500°C for 60 min

EDS line scan was used to analyze the transition zone and to identify the chemical concentration gradient of Zr/Hf across the oxide scale thickness. The results are presented in Fig. 5.17. Some spots of Hf-rich solid solution can be found in the porous ZrO_2 scale. It is assumed the spots formed due to the grain boundary diffusion of Hf into the ceramic during vacuum-annealing (Fig. 5.9) [137].

Table 5.5: EDS analysis of HfO_2 coatings on ZrB_2 (AC and VA) after ramped oxidation (R/C) at 1500°C for 60 min (compare Fig. 5.12 and Fig. 5.16) [137]

Condition	Spec.	O (at.%)	C (at.%)	Hf (at.%)	W (at.%)	Zr (at.%)	Zr/Hf	Phase (Estimated)
AC	B06	61.2	-	18.1	0	20.6	53.2	$(Hf,Zr)O_2$
	B07	62.1	-	0.5	0	37.4	98.7	ZrO_2
VA	B08	63.6	-	17.1	0	19.3	53.0	$(Hf,Zr)O_2$
	B09	63.0	-	0.5	0.1	36.0	98.6	ZrO_2

Table 5.6 provides the average scale thicknesses of the reaction scale, the porous oxide scale, and total oxide scale for the tested specimens under ramped oxidation (R/C) at 1500°C for 60 min.

Table 5.6: Oxide scale thickness of HfO_2 coated specimens after ramped oxidation (R/C) at 1500°C for 60 min [137]

Condition	Temperature	Time (min)	RS (µm)	PS (µm)	TS (µm)	PS/TS (%)	$\ln(K_{P(PS)})$
AC	1500°C	60	19	91	110	82.7	9.4
VA	1500°C	60	11	109	120	90.8	9.6

5.2.3 Rapid Oxidation Experiments of HfO_2 Coated ZrB_2

Rapid oxidation experiments (P/Q) were performed with HfO_2 coated ZrB_2 (VA) (compare Fig. 4.10). Top-view photographs of oxidized specimens for 60 min or 240 min at 1500°C, 1600°C and 1700°C are presented in Fig. 5.18.

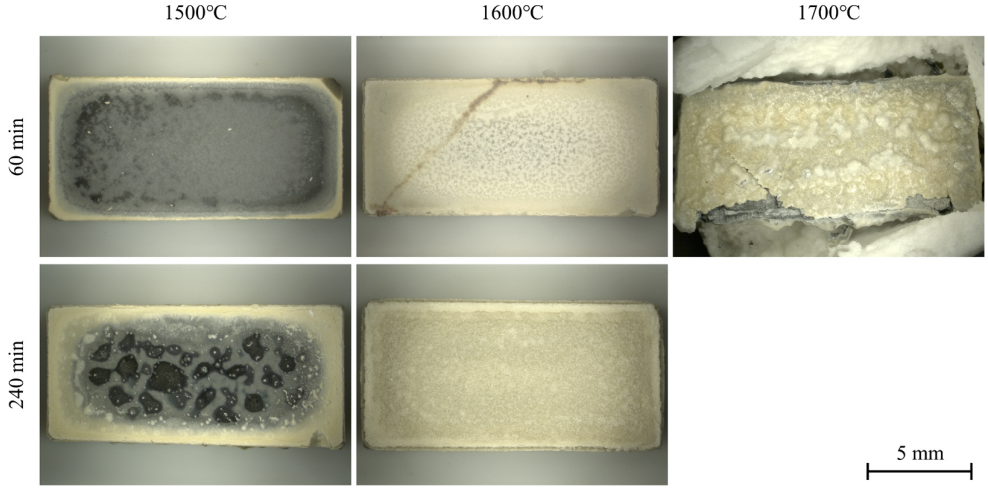

Fig. 5.18: Top-view photographs of HfO_2 coated ZrB_2 (VA) after rapid oxidation (P/Q) at distinct temperatures for a prescribed exposure time of 60 min and 240 min

Specimens tested at 1500°C for 60 min revealed a darkish coloration in the center. The edges of the specimens were covered by white yellowish oxide. The amount of yellowish oxide at the edges increased with respect to the oxidation time, starting from the edges and growing into the center of the specimen. At 1600°C most of the surface was covered with yellowish oxides. Darker spots were found in the center. After 240 min at 1600°C the specimen was completely covered with yellowish oxide. Spallation of the formed oxide scale was not observed. Finally, the oxidation at 1700°C for 60 min led to the destruction of the specimen and the Al_2O_3 crucible. Both sintered together. The preparation of the specimen for X-ray analysis as well as surface analysis via SEM was not possible. Cracks formed at the surface and induced the partial spallation of the oxide scale. The X-ray diffraction pattern of HfO_2 coated ZrB_2 (VA) after 60 min and 240 min of rapid oxidation (P/Q) at 1500°C and 1600°C are presented in Fig. 5.19. As mentioned above, the preparation of the specimen tested at 1700°C was not possible. ZrO_2 (PDF00-037-1484) and HfO_2 (PDF00-034-0104) were assigned for the diffractogram. Associated Miller indices of the crystal lattice planes of the oxides are marked in the diffraction pattern [137].

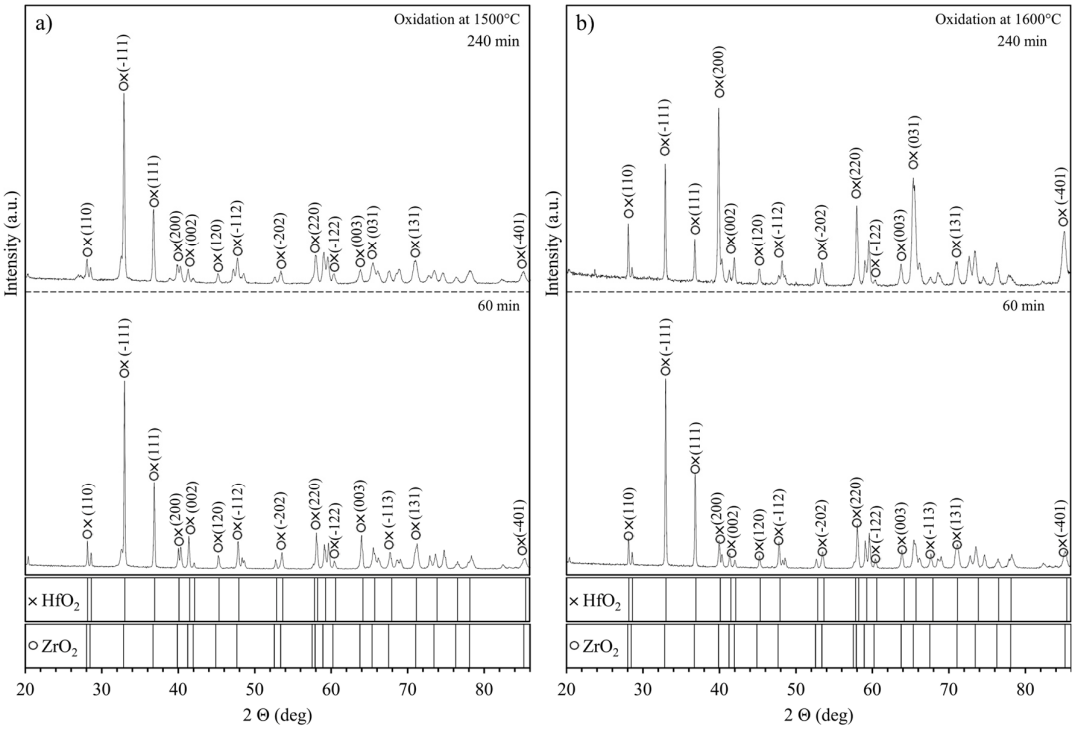

Fig. 5.19: X-ray diffraction pattern of HfO_2 coated ZrB_2 (VA) after rapid oxidation (P/Q) for 60 min and 240 min: a) at 1500°C; b) at 1600°C

Polished cross-sections were analyzed and oxide scale thicknesses were measured. The Fig. 5.20, Fig. 5.21, and Fig. 5.22 presents BSE micrographs of the oxide scales of HfO_2 coated ZrB_2 (VA) after rapid oxidation (P/Q) at 1500°C, 1600°C, and 1700°C for 60 min and 240 min. Corresponding micrographs in high magnification show the former interface zone of the coating/substrate. Blue-dashed lines mark the transition between the reaction scale (RS) and the porous ZrO_2 scale (PS). The oxidation front of ZrB_2 is marked with the red dashed line [137].

Polished cross-sectional BSE micrographs of the specimens tested at 1500°C via rapid oxidation are presented in Fig. 5.20. After just 60 min of oxidation, the initial coating transformed into a reaction scale of single grains with an average diameter of ~7 µm. The chemical composition of the reaction scale was measured as ~19 at.% Hf, ~18 at.% Zr, and ~63 at.% O (Spec.B10). Detailed EDS data are provided in Table 5.7. The grains of (Hf,Zr)O_2 reacted with the underlying porous ZrO_2 scale (Spec.B11) and formed a solid solution, anchoring the formed grains chemically to the underlying porous ZrO_2 scale (Spec.B12). A similar architecture for the oxide scale was observed after 240 min of oxidation. Single grains of a mixed oxide solid solution (Hf,Zr)O_2 with a diameter of ~8 µm were observed at the uppermost section of the oxide scale, forming a reaction scale of ~16 µm. The chemical composition was measured as ~18 at.% Hf, ~21 at.% Zr, and ~61 at.% O (Spec.B13). The grains of (Hf,Zr)O_2 reacted with the underlying porous ZrO_2 scale (Spec.B15) and formed a solid solution (Spec.B14). The BSE contrast information in the micrograph revealed the presence of a darker layer, which covered the single grains of (Hf,Zr)O_2. The chemical analysis of that layer revealed a composition of ~5 at.% Hf, ~32 at.% Zr, and ~63 at.% O (Spec.B16) [137].

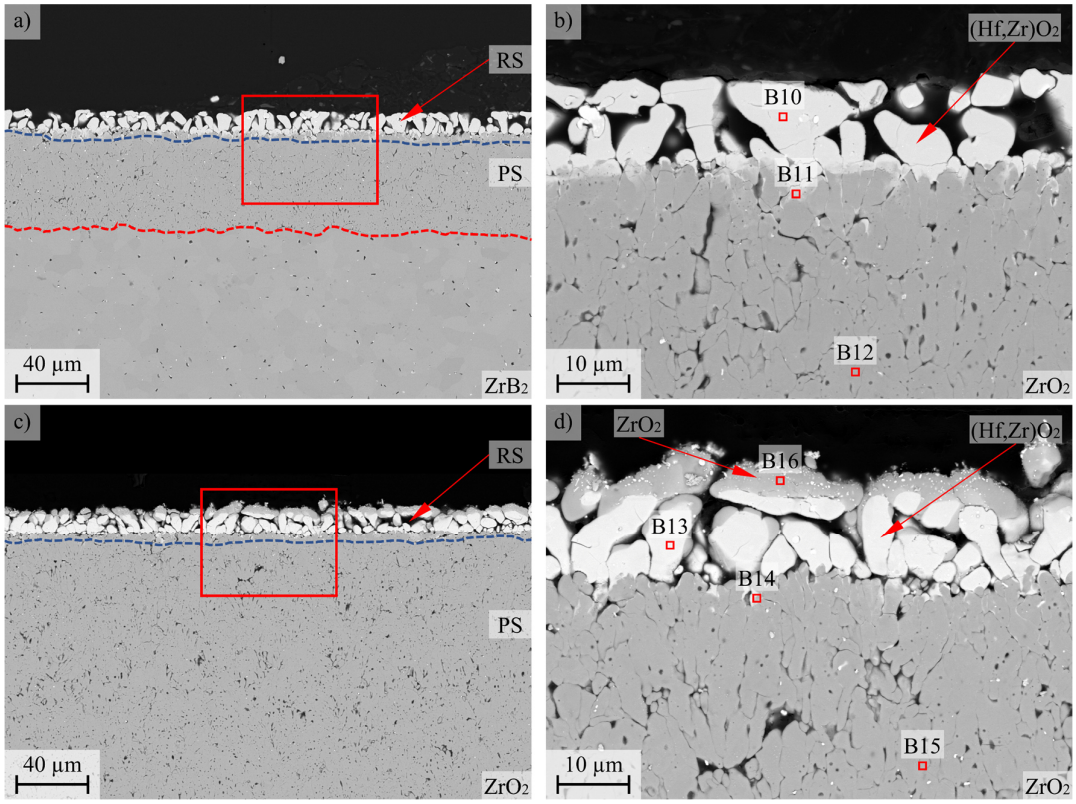

Fig. 5.20: BSE cross-sectional micrographs of HfO_2 coated ZrB_2 (VA) after rapid oxidation (P/Q) at 1500°C: a) Overview after 60 min ; b) Reaction scale after 60 min [137]; c) Overview after 240 min; d) Reaction scale after 240 min [137]

Table 5.7: EDS analysis of HfO_2 coated ZrB_2 (VA) after rapid oxidation (P/Q) for 60 min and 240 min at 1500° (compare Fig. 5.20) [137]

Condition	Spec.	O (at.%)	C (at.%)	Hf (at.%)	W (at.%)	Zr (at.%)	Zr/Hf	Phase (Estimated)
1500°C, 60 min	B10	62.4	-	19.2	0	18.4	48.9	$(Hf,Zr)O_2$
	B11	62.9	-	2.2	0.2	34.6	94.0	$(Zr,Hf)O_2$
	B12	63.2	-	0.9	0.1	35.7	97.5	ZrO_2
1500°C, 240 min	B13	61.3	-	17.8	0	20.9	54.0	$(Hf,Zr)O_2$
	B14	60.9	-	5.1	0	34.0	87.0	$(Zr,Hf)O_2$
	B15	62.2	-	1.7	0.1	36.0	95.5	ZrO_2
	B16	63.4	-	4.7	0.1	31.8	87.1	ZrO_2

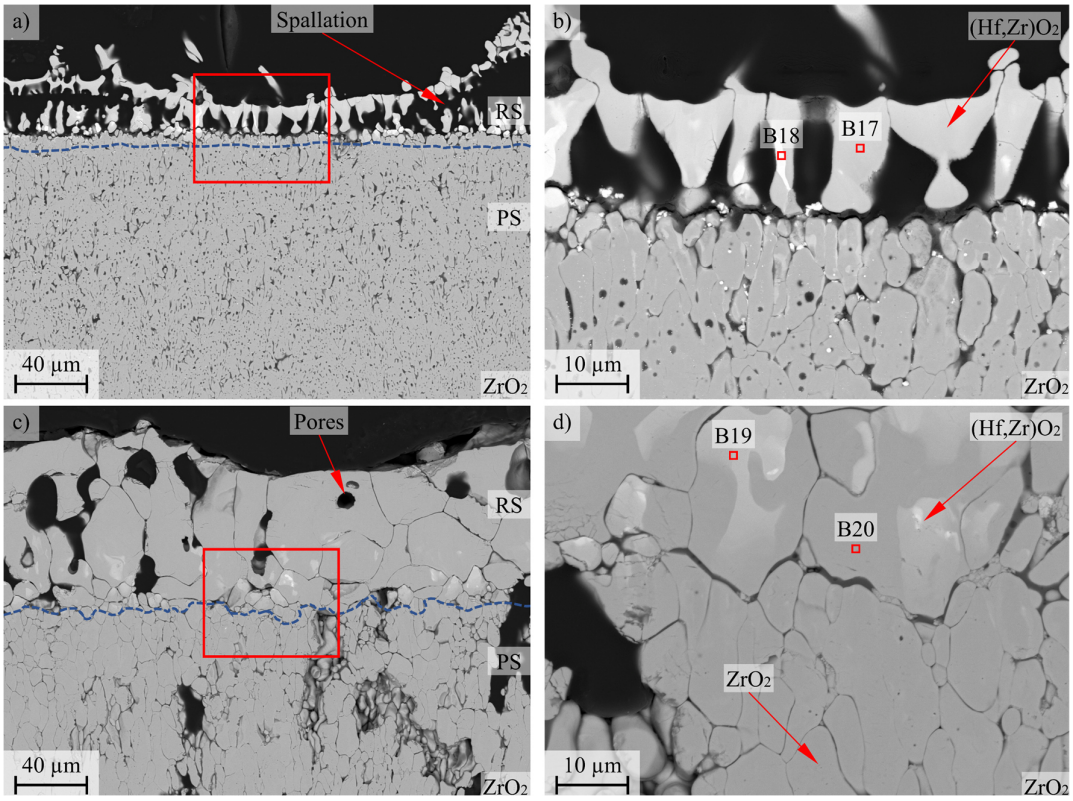

Fig. 5.21: BSE cross-sectional micrograph of HfO_2 coated ZrB_2 (VA) after rapid oxidation (P/Q) at 1600°C: a) Overview after 60 min; b) Reaction scale after 60 min [137]; c) Overview after 240 min; d) Reaction scale after 240 min [137]

Table 5.8: EDS analysis of HfO_2 coated ZrB_2 (VA) after rapid oxidation (P/Q) for 60 min and 240 min at 1600°C (compare Fig. 5.21) [137]

Condition	Spec.	O (at.%)	C (at.%)	Hf (at.%)	W (at.%)	Zr (at.%)	Zr/Hf	Phase (Estimated)
1600°C, 60 min	B17	63.5	-	9.1	0	27.4	75.1	$(Hf,Zr)O_2$
	B18	64.1	-	20.5	0.2	15.4	42.9	$(Hf,Zr)O_2$
1600°C, 240 min	B19	62.9	-	10.3	0.1	26.7	72.2	$(Hf,Zr)O_2$
	B20	63.1	-	2.2	0.1	34.6	94.0	ZrO_2

BSE micrographs of the polished cross-sections of HfO_2 coated ZrB_2 (VA) oxidized at 1600°C for 60 min and 240 min are presented in Fig. 5.21. Similar to the specimens tested at 1500°C, the oxide scale consists of a reaction scale of mixed oxides $(Hf,Zr)O_2$ with a thickness of ~31 µm and an underlying porous ZrO_2 scale. EDS analysis for the specimens tested at 1600°C is provided in Table 5.8. The initial HfO_2 coating with dense microstructure has transformed into a layer with several defects such as cracks and pores. Partial spallation of the reaction scale was observed at a few locations (Fig. 5.21a). The chemical composition inside the reaction scale was measured as ~9 at.% Hf, ~27 at.% Zr, and ~64 at.% O (Spec.B17). Several spots were found in the reaction scale, which revealed a content of up to ~21 at.% Hf (Spec.B18). However, on average the amount of Zr inside the reaction scale exceeds the content of Hf. The oxidation after 240 min at 1600°C formed a thick overlaying reaction scale with a composition of ~2 at.% Hf, ~35 at.% Zr, and ~63 at.% O (Spec.B20). Several spots inside the reaction scale were found with up to ~10 at.% Hf (Spec.B19). These spots appeared more bright in the micrograph due to the BSE contrast information. Furthermore, enlarged pores formed inside the reaction scale with a diameter of ~18 µm (Fig. 5.21c). The thickness of the reaction scale increased significantly to ~83 µm [137].

As mentioned earlier, the oxidation for 60 min at 1700°C led to an extensive degradation of the HfO_2 coated ZrB_2 (VA) and caused sintering damage with the Al_2O_3 crucible. The cross-section is presented in Fig. 5.22 and revealed a significant effect on the appearance and behavior of the formed oxide scale. Similar to the specimen tested for 240 min at 1600°C, the reaction scale increased in thickness up to ~112 µm. The analysis of the former interface zone of the coating/substrate in area [C] revealed sparsely distributed spots with bright contrast information. The chemical composition for the reaction scale was measured as ~2 at.% Hf, ~35 at.% Zr, and ~63 at.% O (Spec.B22), whereas the bright spots revealed a content up to ~15 at.% Hf (Spec.B21). Pores were dominant in the reaction scale and reached an average diameter of ~32 µm. The underlying porous ZrO_2 in the area [D] was found to be infiltrated by an Al_2O_3-rich phase (Spec.B24). It can be assumed the infiltration of the porous oxide scale by the Al_2O_3-containing phase manipulated the experiment. Therefore, the significance of this experiment is less consequential. Results for the EDS spot analysis of the tested specimen at 1700°C are provided in Table 5.9 [137].

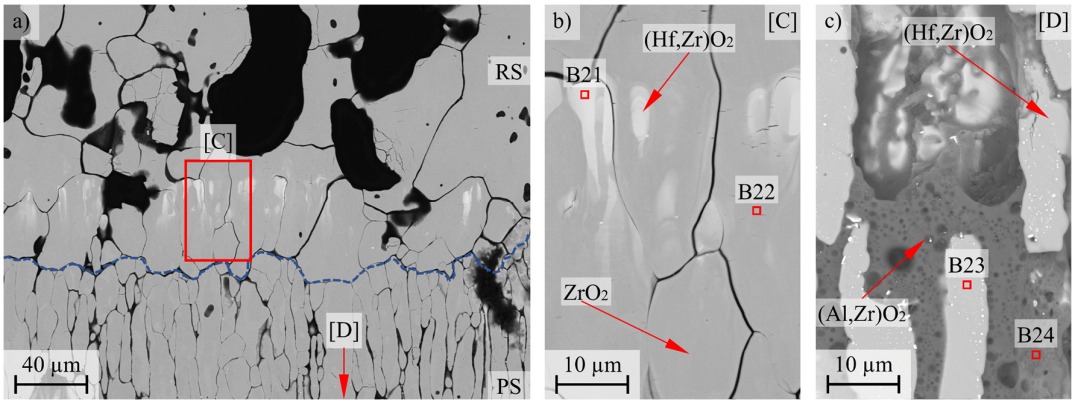

Fig. 5.22: BSE cross-sectional micrographs of HfO_2 coated ZrB_2 (VA) after rapid oxidation (P/Q) at 1700°C: a) Overview after 60 min; b) Reaction scale after 60 min (area [C]); c) Porous ZrO_2 scale with Al_2O_3 rich phase ($Al_{18}B_4O_{33}$) after 60 min (area [D])

Table 5.9: EDS analysis of HfO_2 coatings on ZrB_2 (VA) after rapid oxidation (P/Q) for 60 min at 1700°C (compare Fig. 5.22)

Condition	Spec.	O (at.%)	C (at.%)	Hf (at.%)	Al (at.%)	Zr (at.%)	Zr/Hf	Phase (Estimated)
1700°C, 60 min	B21	63.7	-	1.8	0	34.5	95.0	ZrO_2
	B22	63.5	-	15.2	0	21.3	58.4	$(Hf,Zr)O_2$
	B23	64.2	-	1.7	0	34.1	95.3	ZrO_2
	B24	67.6	-	0	32.1	0.3	-	$Al_{18}B_4O_{33}$

5.2.4 Kinetic Calculations of HfO_2 Coated ZrB_2

The formed oxide scales on HfO_2 coated ZrB_2 (VA) were subdivided into an uppermost reaction scale RS, an underlying porous ZrO_2 scale PS, and the total oxide scale TS (RS+PS). The reaction scale contained >2 at.% Hf, whereas the porous ZrO_2 consisted of pure ZrO_2. The holistic oxide scales, formed on HfO_2 coated ZrB_2 (VA) after the prescribed oxidation time at distinct temperatures are shown in Fig. 5.23. The reaction scales are marked with a blue dashed line, whereas the oxidation front of ZrB_2 is marked with a red dashed line. The scale segments (RS, PS, TS) were measured for all tested specimens, following the measurement and calculation method described in Chapter 4.5.7 (Fig. 4.13b). The average scale thicknesses are provided in Table 5.10. Results revealed an increase in the porous oxide scale thickness by time and temperature. This trend is visualized in Fig. 5.24a, presenting the squared oxide scale thickness of the PS of isothermal tested specimens over time. The parabolic oxidation rate constants for the PS were calculated according to the differential equation of linear-parabolic oxidation kinetics by Deal and Grove (Equ. 2.14) [70, 138]. As visible in Fig. 5.24a, the oxidation rate constants increase by temperature and exposure time. For both conditions, 1500°C and 1600°C, a transition of the oxidation behavior can be seen after 60 min of oxidation (slope of the plots, compare Fig. 2.10c) [137].

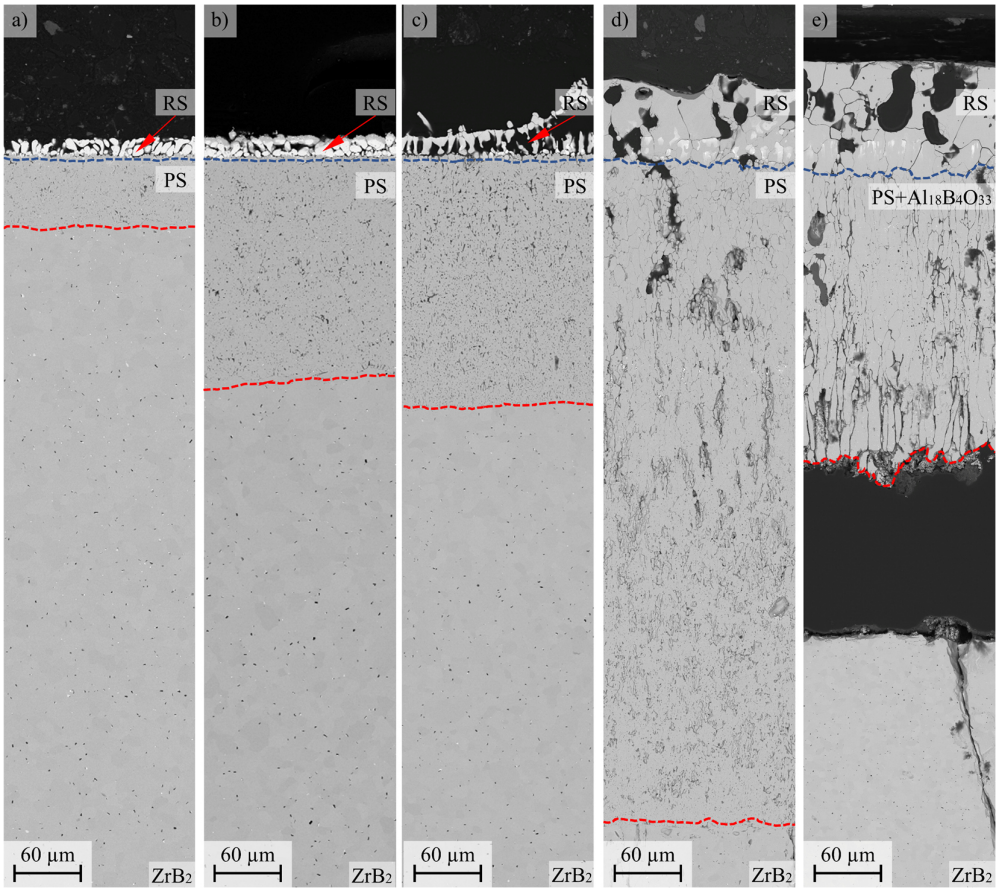

Fig. 5.23: *BSE micrographs of the holistic oxide scales formed on HfO_2 coated ZrB_2 (VA) for isothermal oxidation: a) 60 min at 1500°C; b) 240 min at 1500°C; c) 60 min at 1600°C; d) 240 min at 1600°C; e) 60 min at 1700°C [137]*

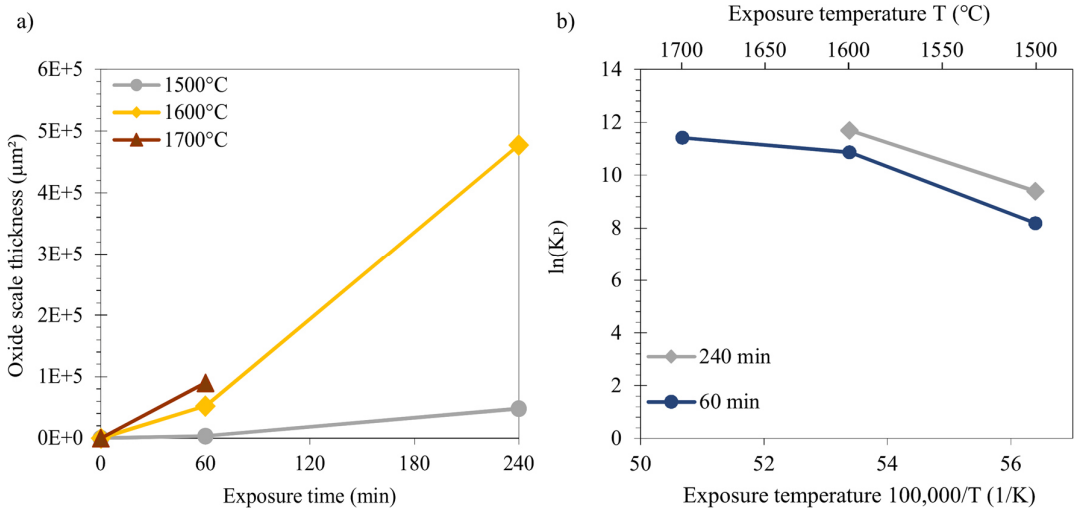

Fig. 5.24: *HfO_2 coated ZrB_2 (VA) after rapid oxidation (P/Q): a) Thickness of the porous oxide scale (PS) squared vs. time; b) Arrhenius plot with calculated parabolic oxidation rate constants vs. temperature*

Table 5.10: Oxide scale thickness and calculated parabolic rate constant of HfO_2 coated ZrB_2 (VA) for the porous ZrO_2 scale after rapid oxidation (P/Q) [137]

Condition	Temperature	Time (min)	RS (µm)	PS (µm)	TS (µm)	PS/TS (%)	$\ln(K_{P(PS)})$
HfO_2 coated (VA)	1500°C	60	12	60	73	82.1	8.2
		240	16	219	236	92.7	9.4
	1600°C	60	31	229	262	87.4	10.9
		240	83	691	779	88.7	11.7
	1700°C	60	112	300	411	72.9	11.4

Further, the activation energy for the temperature regime 1500°C to 1600°C and 1600°C to 1700°C were calculated, using Equ. 2.15. The results are visualized in Fig. 5.24b in form of an Arrhenius plot, showing the change of oxidation rate constants over the temperature. The calculated values are provided in Table 5.11. As visible in the diagram, a decreasing trend for the activation energy can be seen for higher temperature regimes (decreasing slope of the trend with the temperature). The reason for this behavior will be thoroughly argued in the discussion [137].

Table 5.11: Calculated activation energies of HfO_2 coated ZrB_2 (VA) after rapid oxidation (P/Q) for the temperature regime 1500°C to 1600°C and 1600°C to 1700°C after 60 min and 240 min of oxidation

Condition	Exposure Time (min)	$E_{A1500\text{-}1600}$ (kJ/mol)	$E_{A1600\text{-}1700}$ (kJ/mol)
HfO_2 coated (VA)	60	740	166
	240	635	-

5.3 Metallic Niobium Coatings on ZrB_2

5.3.1 Development of Nb Coatings on ZrB_2

This section is based on the published paper of Förster et al. "Oxidation behavior of Nb-coated zirconium diboride" (https://doi.org/10.1016/j.jeurceramsoc.2023.04.029). Content and texts may differ in part from the publication [139].

Metallic Nb coatings were deposited by magnetron sputtering, using a metallic Nb target (Table 4.2, Target T2). ZrB_2 specimens were polished with a surface finish of 3 µm grit size and ultrasonically cleaned. The parameters for the magnetron sputtering processes, to apply metallic Nb coatings on ZrB_2, are provided in Table 5.12. The first deposition run with metallic Nb coatings was performed on Al_2O_3 substrates to investigate the deposition rate. Run5 revealed a deposition rate of ~5.6 µm/h. Specimens of ZrB_2 were coated with consecutive runs. The deposition rate decreased from Run6 with ~5.5 µm/h to Run7 with ~5.3 µm/h and led to a coating thickness of ~9 µm. Parallel the voltage decreased. This behavior will be discussed later in the section of the discussion of metallic Nb coating development [139].

Table 5.12: Parameters for magnetron sputtering of metallic Nb coatings on ZrB_2 with metallic Nb target

Run	Time (min)	Power (W)	Voltage (V)	Argon (sccm)	Oxygen (sccm)	Thickness (µm)	Deposition (µm/h)	Oxygen in Scale (at.%)
Run5	100	500	368	20	0	9.3	5.6	0
Run6	100	500	352	20	0	9.1	5.5	0
Run7	100	500	332	20	0	8.8	5.3	0

The X-ray diffraction pattern of Nb coated Al_2O_3 substrate (AC) is presented in Fig. 5.25a. The detected reflections were assigned to metallic Nb (PDF00-035-0789). Associated Miller indices of the crystal lattice planes are marked in the diffraction pattern [139].

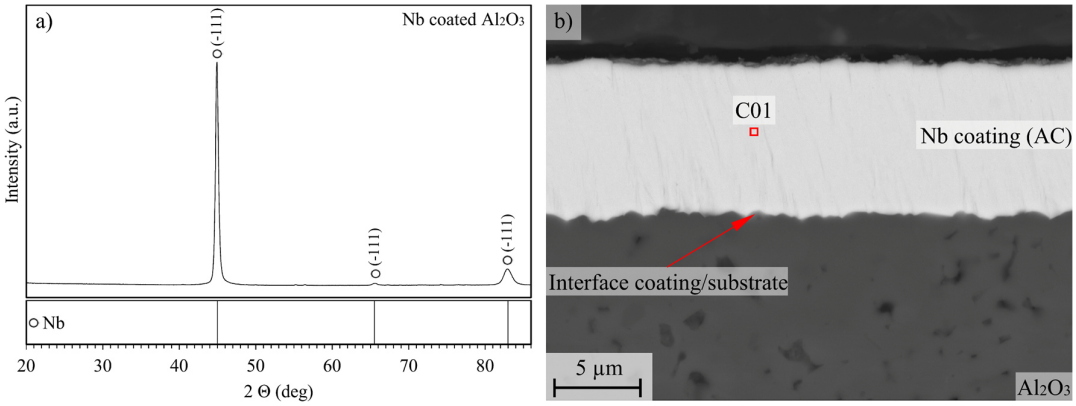

Fig. 5.25: Metallic Nb coating on Al_2O_3 substrate (AC): a) X-ray diffraction pattern; b) BSE cross-sectional micrograph [139]

A BSE cross-sectional micrograph of the applied Nb coating on Al_2O_3 substrate (AC) is presented in Fig. 5.25b. The micrograph confirmed a uniform thickness of ~9 µm for the metallic Nb coating, exhibiting a dense morphology without defects such as pores and cracks. Results of the EDS analysis of the applied HfO_2 coating are provided in Table 5.13. The chemical analysis revealed a contamination of Titanium by <1 at.% (Spec.C1). The hypothesized reason for the contamination and its effect will be discussed later. Considering the unit cells and the Wyckoff positions for Nb atoms in metallic Nb and in Nb_2O_5, the applied Nb coating might experience a volume expansion of ~170 vol% during oxidation (Table 3.2). Therefore, spallation of the metallic Nb coating is expected to appear during oxidation [139].

Nb coated ZrB_2 (AC) were vacuum-annealed (Fig. 4.6) to induce the mutual interdiffusion of ZrB_2 and metallic Nb at the interface zone of the coating/substrate. Top-view photographs of Nb coated ZrB_2 before and after vacuum annealing are presented in Fig. 5.26. No spallation of the metallic Nb coating or defects such as cracks or open pores were observed at the surface of the coated ZrB_2 after vacuum-annealing (VA). The silver metallic coloration of the Nb coating changed to a yellowish hue during the vacuum-annealing procedure. The effect of vacuum-annealing on the chemical composition and microstructure of the Nb coating is presented in Fig. 5.27 [139].

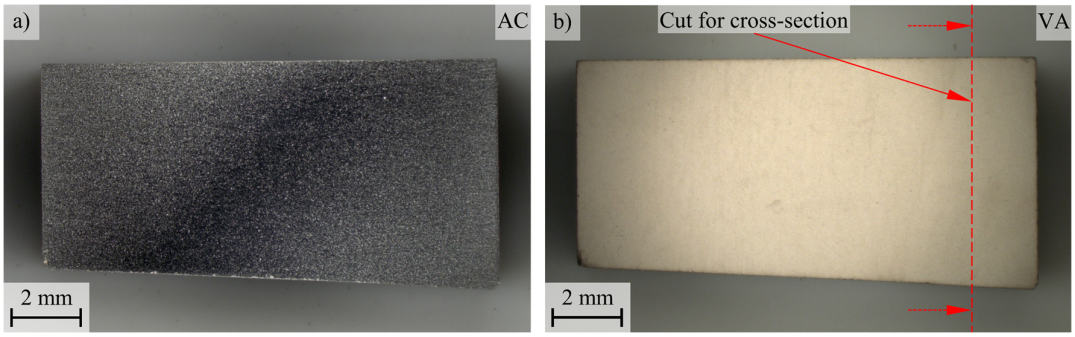

Fig. 5.26: Top-view photographs of Nb coated ZrB_2: a) As coated (AC); b) Vacuum-annealed (VA) with marked cut (red dashed line) to prepare a cross-section for further investigation

The X-ray diffraction pattern for Nb coated ZrB_2 (VA) revealed reflections for NbC (PDF00-038-1364). Further, reflections for NbB_2 (PDF03-065-0512) were found in a high magnification of the pattern. Associated Miller indices of the crystal lattice planes are marked in the diffraction patterns (Fig. 5.27a). BSE cross-sectional micrograph of Nb coated ZrB_2 (VA) revealed the presence of two discrete layers with a total thickness of ~9 µm. Detailed results of the EDS analysis for the Nb coated ZrB_2 (AC and VA) are provided in Table 5.13. A scale of ~7 µm thick with a chemical composition of ~13 at.% Nb and ~35 at.% C (Spec.C2) was attached to the ZrB_2 substrate. An outer dark layer of additional ~2 µm thick (darkish) revealed a chemical composition of ~9.5 at.% Nb and ~23 at.% C (Spec.C3). EDS is not a reliable method for the differentiation and quantification of lightweight atoms such as boron and carbon (compare Chapter 4.5.5). However, the presence of boron in the uppermost section of the annealed coating is unambiguous and aligns with the results of the X-ray diffraction, identifying the phases NbC and NbB_2. A characteristic porosity was observed at the interface zone of the coating/substrate, formed inside the vacuum-annealed Nb coating [139].

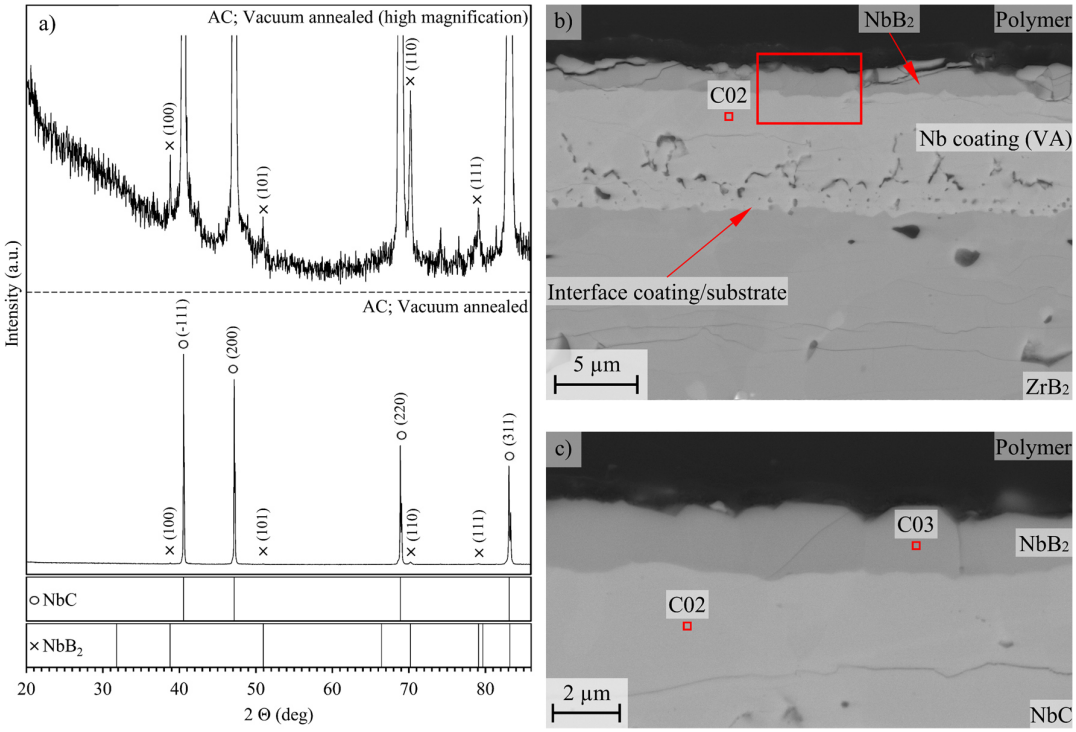

Fig. 5.27: *Nb coated ZrB_2 after vacuum annealing (VA): a) X-ray diffraction pattern; b) BSE cross-sectional micrograph of the vacuum-annealed coating; c) High magnification of the uppermost section of the vacuum-annealed Nb coating*

Table 5.13: *EDS analysis of unoxidized Nb coated ZrB_2 (AC and VA) (compare Fig. 5.25 and Fig. 5.27)*

Condition	Spec.	B (at.%)	O (at.%)	C (at.%)	Ti (at.%)	Zr (at.%)	Nb (at.%)	Zr/Hf	Phase (Estimated)
AC	C01	-	-	-	0.8	0	99.2	95.0	Nb
VA	C02	51.5	0.3	34.9	0	0	13.3	95.3	NbC
	C03	66.0	0.6	22.5	1.2	0.2	9.5	2.0	NbB_2

HAADF micrographs of a TEM lamella of Nb coated ZrB_2 (VA) are presented in Fig. 5.28. Area [E] shows the uppermost section of the annealed Nb coating and area [F] shows the interface zone of the coating/substrate. STEM-EDS results are provided in Table 5.14. The electron diffraction of the uppermost section of the Nb coating (VA) revealed a hexagonal crystal structure (Diffraction I). Considering the results of the STEM-EDS (Spec.C4) and the X-ray diffraction pattern (Fig. 5.27a), this phase was identified to be hexagonal NbB_2 with the space group P6/mmm. An indexed electron diffraction pattern for NbB_2 is presented in Fig. 5.29a. A cubic crystal structure was identified for the intermediate section (Diffraction II). STEM-EDS analysis confirmed the presence of metallic Nb and C (Spec.C5). Considering the reflections for NbC in the X-ray diffraction pattern of Nb coated ZrB_2 (VA) (Fig. 5.27a), the phase was assigned to be cubic NbC with the space group Fm-3m.

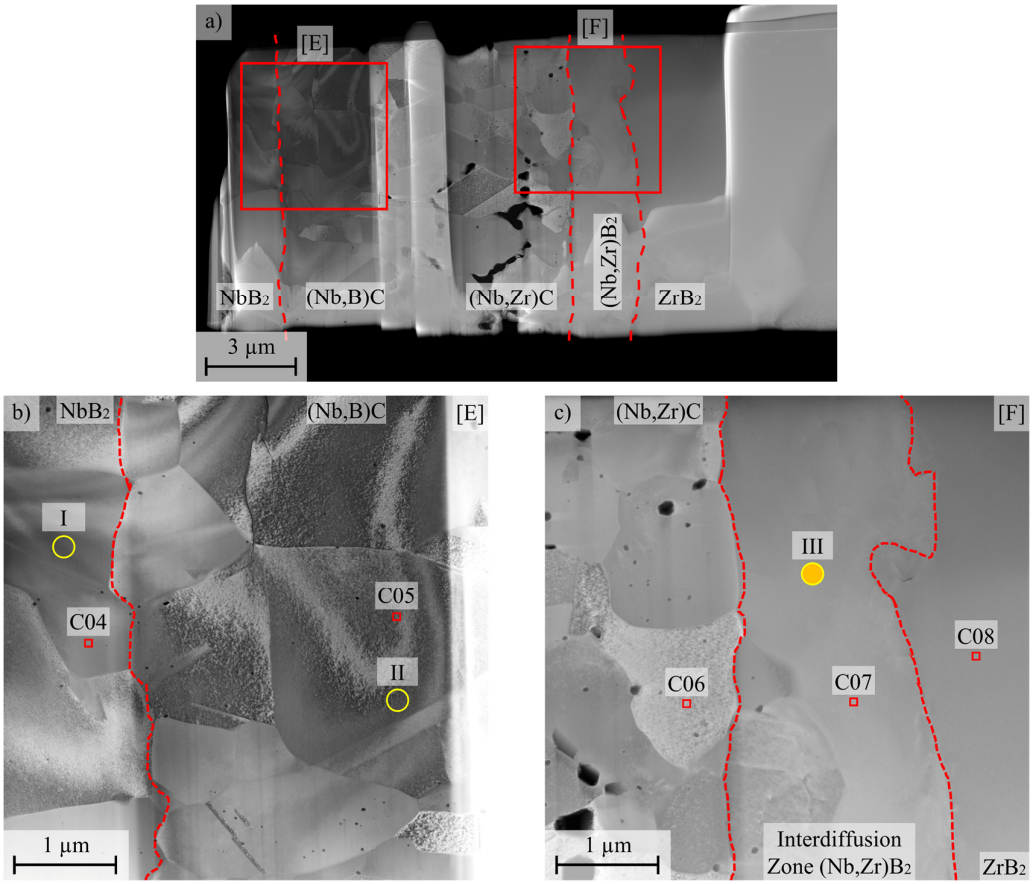

Fig. 5.28: *HAADF micrographs of Nb coated ZrB_2 (VA): a) Overview of TEM lamella; b) Uppermost section of the coating (area [E]); c) Interface of the coating/substrate (area[F]).*

An indexed electron diffraction pattern for NbC is presented in Fig. 5.29b. The interdiffusion zone (IDZ) was observed at the coating/substrate interface and was found to be ~2 µm thick (Fig. 5.28c). The chemical composition in the IDZ revealed a mixture of Nb and ZrB_2 (Spec.C7). No carbon was identified in the IDZ. The electron diffraction pattern (Diffraction III) of the IDZ was taken and a hexagonal crystal structure was identified. The assignment to a discrete phase via D-spacing analysis was not possible. However, a boron-based transition metal mixture $(Nb,Zr)B_2$ is assumed.

Table 5.14: *STEM-EDS analysis of Nb coating on ZrB_2 (VA) (compare Fig. 5.28)*

Condition	Spec.	B (at.%)	O (at.%)	C (at.%)	Ti (at.%)	Zr (at.%)	Nb (at.%)	Zr/Hf	Phase (Estimated)
VA	C04	71.0	-	0.5	4.6	0.2	23.7	0.8	NbB_2
	C05	53.1	-	10.0	0.2	0.3	36.3	0.8	NbC
	C06	52.2	-	4.3	0.2	2.0	41.2	4.6	NbC
	C07	68.6	-	0	0.1	15.9	15.4	50.8	$(Nb,Zr)B_2$
	C08	64.8	-	0	0.2	34.9	0.2	99.4	ZrB_2

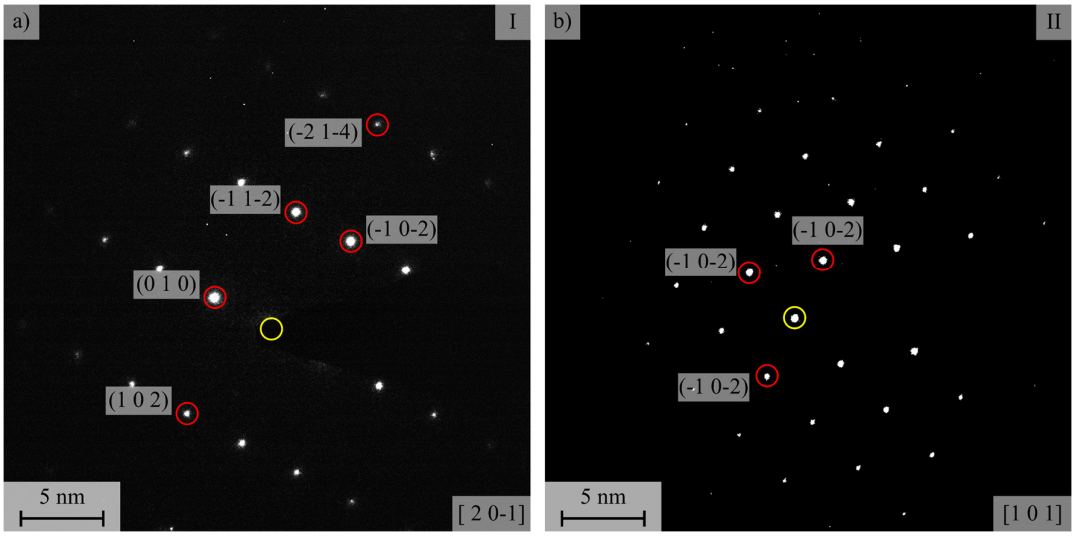

Fig. 5.29: Electron diffraction pattern of Nb coated ZrB_2 (VA) (compare Fig. 5.28): a) Uppermost section of NbB_2 (Diffraction I, NbB_2); b) Intermediate section of NbC (Diffraction II, NbC)

5.3.2 Ramped Oxidation Experiments of Nb Coated ZrB_2

Specimens of Nb coated ZrB_2 (AC and VA) were oxidized in a tube furnace at 1500°C for 60 min using ramped oxidation (R/C) (Fig. 4.10). The appearance of Nb coated ZrB_2 (AC) after oxidation can be seen in Fig. 5.30a. The oxidized surface revealed a silver/brownish coloration with an increased roughness [139].

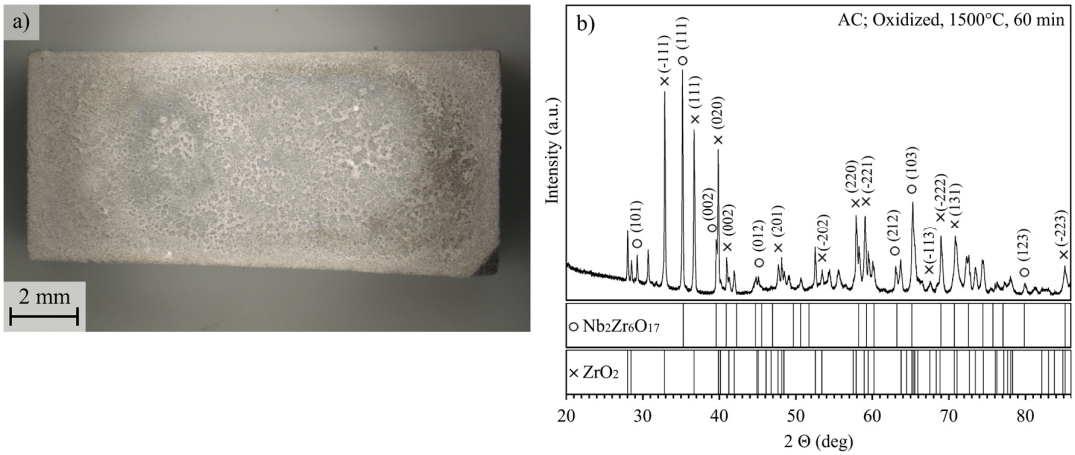

Fig. 5.30: Nb coated ZrB_2 (AC) after ramped oxidation (R/C) for 60 min at 1500°C: a) Top-view photograph; b) X-ray diffraction pattern

The X-ray diffraction pattern in Fig. 5.30b was assigned for m-ZrO_2 (PDF00-037-1484) and the orthorhombic mixed oxide phase $Nb_2Zr_6O_{17}$ (PDF00-009-0251). Associated Miller indices of the crystal lattice planes are marked in the diffraction pattern [139].

Top-view BSE micrographs of the tested specimen are presented in Fig. 5.31. Detailed results for the EDS analysis of the specimen are provided in Table 5.15.

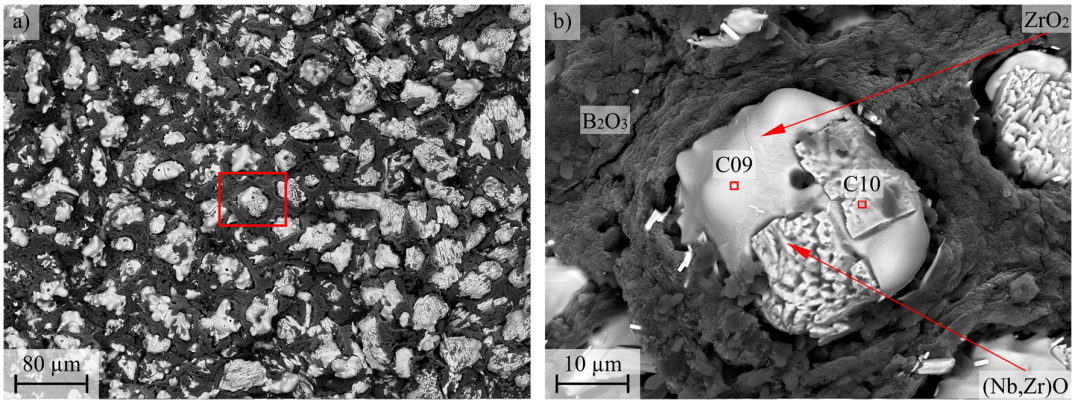

Fig. 5.31: BSE top-view micrographs in the center of Nb coated ZrB_2 (VA) after rapid oxidation (R/C) for 60 min at 1500°: a) Overview at lower magnification; b) High magnification of a partially reacted ZrO_2 grain at the surface beside a thin and comprehensive B_2O_3 layer [139]

The surface of the oxidized specimen was covered by a dark phase (BSE contrast). EDS analysis revealed a chemical composition of ~96 at.% O and traces for C, Zr, and Nb for the darkish phase. Considering results in several publications, the dark phase was assigned to be B_2O_3 glass [39, 66]. Arbitrary-shaped grains with an average size of ~28 µm were found inside the B_2O_3 glass. According to the EDS spot analysis, the grains consist of ~32 at.% Zr, and ~68 at.% O (Spec.C9). Engraved areas of the grains exhibited a chemical composition of ~6 at.% Nb, ~28 at.% Zr, and ~66 at.% O (Spec.C10) [139].

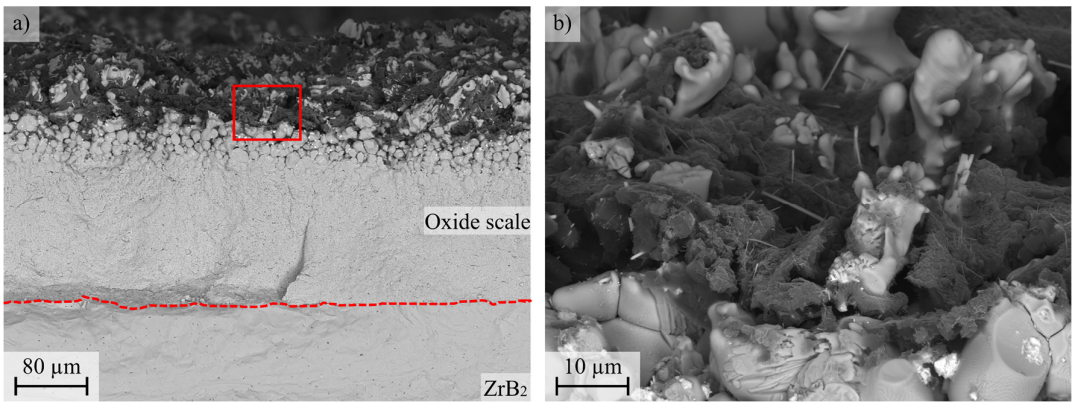

Fig. 5.32: BSE micrographs of fractured cross-section of Nb coated ZrB_2 (VA) after ramped oxidation (R/C) for 60 min at 1500°C: a) Overview at lower magnification; b) High magnification micrograph of B_2O_3 layer at the surface [139]

BSE cross-sectional micrographs of the fractured surface are presented in Fig. 5.32, revealing a ~10 µm thick B_2O_3 layer at the uppermost section of the formed oxide scale. A porous ZrO_2 scale (PS) was found beneath the glass layer. Polished cross-sections of the specimen are presented in Fig. 5.33, which exhibits a two-layered structure. The reaction scale (RS) contained globular grains of ZrO_2 (Spec.C13) with an average size of ~6 µm. Another phase was observed between the single globular grains of the uppermost section with the chemical composition of ~33 at.% Nb, ~4 at.% Zr, and ~63 at.% O (Spec.C12). The RS has formed on top of a porous ZrO_2 scale (PS) (Spec.C11). The total oxide scale was measured as ~186 µm [139].

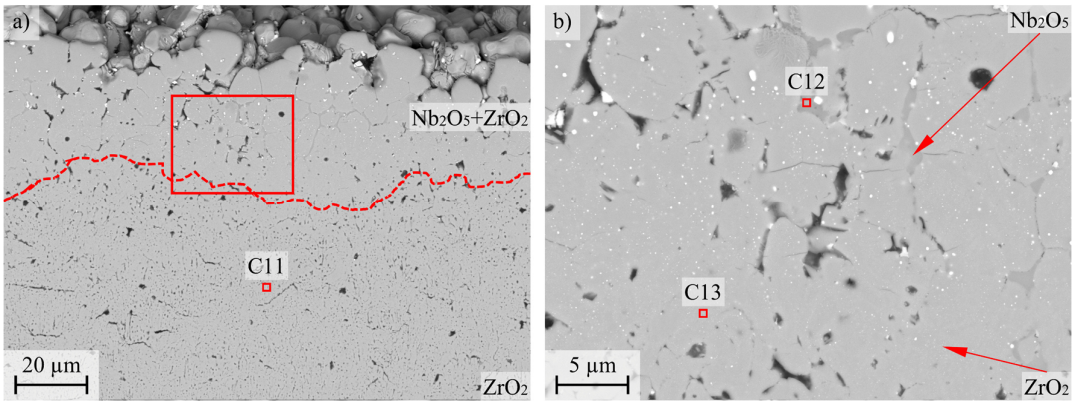

Fig. 5.33: BSE cross-sectional micrographs of Nb coated ZrB_2 (AC) after ramped oxidation (R/C) for 60 min at 1500°C

Table 5.15: EDS analysis of Nb coated on ZrB_2 (AC) after ramped oxidation (R/C) for 60 min at 1500°C (compare Fig. 5.31 and Fig. 5.33)

Condition	Spec.	O (at.%)	C (at.%)	Hf (at.%)	Ti (at.%)	Zr (at.%)	Nb (at.%)	Zr/Hf	Phase (Estimated)
1500°C, 60 min,	C09	67.0	0	0.2	0.1	32.3	0.3	99.1	ZrO_2
	C10	65.9	0	0.3	0.1	27.4	6.2	81.5	$Nb_2Zr_6O_{17}$
	C11	64.1	0.3	0	0.1	34.9	0.6	98.3	ZrO_2
	C12	62.5	0	0.1	0.2	4.2	32.9	11.3	Nb_2O_5
	C13	65.7	0.3	0	0.1	33.1	0.8	97.6	ZrO_2

Vacuum-annealed ZrB_2 substrate with Nb coating (VA) revealed contrary results. A top-view photograph and the X-ray diffraction pattern of the specimen is presented in Fig. 5.34. Detailed EDS results for this specimen are provided in Table 5.17. The oxidized specimen revealed a darkish coloration with a shiny glassy appearance. The X-ray diffractogram of the tested specimen was assigned for m-ZrO_2 (PDF000-037-1484) and $Nb_2Zr_6O_{17}$ (PDF000-009-025 1). Miller indices of the single crystal lattice planes are marked in the pattern (Fig. 5.34b) [139].

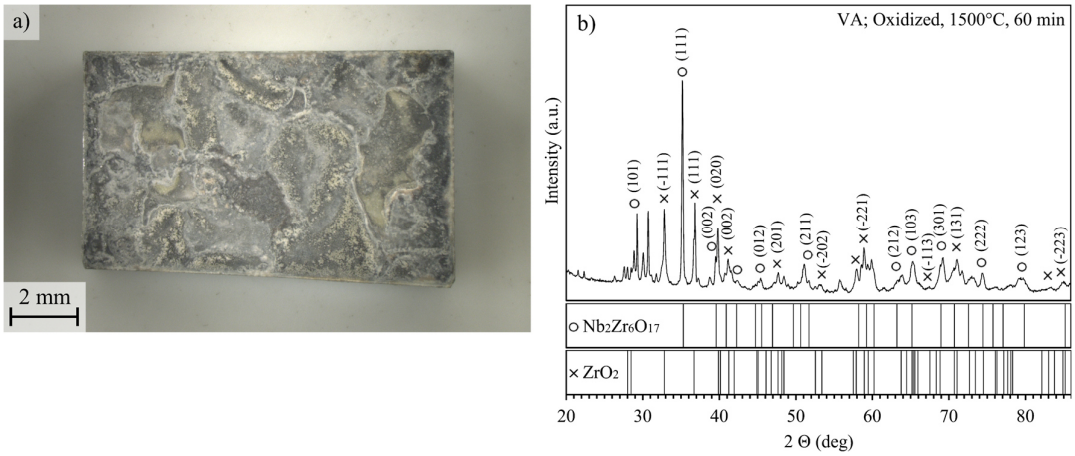

Fig. 5.34: Nb coated ZrB_2 (VA) after ramped oxidation (R/C) for 60 min at 1500°C: a) Top-view photograph; b) X-ray diffraction pattern

BSE top-view micrographs are presented in Fig. 5.35a-b. The surface was completely covered with B_2O_3 glass [39]. Sparsely distributed globular grains were found inside the B_2O_3 glass. The single grains were ~5 µm in diameter, exhibiting a smooth surface with a chemical content of ~1 at.% Nb (Spec.C14). Further, holes with a diameter of ~7 µm were present inside the glassy layer [139].

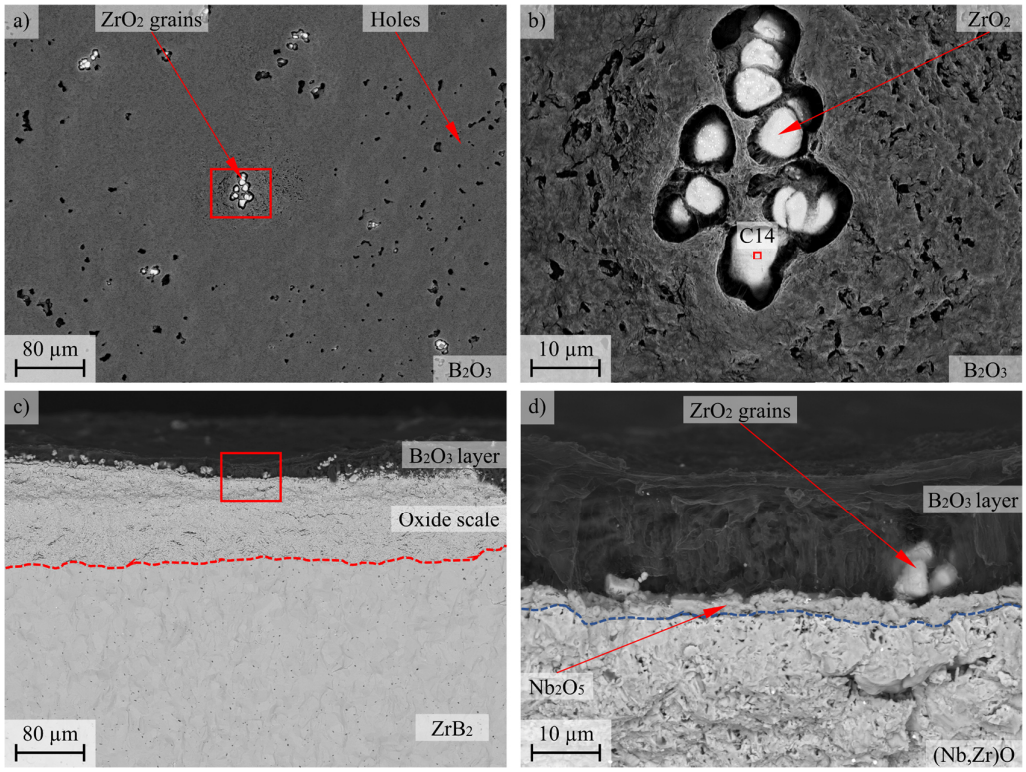

Fig. 5.35: BSE micrographs of Nb coated ZrB_2 (VA) after ramped oxidation (R/C) for 60 min at 1500°C: a) Top-view micrograph in low magnification; b) Top-view micrograph in high magnification; c) Overview of fractured cross-section; d) High magnification of the fractured cross-section [139]

The fractured cross-section in Fig. 5.35c-d proved the presence of a ~18 µm thick and continuous B_2O_3 layer. ZrO_2 grains with a diameter of ~8 µm were present inside the glassy layer. The formed oxide layer revealed a dual layer, subdivided into a reaction scale (RS, containing a layer of Nb_2O_5 and (Nb,Zr)O) on top of a porous ZrO_2 scale (PS) [139].

Table 5.16 provides the average scale thicknesses of the reaction scale (RS) and porous oxide scale (PS) for Nb coated ZrB_2 (AC, VA) after ramped oxidation at 1500°C for 60 min.

Table 5.16: Oxide scale thickness of Nb coated ZrB_2 (AC, VA) after ramped oxidation (R/C) at 1500°C for 60 min (compare Fig. 5.32 and Fig. 5.35)

Condition	Temperature	Time (min)	RS (µm)	PS (µm)	TS (µm)	PS/TS (%)	$\ln(K_{P(PS)})$
Nb coated (AC), R/C	1500°C	60	20	166	186	89.2	10.2
Nb coated (VA), R/C	1500°C	60	48	45	93	48.4	7.6

The polished cross-section of the most protective area of the oxide scale with the lowest porous ZrO_2 formation is presented in Fig. 5.36. The BSE micrographs show an intact Nb_2O_5 layer with the chemical composition of ~27 at.% Nb, ~5 at.% Zr, ~1 at.% Ti, and ~67 at.% O (Spec.C15). A porous ZrO_2 scale (Spec.C17) formed underneath the Nb_2O_5 layer. Both layers were separated by a thin white layer with the composition of ~69 at.% Nb, ~8 at.% Zr, and ~23 at.% O (Spec.C16). Several globular grains with a diameter of ~3 µm were found to be embedded in the uppermost section of the Nb_2O_5 layer (Fig. 5.36b) [139].

Micrographs with 30 kV acceleration voltage in Fig. 5.36c revealed precise contrast variance for two niobia phases at the uppermost section of the oxide scale and a core-shell structure for the grains inside the niobia. A colored schematic is added to the picture to clarify the BSE contrast information for the observed phases. Whereas the darker Nb_2O_5 contained ~3 at.% Zr (Spec.C19), the brighter phase contained ~5 at.% Zr (Spec.C15, Spec.C20). The observed grains inside the Nb_2O_5 revealed a darker core and a bright shell structure as a enclosing layer. The dark core revealed ~4 at.% Nb (Spec.C21), and the bight shell ~8 at.% Nb (Spec.C22). For a detailed analysis of the observed core-shell structure and the Nb_2O_5 phases, a TEM lamella of the grain was cut [139].

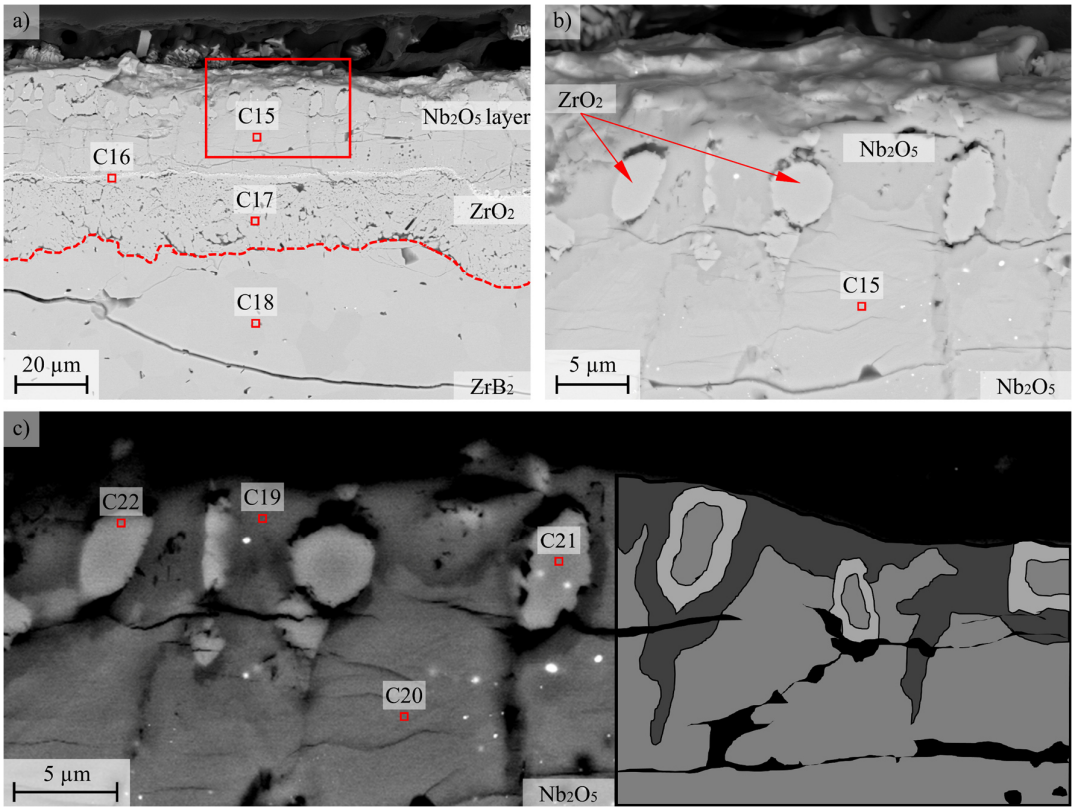

Fig. 5.36: *BSE micrographs of Nb coated ZrB_2 (VA) after ramped oxidation (R/C) for 60 min at 1500°C: a-b) polished cross-section with 15 kV acceleration voltage at the most protective area of the tested specimen; c) polished cross-section with 30 kV acceleration voltage [139]*

Table 5.17: *EDS analysis of Nb coated on ZrB_2 (VA) after ramped oxidation (R/C) for 60 min at 1500°C (compare Fig. 5.35 and Fig. 5.36)*

Condition	Spec.	O (at.%)	C (at.%)	Hf (at.%)	Ti (at.%)	Zr (at.%)	Nb (at.%)	Zr/Hf	Phase (Estimated)
1500°C, 60 min	C14	67.2	-	0.2	0.1	32.0	0.5	98.5	ZrO_2
	C15	67.4	-	0.1	0.9	4.9	26.7	15.3	Nb_2O_5
	C16	22.2	-	0.2	0.5	7.9	69.1	10.3	Nb_2O_5
	C17	63.3	-	0.4	0.1	35.7	0.5	98.6	ZrO_2
	C18	83.9	-	0.1	0	15.3	0.7	95.6	ZrB_2
	C19	68.3	-	0.1	1.3	2.8	27.5	7.9	Nb_2O_5
	C20	67.9	-	0.1	0.8	4.7	26.5	15.3	Nb_2O_5
	C21	63.6	-	0.1	0.2	32.0	4.1	88.6	ZrO_2
	C22	68.1	-	0.2	0.1	24.1	7.6	76.0	$Nb_2Zr_6O_{17}$

A HAADF micrograph of the prepared lamella and a high-magnification image of the analyzed grain with the core-shell structure are presented in Fig. 5.37. The grain core was analyzed in the

area [G] and the shell structure in the area [H]. Detailed results about the chemical compositions, measured in the analyzed areas via STEM-EDS, are listed in Table 5.18 [139].

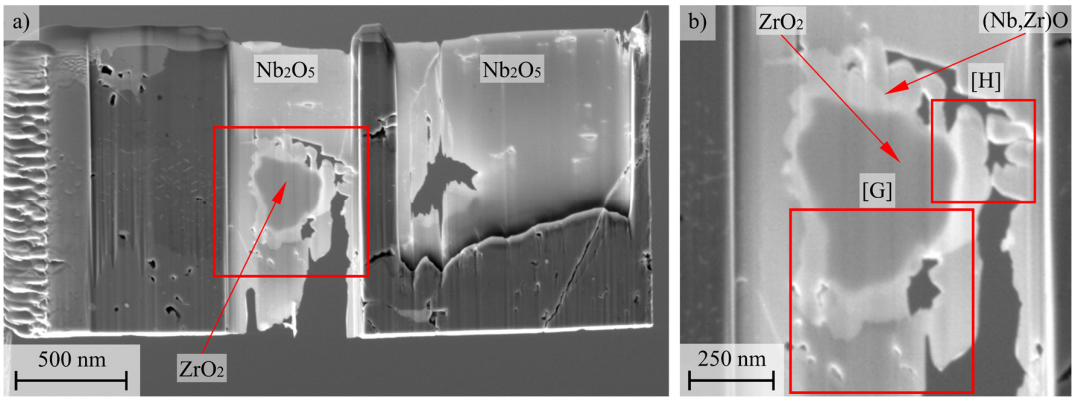

Fig. 5.37: a) Overview of TEM lamella of Nb coated ZrB_2 (VA) after ramped oxidation (R/C) for 60 min at 1500°C; b) High magnification micrograph of the core-shell structured grains inside the Nb_2O_5

A HAADF micrograph of the area [G] and the corresponding electron diffraction pattern for the grain core (Diffraction IV) are presented in Fig. 5.38a. The chemical composition was measured as ~33 at.% Zr and ~67 at.% O (Spec.C23). A monoclinic crystal structure was identified via electron diffraction. The data enables the assignment as m-ZrO_2 for the grain core with the space group P21/c. The indexed electron diffraction pattern for m-ZrO_2 is presented in Fig. 5.38b. A HAADF micrograph of the area [H] and the corresponding electron diffraction pattern of the shell structure is presented in Fig. 5.39. The electron diffraction revealed an orthorhombic crystal for the shell structure around the m-ZrO_2 grains (Diffraction V) [139].

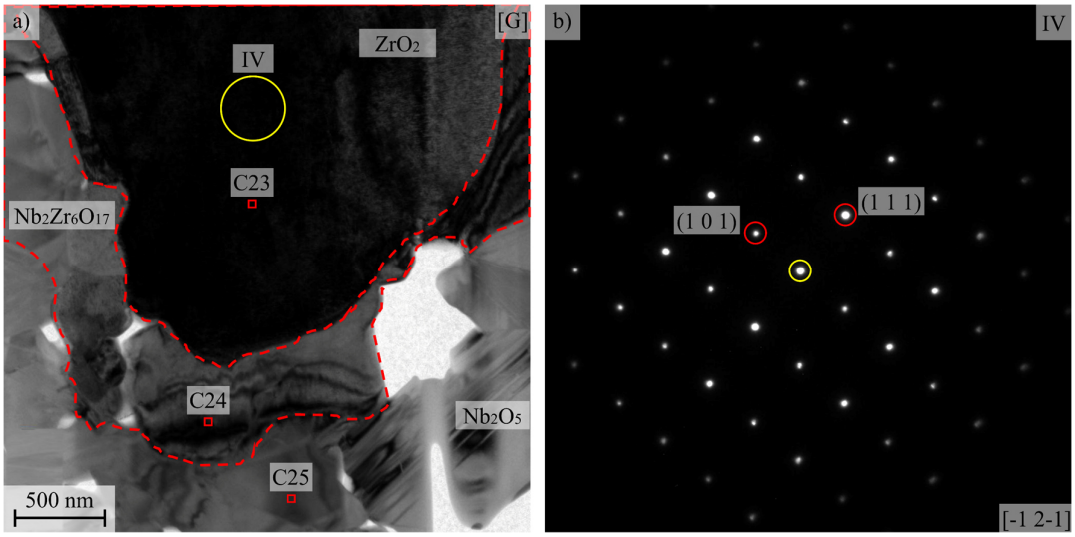

Fig. 5.38: Nb coated ZrB_2 (VA) after ramped oxidation at 1500°C for 60 min: a) High magnification micrograph of the core-shell structure of ZrO_2 grains in Nb_2O_5 matrix (area [G]); b) Electron diffraction pattern of the ZrO_2 core with assigned crystal lattice plane (Diffraction IV, m-ZrO_2) [139]

Secondary reflections appeared between the main reflections in the diffraction pattern (Fig. 5.39b, blue circled). These secondary reflections indicate a modulated crystal structure with a commensurably complex lattice. According to the literature, the secondary reflections are characteristic of the solid solution $Nb_2Zr_6O_{17}$[81, 119, 123]. Considering the chemical composition of ~8 at% Nb, ~23 at% Zr, and ~69 at.% O (Spec.C24), the shell around the m-ZrO_2 core was assigned to be $Nb_2Zr_6O_{17}$ with the space group Ima2 [139].

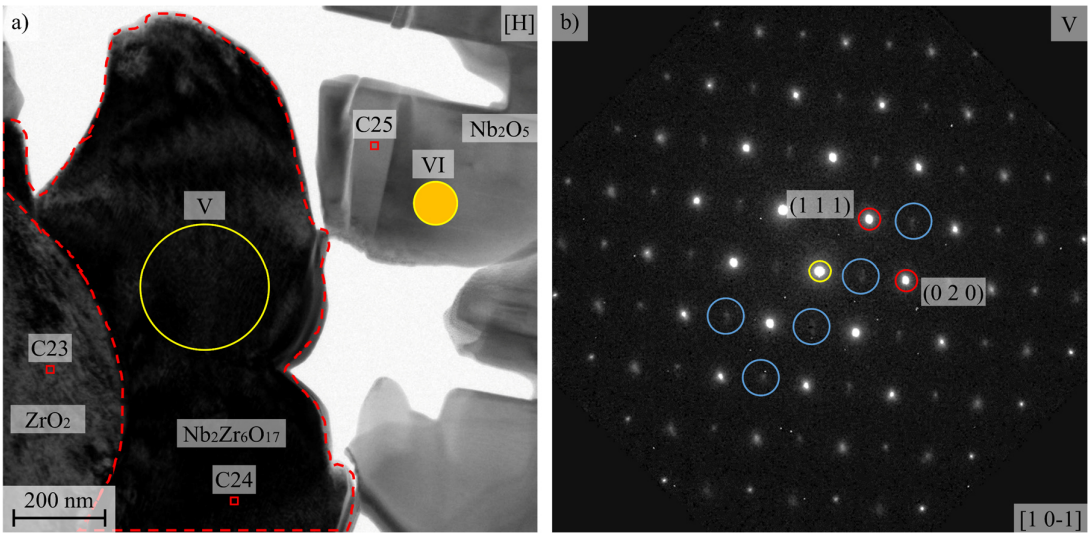

Fig. 5.39: Nb coated ZrB_2 (VA) after ramped oxidation at 1500°C for 60 min: a) High magnification micrograph of the core-shell structure of ZrO_2 grains in Nb_2O_5 matrix (area [H]); b) Electron diffraction pattern of the mixed oxide shell with assigned crystal lattice (Diffraction V, $Nb_2Zr_6O_{17}$) [139]

An electron diffraction pattern of the Nb_2O_5 was taken (Fig. 5.39, Diffraction pattern VI). The diffraction pattern was not assigned to a specific phase of Nb_2O_5 since the Ti-contamination (~1 at.% Ti) induced the formation of various complex polymorphs with various crystal structures (Spec.C25) [113, 114, 139]

Table 5.18: STEM-EDS analysis of Nb coated ZrB_2 (VA) after ramped oxidation (R/C) for 60 min at 1500°C (compare Fig. 5.38 and Fig. 5.39)

Condition	Spec.	O (at.%)	C (at.%)	Hf (at.%)	Ti (at.%)	Zr (at.%)	Nb (at.%)	Zr/Hf	Phase (Estimated)
1500°C, 60 min,	C23	67.3	-	0.3	0.3	28.5	3.6	88.8	ZrO_2
	C24	68.1	-	0.3	0.1	23.0	8.6	72.8	$Nb_2Zr_6O_{17}$
	C25	71.1	-	0.1	0.8	1.3	26.7	4.6	Nb_2O_5

5.3.3 Rapid Oxidation Experiments of Nb Coated ZrB_2

Top-view photographs of Nb coated ZrB_2 (VA) after rapid oxidation (P/Q) for 15 min, 30 min, and 60 min at 1500°C, 1600°C, and 1700°C are presented in Fig. 5.40.

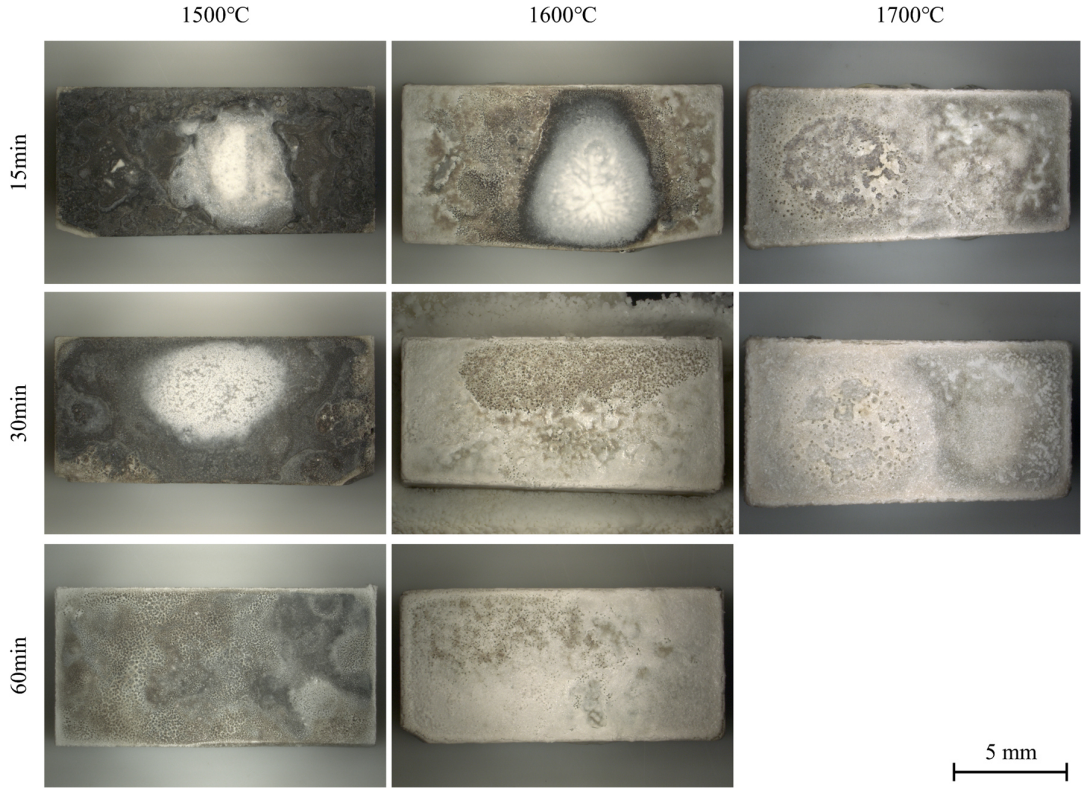

Fig. 5.40: Top-view photographs of Nb coated ZrB_2 (VA) after rapid oxidation (P/Q) at 1500°C, 1600°C, and 1700°C for an exposure of 15 min, 30 min, and 60 min

As visible in the photographs, the temperature and the exposure time had a dramatic effect on the appearance of the specimens and the phases at the oxidized surface, i.e. more dark surface appearance at lower temperatures and more white-brownish coloration with several pores and increased roughness at higher temperatures and longer times. Partial spallation of the uppermost oxide scale at a few places was observed for the exposure at 1600°C for 30 in and 60 min as well as for the exposure at 1700°C for 15 min and 30 min.

X-ray diffraction patterns were taken for each specimen after rapid oxidation (P/Q). The diffraction patterns after an exposure of 15 min, 30 min, and 60 min are presented in Fig. 5.41. Reflections for m-ZrO_2 (PDF00-037-1484), the mixed oxide phase $Nb_2Zr_6O_{17}$ (PDF00-009-0251), Nb_2O_5 (PDF00-028-0317) and NbO_2 (PDF00-068-0147) were assigned to the pattern. The Miller indices of the single lattice planes of the crystals are added to the pattern.

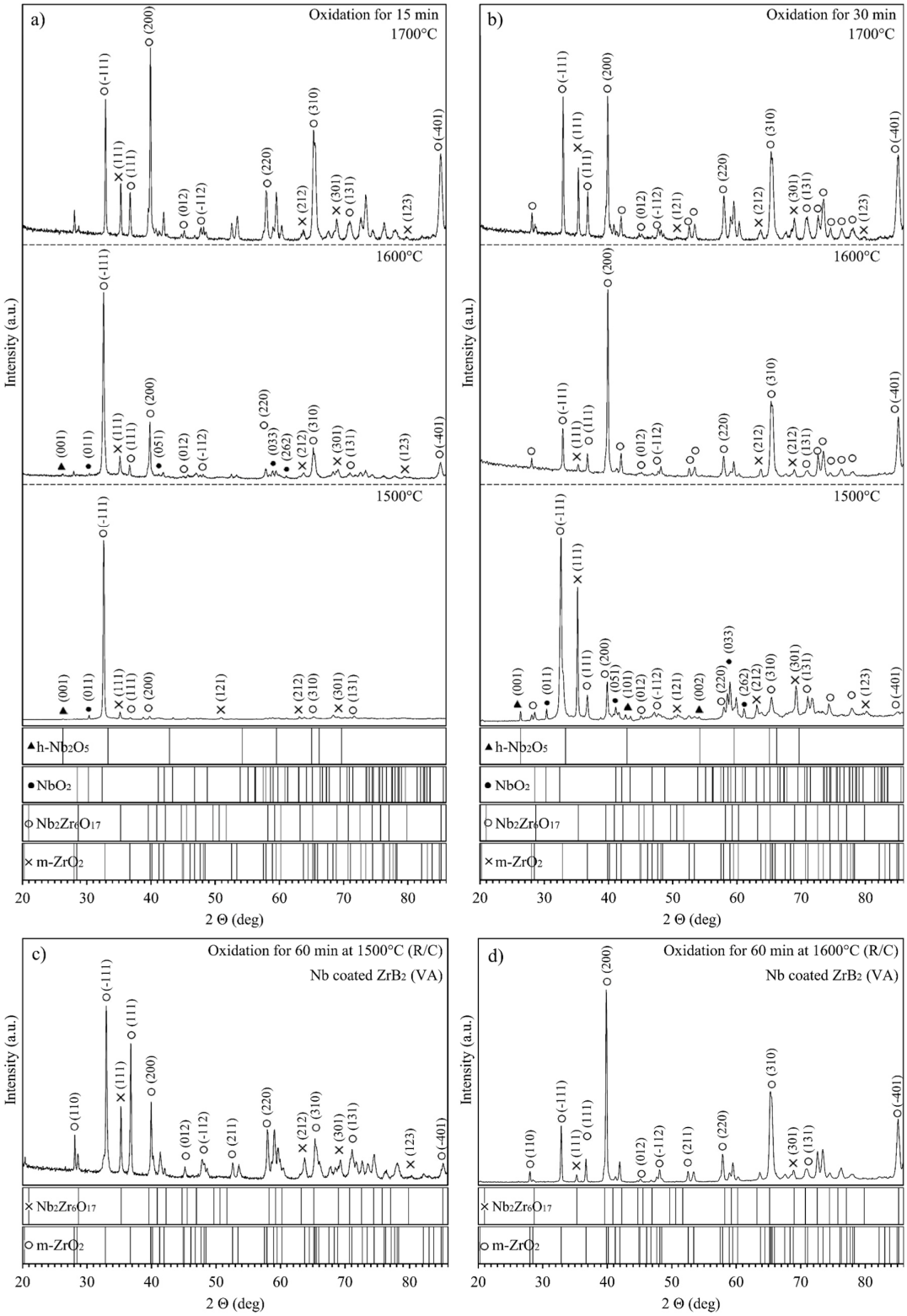

Fig. 5.41: X-ray diffraction pattern of Nb coated ZrB_2 (VA) after rapid oxidation (P/Q) at 1500°C, 1600°C, and 1700°C: a) for 15 min; b) for 30 min, c) for 60 min at 1500°C, d) for 60 min at 1600°C

SEM top-view analysis of the surfaces was performed. EDS data for the analyzed surfaces are provided in Table 5.19 with marked oxidation parameters and estimated phases. BSE top-view micrographs in Fig. 5.42 show the surface after 15 min at 1500°C. Globular grains with an average grain size of ~1 µm were found in the area [J], directly in the center of the specimen. The chemical composition of the globular oxide grains was found to be ~8 at.% Nb, ~7 at.% Zr, and ~85 at.% O (Spec.C26). Dendrite formed in the glass in area [K]. The chemical analysis was not precise and revealed ~96 at.% O and traces of Zr (Spec.C27).

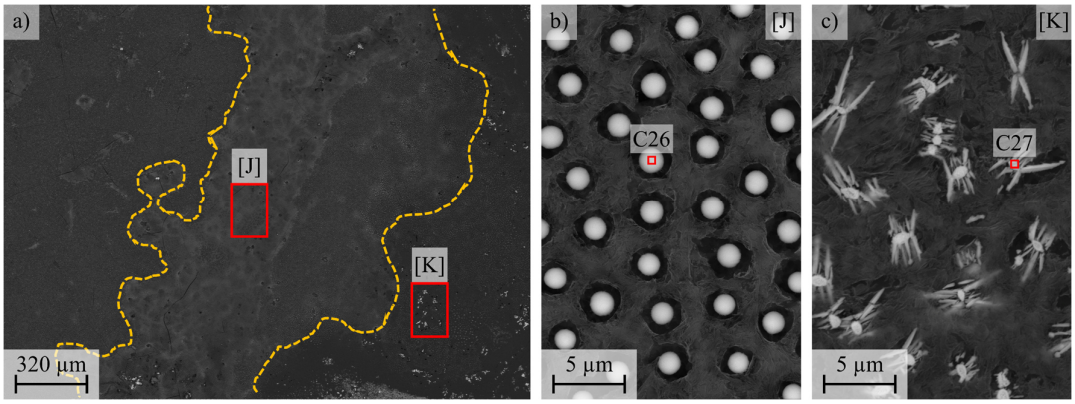

Fig. 5.42: BSE top-view micrograph in the center of Nb coated ZrB_2 (VA) after rapid oxidation (P/Q) for 15 min at 1500°C: a) Overview at lower magnification of B_2O_3 covered surface with marked areas ([J] and [K]) and distinct features; b) High magnification micrograph with globular precipitates (area [J]); c) High magnification micrograph with dendrite precipitates (area [K])

The glassy B_2O_3 layer remained at the surface after 30 min at 1500°C. However, the recession of the B_2O_3 liquid can be observed at the sharp edges of the specimens (compare Fig. 5.40). A BSE surface micrograph near the sharp edges is presented in Fig. 5.43. A higher magnification reveals the formation of engraved grains with an average size of ~6 µm, containing ~7 at.% Nb, ~27 at.% Zr, and ~66 at.% O (Spec.C28). An Nb-rich layer with a needle-like microstructure was found beneath the engraved grains. The chemical composition for the Nb-rich layer was measured as ~27 at.% Nb, ~6 at.% Zr, and ~67 at.% O (Spec.C29).

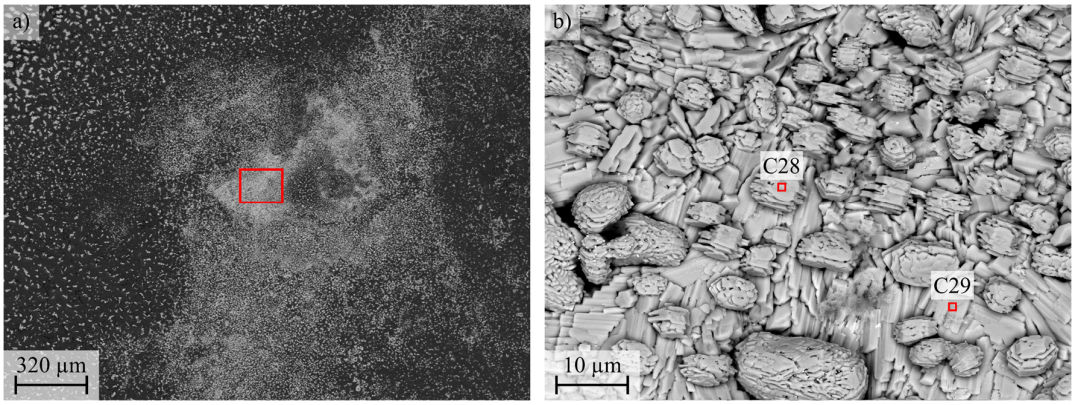

Fig. 5.43: BSE top-view micrograph near the sharp edges of Nb coated ZrB_2 (VA) after rapid oxidation (P/Q) for 30 min at 1500°C: a) Overview B_2O_3 covered surface at lower magnification; b) High magnification with exposed Nb_2O_5 layer and engraved grains of mixed oxide grains

Glass was still present after 15 min of oxidation at 1600°C in the center of the specimen (compare Fig. 5.40). A BSE top-view micrograph of the center of the tested specimen is presented in Fig. 5.44. Several globular particles with an average diameter of ~1 µm were found on the surface and exhibited a chemical composition of ~8 at.% Nb, ~7 at.% Zr, and ~85 at.% O (Spec.C30).

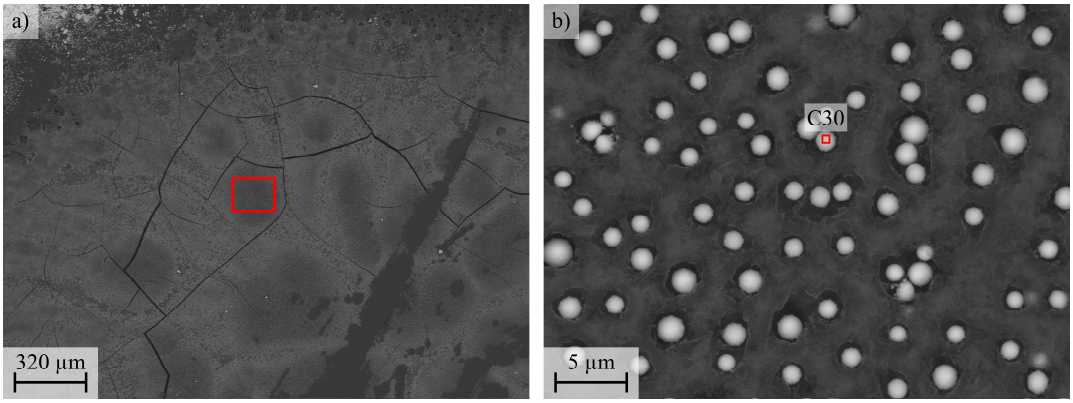

Fig. 5.44: BSE top-view micrograph in the center of Nb coated ZrB_2 (VA) after rapid oxidation (P/Q) for 15 min at 1600°C: a) Overview at lower magnification; b) High magnification micrograph with globular mixed oxide grains

Enhanced exposure of 30 min at 1600°C led to the evaporation of the B_2O_3 liquid and the formation of a dry surface as presented in Fig. 5.45. The area [L] revealed a coverage by ZrO_2 with ~1 at.% Nb as well as traces of Hf, W, and Ti (Spec.C31). Residual needle-like structures with ~7 at.% Nb (Spec.C32) were found at the surface. Area [M] represents a spalled section of the uppermost oxide scale, which exposed the B_2O_3 glass, filling defects in the underlying oxide scale.

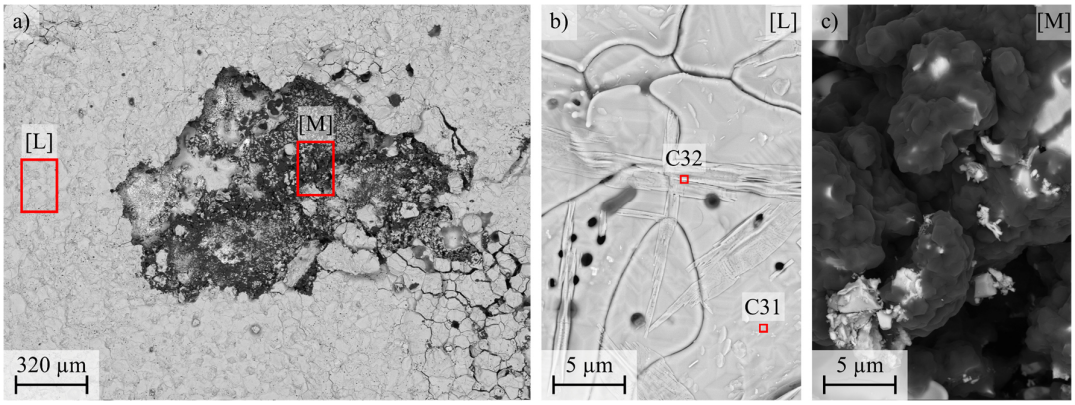

Fig. 5.45: BSE top-view micrograph in the center of Nb coated ZrB_2 (VA) after rapid oxidation (P/Q) for 30 min at 1600°C: a) Overview at lower magnification of dry surface with spalled chunk, exposing residual B_2O_3 liquid; b) High magnification micrograph of dry ZrO_2 (area [L]); c) High magnification of exposed B_2O_3 (area [M])

The surface condition after the oxidation at 1700°C for 15 min are presented in Fig. 5.46. The exposure led to the rapid evaporation of the glassy B_2O_3 at the surface, leaving dry ZrO_2 (Spec.C33). Traces of a Nb-containing phase with a needle-like structure were found at the surface. The EDS analysis confirmed ~9 at.% Nb and ~23 at.% Zr and ~68 at.% O for the needle-like structures (Spec. C34). The overview revealed an even and comprehensive surface, covered with ZrO_2 and residuals of the mixed oxide phase.

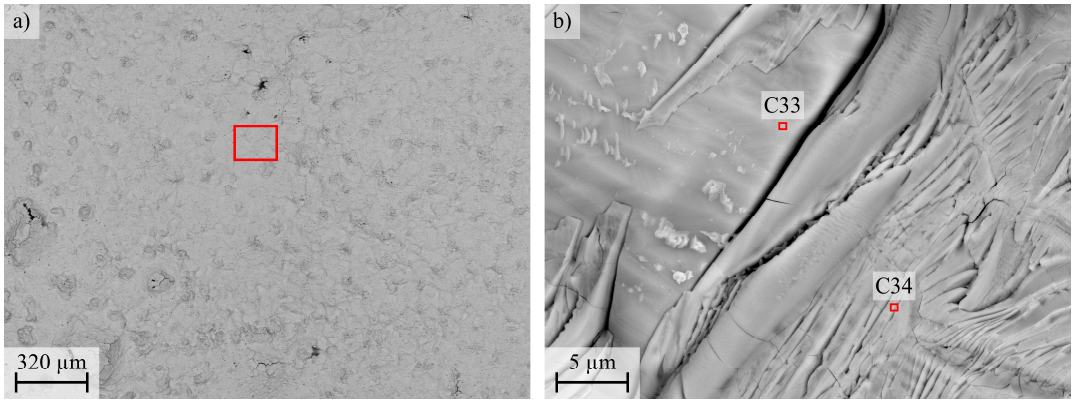

Fig. 5.46: BSE top-view micrograph in the center of Nb coated ZrB_2 (VA) after rapid oxidation (P/Q) for 15 min at 1700°C: a) Overview at lower magnification with a comprehensive oxide layer at the surface; b) High magnification micrograph of ZrO_2 and needle-like structures containing Nb

The exposure for 30 min at 1700°C led to similar conditions at the surface as visible in Fig. 5.47. No B_2O_3 glass was observed at the ZrO_2 surface (Spec.C35). A Nb-containing phase was sparsely distributed at the surface and contained ~3 at.% Nb and ~29 at.% Zr (Spec.C36). The surface revealed an uneven appearance with several holes. The holes at the surface had an average diameter of ~147 µm. Beside the holes, fine open porosity can be observed.

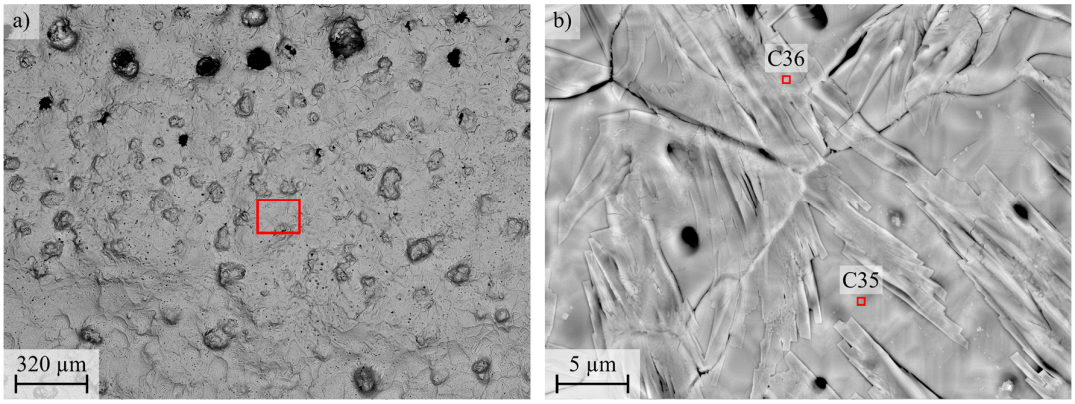

Fig. 5.47: BSE top-view micrograph in the center of Nb coated ZrB_2 (VA) after rapid oxidation (P/Q) for 30 min at 1700°C: a) Overview at lower magnification of an oxide layer with several holes and uneven surface; b) High magnification micrograph of ZrO_2 and needle-like structures containing Nb

Table 5.19: EDS surface analysis of Nb coated ZrB_2 (VA) after rapid oxidation (P/Q) at 1500°C, 1600°C, and 1700°C for 15 min and 30 min of oxidation (compare Fig. 5.42 to Fig. 5.47)

Condition	Spec.	O (at.%)	C (at.%)	Hf (at.%)	Ti (at.%)	Zr (at.%)	Nb (at.%)	Zr/Hf	Phase (Estimated)
1500°C, 15 min	C26	85.5	-	0	0	6.9	7.5	47.9	(Nb,Zr)O
	C27	95.9	-	0	0	3.6	0.4	90	ZrO_2
1500°C, 30 min	C28	66.5	-	0.1	0.2	5.9	26.8	18.0	Nb_2O_5
	C29	65.9	-	0.3	0	26.9	6.8	79.8	$Nb_2Zr_6O_{17}$
1600°C, 15 min	C30	85.0	-	0	0	7.2	7.7	48.3	(Nb,Zr)O
1600°C, 30 min	C31	65.2	-	0.5	0.2	33.2	0.9	97.4	ZrO_2
	C32	65.1	-	0.4	0.9	28.4	5.1	84.8	$Nb_2Zr_6O_{17}$
1700°C, 15 min	C33	63.9	-	0.5	0.1	33.9	1.6	95.5	ZrO_2
	C34	68.1	-	0.3	0.9	21.9	8.8	71.3	$Nb_2Zr_6O_{17}$
1700°C, 30 min	C35	66.5	-	0.5	0.1	31.7	1.1	96.6	ZrO_2
	C36	67.1	-	0.2	0.4	29.0	3.2	90.1	ZrO_2

Polished cross-sections were analyzed and oxide scale thicknesses were measured. BSE micrographs of the holistic oxide scales of Nb coated ZrB_2 (VA) after rapid oxidation (P/Q) at 1500°C, 1600°C, and 1700°C for 15 min, 30 min, and 60 min are presented in Fig. 5.48 to Fig. 5.51. Corresponding micrographs in high magnification show the former interface zone of the coating/substrate. The blue-dashed lines mark the transition between the reaction scale (RS) and the porous ZrO_2 scale (PS). The oxidation front of ZrB_2 is marked with a red dashed line. The scale thicknesses for the RS, the PS, and the total oxide scale TS are provided in Table 5.23.

The formed oxide scale after 15 min at 1500°C is presented in Fig. 5.48a-b. The uppermost section of the formed RS consisted of Nb_2O_5 (~51 µm thick) with a chemical composition of ~30 at.% Nb, ~4 at.% Zr, and ~66 at.% O (Spec.C37). Further, a ~4 µm thick and dense intermediate layer of NbO with a chemical composition of ~61 at.% Nb, ~5 at.% Zr, and ~34 at.% O formed underneath the Nb_2O_5 (Spec.C38), covering porous ZrO_2 (~31 at.% Zr and ~69 at.% O) (Spec.C39). EDS results are provided in Table 5.20.

A similar oxide scale architecture, containing an RS and an underlying porous ZrO_2 scale with B_2O_3-filled porosities, was found after 30 min at 1500°C (Fig. 5.48c-d). The formed RS can be subdivided into three layers. An outermost Nb_2O_5 layer with a thickness of ~9 µm and a chemical composition of ~34 at.% Nb, ~5 at.% Zr, and ~61 at.% O (Spec.C40) formed at the surface. The scale covered a dense ZrO_2 layer of ~45 µm in thickness with dissolved Nb_2O_5 (Spec.C44). Globular grains with an average diameter of ~6 µm and a core-shell structure (ZrO_2 as a core, $Nb_2Zr_6O_{17}$ as a shell) can be found between the Nb_2O_5 layer and the dense ZrO_2 scale. The grains were enclosed by the former NbO phase, which revealed a chemical composition of ~51 at.% Nb, 14 at.% Zr, and ~35 at.% O (Spec.C41) after 30 min of oxidation. BSE contrast information proved a variation of the Zr content in the NbO phase. Lower sections of the NbO contained ~20 at.% Zr and appeared darker (Spec.C42). The porous ZrO_2 scale, which formed beneath the multilayer reaction scale, increased in size from ~19 µm after 15 min to ~29 µm after 30 min.

Another characteristic of the oxidation after 30 min of oxidation is the formation of horizontal cracks in the porous ZrO_2.

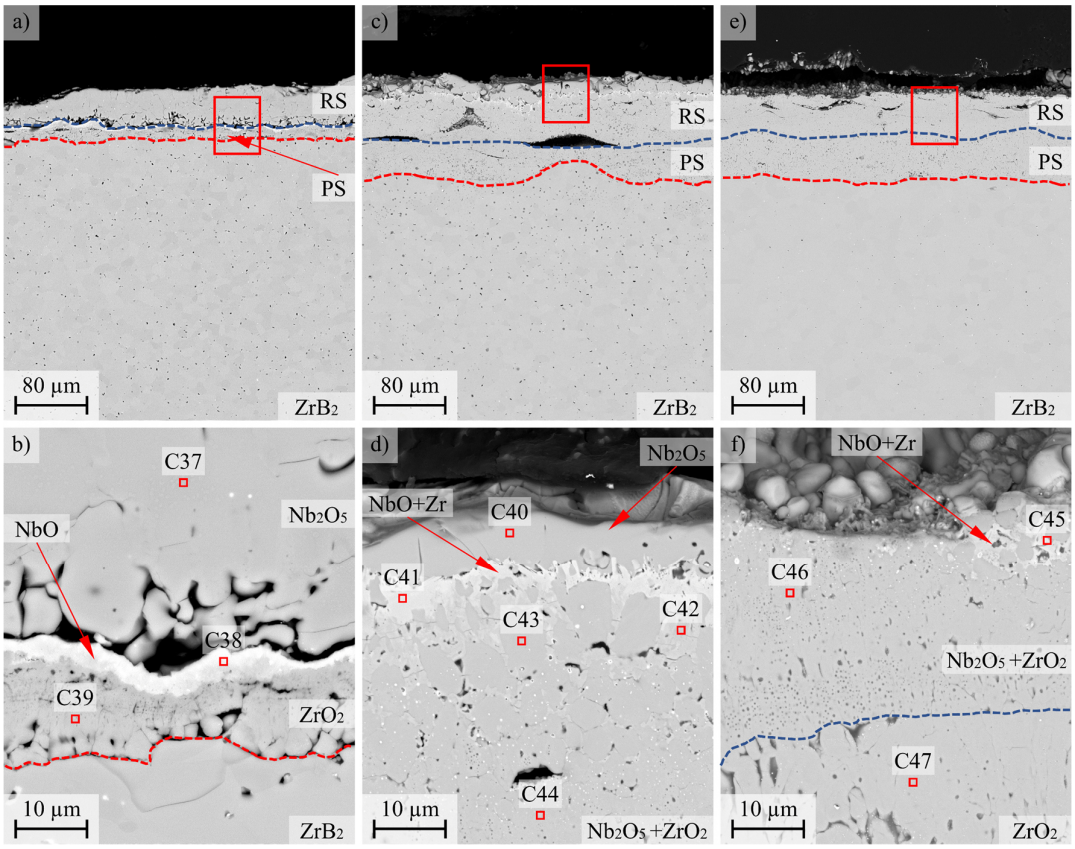

Fig. 5.48: *BSE cross-sectional micrographs of Nb coated ZrB_2 (VA) after rapid oxidation (P/Q) at 1500°C: a) Holistic oxide scale, 15 min; b) Former interface zone, 15 min; c) Holistic oxide scale, 30 min; d) Former interface zone, 30 min; e) Holistic oxide scale, 60 min; f) Former interface zone, 60 min*

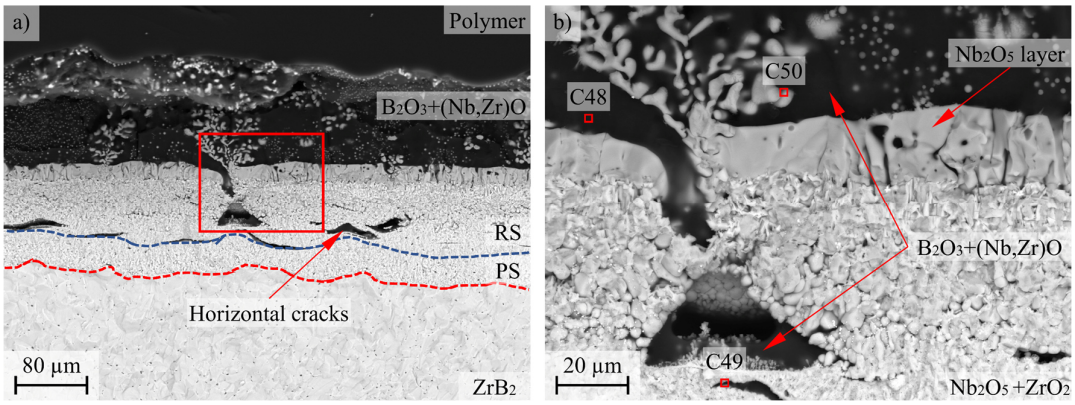

Fig. 5.49: *BSE micrographs of fractured cross-section of Nb coated ZrB_2 (VA) after rapid oxidation (P/Q) for 30 min at 1500°C (compare Fig. 5.49c-d): a) Overview of fractured cross-section with holistic B_2O_3 layer thickness; b) High magnification micrograph of B_2O_3 coverage with convection cell*

The fractured cross-section of the tested specimen for 30 min at 1500°C is presented in Fig. 5.49 and proves the comprehensive coverage of the oxide scale by B_2O_3. Horizontal cracks were filled with B_2O_3 liquid and were found to be reservoirs for B_2O_3 liquid. Further, the picture shows vividly the breakthrough of the B_2O_3 liquid through the porous ZrO_2 and the liquid Nb_2O_5 layer. The "eruption" of the liquid B_2O_3 enables the migration of the glass to the surface (Spec.C48). Several particles were pushed into the uppermost liquid layer due to the flux of B_2O_3 glass to the surface. The particles consisted of ~4 at.% Nb, ~16 at.% Zr, and ~80 at.% O (Spec.C50). Finally, the liquid B_2O_3 layer was measured to be ~98 µm in thickness and covered most of the oxide scale.

The exposure for 60 min at 1500°C led to the complete absence of the continuous uppermost Nb_2O_5 layer as presented in the polished cross-section in Fig. 5.48e-f. Residuals of the NbO-rich phase with a chemical composition of ~42 at.% Nb, ~20 at.% Zr, and ~38 at.% O were observed in the uppermost section of the oxide scale (Spec.C45). Most of the deposited Nb coating left the surface. The residual reaction scale consisted of dense ZrO_2 with ~3 at.% Nb (Spec.C46). The thickness of the reaction scale was found to be ~40 µm in thickness.

Table 5.20: EDS analysis of cross-sections of Nb coated ZrB_2 (VA) after rapid oxidation (P/Q) at 1500°C for 15 min, 30 min, and 60 min (compare Fig. 5.48 and Fig. 5.49)

Condition	Spec.	O (at.%)	C (at.%)	Hf (at.%)	Ti (at.%)	Zr (at.%)	Nb (at.%)	Zr/Hf	Phase (Estimated)
1500°C, 15 min	C37	65.6	-	0.1	0.1	3.9	30.1	11.5	Nb_2O_5
	C38	34.2	-	0	0.1	4.6	60.6	7.1	NbO
	C39	66.7	-	0.4	0.1	30.8	1.6	95.1	ZrO_2
1500°C, 30 min	C40	61.7	-	0.1	0.2	4.5	33.5	11.8	Nb_2O_5
	C41	34.5	-	0.1	0	14.3	50.9	21.9	NbO
	C42	34.8	-	0.2	0	19.9	44.5	30.9	NbO
	C43	61.5	-	0.4	0.1	33.9	3.9	89.7	ZrB_2
	C44	62.3	-	0.4	0	33.9	2.9	92.1	ZrO_2
1500°C, 60 min	C45	38.1	-	0	0.3	20.1	41.5	32.6	(Nb,Zr)O
	C46	59.3	-	0.4	0.1	36.9	2.9	92.7	ZrO_2
	C47	60.6	-	0.4	0.1	38.3	0.2	99.5	ZrO_2
1500°C, 15 min (Fractured)	C48	97.1	-	0	0	2.2	0.7	75.9	B_2O_3
	C49	84.0	-	0	0	7.7	8.2	48.4	$Nb_2Zr_6O_{17}$
	C50	80.3	-	0.2	0	15.9	3.5	82.0	$Nb_2Zr_6O_{17}$

BSE cross-sectional micrographs of the polished oxide scale of Nb coated ZrB_2 (VA) after rapid oxidation at 1600°C for different exposure times are presented in Fig. 5.50. The figure includes high-magnification BSE micrographs of the former interface zone of the coating/substrate. The blue-dashed line marks the transition between the reaction scale and the porous oxide scale, whereas red dashed lines mark the oxidation front of ZrB_2. Table 5.21 provides the EDS results.

The oxide scale after 15 min of oxidation at 1600°C (Fig. 5.50a-b) featured an RS at the uppermost section with a sparsely distributed Nb-rich phase of ~47 at.% Nb, ~14 at.% Zr, and ~41 at.% O (Spec.C52). No pure NbO nor a Nb_2O_5 layer was present after oxidation. Almost all of the deposited Nb coating has been consumed in the reaction scale (~81 µm thick). Globular grains with a core-shell structure of ZrO_2 and $Nb_2Zr_6O_{17}$ revealed an average size of ~9 µm. The chemical composition of the core was found to be ~3 at.% Nb, ~35 at.% Zr, and ~62 at.% O (Spec.C51). A dense ZrO_2 oxide scale with a chemical composition of ~3 at.% Nb, ~46 at.% Zr, and ~51 at.% O (Spec.C53) was found at the transition area of the reaction scale to the underlying porous ZrO_2.

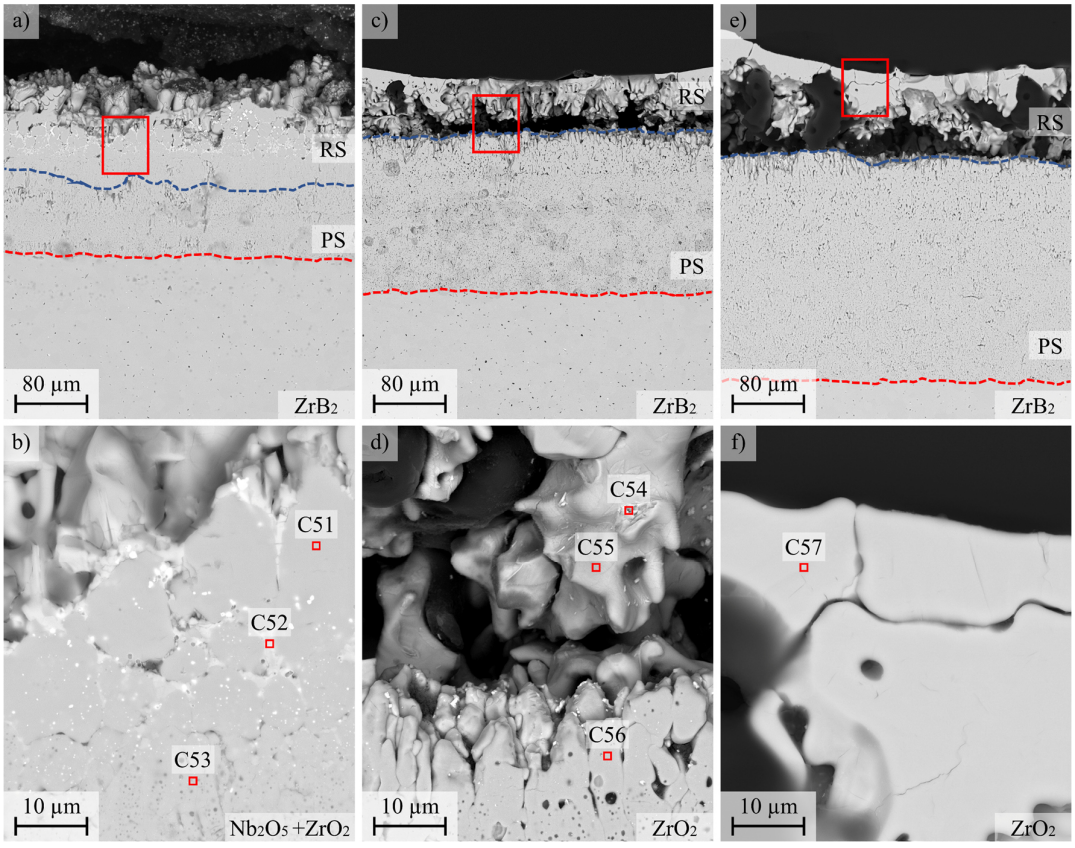

Fig. 5.50: BSE cross-sectional micrographs of Nb coated ZrB_2 (VA) after rapid oxidation (P/Q) at 1600°C: a) Holistic oxide scale, 15 min; b) Former interface zone, 15 min; c) Holistic oxide scale, 30 min; d) Former interface zone, 30 min; e) Holistic oxide scale, 60 min; f) Former interface zone, 60 min

The exposure of 30 min at 1600°C induced a transformation in the architecture of the oxide scale (Fig. 5.50c-d). The reaction scale revealed several holes, cracks, and gaps. All in all, the thickness

of the reaction scale was found to be ~58 µm and covered the porous ZrO_2, which increased from ~ 66 µm after 15 min to ~152 µm after 30 min. A gap of ~10 µm appeared between the ruptured RS and the porous ZrO_2. Residuals of a Nb-containing phase were found in the gap with a chemical composition of ~2 at.% Nb, ~30 at.% Zr, and ~68 at.% O (Spec.C54). Almost the complete Nb coating left the oxide scale (Spec.C55, Spec.C56).

A similar architecture for the oxide scale was observed after 60 min of exposure (Fig. 5.50e-f). However, the ruptured reaction scale revealed densification at the uppermost section and led to a comprehensive ZrO_2 scale (Spec.C57). No Nb-containing phases were observed in the cross-section, indicating the complete loss of the coating material. The gap between the lifted reaction scale and the porous ZrO_2 scale was still present and was not closed. The underlying porous ZrO_2 increased to ~236 µm in thickness.

Table 5.21: EDS analysis of polished cross-sections of Nb coated ZrB_2 (VA) after rapid oxidation (P/Q) at 1600°C for 15 min, 30 min, and 60 min (compare Fig. 5.50)

Condition	Spec.	O (at.%)	C (at.%)	Hf (at.%)	Ti (at.%)	Zr (at.%)	Nb (at.%)	Zr/Hf	Phase (Estimated)
1600°C, 15 min	C51	62.2	-	0.4	0	34.9	3.1	91.8	Nb_2O_5
	C52	38.7	-	0	0.1	13.7	46.5	22.8	NbO
	C53	61.7	-	0.4	0.1	45.9	3.3	93.3	ZrO_2
1600°C, 30 min,	C54	67.5	-	0.4	0.1	30.1	1.8	94.4	Nb_2O_5
	C55	68.2	-	0.4	0.1	30.7	0.5	98.4	ZrB_2
	C56	59.4	-	0.5	0.2	38.9	0.5	98.7	ZrO_2
1600°C, 60 min	C57	62.8	-	0.4	0	35.7	1.1	97.0	$Nb_2Zr_6O_{17}$

Finally, the oxidation of Nb coated ZrB_2 (VA) at 1700°C revealed the formation of an oxide scale, which consisted of a dense reaction scale and porous ZrO_2. Micrographs of the polished oxide scales and high magnification micrographs of the former interface zone of the coating/substrate are presented in Fig. 5.51 with corresponding EDS results in Table 5.22. The red dashed line represents the oxidation front of ZrB_2 and the blue-dashed line represents the transition of the uppermost reaction scale (RS) to the porous ZrO_2 scale (PS).

After 15 min of oxidation, several crystals with ~9 at.% Nb, ~23 at.% Zr, and ~68 at.% O (Spec.C58) or with ~5 at.% Nb, ~21 at.% Zr, ~23 at.% W, and ~51 at.% O (Spec.C61) were found at the former interface zone of the coating/substrate. Approximately ~1 at.% Nb was observed for the dense ZrO_2 of the RS (Spec.C59). A gap of ~14 µm separated the reaction scale and the underlying porous ZrO_2. BSE micrographs of the fractured cross-section of Nb coated ZrB_2 (VA) after rapid oxidation at 1700°C for 15 min are presented in Fig. 5.51c-d. The gap between the reaction scale and porous ZrO_2 seemed to be filled with residual B_2O_3 glass. EDS analysis of the fractured cross-section confirmed ~96 at.% O for the blackish phase inside the gap (Fig. 5.51d).

EDS analysis confirmed the chemical composition of ~36 at.% Zr and ~64 at.% O for the underlying porous ZrO_2 scale (Spec.C60), which was found to be ~128 µm in thickness.

The exposure at 1700°C for 30 min revealed an increase in the reaction scale from ~114 µm after 15 min to ~163 µm after 30 min (Fig. 5.51e-f). The reaction scale contained larger holes with a diameter of ~40 µm at the uppermost section and smaller pores with a diameter of ~2 µm near the former interface zone of the coating/substrate. EDS analysis did not reveal any Nb-content in the cross-section (Spec.C62). Several oxide crystals containing ~28 at.% W, ~3 at.% Zr, and ~69 at.% O were found at the former interface zone (Spec.C64). The gap between the RS and the PS were almost closed, anchoring the reaction scale to the underlying porous ZrO_2. The porous ZrO_2 revealed ~36 at.% Zr and ~64 at.% O (Spec.C63). No Nb content was identified. The thickness of the porous ZrO_2 increased from ~128 µm after 15 min to ~182 µm after 30 min.

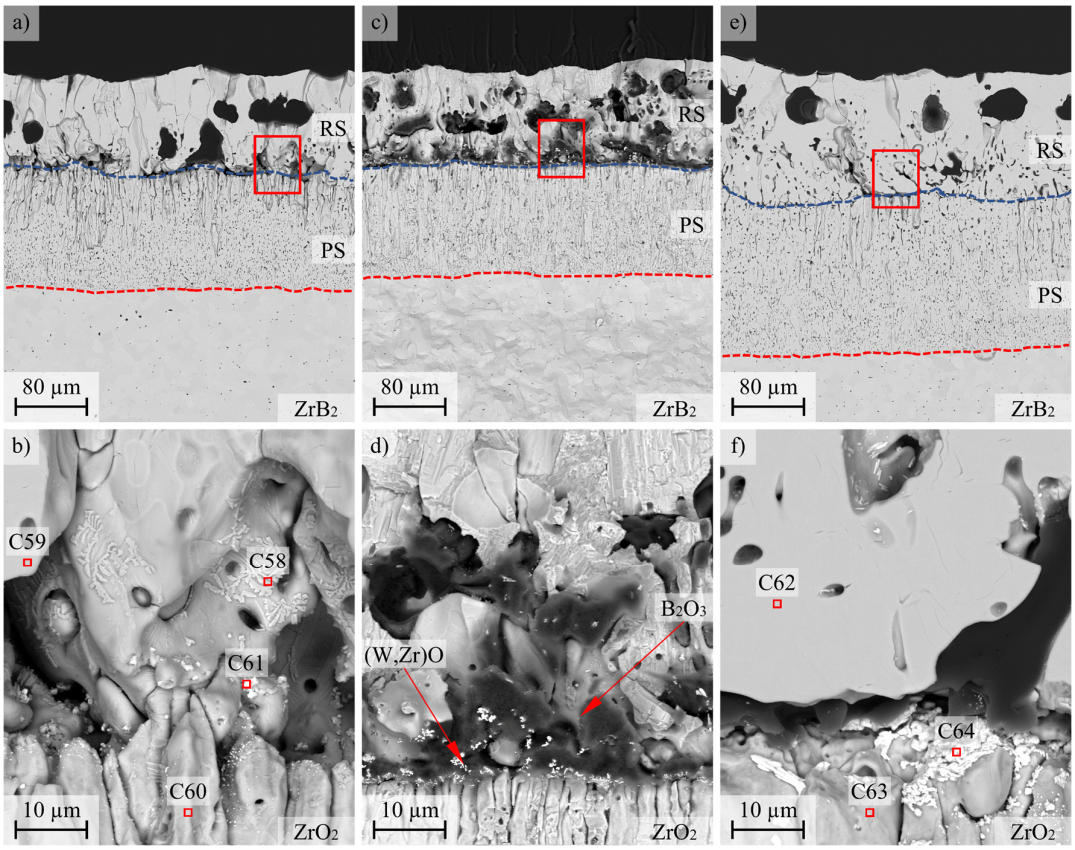

Fig. 5.51: BSE cross-sectional micrographs of Nb coated ZrB_2 (VA) after rapid oxidation (P/Q) at 1700°C: a) Holistic oxide scale, 15 min; b) Former interface zone, 15 min; c) Holistic oxide scale, 15 min, fractured surface with B_2O_3 filling; d) Fractured interface zone, 15 min; e) Holistic oxide scale, 30 min; f) Former interface zone, 30 min

Table 5.22: EDS analysis of polished cross-sections of Nb coated ZrB_2 (VA) after rapid oxidation (P/Q) at 1700°C for 15 min and 30 min (compare Fig. 5.51)

Condition	Spec.	O (at.%)	W (at.%)	Hf (at.%)	Ti (at.%)	Zr (at.%)	Nb (at.%)	Zr/Hf	Phase (Estimated)
1700°C, 15 min	C58	67.5	0	0.2	0.4	23.0	8.7	72.6	$Nb_2Zr_6O_{17}$
	C59	63.1	0	0.5	0.1	35.4	0.9	97.5	ZrO_2
	C60	63.5	0.3	0.4	0.1	35.1	0.6	98.3	ZrO_2
	C61	50.6	22.1	0.3	0.6	21.3	5.1	80,7	$Nb_2Zr_6O_{17}$
1700°C, 30 min	C62	62.5	0.2	0.5	0.1	36.0	0.7	98.1	ZrO_2
	C63	64.9	1.4	0.4	0.1	34.6	0.6	98.3	ZrO_2
	C64	68.4	27.6	0.2	0.4	3.4	0	100	WO_3

5.3.4 Kinetic Calculations of Nb Coated ZrB_2

The oxide scale formed on Nb coated ZrB_2 (VA) was subdivided into a reaction scale (RS) with at least 2 at.% Nb and/or dense ZrO_2, and a porous scale of ZrO_2. The parabolic oxidation rate constants were calculated for the porous ZrO_2 scale according to Deal and Groov's differential equation for linear-parabolic oxidation kinetics (compare Equ. 2.14) [70, 138]. Finally, the ratio of the porous scale to the total oxide scale TS was determined. All values are provided in Table 5.23 and visualized in Fig. 5.52a, showing the thickness of the porous oxide scale squared vs. the exposure time.

Table 5.23: Oxide scale thickness of the reaction scales and porous oxide scales as well as the calculated parabolic rate constants for the porous ZrO_2 scales of Nb coated ZrB_2 (AC, VA) after ramped (R/C) or rapid oxidation (P/Q)

Condition	Temperature	Time (min)	RS (µm)	PS (µm)	TS (µm)	PS/TS (%)	$\ln(K_{P(PS)})$
Nb coated (VA)	1500°C	15	51	19	70	21.3	7.3
		30	54	29	83	25.9	7.4
		60	40	69	109	38.8	8.5
	1600°C	15	81	66	147	31.0	9.8
		30	73	152	225	40.3	10.7
		60	100	236	336	41.3	10.9
	1700°C	15	114	128	242	34.6	11.1
		30	163	182	345	34.5	11.1

The data reveals that the thickness of the porous oxide scale is increasing with respect to the oxidation temperature and exposure time. However, the temperature has a dramatic effect on the progression of the oxidation as visible in Fig. 5.52a (slope corresponds with the calculated

parabolic rate constants ln($K_{P(PS)}$) in Table 5.23). The oxidation at 1500°C shows a transition after 30 min of oxidation, increasing the parabolic oxidation rate constants by time. A similar effect can be seen for the oxidation at 1600°C. The progression of oxidation changed after 15 min, transforming into parabolic oxidation with increased oxidation rate constant. In contrast, the exposure at 1700°C revealed steady parabolic oxidation with an increased rate constant. As visible in Fig. 5.52a, the rate constants for the parabolic oxidation at 1700°C align with the oxidation rate constants at 1600°C for an exposure >15 min (similar slope of the graphs).

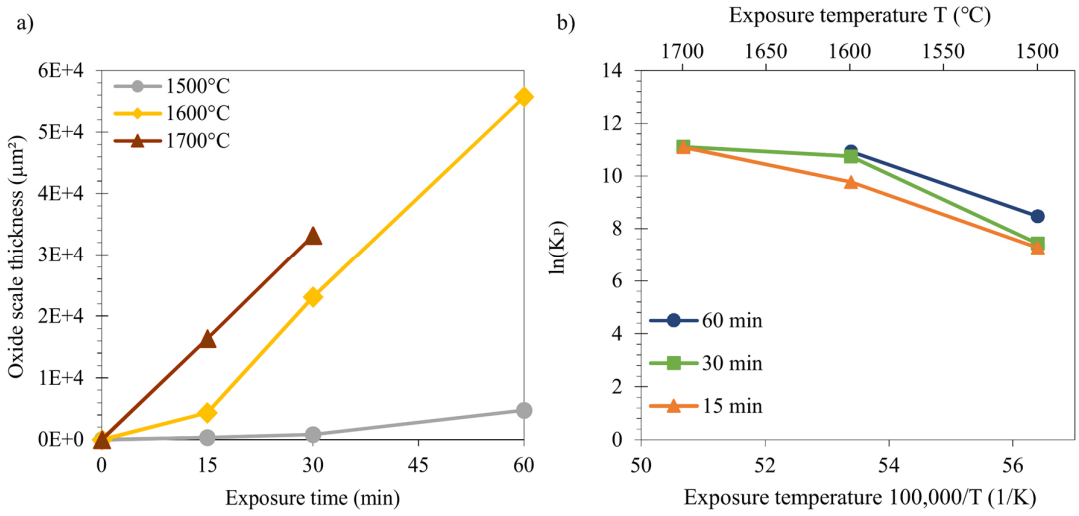

Fig. 5.52: a) Oxide scale thickness squared vs. exposure time for the isothermal oxidation at 1500°C, 1600°C, and 1700°C; b) Arrhenius plot for the oxidation process for an exposure of 15 min, 30 min, and 60 min

Further, the activation energies for the oxidation were calculated (compare Equ. 2.15). The results are provided in Table 5.24 and are visualized in the Arrhenius plot in Fig. 5.52b. As visible in the plots, the activation energies for the Nb coated ZrB_2 (VA) decrease with increasing temperature regime from 1500°C to 1600°C, and 1600°C to 1700°C (decreasing slope of the plots). However, the highest activation energy was found after 30 min within the temperature regime of 1500°C to 1600°C. Long-term oxidation for up to 60 min led to increased rate constants. However, the activation energy was found to be similar to the oxidation for 15 min. The reason for this peculiar behavior will be thoroughly argued in the discussion section.

Table 5.24: Calculated oxidation rate constants and activation energies for the formation of porous ZrO_2 scales on Nb coated ZrB_2 (VA) for rapid oxidation (P/Q) in a temperature range between 1500°C to 1600°C and 1600°C to 1700°C

Condition	Exposure Time (min)	$E_{A1500-1600}$ (kJ/mol)	$E_{A1600-1700}$ (kJ/mol)
Nb coated (VA)	15	688	407
	30	915	111
	60	679	

5.4 Gadolinium Oxide Coatings on ZrB_2

5.4.1 Development of GdO Coatings on ZrB_2

Oxygen-doped gadolinium coatings ($Gd_iO_{(1-i)}$; [$i \in \mathbb{R} \mid 0.5 \leq i \leq 1$]) were deposited by reactive magnetron sputtering, using a metallic gadolinium target (Table 4.2, Target T3) and high-purity oxygen. Appropriate parameters for the reactive sputtering process were used to carry out a multilayer coating experiment (Run8). Different oxygen gas flow rates were tested for similar processing conditions to analyze the effect on the deposition rate and the chemical composition. The fractured cross-section of the multilayer coating experiment on Al_2O_3 substrate is illustrated Fig. 5.53. A schematic represents the multilayer coating and describes the set parameters. Detailed processing parameters, measured scale thicknesses, calculated deposition rates, and measured oxygen content inside the single layers are provided in Table 5.25.

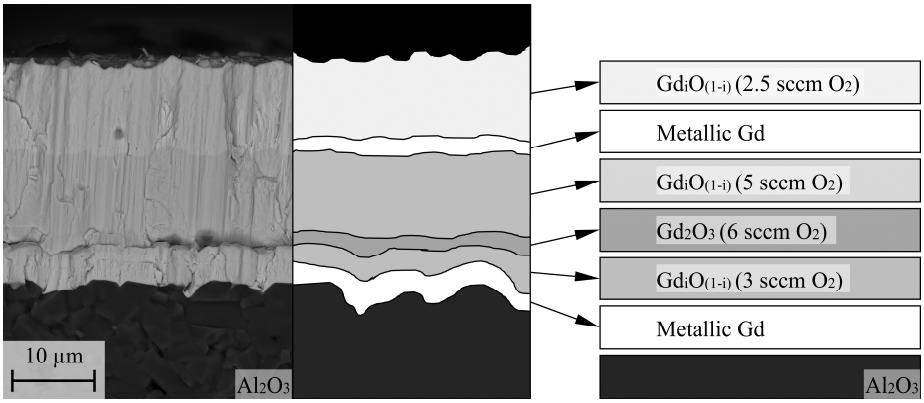

Fig. 5.53: BSE micrograph of fractured cross-section of multilayer parameter study for $Gd_iO_{(1-i)}$ (Run8) with an appropriate schematic of the single layers and used process parameters (sccm O_2)

Table 5.25: Parameters for reactive magnetron sputtering of oxygen-doped Gd coatings ($Gd_iO_{(1-i)}$)

Run	Time (min)	Power (W)	Voltage (V)	Argon (sccm)	Oxygen (sccm)	Thickness (µm)	Deposition (µm/h)	Oxygen in scale (at.%)
Run8	5	500	410	20	0	2.6	31.58	15.4
	15	500	401	20	3.0	2.2	8.77	26.3
	23	500	198	20	6.0	2.0	5.26	57.3
	60	500	250	20	5.0	9.7	9.65	42.1
	5	500	403	20	0	1.8	21.05	11.2
	60	500	405	20	2.5	10.1	10.1	32.5
Run9	300	500	179	20	6.0	5.5	1.10	61.7
Run10	120	500	408	20	2.5	14.6	7.30	38.2

The more oxygen the $Gd_iO_{(1-i)}$ coating contains, the darker the coloration of the layer in the BSE micrographs. The effect of the oxygen flow (sccm) on the deposition rates of $Gd_iO_{(1-i)}$ coating and the corresponding chemical composition is provided in Table 5.25. The data indicates a high inconsistency in the deposition rate and chemical composition with respect to the oxygen gas flow. This will be discussed extensively in the discussion of the results. Appropriate parameters for coatings with the chemical composition for Gd_2O_3 (~38 at.% Gd and ~62 at.% O) were found to be 6 sccm oxygen with ~178 V (compare Run9). The low deposition rate of ~1.1 µm/h would be disadvantageous for depositing a thicker Gd_2O_3 coating (~9µm) on ZrB_2 specimens. Therefore, a $Gd_iO_{(1-i)}$ coating with a deposition rate of ~7.3 µm/h (~62 at.% Gd and ~38 at.% O) and a thickness of ~15 µm was applied on Al_2O_3 substrates. Appropriate sputter parameters were found to be 2.5 sccm O_2 with ~408 V (compare Run10). To induce the crystallization and oxidation of the $Gd_iO_{(1-i)}$ coating into a Gd_2O_3 scale with cubic crystal structure, coated specimens of Run9 and Run10 were pre-oxidized (PO) in a box furnace. Specimens were put in the hot furnace at 600°C and subsequently quenched after 15 min in lab air.

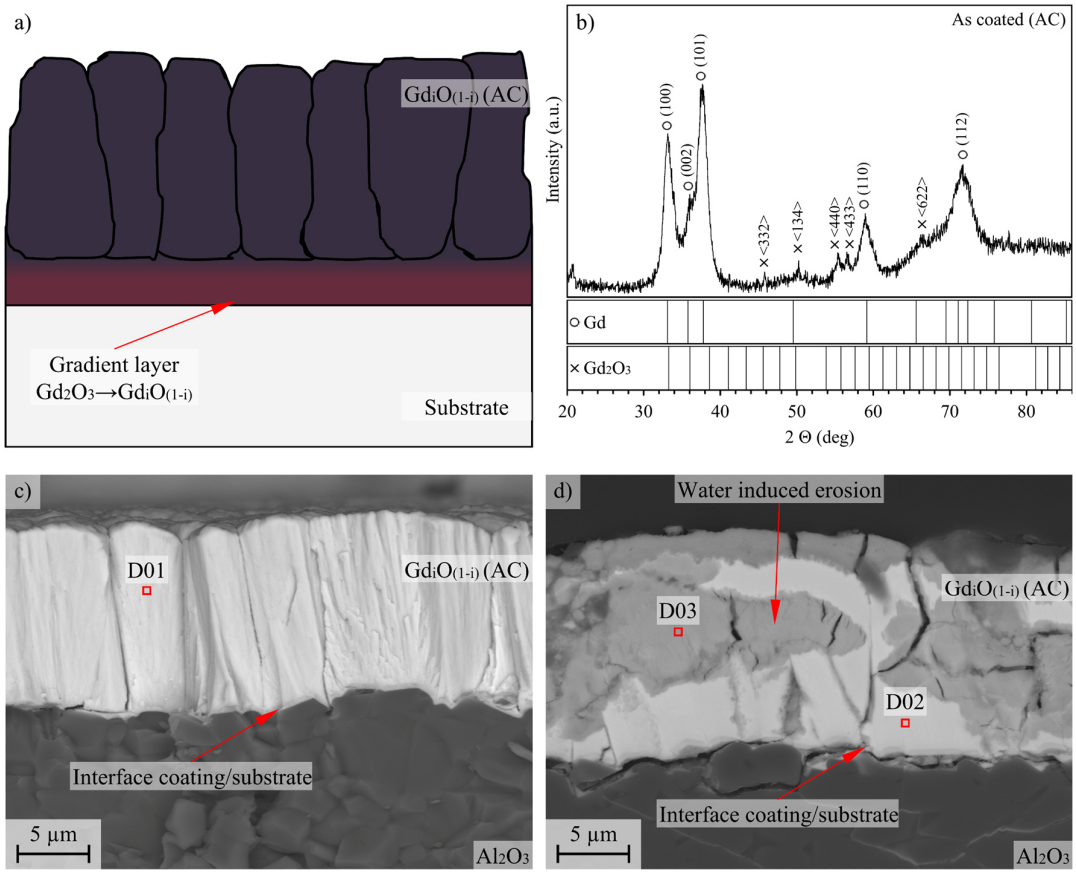

Fig. 5.54: a) Schematic of the applied GdO coating; b) X-ray Diffraction pattern of GdO coated Al_2O_3; c) Fractured cross-section of GdO coated Al_2O_3; d) Polished cross-section of GdO coated Al_2O_3 (water induced erosion)

The $Gd_iO_{(1-i)}$ coating of Run10 spalled during the heat treatment, whereas the sputtered Gd_2O_3 layer of Run9 withstood the heat treatment. To avoid the spallation of the $Gd_iO_{(1-i)}$ coating during oxidation, a two-layer system was created, containing a thin intermediate Gd_2O_3 layer (~600 nm) and an overlaying $Gd_iO_{(1-i)}$ scale of ~11 µm thickness. As the majority of the coating is $Gd_iO_{(1-i)}$, from now on the coating will be mentioned as GdO throughout the following section. Deposition parameters for the GdO coating are provided in Table 5.26, Run11. A schematic of the developed GdO coating, the X-ray diffraction pattern, the fractured cross-section, and the polished cross-section is presented in Fig. 5.54.

Table 5.26: Reactive magnetron sputtering parameters for the GdO coating on ZrB_2 (compare Fig. 5.54)

Run	Time (min)	Power (W)	Voltage (V)	Argon (sccm)	Oxygen (sccm)	Thickness (µm)	Deposition (µm/h)	Oxygen in scale (at.%)
	90	500	190	20	4.5	0.6	0.40	59.7
Run11	30	500	190-390	20	2.5	-	-	
	120	500	390	20	2.5	12.1	6.05	40.1

The X-ray diffraction pattern of the GdO coated specimens revealed metallic Gd (PDF01-080-6667) and a few reflections for Gd_2O_3 (PDF01-083-6010). Corresponding Miller indices for the assigned reflections were marked in the diffractogram (Fig. 5.54b). The fractured cross-section of the GdO coated Al_2O_3 substrate revealed a columnar grain structure (see Fig. 5.54c). The chemical composition was found to be ~59 at.% Gd, ~1 at.% Al, and ~40 at.% O (Spec.D01-D02). Polished cross-sections were not be able to prepared due to the water affinity of metallic gadolinium [124, 140]. Fig. 5.54d proved the intensive reaction of the GdO coating with water during the polishing procedure. Several spots were eroded due to the water and formed a phase with the chemical composition for ~18 at.% Gd, and ~82 at.% O (Spec.D03). It is assumed that it might have formed $Gd(OH)_3$, following (Equ. 3.6) [140].

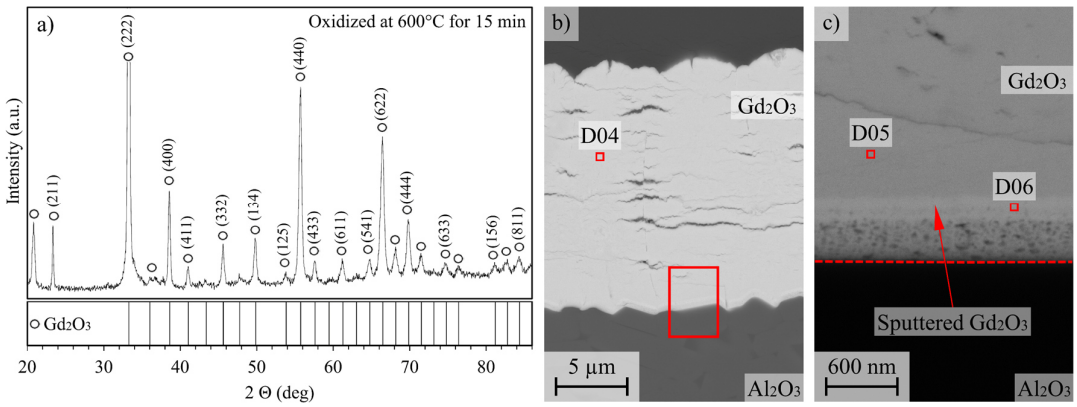

Fig. 5.55: a) X-ray Diffraction pattern of GdO coated Al_2O_3 after low temperature oxidation at 600°C for 15 min; b) BSE cross-sectional micrograph of oxidized GdO coating on Al_2O_3 substrate; c) High magnification micrograph of the interface zone of the GdO coating

The pre-oxidation (PO) of the GdO coating at 600°C for 15 min has not resulted in spallation of the coating. The X-ray diffraction pattern as well as polished cross-sections of the oxidized GdO coating are presented in Fig. 5.55. Crystalline Gd_2O_3 with a cubic phase was assigned to the reflections of the diffractogram (PDF01-083-6010). Corresponding Miller indices for the c-Gd_2O_3 are marked in the diffractogram. The results of the EDS analysis are provided in Table 5.27.

Table 5.27: EDS spot analysis of GdO coated Al_2O_3 substrate as coated (AC) and pre-oxidized (PO) at 600°C for 15 min (compare Fig. 5.54 and Fig. 5.55)

Condition	Spec.	O (at.%)	Al (at.%)	Gd (at.%)	Al/Gd	Phase (Estimated)
AC	D01	39.8	1.4	58.8	1.9	$Gd_iO_{(1-i)}$
	D02	40.3	1.1	58.6	1.8	$Gd_iO_{(1-i)}$
	D03	81.6	0	18.4	0	$Gd(OH)_3$
600°C, 15 min	D04	58.7	0	41.3	0	Gd_2O_3
	D05	58.6	0.6	40.8	1.5	Gd_2O_3
	D06	57.4	6.5	36.2	15.2	(Gd,Al)O

The chemical composition of the oxidized GdO coating revealed ~41 at.% Gd and ~59 at.% O, which can be assigned to Gd_2O_3 (Spec.D04-D05). Since Gd_2O_3 is not soluble in water, polished cross-sections were prepared for the pre-oxidized specimens. Several horizontal cracks appeared inside the oxidized coating (Fig. 5.55b). However, no cracks were observed in the sputtered Gd_2O_3 layer at the interface between the coating/substrate (Fig. 5.55c). EDS analysis revealed that Al diffused into the sputtered Gd_2O_3 during pre-oxidation, forming a solid solution (Spec.D06). This might be a reason for the improved adhesion and need to be considered.

5.4.2 Ramped Oxidation Experiments of GdO Coated ZrB_2

GdO coated ZrB_2 (AC, PO) was oxidized in a tube furnace at 1500°C for 60 min using ramped oxidation (R/C) (compare Fig. 4.10). Top-view photographs of the GdO coated specimens and oxidized condition are presented in Fig. 5.56. The comparison between AC and PO revealed no significant differences after high temperature oxidation. A glassy phase with a white appearance formed in the middle of the surface and covered ~53 % of the total surface area.

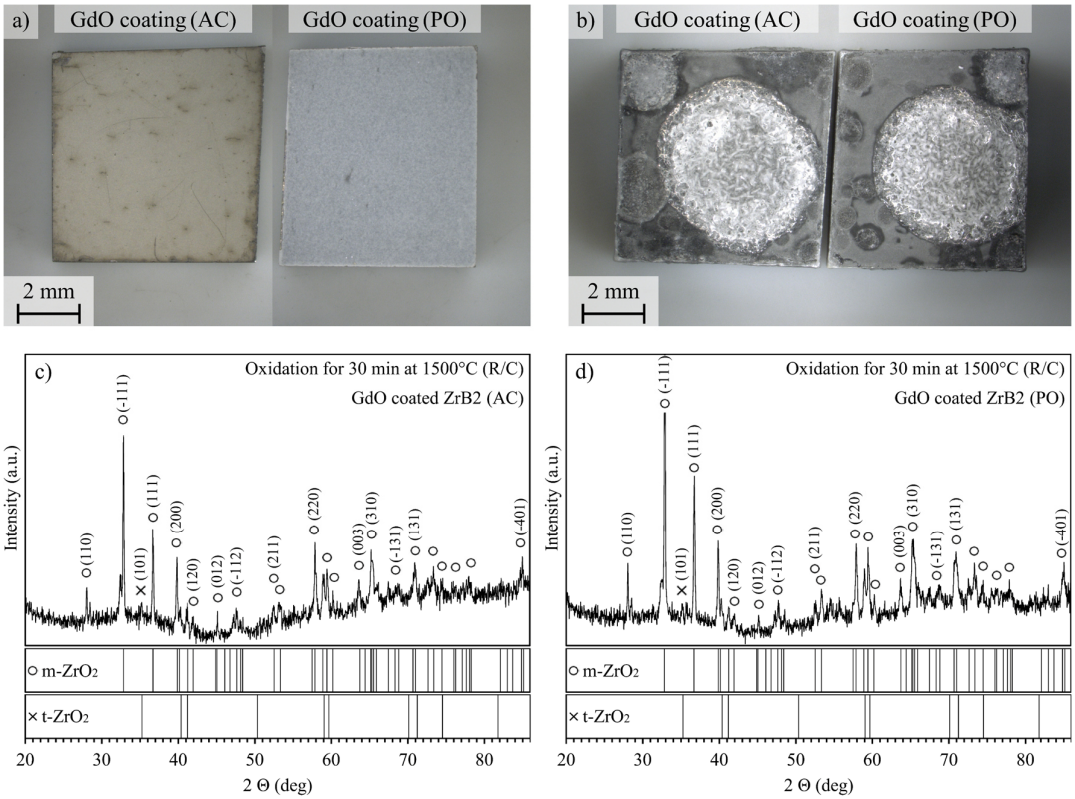

Fig. 5.56: *a) Comparison of GdO coated ZrB_2 (As Coated [AC], Pre-oxidized at 600°C); b) Comparison of GdO coated ZrB_2 (AC, pre-oxidized) after ramped oxidation (R/C) at 1500°C for 60 min, c) X-ray diffraction pattern of GdO coated ZrB_2 (AC) after ramped oxidation; d) X-ray diffraction pattern of GdO coated ZrB_2 (pre-oxidized) after ramped oxidation*

The X-ray diffraction pattern revealed similar results for both conditions. The reflections were assigned to m-ZrO_2 (PDF00-037-1484) and t-ZrO_2 (PDF01-079-1764). BSE micrographs of the surface and fractured cross-section of the specimen (AC) are shown in Fig. 5.57. EDS results are provided in Table 5.28. As visible, the surface as well as the sharp edges of the specimens were covered by a Gd-based phase with a chemical composition of ~20 at.% Gd, ~17 at.% Zr, and ~63 at.% O (Spec.D07). ZrO_2 grains can be observed beneath the liquid scale (Spec.D08). The fractured cross-section revealed the infiltration of the formed ZrO_2 scale (Spec.D09) (Fig. 5.57c-d). The infiltration depth is marked with a blue-dashed line, whereas the red-dashed line marks the oxidation front for ZrB_2 (Fig. 5.57c). The infiltration at the sharp edge was found to be ~11 µm thick (Fig. 5.57d).

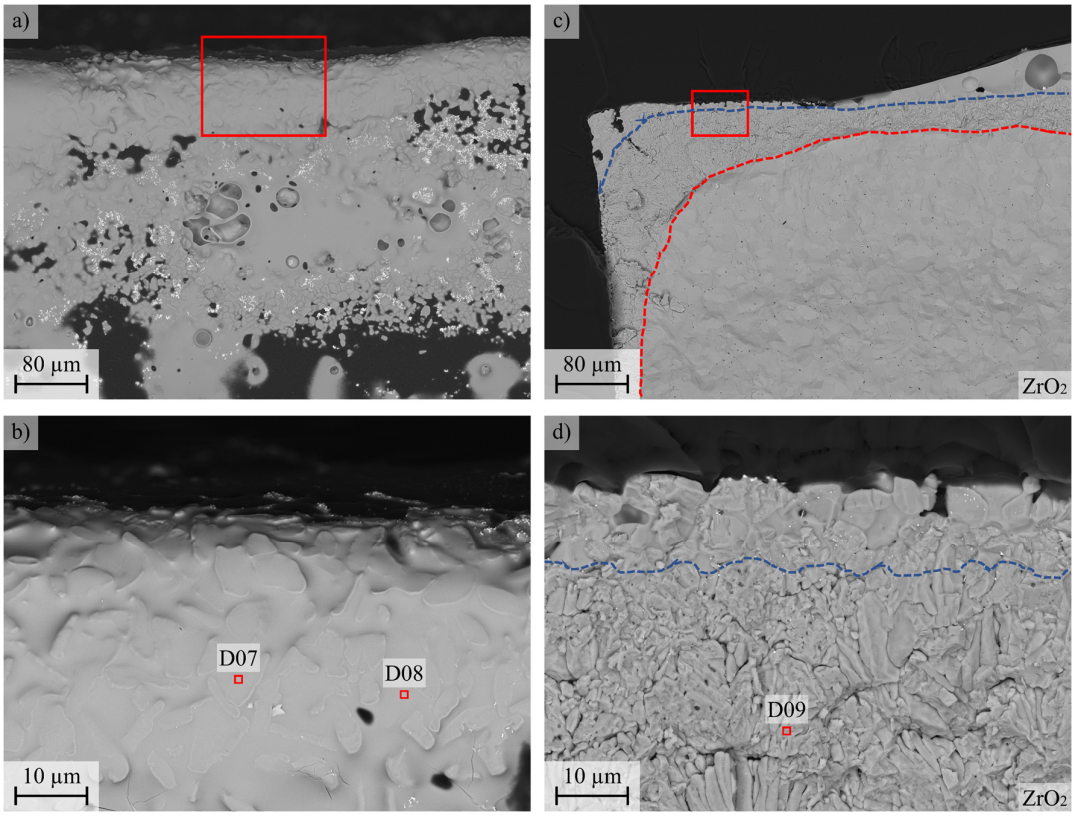

Fig. 5.57: Top-view BSE micrographs of the oxidized edge of GdO coated ZrB_2 (AC): a) Overview; b) High magnification; BSE cross-sectional micrograph of fractured surface at the edge with marked infiltration of a Gd-rich phase in porous ZrO_2 (blue-dashed line): c) Overview, d) High magnification

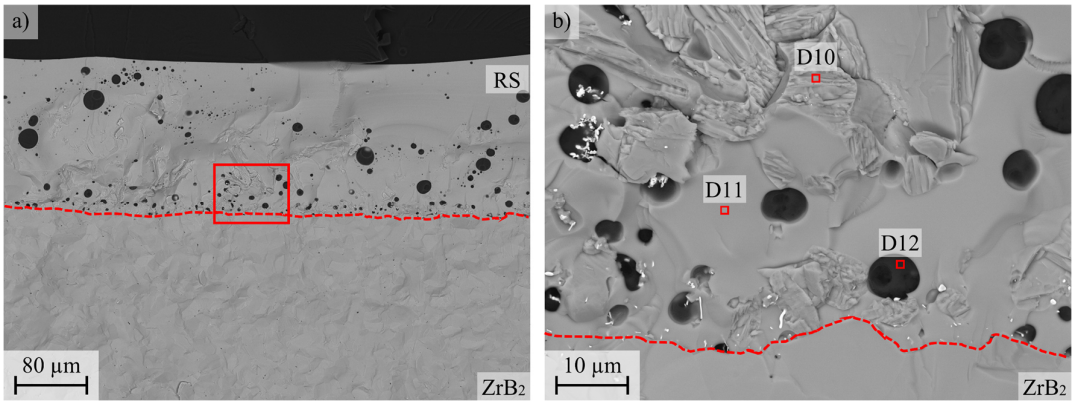

Fig. 5.58: BSE cross-sectional micrograph of fractured surface of GdO coated ZrB_2 (AC) after oxidation for 60 min at 1500°C, located in the center of the specimen: a) Overview; b) High magnification at the interface zone

The Fig. 5.58 shows micrographs of the fractured cross-section of the specimen. A thick layer of a Gd-based phase covered the center of the specimen. EDS proved a content of ~4 at.% Zr (Spec.D11). Several globular bubbles, filled with a darkish phase (Spec.D12, oxygen content ≥90 at.%) appeared in the Gd-based layer. Furthermore, the coating/substrate interface was still intact and did not indicate any porous ZrO_2 scale formation. Sparsely distributed ZrO_2 grains were found inside the Gd-rich phase (Spec.D10). The red dashed line marks the oxidation front of ZrB_2.

The EDS data revealed a significantly increased amount of oxygen for the Gd-rich phase (>82 at.% O, Spec.D11). Similar results can be observed for B_2O_3 glass (Spec.D12, ~90 at.% O). Since boron is not quantifiable via EDS, boron might be counted for oxygen and lead to the excess of oxygen in the compositions. Therefore, it is assumed that the Gd-rich phase might be a solution of Gd_2O_3 and B_2O_3 (in the following (Gd,B)O)). A detailed explanation, assigning the phase as (Gd,B)O is presented in the discussion.

Table 5.28: EDS spot analysis of the oxidized GdO coated ZrB_2 (AC) after ramped oxidation (R/C) at 1500°C for 60 min (compare Fig. 5.57 and Fig. 5.58)

Condition	Spec.	O (at.%)	Hf (at.%)	W (at.%)	Zr (at.%)	Gd (at.%)	Zr/Gd	Phase (Estimated)
1500°C, 60 min	D07	62.5	0	0	17.2	20.2	46.0	(Gd,Zr)O
	D08	67.7	0.3	0	30.9	1.1	96.5	ZrO_2
	D09	69.2	0.3	0.1	29.3	1.1	96.3	ZrO_2
	D10	66.9	0.3	0.1	31.9	0.8	97.5	ZrO_2
	D11	82.3	0.1	0.1	3.6	13.9	20.5	(Gd,B)O+ ZrO_2
	D12	90.2	0	0	1.2	8.6	12.5	B_2O_3

Considering the results, a pre-oxidation step was not found to be a mandatory process step for oxidation protection by the GdO coating. Therefore, rapid oxidation experiments were performed with GdO coated ZrB_2 (AC).

5.4.3 Rapid Oxidation Experiments of GdO Coated ZrB_2

Top-view photographs of oxidized GdO coated ZrB_2 (AC) at different temperatures and for different exposure times are presented in Fig. 5.59. Specimens revealed a darkish surface coloration after oxidation at 1500°C. A whitish translucent glass with several bubble inclusions formed at the surface. The surface coverage by the glass increased with respect to the exposure time till 60 min. Dry and yellowish oxides can only be found at the sharp edges of the oxidized specimens. At 1600°C, the dominant oxide formation at the edges could already be seen after 15 min. The oxidation front of the yellowish oxide grew from the edges into the center of the specimens as the oxidation time progressed. However, the center of the specimen still exhibited a dark discoloration. Finally, the oxidation at 1700°C showed the yellowish oxides already after 15 min and full coverage with the yellowish oxides after 30 minutes.

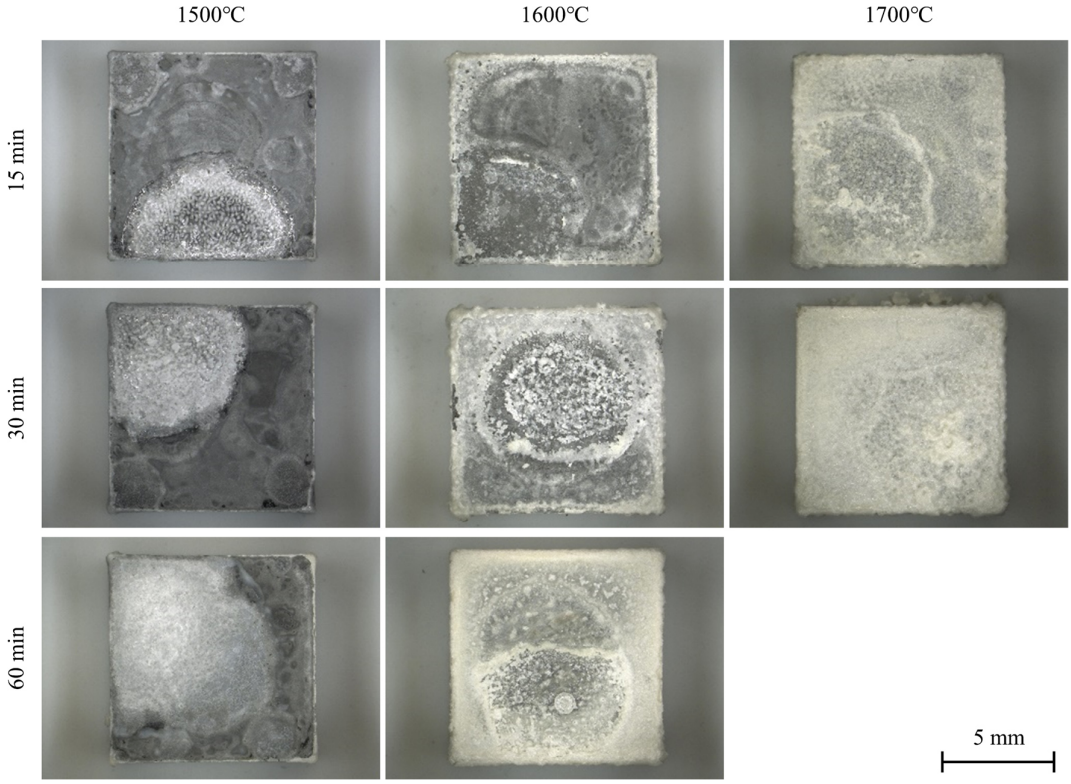

Fig. 5.59: Top-view photographs of GdO coated ZrB_2 after rapid oxidation (P/Q) at 1500°C, 1600°C, and 1700°C for 15 min, 30 min, and 60 min

X-ray diffraction was performed with all tested specimens. The diffraction patterns for the oxidation of 15 min and 30 min are presented in Fig. 5.60. Reflections for monoclinic ZrO_2 (PDF00-037-1484) and tetragonal ZrO_2 (PDF01-079-1764) were identified for the detected diffraction patterns. No characteristic reflections for Gd-containing phases such as Gd_2O_3, $Gd_2Zr_2O_7$, or GdB_3O_6 were observed for any experimental condition via X-ray diffraction analysis.

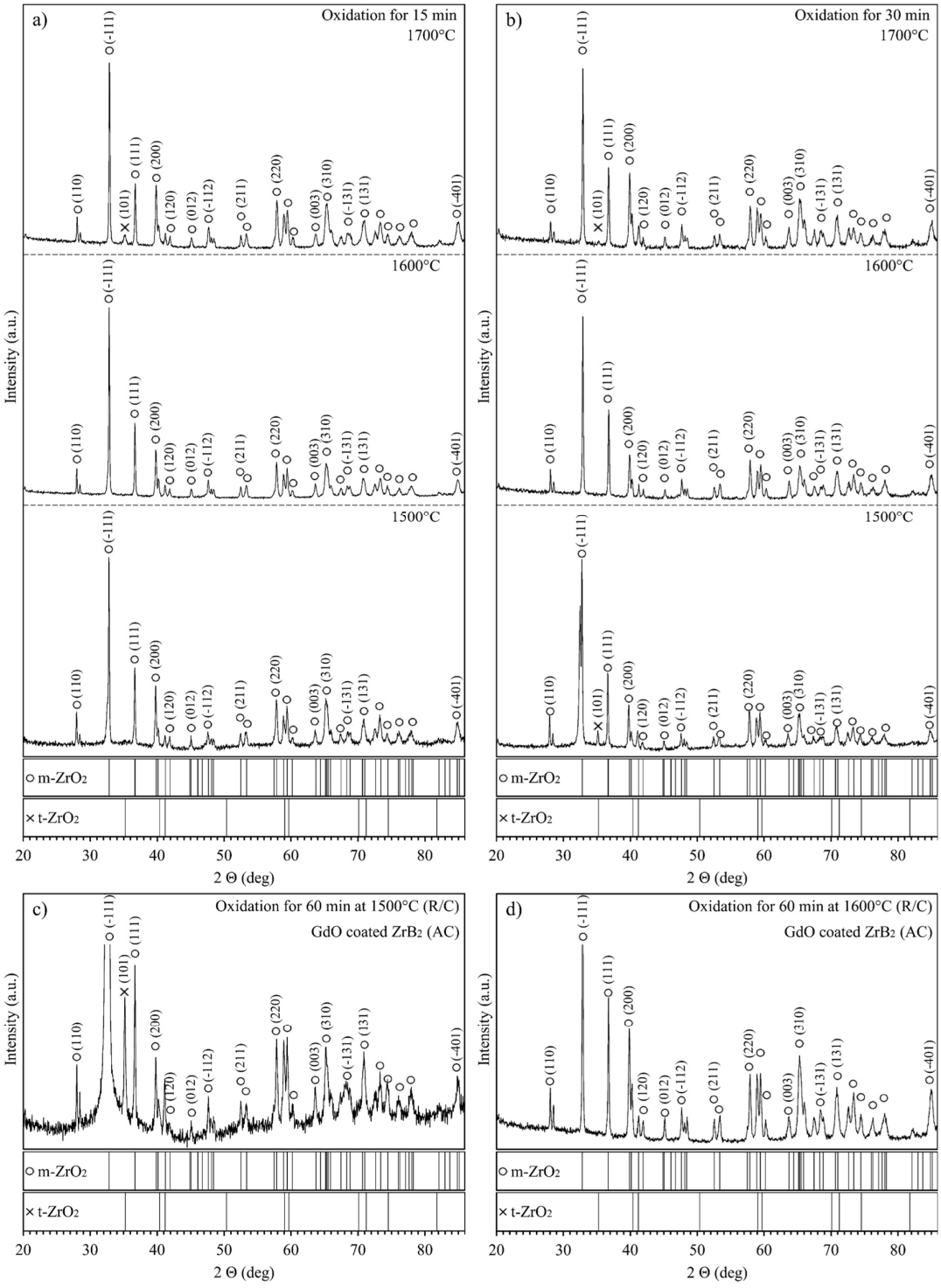

Fig. 5.60: X-ray diffraction pattern of GdO coated ZrB_2 after rapid oxidation (P/Q) at 1500°C, 1600°C, and 1700°C: a) for 15 min; b) for 30 min; c) for 60 min at 1500°C, d) for 60 min at 1600°C

BSE top-view micrographs of tested specimens are presented in Fig. 5.61 to Fig. 5.66. The EDS data for the analyzed surfaces are provided in Table 5.29. The oxidation for 15 min at 1500°C led

to the formation of a comprehensive coverage with (Gd,B)O (area [O], Spec.D15). Near the sharp edges of the specimen, ZrO_2 grains were mounted in (Gd,B)O (area [P], Spec.D013-D014). The grains were found to have an average size of ~9 µm in diameter. According to the literature, the dark areas in the BSE micrograph were identified as B_2O_3-rich pools [39].

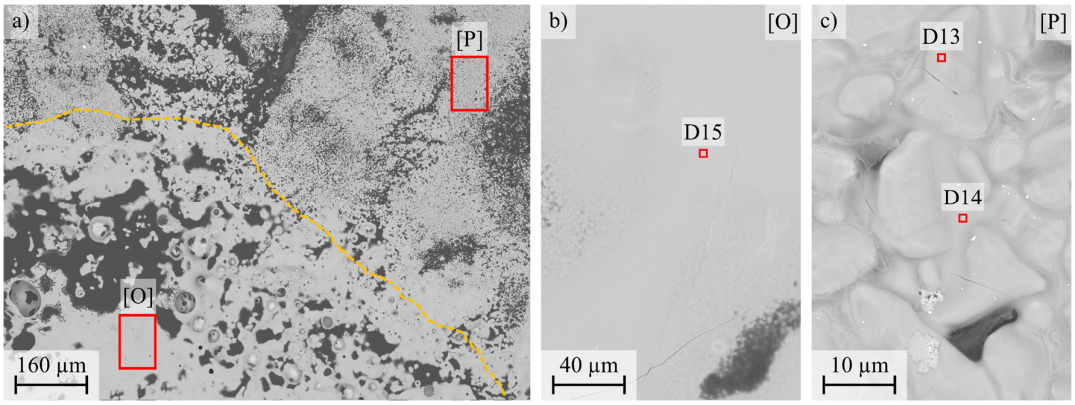

Fig. 5.61: BSE top-view micrographs of the GdO coated ZrB_2 after rapid oxidation (P/Q) at 1500°C for 15 min: a) Overview; b) High magnification of (Gd,B)O (area [O]); c) High magnification of (Gd,B)O mounted ZrO_2 grains (area [P])

The surface condition of GdO coated ZrB_2 after 30 min at 1500°C is presented in Fig. 5.62. The center of the specimen was covered with (Gd,B)O (Spec.D16) and B_2O_3 glass, revealing a darker discoloration in the BSE micrographs. Small globular grains with an average diameter of ~2.9 µm and a chemical composition for ~6 at.% Gd, ~12 at.% Zr, and ~82 at.% O (area [Q], Spec.D19) were found inside the B_2O_3 glass. ZrO_2 grains with a chemical composition of ~1 at.% Gd, ~34 at.% Zr, and ~65 at.% O were found near the sharp edges of the specimen (area [R], Spec.D17). The grains are enclosed in (Gd,B)O (Spec.D18).

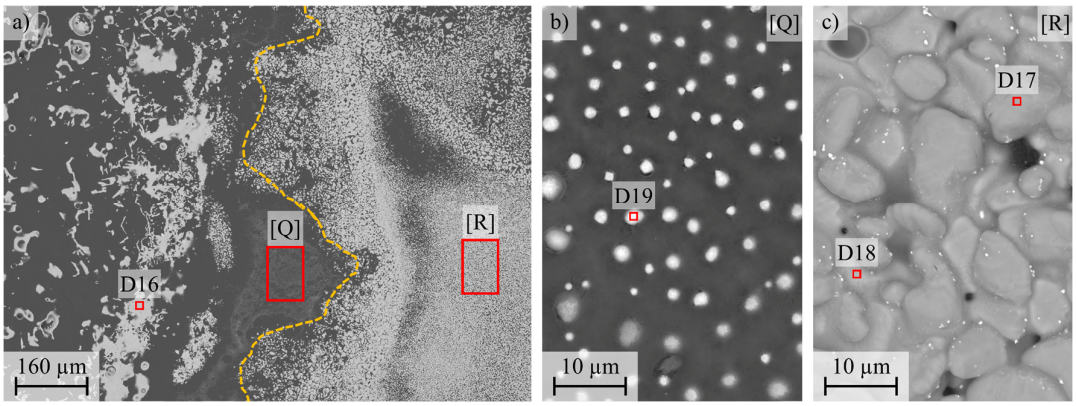

Fig. 5.62: BSE top-view micrographs of the GdO coated ZrB_2 after rapid oxidation (P/Q) at 1500°C for 30 min: a) Overview; b) High magnification of (Gd,B)O (area [Q]); c) High magnification of (Gd,B)O mounted ZrO_2 grains (area [R])

After 15 min at 1600°C, the surface was covered by B_2O_3 glass as presented in Fig. 5.63. Arbitrarily shaped ZrO_2 grains with a chemical composition of up to ~6 at.% Gd, ~19 at.% Zr, and ~75 at.% O were found in the glass (Spec.D20-D21).

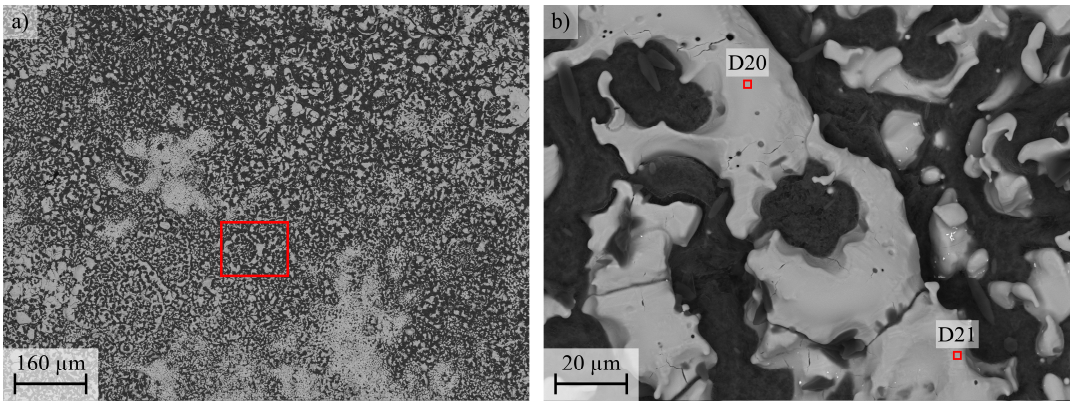

Fig. 5.63: BSE top-view micrographs of the GdO coated ZrB_2 after rapid oxidation (P/Q) at 1600°C for 15 min: a) Overview; b) High magnification micrograph of exposed ZrO_2 grains at the surface

After the exposure of 30 min at 1600°C the GdO coated ZrB_2 still revealed B_2O_3 glass at the surface (Fig. 5.64). However, the content of B_2O_3 decreased compared to the exposure of 15 min, whereas the amount of exposed ZrO_2 grains increased. The grains of ZrO_2 revealed a chemical composition for ~1 at.% Gd, ~38 at.% Zr, and ~61 at.% O (Spec.D22). Globular particles with an average diameter of ~2 µm were found within the B_2O_3 glass. The grains contained ~11 at.% Gd, ~7 at.% Zr, and an increased amount of ~82 at.% O (Spec.D17).

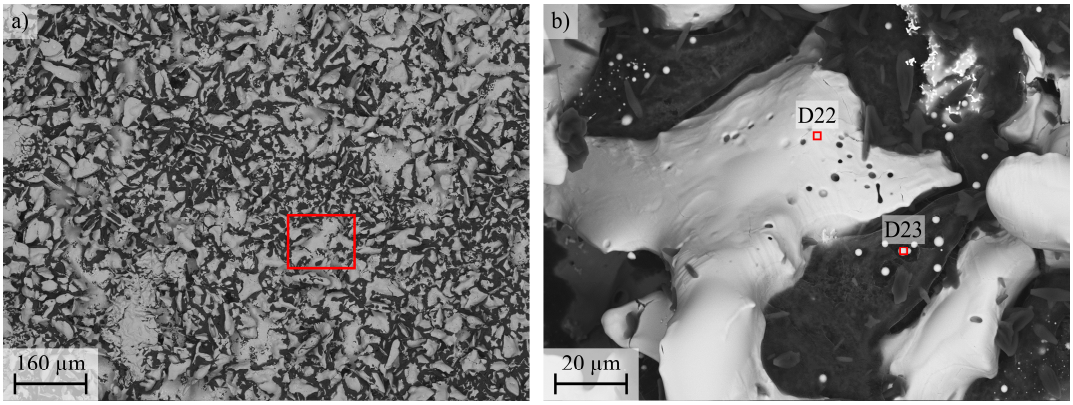

Fig. 5.64: BSE top-view micrographs of the GdO coated ZrB_2 after rapid oxidation (P/Q) at 1600°C for 30 min: a) Overview; b) High magnification micrograph of exposed ZrO_2 grains at the surface.

A clear difference in the surface appearance was visible after 15 min at 1700°C compared to the specimens oxidized at 1500°C or 1600°C for similar exposure time. As presented in Fig. 5.65, the exposure of 15 min at 1700°C led to a dry surface, covered with ZrO_2 and crystals of a Gd-rich phase. Further, the oxidized surface revealed a wavy surface with several cracks. Observed cracks were found to be filled with residual B_2O_3. The dry surface contained ZrO_2 with a chemical composition for ~2 at.% Gd, ~30 at.% Zr, and ~68 at.% O (Spec.D24). Further, a Gd-rich phase with an engraved surface appearance covered the ZrO_2. The chemical composition of the Gd-rich phase was measured as ~34 at.% Gd, ~3 at.% Zr, and ~63 at.% O (Spec.D25).

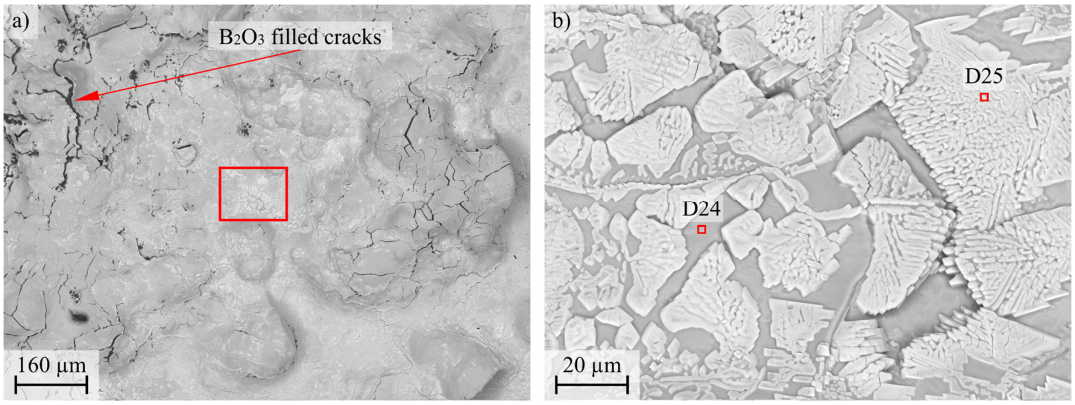

Fig. 5.65: BSE top-view micrographs of the GdO coated ZrB_2 after rapid oxidation (P/Q) at 1700°C for 15 min: a) Overview; b) High magnification micrograph of exposed ZrO_2 grains with Gd_2O_3 crystals at the surface

The surface condition after 30 min can be seen in Fig. 5.66. The amount of the Gd-rich phase on the surface decreased significantly by time at 1700°C. Several pits with a Gd-containing phase were present at the surface. ZrO_2 grains with a chemical composition of ~1 at.% Gd, ~29 at.% Zr, and ~70 at.% O (Spec.D27) revealed an average diameter of ~61 µm. Residual Gd-rich phase fields with a chemical composition of ~18 at.% Gd, ~18 at.% Zr, and ~64 at.% O (Spec.D26) were present at the surface. Furthermore, high magnification proved the presence of residual B_2O_3 at the grain boundaries.

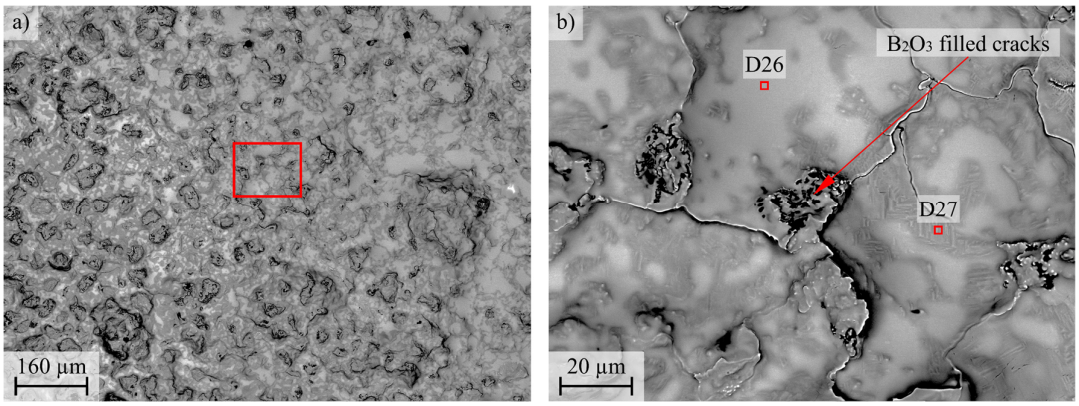

Fig. 5.66: BSE top-view micrographs of the GdO coated ZrB_2 after rapid oxidation (P/Q) at 1700°C for 30 min: a) Overview; b) High magnification micrograph of exposed ZrO_2 grains and (Gd,Zr)O phase fields at the surface

In the following, BSE cross-sectional micrographs of the oxide scales of GdO coated ZrB_2 after rapid oxidation (P/Q) will be presented. The micrographs were always taken in the center of the specimens. The red-dashed lines mark the oxidation front of the ZrB_2, whereas the blue-dashed line marks the transition from the reaction scale RS to the porous ZrO_2 scale PS.

Table 5.29: EDS spot analysis of the oxidized surfaces of GdO coated ZrB_2 after rapid oxidation (P/Q) at 1500°C, 1600°C, and 1700°C for 15 min and 30 min (compare Fig. 5.61 to Fig. 5.66)

Condition	Spec.	O (at.%)	Hf (at.%)	W (at.%)	Zr (at.%)	Gd (at.%)	Zr/Gd	Phase (Estimated)
1500°C, 15 min	D13	65.8	0	0	33.1	1.1	96.8	ZrO_2
	D14	80.4	0.1	0.1	6.9	12.5	35.6	(Gd,B)O+ ZrO_2
	D15	80.0	0.1	0	7.6	12.3	38.2	(Gd,B)O
1500°C, 30 min	D16	80.3	0.1	0	8.3	11.3	42.3	(Gd,B)O+ ZrO_2
	D17	64.4	0.4	0	34.2	0.8	97.7	ZrO_2
	D18	62.5	0	0.1	17.2	20.2	46.0	$Gd_2Zr_2O_7$
	D19	82.2	0.2	0	12.0	5.6	68.2	(Gd,B)O+ ZrO_2
1600°C, 15 min	D20	75.6	0.2	0.1	18.5	5.5	77.1	ZrO_2
	D21	75.6	0.3	0	21.0	3.1	87.1	ZrO_2
1600°C, 30 min	D22	61.2	0.4	0	37.7	0.7	98.2	ZrO_2
	D23	81.8	0.1	0.1	6.6	11.4	36.7	(Gd,B)O+ ZrO_2
1700°C, 15 min	D24	68.4	0.4	0	29.5	1.7	94.6	ZrO_2
	D25	62.4	0.1	0.1	3.2	34.2	8.5	Gd_2O_3
1700°C, 30 min	D26	63.3	0.1	0.8	17.7	18.1	49.4	$Gd_2Zr_2O_7$
	D27	69.4	0.3	0.1	28.9	1.3	95.7	ZrO_2

Cross-sections of GdO coated ZrB_2 tested at 1500°C for different exposure times are presented in Fig. 5.67. EDS results for the tested specimens are provided in Table 5.30. The oxide scale consisted of a (Gd,B)O layer with a thickness of ~226 µm and a chemical composition of ~11 at.% Gd, ~9 at.% Zr, and ~80 at.% O (Spec.D28). The interface zone of the coating/substrate revealed no visible oxidation for the substrate. This reflected the fact that no porous ZrO_2 scale was formed and the (Gd,B)O layer was in direct contact with the ZrB_2 substrate. Sparsely distributed dendrites of ZrO_2 were present in the (Gd,B)O phase. The chemical composition for these dendrites was found to be ~4 at.% Gd, ~33 at.% Zr, and ~63 at.% O (Spec.D29, Spec.D30).

The layer thickness of the (Gd,B)O scale increased to ~322 µm after 30 min of oxidation (Fig. 5.67b). The chemical composition corresponded to ~11 at.% Gd, ~9 at.% Zr, and ~80 at.% O (Spec.D31). Several bubbles with a diameter of up to 39 µm were found in the lower sections of the (Gd,B)O scale. Similar to the oxide scale after 15 min at 1500°C, no porous ZrO_2 scale was found at the interface zone, indicating the prevention of the oxidation of the ZrB_2 substrate. Several ZrO_2 grains with a diameter of ~9 µm and a chemical composition of ~1 at.% Gd, ~36 at.% Zr, and ~63 at.% O were found inside the (Gd,B)O phase (Spec.D32). The chemical composition for the (Gd,B)O phase at the interface zone revealed a composition of ~13 at.% Gd, ~3 at.% Zr, and ~84 at.% O at the interface zone (Spec. D33). In contrast, the (Gd,B)O layer at the uppermost section revealed a composition for ~10 at.% Gd, ~9 at.% Zr, and ~81 at.% O (Spec. D31).

Finally, the oxidation for 60 min at 1500°C revealed a ZrO_2 layer, containing large grains with an average size of ~12 µm at the interface zone of the coating/substrate (Fig. 5.67e-f). The chemical composition of the ZrO_2 grains was measured as ~36 at.% Zr and ~64 at.% O (Spec.D36). The (Gd,B)O scale was ~241 µm thick and revealed a chemical composition for~13 at.% Gd, ~5 at.% Zr, and ~82 at.% O (Spec.D34). Porous ZrO_2 can be observed at the former interface of the coating/substrate as well as several ZrO_2 grains with a diameter of ~12 µm. The uppermost section of the porous ZrO_2 is infiltrated by the (Gd,B)O phase, revealing a ~14 at.% Gd, 4 at.% Zr, and ~82 at.% O (Spec.D35).

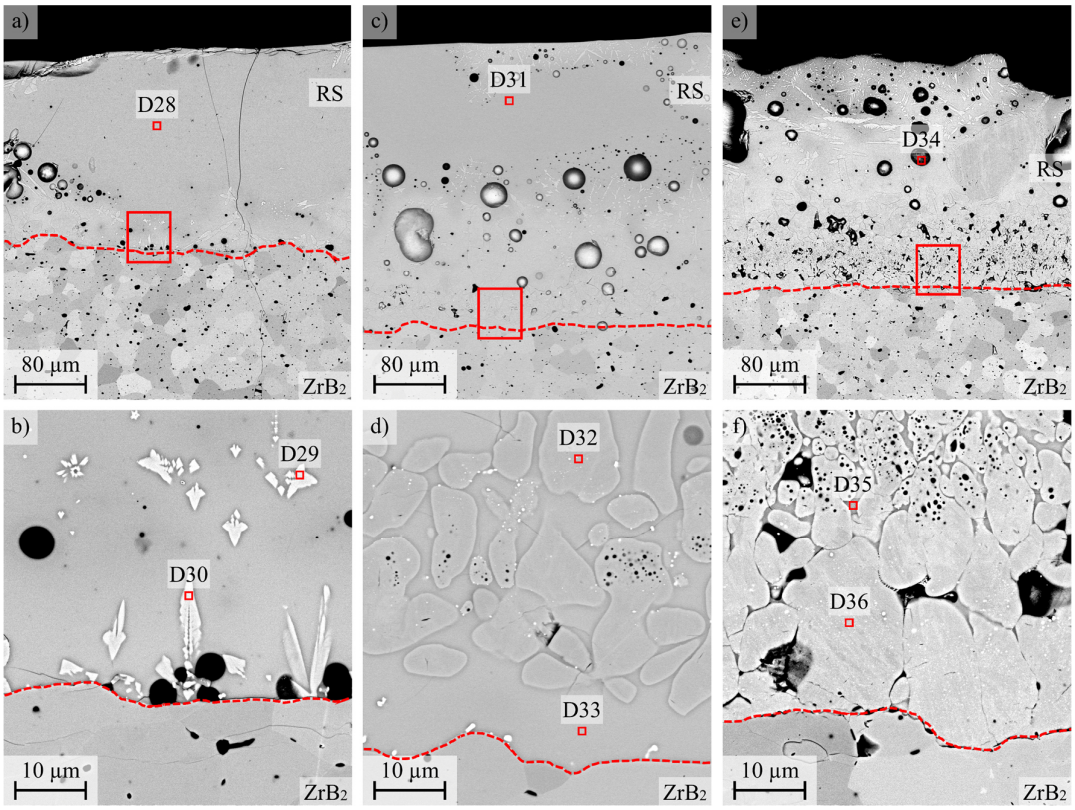

Fig. 5.67: BSE cross-sectional micrographs of GdO coated ZrB_2 after rapid oxidation (P/Q) at 1500°C: a-b) for 15 min; c-d) for 30 min; e-f) for 60 min

As mentioned above, a variation in Zr-content within the (Gd,B)O phase near the interface zone and at the uppermost section of the oxide scale was observed. BSE micrographs with increased contrast and acceleration voltage of 30 kV of the tested specimen for 30 min at 1500°C are presented in Fig. 5.68. The contrast information enables a clear differentiation of the two distinct (Gd,B)O solutions. The uppermost section appeared darker and contained ~9 at.% Zr (Spec.D37). The bright contrast indicates a (Gd,B)O phase near the interface zone, containing only ~4 at.% Zr (Fig. 5.68, Spec.D39). Interestingly, the Zr-content in the (Gd,B)O decreased in the presence of ZrO_2 grains/dendrites, which formed near the former interface zone of the coating/substrate (marked with a yellow dashed line).

Table 5.30: EDS spot analysis of GdO coated ZrB_2 after rapid oxidation (P/Q) at 1500°C for 15 min, 30 min, and 60 min (compare Fig. 5.67)

Condition	Spec.	O (at.%)	Hf (at.%)	W (at.%)	Zr (at.%)	Gd (at.%)	Zr/Gd	Phase (Estimated)
1500°C, 15 min	D28	80.1	0	0	8.8	11.1	44.2	(Gd,B)O+ZrO_2
	D29	62.7	0.3	0	34.0	3.0	91.9	ZrO_2
	D30	62.9	0.1	0	32.8	4.2	88.6	ZrO_2
1500°C, 30 min	D31	80.6	0.1	0	8.7	10.6	45.1	(Gd,B)O+ZrO_2
	D32	63.0	0.4	0	36.1	0.5	98.6	ZrO_2
	D33	82.8	0.1	0	3.7	13.4	21.6	(Gd,B)O+ZrO_2
1500°C, 60 min	D34	82.1	0	0	4.7	13.2	26.3	(Gd,B)O+ZrO_2
	D35	82.1	0	0.1	4.0	13.8	22.5	(Gd,B)O+ZrO_2
	D36	62.9	0.4	0	36.4	0.4	98.9	ZrO_2

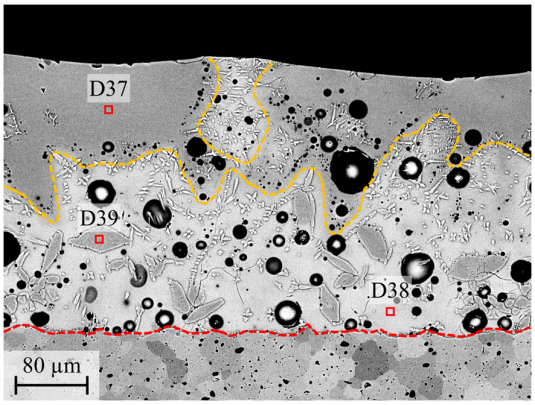

Fig. 5.68: BSE cross-sectional micrograph with increased contrast information of GdO coated ZrB_2 after rapid oxidation (P/Q) at 1500°C for 30 min

A fractured cross-section of the tested specimen for 60 min at 1500°C was analyzed to observe the globular bubbles inside the (Gd,B)O scale. The results are presented in Fig. 5.69. The micrographs expressively demonstrate the presence of B_2O_3 inside the globular bubbles. The chemical composition revealed ~98 at.% O, ~1 at.% C, and traces of Zr and Gd (Spec.D41). The chemical composition demonstrates that the filling is no carbon-based polymer. Furthermore, the bubbles are closed and not connected (no porous network), which prevents any infiltration by the embedding material. Therefore, the filling is assigned as B_2O_3 glass. In addition, sparsely distributed dendrites of ZrO_2 were found in the B_2O_3 bubbles (Spec.34). EDS results of the analyzed cross-sections (Fig. 5.68, Fig. 5.69) are provided in Table 5.31.

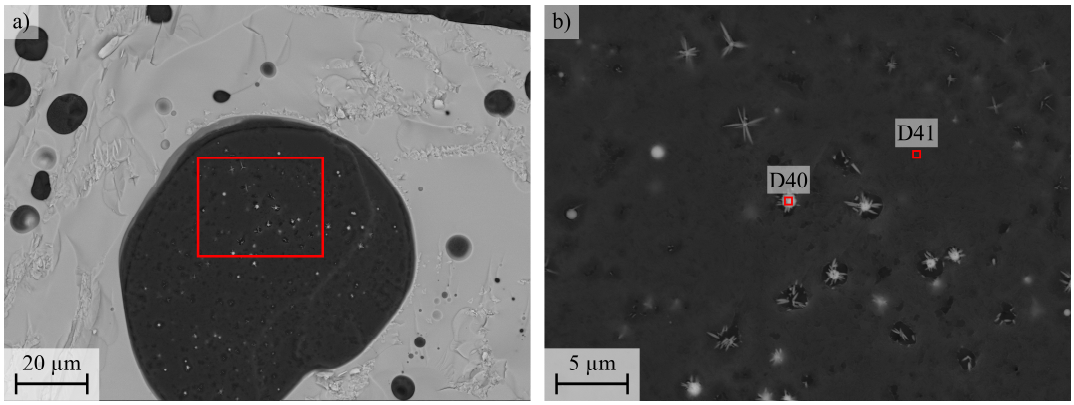

Fig. 5.69: Fractured cross-section of GdO coated ZrB_2 after rapid oxidation (P/Q) at 1500°C for 60 min: a) Overview of B_2O_3 filled bubble in (Gd,B)O scale; b) High magnification of ZrO_2 dendrites in the B2O3-filled bubbles

Table 5.31: EDS spot analysis of GdO coated ZrB_2 after rapid oxidation (P/Q) at 1500°C for 30 min and 60 min (compare Fig. 5.68 and Fig. 5.69)

Condition	Spec.	O (at.%)	Hf (at.%)	W (at.%)	Zr (at.%)	Gd (at.%)	Zr/Gd	Phase (Estimated)
1500°C, 30 min	D37	73.4	0	0	9.1	17.5	34.2	$Gd_2Zr_2O_7$
	D38	80.0	0	0	3.2	17.8	15.2	(Gd,B)O+ZrO_2
	D39	63.5	0	0	36.5	0	100	ZrO_2
1500°C, 60 min	D40	85.8	0	0	11.6	2.2	84.1	ZrO_2
	D41	98.8	0	0	0	0	-	B_2O_3

TEM analysis was performed for the GdO coated ZrB_2 specimen (AC), oxidized for 30 min at 1500°C. The lamella was prepared near the former coating/substrate interface to analyze the formed ZrO_2 grains in the (Gd,B)O phase (compare Fig. 5.68). A HAADF micrograph of a single ZrO_2 grain, embedded in the (Gd,B)O phase, is presented in Fig. 5.70. STEM-EDS results are provided in Table 5.32 and revealed a chemical composition of ~39 at.% Zr and ~61 at.% O for the ZrO_2 grains (Spec.D42) as well as ~18 at.% Gd, ~4 at.% Zr, and ~78 at.% O for the (Gd,B)O phase (Spec.D43). Interestingly, no reaction zone was observed at the interface of the ZrO_2 grain/(Gd,B)O phase (no core-shell structure). Electron diffraction patterns for the ZrO_2 grain are presented in Fig. 5.71 (Diffraction VII and VIII). Both diffraction patterns were assigned to m-ZrO_2. No diffraction reflections were detected for the (Gd,B)O phase (Fig. 5.71b, Diffraction IX). The result indicates an amorphous structure for the (Gd,B)O and aligns with the lack of reflections for Gd-containing phases via X-ray diffraction (compare Fig. 5.60). These results will be discussed extensively in the discussion section.

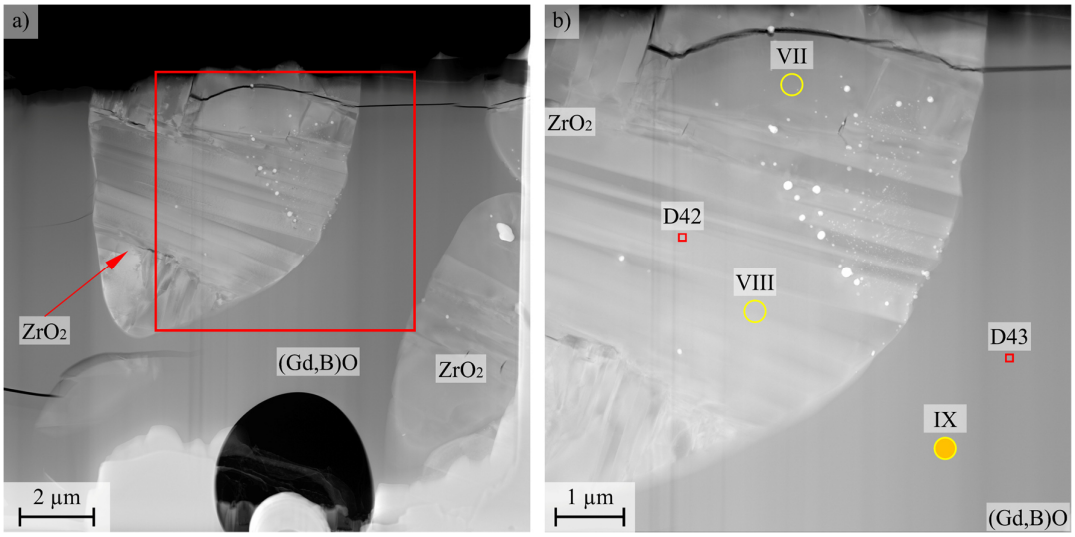

Fig. 5.70: *TEM HAADF micrographs of GdO coated ZrB_2 after rapid oxidation at 1500°C for 30 min: a) Overview of the TEM lamella with ZrO_2 grain in the (Gd,B)O phase; b) High magnification micrograph of the analyzed area with marked points for electron diffraction (Diffraction VII-IX)*

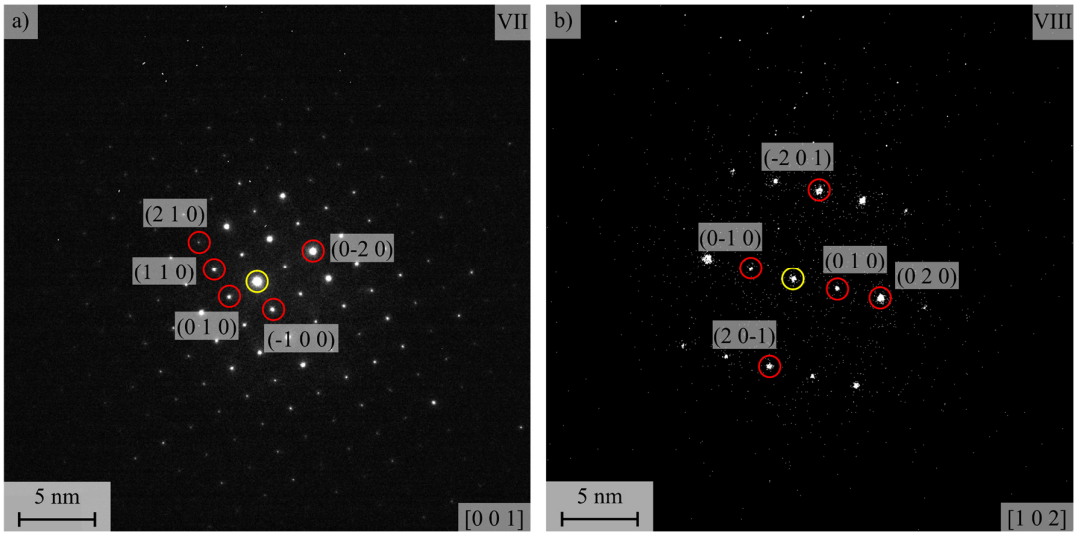

Fig. 5.71: *Electron diffraction pattern of the ZrO_2 grain inside the (Gd,B)O phase after rapid oxidation (P/Q) at 1500°C for 30 min: a) Diffraction VII, indicating m-ZrO_2; b) Diffraction VIII, indicating m-ZrO_2*

Table 5.32: *STEM-EDS spot analysis of the TEM lamella of GdO coated ZrB_2 after rapid oxidation (P/Q) at 1500°C for 30 min (compare Fig. 5.70)*

Condition	Spec.	O (at.%)	Hf (at.%)	W (at.%)	Zr (at.%)	Gd (at.%)	Zr/Gd	Phase (Estimated)
1500°C, 30 min	D42	61.2	0	0	38.8	0	100	ZrO_2
	D43	78.1	0	0	3.8	18.1	17.4	(Gd,B)O

The BSE cross-sectional micrographs of the specimens oxidized at 1600°C for 15 min to 60 min are presented in Fig. 5.72. Associated EDS results are provided in Table 5.33. A ~25 µm thick porous ZrO_2 scale (PS) formed after 15 min of exposure. The porous ZrO_2 scale was covered by a reaction scale (RS), consisting of (Gd,B)O with a chemical composition of ~16 at.% Gd, ~6 at.% Zr, and ~78 at.% O (Spec.D44). Enlarged grains of ZrO_2 with a chemical composition of ~37 at.% Zr and ~63 at.% O (Spec.D45) were present in the reaction scale. The thickness of the reaction scale was found to be ~41 µm in thickness.

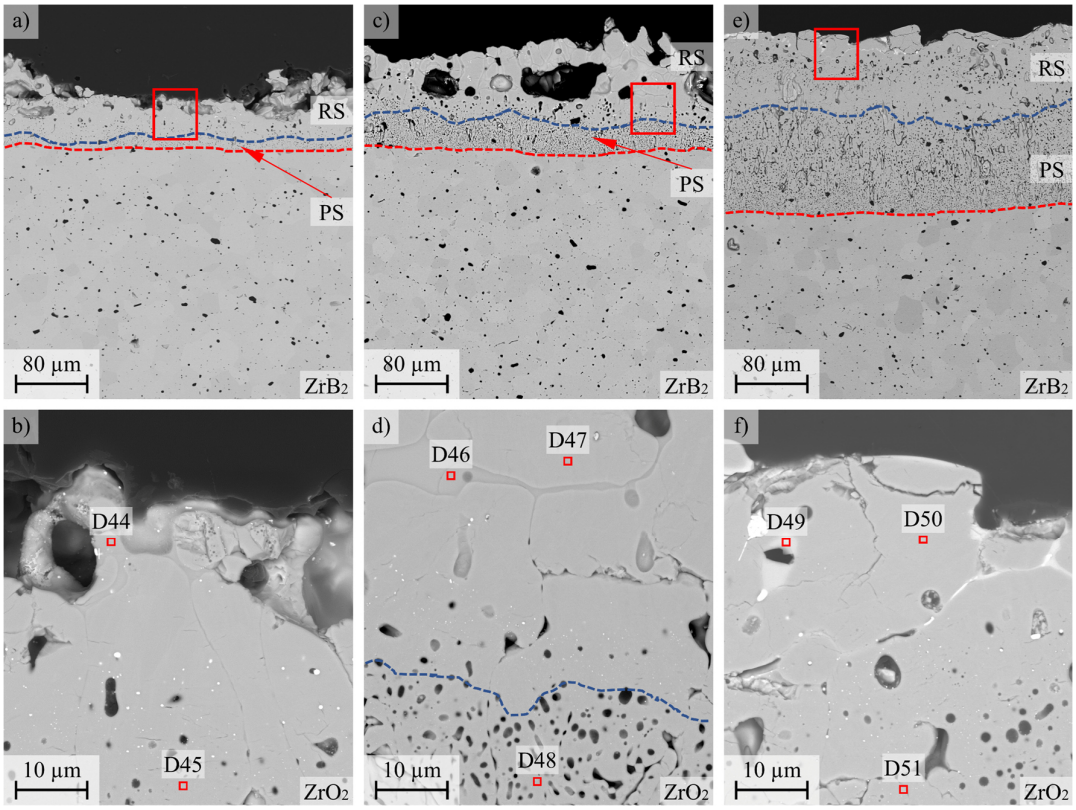

Fig. 5.72: BSE cross-sectional micrographs of GdO coated ZrB_2 after rapid oxidation (P/Q) at 1600°C: a-b) for 15 min; c-d) for 30 min; e-f) for 60 min

After 30 min at 1600°C (Fig. 5.72c-d) the reaction scale revealed a thickness of ~88 µm and consisted of (Gd,B)O with a chemical composition of ~15 at.% Gd, ~4 at.% Zr, and ~81 at.% O (Sped.D46). Grains of ZrO_2 with a composition for ~37 at.% Zr and ~63 at.% O (Spec.D47) were embedded in the (Gd,B)O phase. The reaction scale covered a porous ZrO_2 scale of ~33 µm in thickness (Spec.D48). Further, enlarged pores/holes were found within the reaction scale. The holes revealed a diameter of up to ~73 µm.

Finally, the exposure of 60 min at 1600°C (Fig. 5.72e-f) led to the formation of a reaction scale with a thickness of ~82 µm, covering a porous oxide scale of ~120 µm thick. Enlarged grains with the composition of ~37 at.% Zr and ~63 at.% O were identified as ZrO_2 grains (Spec.D50). Residual spots with (Gd,B)O were found at the surface and along the grain boundaries of enlarged ZrO_2 grains, revealing a composition for ~18 at.% Gd, ~11 at.% Zr, and ~71 at.% O (Spec.51).

Furthermore, sparsely distributed grains with the composition for ~13 at.% Gd, ~5 at.% W, ~4 at.% Zr, and ~78 at.% O were found at the uppermost section of the reaction scale (Spec.D49).

Table 5.33: EDS spot analysis of GdO coated ZrB_2 after rapid oxidation (P/Q) at 1500°C for 15 min, 30 min, and 60 min of oxidation (compare Fig. 5.72)

Condition	Spec.	O (at.%)	Hf (at.%)	W (at.%)	Zr (at.%)	Gd (at.%)	Zr/Gd	Phase (Estimated)
1600°C, 15 min	D44	78.9	0.1	0	5.5	15.5	26.2	(Gd,B)O+ZrO_2
	D45	62.1	0.3	0	37.4	0.2	99.5	ZrO_2
1600°C, 30 min	D46	80.9	0.1	0	3.6	15.4	18.9	(Gd,B)O+ZrO_2
	D47	62.2	0.4	0	37.1	0.3	99.2	ZrO_2
	D48	62.1	0.5	0.1	37.2	0.1	99.7	ZrO_2
1600°C, 60 min	D49	77.4	0.1	5.0	4.2	13.3	24.0	(Gd,W,Zr)O
	D50	62.4	0.5	0	36.8	0.3	99.2	ZrO_2
	D51	70.8	0.1	0	11.4	17.5	39.4	$Gd_2Zr_2O_7$

TEM analysis was performed for the GdO coated ZrB_2 specimen after oxidation for 30 min at 1600°C, revealing a porous and dense ZrO_2 scale as described above. The prepared lamella for the specimen can be seen in Fig. 5.73. The lamella contained two particular areas of interest. Area [S] represents the porous ZrO_2 scale (PS), covering the unoxidized ZrB_2 substrate. Area [T] shows the densified ZrO_2 scale at the uppermost section of the reaction scale (RS).

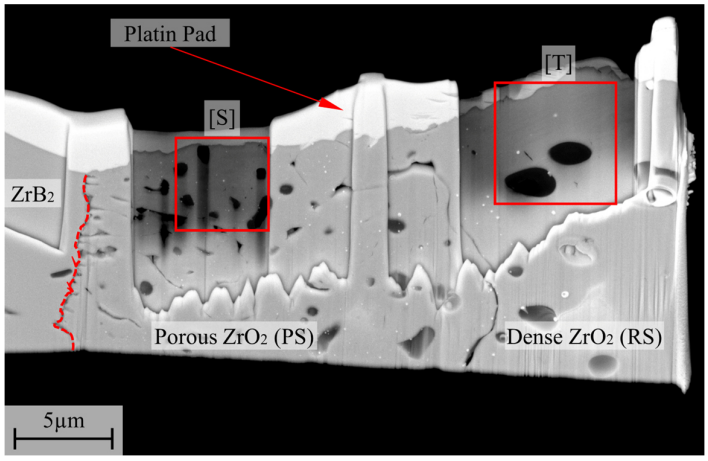

Fig. 5.73: TEM HAADF micrographs of GdO coated ZrB_2 after rapid oxidation (P/Q) at 1600°C for 30 min; Overview of the lamella with an area for porous ZrO_2 (area [S]) and for dense ZrO_2 (area [T])

HAADF micrographs of the area [S] and the area [T] are presented in Fig. 5.74. Detailed STEM-EDS results are provided in Table 5.34. Arbitrary-shaped crystals were found in the porous ZrO_2 scale (area [S]). The pores inside the PS were found to be ~0.5 µm in diameter. A micrograph

with increased magnification of the porous scale is presented in Fig. 5.74b. Fine pores of several nanometers were found in area [U]. The porous area contained a chemical composition of ~37 at.% Zr and ~63 at.% O (Spec.D52).

In contrast, the dense reaction scale in the area [T] revealed two pores with a diameter of ~1.8 µm. These are the only pores, found in the dense reaction scale of the analyzed area [T]. A micrograph with increased magnification of area [W] is presented in Fig. 5.74d. Parallel domains can be observed with a wide of up to ~285 nm. No other defects were found in the analyzed area [W].

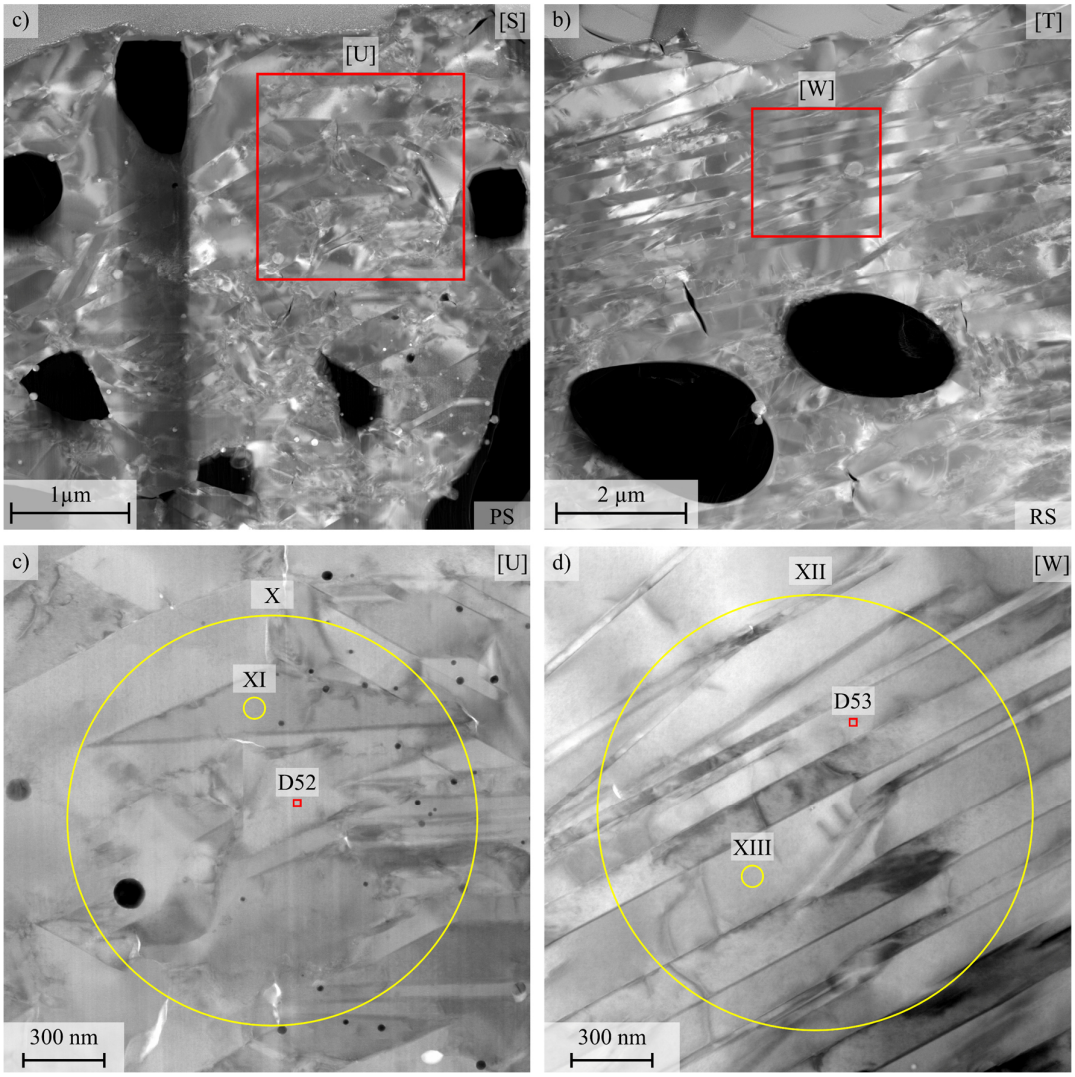

Fig. 5.74: HAADF micrographs of the TEM lamella of GdO coated ZrB_2 after rapid oxidation (P/Q) for 30 min at 1600°C: a) Porous ZrO_2 scale (PS) (area [S]); b) Dense ZrO_2 scale (RS) (area [T]); c) High magnification micrograph of porous ZrO_2 scale (PS) with marked SAED (RS) (area [U]); d) High magnification micrograph of dense ZrO_2 scale (RS) with marked SAED (area [W])

The electron diffraction pattern for the porous ZrO_2 scale and the dense reaction scale are presented in Fig. 5.75 and Fig. 5.76. In both cases, a Debye-Scherrer diffraction of multiple grains was performed to analyze the orientation of the crystals. Furthermore, a SAED of a single crystal was taken to assign the crystal structure. STEM-EDS results are provided in Table 5.34.

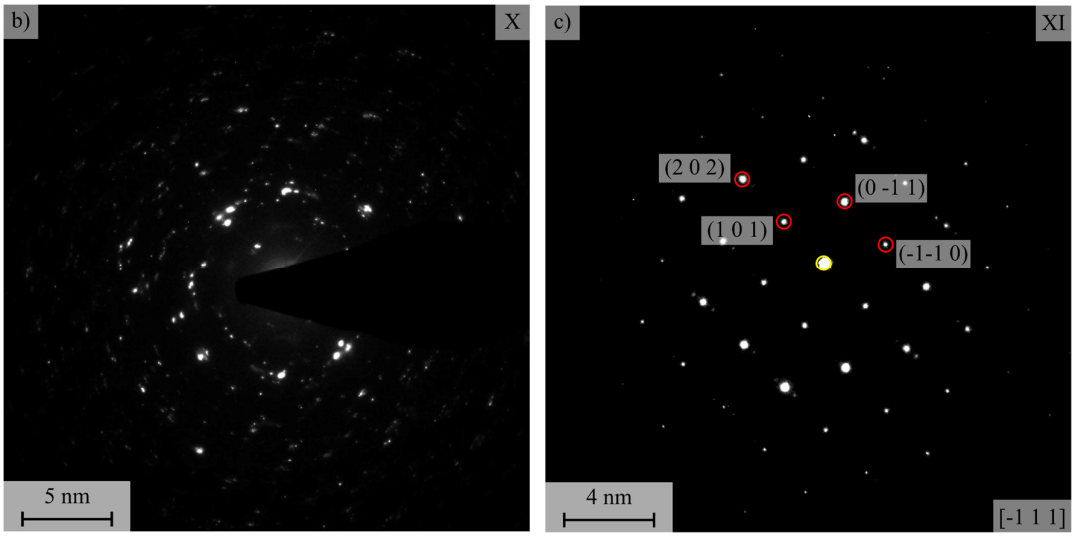

Fig. 5.75: Electron Diffraction of the porous ZrO_2 scale (PS) of GdO coated ZrB_2 after rapid oxidation (P/Q) for 30 min at 1600°C (compare Fig. 5.76b, area [U]): a) Debye-Scherrer diffraction of multiple grains with ring-type reflection (Diffraction X); b) SAED pattern with indicated m-ZrO_2

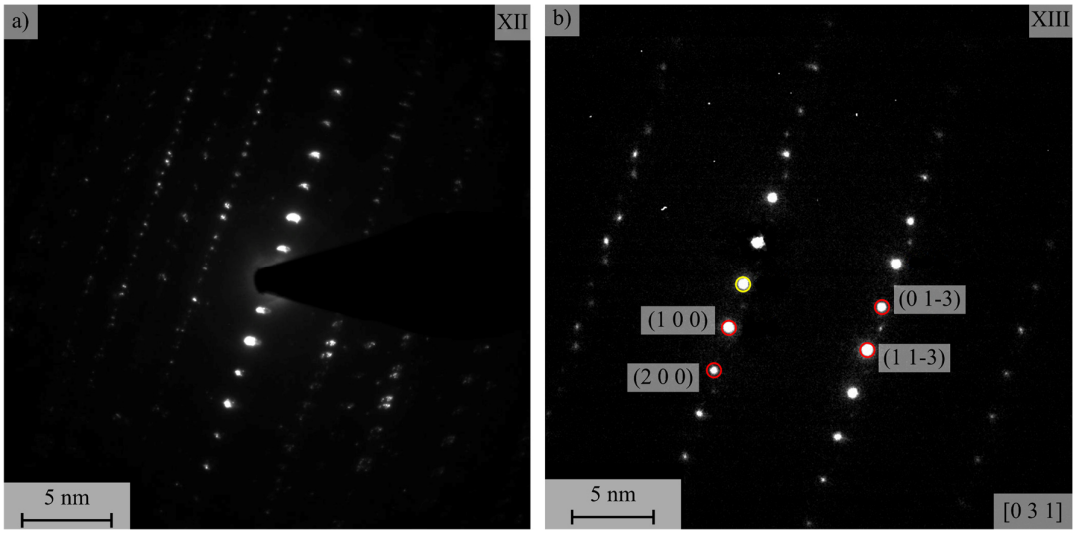

Fig. 5.76: Electron Diffraction of the dense ZrO_2 scale (RS) of GdO coated ZrB_2 after rapid oxidation (P/Q) for 30 min at 1600°C (compare Fig. 5.76d, area [W]): a) Debye-Scherrer diffraction of multiple grains with linear-type reflection (Diffraction XII); b) SAED pattern with indicated m-ZrO_2

Table 5.34: STEM-EDS spot analysis of the TEM lamella of GdO coated ZrB_2 after rapid oxidation (P/Q) at 1600°C for 30 min of oxidation (compare Fig. 5.74)

Condition	Spec.	O (at.%)	Hf (at.%)	W (at.%)	Zr (at.%)	Gd (at.%)	Zr/Gd	Phase (Estimated)
1600°C, 30 min	D52	63.6	0	0	36.4	0	100	ZrO_2
	D53	62.9	0.1	0	37.1	0	100	ZrO_2

The Debye-Scherrer diffraction pattern of the porous ZrO_2 can be seen in Fig. 5.75a. The pattern revealed a ring-type reflection (Diffraction X). This indicates multiple orientations of the diffracted crystals. The SAED pattern for a single crystal is presented in Fig. 5.75b. The reflection pattern was assigned for m-ZrO_2 (Diffraction XI), considering the STEM-EDS results (Spec.D52). In contrast, Fig. 5.76a shows the Debye-Scherrer diffraction pattern of the parallel domains inside the dense ZrO_2 reaction scale. The pattern revealed a linear-type reflection (Diffraction XII). This indicates similar crystal orientation for the parallel domains and might imply twinning in the dense reaction scale. However, the SAED pattern of a single domain is presented in Fig. 5.76b. The pattern was assigned to m-ZrO_2 (Diffraction XIII), considering the STEM-EDS results (Spec.D53).

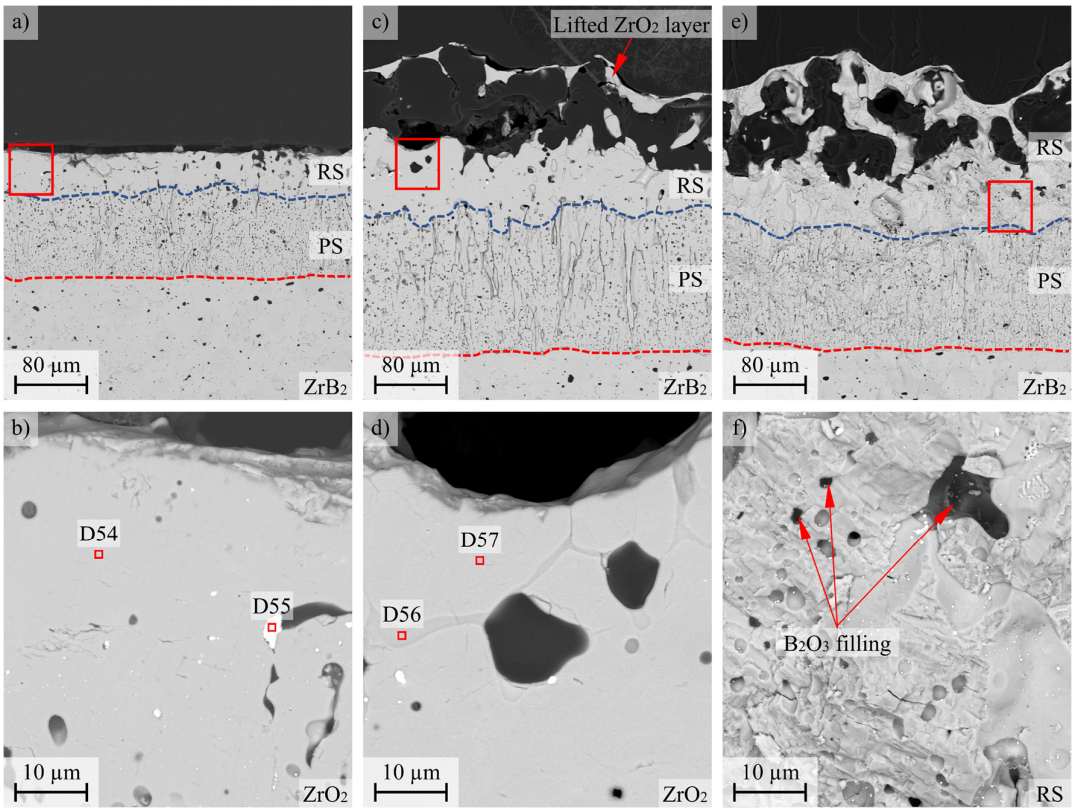

Fig. 5.77: BSE cross-sectional micrographs of GdO coated ZrB_2 after rapid oxidation (P/Q) at 1700°C: a-b) after 15 min; c-d) after 30 min; e-f) fractured cross-section after 30 min

Finally, the cross-sections of the GdO coated ZrB_2 (AC) after 15 min and 30 min at 1700°C are presented in Fig. 5.77. The associated EDS results are provided in Table 5.35. No comprehensive layer of (Gd,B)O was found after 15 min of oxidation. However, a dense reaction scale of ~38 µm in thickness consisted of enlarged ZrO_2 grains with a chemical composition for~37 at.% Zr and ~63 at.% O (Spec.D54). Sparsely distributed grains with a size up to ~3 µm were incorporated in the dense reaction scale. The EDS analysis revealed a chemical composition for ~2 at.% Gd, ~27 at.% W, and ~71 at.% O (Spec.D55).

The exposure of 30 min (Fig. 5.77c-d) led to an increase in the thickness of the reaction scale to ~72 µm and contained enlarged ZrO_2 grains (Spec.D57). Residuals of a Gd-containing phase could be found at the grain boundaries of the enlarged ZrO_2 grains. The chemical composition was measured as ~16 at.% Gd, ~15 at.% Zr, and ~69 at.% O (Spec.D56). The fractured cross-section of the specimen revealed several B_2O_3-filled porosities in the reaction scale (Fig. 5.77 e-f). Finally, a thin and detached ZrO_2 layer (~10 µm) formed at the uppermost section. As this layer was separated by a large gap (~73 µm) it was not considered as the reaction scale.

Table 5.35: EDS spot analysis of GdO coated ZrB_2 after rapid oxidation (P/Q) at 1700°C for 15 min and 30 min of oxidation (compare Fig. 5.77)

Condition	Spec.	O (at.%)	Hf (at.%)	W (at.%)	Zr (at.%)	Gd (at.%)	Zr/Gd	Phase (Estimated)
1700°C, 15 min	D54	62.5	0.5	0	36.8	0.2	99.5	ZrO_2
	D55	70.6	0	27.4	0	2.0	0	WO_3
1700°C, 30 min	D56	71.0	0.1	0.2	15.2	15.5	49.5	$Gd_2Zr_2O_7$
	D57	61.7	0.4	0	37.7	0.2	99.5	ZrO_2

5.4.4 Kinetic Calculations of GdO Coated ZrB_2

The oxide scale architecture formed on GdO coated ZrB_2 can be subdivided into a reaction scale (RS), containing (Gd,B)O liquid, Gd_2O_3 and/or dense ZrO_2, as well as an underlying porous ZrO_2 scale (PS). The average thicknesses of the reaction scale, the porous ZrO_2 scale, and the total oxide scale TS were measured as described in Fig. 4.13. The percentage of porous ZrO_2 scale thickness to the total oxide scale thickness was determined and the parabolic oxidation rate constant for the porous ZrO_2 scale was calculated for each tested specimen. All the results are provided in Table 5.36.

Table 5.36: Oxide scale thickness and calculated parabolic rate constant of GdO coated ZrB_2 for the porous ZrO_2 scale after rapid oxidation (P/Q)

Condition	Temperature	Time (min)	RS (µm)	PS (µm)	TS (µm)	PS/TS (%)	ln($K_{P(PS)}$)
GdO coated (AC)	1500°C	15	226	0[1]	226	0	0[2]
		30	322	0[2]	322	0	0[2]
		60	241	18	259	6.9	5.8
	1600°C	15	41	25	66	37.8	7.8
		30	88	33	121	27.3	7.7
		60	82	120	202	59.4	9.6
	1700°C	15	38	107	145	73.8	10.7
		30	72	162	234	69.2	10.9

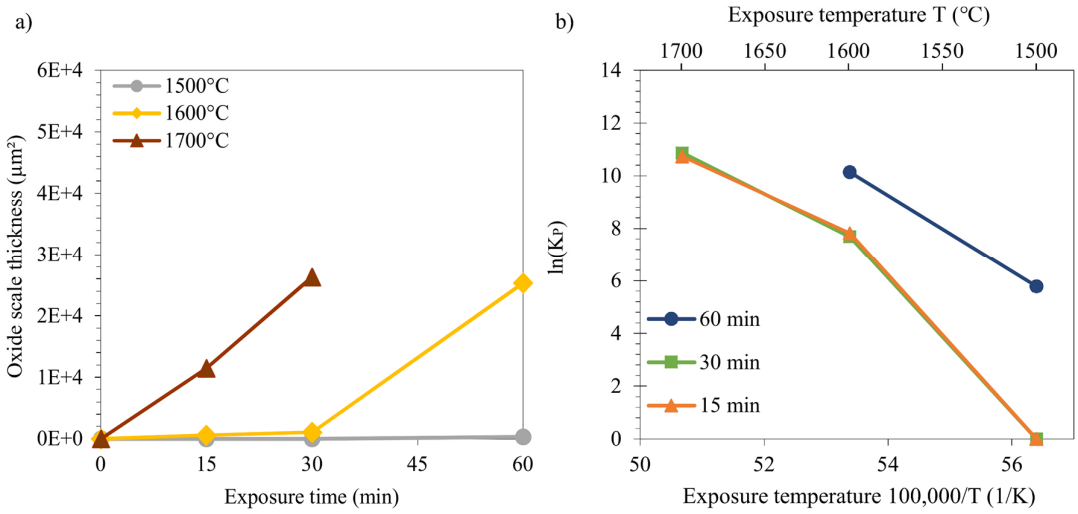

Fig. 5.78: a) Porous ZrO_2 oxide scale thickness squared vs. the exposure time; b) Arrhenius plot for the oxidation of GdO coated ZrB_2 for 15 min, 30 min, and 60 min at different temperatures between 1500°C to 1700°C

The porous ZrO_2 scale squared over the exposure time is presented in Fig. 5.78a. According to the differentiation equation of linear-parabolic oxidation kinetics by Deal and Grove, the squared oxide scale thickness enables the determination of the parabolic rate constant (Fig. 2.11, Equ. 2.14) [70, 138]. Hereby, the slope of the plots corresponds with the oxidation rate constant. As visible in Fig. 5.78a, protection against oxidation was achieved for an exposure of up to 30 min at 1500°C. Further exposure increased the oxidation rate constant. At 1600°C, the oxidation follows parabolic oxidation with significantly reduced parabolic rate constants up to 30 min of

[1] Parabolic rate constant K_P (µm/min) was set to 1 (ln(1)=0) to conform with the mathematical laws for calculating the kinetics and activation energies (for conditions without evaluable PS)

exposure (steady slope). A transition of the oxidation process can be seen after 30 min of oxidation (abrupt increase of the rate constant). Finally, the oxidation at 1700°C follows constant parabolic oxidation kinetics up to 30 min of oxidation with increased rate constants compared to the oxidation at 1500°C and 1600°C.

Further, the activation energies for the oxidation process in the temperature regime of 1500°C to 1600°C and 1600°C to 1700°C for 15 min, 30 min, and 60 min were calculated by using Equ. 2.15. The results are provided in Table 5.37. Further, Fig. 5.78b presents an Arrhenius plot, which visualizes the calculated activation energies (corresponds with the slope of the plots, compare Fig. 2.10c). Similar activation energies were found for the exposure times of 15 min and 30 min in the temperature regime of 1500°C to 1700°C (identical oxidation rate constants were calculated). An enhanced dependency of the oxidation rate constants on the temperature can be seen in the regime of 1500°C to 1600°C, which corresponds with increased activation energy (increased slope of the plots)

The activation energies decrease in the temperature regime of 1600°C to 1700°C (flatter slope). However, the oxidation rate constants increase with respect to the temperature and indicate an acceleration of the oxidation. The reason for this peculiar behavior will be thoroughly argued in the discussion section.

Table 5.37: Calculated activation energies of GdO coated ZrB_2 for rapid oxidation (P/Q) in the temperature regime of 1500°C to 1600°C and 1600°C to 1700°C for 15 min, 30 min, and 60 min

	Exposure Time (min)	$E_{A1500\text{-}1600}$ (kJ/mol)	$E_{A1600\text{-}1700}$ (kJ/mol)
GdO coated (AC)	15	2161	894
	30	2123	978
	60	1048	-

6 Discussion

6.1 Effect of HfO_2 Coatings on ZrB_2

This section is based on the published paper "Hafnium oxide coating to improve the oxidation behavior of zirconium diboride" (https://doi.org/10.1016/j.jeurceramsoc.2024.116774) by Förster et al. Content and texts may differ in part from the publication [137].

6.1.1 Processing of Reliable HfO_2 Coatings on ZrB_2

6.1.1.1 Reactive Sputtering of HfO_2 Coatings on ZrB_2

Considering the model for reactive sputtering by Berg et al., the sputtering rate and consequently the deposition rate on the substrate decreases with increasing oxygen gas flow. This can be explained by the formation of oxides at the target surface (poisoning) with a decreased sputtering rate (compare Fig. 2.18, Equ. 2.23, Equ. 2.24). Thereby, an abrupt drop in the sputtering condition can be seen at a specific oxygen flow [103-105]. Regarding the parameter study of reactive sputtered HfO_2 coatings (Fig. 5.5), the forecasted progression of the deposition rate by Berg et al. can be observed for the reactive sputtered HfO_2 coatings. An oxygen gas flow of ϕ_{O2}=4-5 sccm induced an abrupt drop in the deposition rate (Fig. 5.6). Gas flows >5 sccm led to oxidic sputtering conditions with a low deposition rate of ~2 µm/h and a chemical composition for HfO_2 (Fig. 5.7b, Spec.B1). Gas flows ≤4 sccm revealed metallic-like coatings with an oxygen deficit of <32 at.% and a deposition rate of ~7 µm/h. As mentioned in the literature, reactive sputtering processes can not be controlled reliably by the oxygen gas flow rather than with the partial pressure of oxygen (pO_2) during sputtering (Fig. 2.19b) [105]. Since the measurement of the partial pressure was not possible during the deposition, the reactive sputtering process was performed with 5 sccm and extended processing time of ~240 min (oxidic sputtering parameters, poisoned target). Coating experiments with 5 sccm have been carried out multiple times (Run2-Run4) to verify the reproducibility with a constant deposition rate of ~2 µm/h (Table 5.3). Working exclusively in the oxidic area with a poisoned target ensured constant sputtering conditions of full oxidized HfO_2, forming an oxidic coating at the substrates (compare Fig. 2.19).

Surface preparation plays an important role in the adhesion of thin PVD magnetron sputtered coatings. This depends on the combination of the substrate and coating material [106]. A significant effect of the surface roughness of ZrB_2 on the adhesion of the reactive magnetron sputtered coating can be observed for the combination of HfO_2/ZrB_2. Whereas polished surfaces (3 µm grit size) caused spallation of the applied HfO_2 coating after exposure to the atmosphere, ground surfaces (10 µm grit size) prevented the spallation. The reactive sputtered HfO_2 coating might anchors physically into the rough surface of the substrate, which increases the adhesive strength at the coating/substrate interface and prevents spallation after exposure to atmosphere. It is hypothesized that certain surface roughness for the substrate must be provided for HfO_2 coatings to ensure adequate adhesion. More roughness might lead to the spallation of the coating by inducing internal stresses inside the coating [101, 137]. Further investigation needs to be carried out for HfO_2 coatings on ZrB_2 and other diboride-based materials for detailed information about the effect of the roughness.

6.1.1.2 Vacuum-annealing of HfO_2 Coated ZrB_2 at ~1800°C

The X-ray diffraction pattern of the HfO_2 coatings on ZrB_2 revealed widened reflection peaks for m-HfO_2, which might indicate a semi-crystalline coating (see Fig. 5.7a). According to Berg et al., reactively sputtered coatings usually consist of chemically reacted compounds (i.e. HfO_2) and a non-crystallized solid solution of the target material, doped with the reactive gas (i.e. HfO_x) [103-105]. To induce crystallization of the reactive sputtered coating, vacuum-annealing was performed in a graphite furnace. The distinct reflection peaks for the X-ray diffraction pattern after vacuum-annealing proved the crystallization process during the annealing procedure (Fig. 5.9a). Contrary to the expectations, it formed oxygen-doped HfC ($HfC_{(0.84)}O_{(0.16)}$) instead of m-HfO_2. Various species of HfCO were revealed by cross-sectional analysis and EDS (Fig. 5.9b, Spec.B02-B04). The assumed mechanisms during vacuum-annealing of HfO_2 coated ZrB_2 is presented in Fig. 6.1, considering the loss of oxygen during ramping [137].

Santucci et al. investigated the behavior of reactive sputtered WO_3 films during vacuum heat treatment at temperatures >300°C. Weakly linked oxygen in the reactive sputtered coating left the system during vacuum heat treatment and induced the reduction of the oxide scale [141]. A similar effect was observed for Nb_2O_5 coatings during vacuum heat treatment at 300°C for 30 min [112]. Further, Rodenbücher et al. investigated the formation of HfC by oxygen-doped HfO_x layers at 700°C. Oxygen vacancies in the oxygen-doped HfO_x reduced the needed activation energy for the reaction of HfC [142]. The sublimation of graphite particles during vacuum-heat treatment in the range of 1500°C to 1900°C was observed by Long et al. In consideration, this might admit the following process for HfO_2 coatings on ZrB_2 during vacuum-annealing in a graphite furnace. The ramping procedure in vacuum (~5°C/min, compare Fig. 4.6) might induce the loss of weakly bonded oxygen in the reactive sputtered HfO_2 coating. This would explain the significant reduction of oxygen from initial ~65 at.% (AC, Fig. 5.7b, SpecB01) to ~5 at.% (VA, Fig. 5.9b, Spec.B02-B05). Free carbon could form during vacuum heat treatment at 1800°C[1] by the sublimation of carbon particles of the graphite furnace parts. The oxygen-doped HfO_x coating would be carburized and form HfCO. A general reaction an concept for the formation of a HfCO scale by an oxygen-doped HfO_x coating during vacuum-annealing in a graphite furnace is proposed by Equ. 6.1 (compare Fig. 4.6) [137].

[1] Compare Fig. 4.6, vacuum-annealing. The process was carried out for 60 min at 1800°C and for 180 min at 1750°C due to a malfunction of the thermocouple

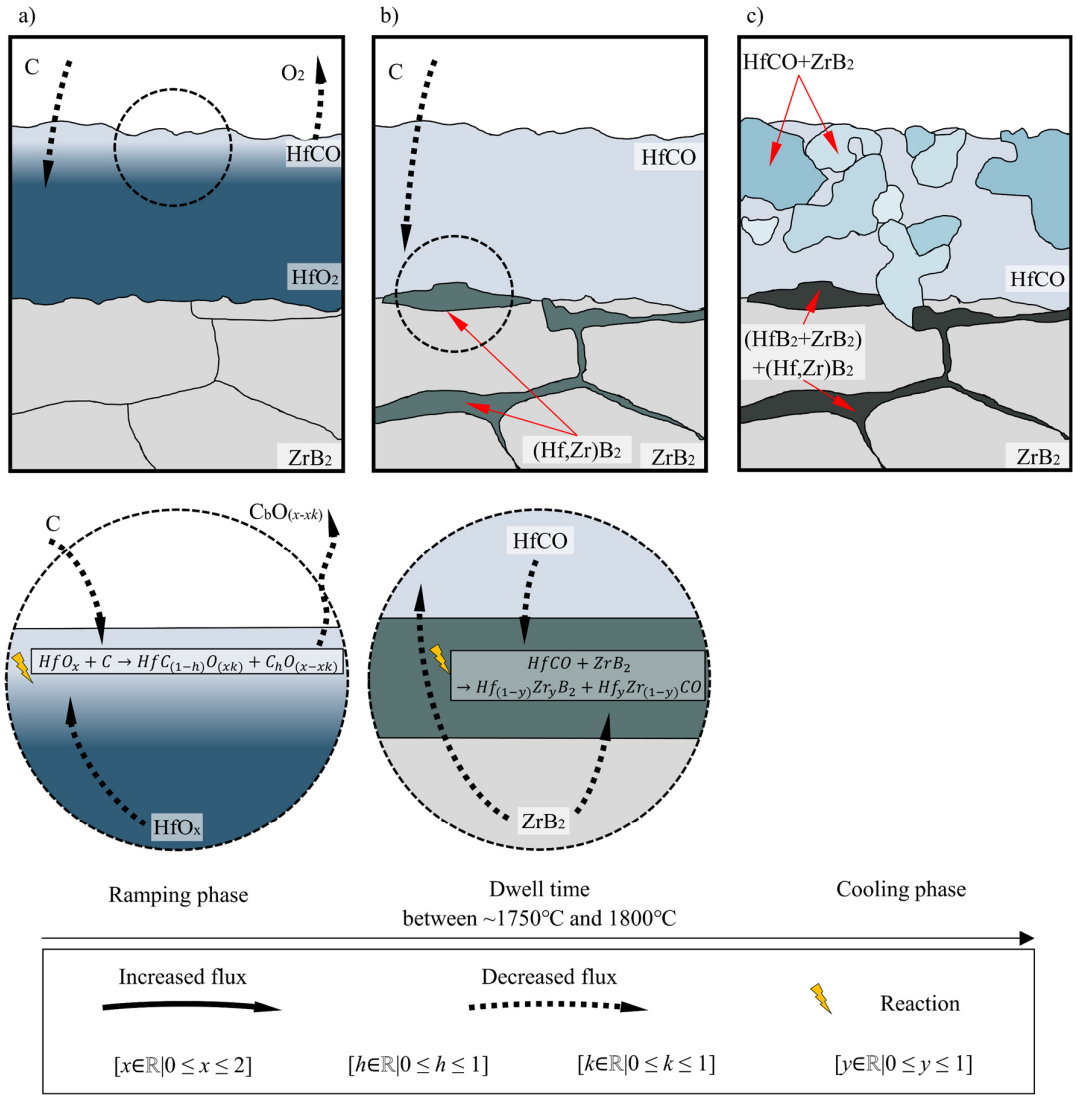

Fig. 6.1: Proposed model for the formation of a multi-phase HfCO scale during vacuum-annealing of HfO_2 coated ZrB_2 in a graphite furnace: a) Reduction and carburization of the HfO_2 coating during ramping procedure (T~1500°C); b) Diffusion of HfCO along the grain boundaries of ZrB_2 and solid solution formation (T~1800°C); c) Vacuum-annealed HfO_2 coating at atmosphere (T~20°C)

$$HfO_x + C \rightarrow HfC_{(1-h)}O_{xk} + C_hO_{(x-xk)} \qquad \text{Equ. 6.1}$$

with $[x \in \mathbb{R} \mid 0 < x < 2]$, $[h \in \mathbb{R} \mid 0 \leq h \leq 1]$, $[k \in \mathbb{R} \mid 0 \leq k \leq 1]$ inducing the formation of free Hf (x=2, h=1, k=0), HfC (x=2, h=0, k=0), or HfCO. (E.g. $HfC_{(0.84)}O_{(0.16)}$ (x=0.32, h=0.16, k=0.5).

The reaction of HfO_2 and C (Equ. 6.1) is depicted Fig. 6.1a. EDS analysis confirmed the presence of Zr inside the HfCO scale as well as the presence of Hf-rich phases along the grain boundaries of the ZrB_2 grains near the interface zone. This might emphasize the diffusion of Zr cations into the HfCO scale as well as the diffusion of Hf cations into the ZrB_2 along the grain boundaries

during vacuum-annealing. Boron can not be quantified via EDS in a reliable way. However, the diffusion of boron into the HfCO scale can not be excluded. The diffusion of Zr and B (represented as ZrB_2 in the schematic) into the HfCO scale is illustrated in Fig. 6.1b [137].

The ternary phase diagram of the system Hf-Zr-B was investigated by Pan et al. and proves the formation of a boron-based solid solution $(Hf_{0.5}Zr_{0.5})B_2$ in the temperature range of 597°C to 3230°C. Below 597°C the solid solution decomposes into HfB_2 with a solubility of ~11 at.% Zr as well as ZrB_2 with a limited solubility of up to ~6 at.% Hf [143]. Minor reflections in the X-ray diffraction pattern of vacuum-annealed specimens indicated the presence of ZrB_2, HfB_2 or a boron-based solid solution of Zr and Hf (Fig. 4.2b, Fig. 5.9a). According to the EDS analysis, a corresponding chemical composition $(Hf_{(1-a)}Zr_a)B_2$ might form along the grain boundaries of the ZrB_2 substrate (Fig. 5.9b, Spec.B05). The formation of mixed borides and zirconium containing carbonates is proposed Equ. 6.2 [137].

$$HfCO + ZrB_2 \rightarrow Hf_{(1-y)}Zr_yB_2 + Hf_yZr_{(1-y)}CO \qquad \text{Equ. 6.2}$$

with $[y \in \mathbb{R} \mid 0 \leq y \leq 1]$ inducing HfB_2 and ZrCO (y=0), ZrB_2 and HfCO (y=1, no reaction), or a diboride-based solid solution and a mixed carbonate. During cooling below 597°C the boron-based solid solution might decompose and form HfB_2 with dissolved Zr ($(Hf,Zr)B_2$) (compare Fig. 5.9, Spectrum B05; Fig. 6.1b).

6.1.2 Oxidation Mechanisms of HfO_2 Coated ZrB_2

The oxidation of HfO_2 coated ZrB_2 leads to the formation of a dual layer oxide scale, consisting of a $(Hf,Zr)O_2$ layer at the uppermost section and an underlying porous ZrO_2 scale. Corresponding oxidation mechanisms for the different temperature ranges and exposure times will be discussed in the following.

6.1.2.1 Ramped Oxidation of HfO_2 Coated ZrB_2 (AC vs. VA) at 1500°C

Ramped oxidation (R/C) experiments of HfO_2 coated ZrB_2 (AC, VA) have shown a beneficial effect on the oxidation resistance of ZrB_2. The applied coating is successful in reducing the porous ZrO_2 scale growth during oxidation at 1500°C. It can be assumed that the dense coating enforces vacancy diffusion or interstitial diffusion of oxygen molecules along the applied coating thickness rather than accelerated Knudsen diffusion through the pores and cracks of porous ZrO_2. It implies the fact that as long as a dense m-HfO_2 is present, the oxidation will be controlled by diffusion through the dense coating [137, 144].

The comparison of AC and VA specimens demonstrated the effect of vacuum-annealing on the boria coverage, the microstructure of the oxide scale, and the chemical composition of the uppermost reaction scale (Fig. 5.10 to Fig. 5.14). As mentioned above, the HfO_2 coating was a semi-crystalline coating with amorphous content after deposition (Fig. 5.7a). The oxidation of HfO_2 coated ZrB_2 (AC) would induce accelerated crystallization of the coating during oxidation. Consequently, the rapid crystallization might cause inner stresses and induce partial spallation of the coating as well as the formation of cracks across the coating thickness (Fig. 5.12). Oxygen molecules could pass the ruptured m-HfO_2 scale. As a result, a ruptured solid coating would not prevent

the oxidation of ZrB_2 and would induce the formation of liquid B_2O_3 at the interface zone. Further, the m-HfO_2 reacted with the formed porous ZrO_2. Both oxides are soluble in each other [109]. A significant enrichment of the reaction scale by Zr would have the consequence of forming m-$(Hf,Zr)O_2$ with reduced transition temperatures <1500°C (instead of 1790°C for HfO_2, compare Fig. 3.1b). This admits the phase transition from m-$(Hf,Zr)O_2$ to t-$(Hf,Zr)O_2$ and the formation of several defects, cracks, and pores inside the reaction scale [137].

In comparison, the preceding vacuum-annealing procedure induced a cautious crystallization of the coating and prevented cracks. As mentioned above, the coating experienced a phase transformation from HfO_2 to HfCO during vacuum-annealing (Fig. 5.9). The interdiffusion of Hf cations along the grain boundaries of ZrB_2 and the formation of diboride-based solid solutions increased the adhesion of the uppermost coating to the substrate (chemically bonded to the substrate). This prevented the partial spallation of the coating during oxidation. As mentioned above, the reduction of oxygen in oxide scales during vacuum-annealing at temperatures >300°C was observed in multiple cases (WO_3, Nb_2O_5). The heat treatment in an oxygen rich atmosphere (e.g. synthetic air or lab air) induced the re-oxidation of the former oxides [141]. In consideration of this behavior, it is proposed that the formed HfCO (carburized HfO_2 scale with oxygen deficit) might re-oxidize to m-HfO_2 during the initial seconds of oxidation at temperatures ≥1500°C. The Equ. 6.3 is proposed to describe the oxidation of the HfCO scale, concerning the well-known oxidation process of baseline HfC [137, 141, 145, 146].

$$HfCO + O_2 \rightarrow HfO_2 + CO \qquad \text{Equ. 6.3}$$

The dense and re-oxidized m-HfO_2 scale would assure diffusion-controlled oxidation as mentioned above. Oxygen vacancies inside the m-HfO_2 might enable vacancy diffusion of oxygen molecules through the protective scale. In addition, interstitial diffusion of oxygen through the applied scale might be induced due to the elevated temperatures. Both mechanisms would decelerate the oxygen mobility to the oxidation front of ZrB_2 and would offer a certain oxidation protection of the substrate [72, 147]. Once porous t-ZrO_2 and liquid B_2O_3 form underneath the m-HfO_2, boria might accumulate beneath the dense mixed oxide scale. The accumulation of liquid B_2O_3 exerts pressure on the m-HfO_2 scale and would enforce its destruction, creating defects like cracks (Fig. 5.16). These cracks would then act as channels and enable the evaporation of the liquid B_2O_3 (Fig. 5.15b-c). The formation of a mixed oxides m-$(Hf,Zr)O_2$ and the enrichment of the reaction scale due to Zr diffusion would induce the phase transition to t-$(Hf,Zr)O_2$ (lowered transition temperature <1500°C with increased Zr content). As a consequence, the transition will induces several defects and cracks inside the reaction scale. From this moment on, oxygen could pass the ruptured oxide scale and react with the ZrB_2 substrate (Fig. 5.17). Therefore, the ruptured reaction scale will not offer diffusion-controlled oxidation for extended oxidation time [109, 137, 148].

However, grain boundary diffusion of Hf cations into the ZrB_2 and the cautious crystallization of the applied coating during vacuum-annealing prevented partial spallation of the coating during oxidation and improved its protective nature. Therefore, vacuum-annealing was found to be a key processing step for improved performance.

6.1.2.2 Rapid Oxidation of HfO_2 Coated ZrB_2 (VA) at 1500°C

The assumed oxidation mechanism of HfO_2 coated ZrB_2 (VA) at 1500°C for rapid oxidation (P/Q) with a thermal shock is presented in Fig.6.2. The short-term oxidation (red frame) is extrapolated based on the results of long-term oxidation ≥60 min. As presented in Fig. 5.9b and Fig. 6.1c, the dense coating contained multiple phases of HfCO with varying amounts of dissolved Zr after vacuum-annealing (up to ~24 at.% Zr, Fig. 5.9, Spec.B02-B04). The dense coating inhibited the oxygen mobility to the underlying substrate by forcing volume diffusion of oxygen molecules during the initial stages of oxidation (reduced diffusivity of oxygen molecules through the dense coating compared to Knudsen diffusion through the porous ZrO_2 scale) [137, 144, 145, 149].

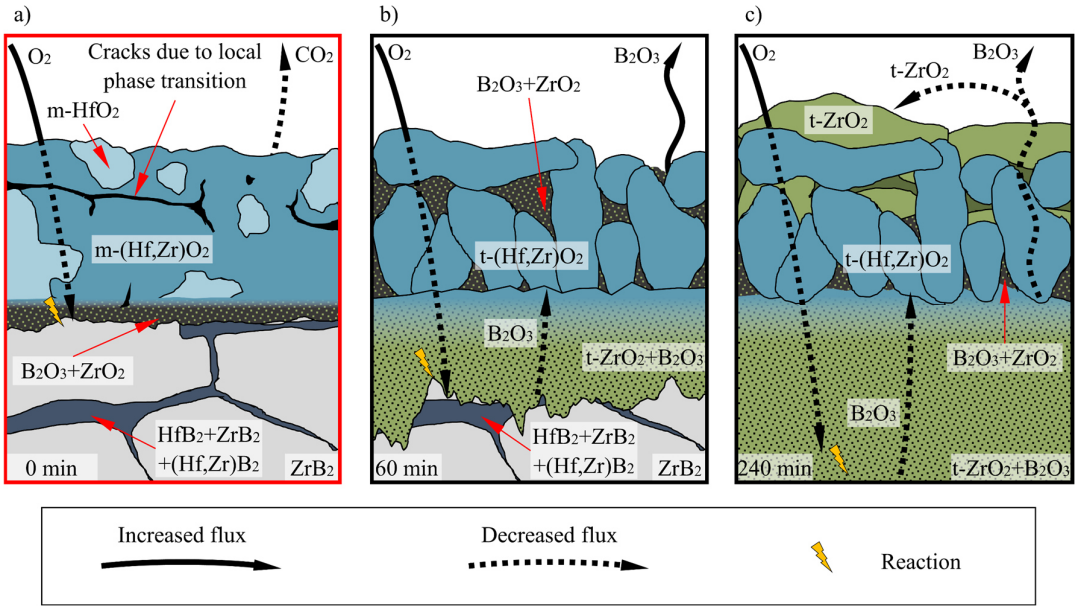

Fig. 6.2: Proposed oxidation mechanisms of HfO_2 coated ZrB_2 (VA) at 1500°C: a) after 0 min of oxidation (extrapolation); b) after 60 min of oxidation; c) after 240 min of oxidation

According to the oxidation mechanism of HfC, the HfCO scale will oxidize to m-HfO_2, following the proposed reaction in Equ. 6.3. Gaseous reaction products such as CO would leave the system, inducing the decarburization of the scale [137, 146, 150]. The dense scale would prevent the oxygen mobility to the reaction front of ZrB_2 by volume diffusion and causing passive oxidation for a distinct oxidation period [147]. The diffusion of Zr cations into the HfCO scale might induce the formation of m-$(Hf,Zr)O_2$ during oxidation. Minor cracks could appear in m-$(Hf,Zr)O_2$, weakening the reaction scale (Fig. 6.2a) [137].

Henceforth, the oxidation mechanism simply follows as it was explained in ramped oxidation case. Once, oxygen diffuses through the protective scale via vacancy diffusion or interstitial diffusion, the underlying ZrB_2 will oxidize and form B_2O_3 liquid and porous t-ZrO_2. The liquid B_2O_3 will accumulate beneath the dense m-HfO_2 scale and exerts pressure. Finally, the liquid detaches the protective coating from the porous t-ZrO_2 scale. This will introduce large cracks, running through the entire m-HfO_2 scale from the surface to the porous t-ZrO_2 (Fig. 5.20a-b). Boria would leave the system through the cracks and evaporate at the surface. The reaction of the porous t-

ZrO_2 and the ruptured m-HfO_2 scale leads to the formation of a Zr-rich reaction scale. Once the Zr content of the reaction scale exceeds ~16 at.%, the phase transition of the reaction scale from monoclinic to tetragonal structure is inevitable at 1500°C. The formation of t-(Hf,Zr)O_2 induces more defects. This entire process ends up with increased oxygen mobility, reaction-controlled oxidation at the oxidation front of ZrB_2, and more boria evaporation (Fig. 6.2b) [137].

It is well known that ZrO_2 is soluble in B_2O_3 for up to 12 mol% [78, 151]. Dissolved ZrO_2 might precipitate inside and on top of the reaction scale during B_2O_3 evaporation, forming a dense secondary t-ZrO_2 scale as an uppermost layer. With respect to time, pores and cracks between the single grains of the reaction scale became filled by t-ZrO_2 (Fig. 6.2c). The continuous precipitation of secondary t-ZrO_2 at the surface increased the thickness of the reaction scale from ~12 µm after 60 min to ~16 µm after 240 min by forming a comprehensive t-ZrO_2 scale at the ruptured reaction scale (Table 5.8, Fig. 5.20c-d). It is expected, once the reaction scale is covered by a dense layer of secondary t-ZrO_2, the oxide scale might be protective again by enforcing volume diffusion through the dense and solid oxide scale [137].

6.1.2.3 Rapid Oxidation of HfO_2 Coated ZrB_2 (VA) at 1600°C and 1700°C

The proposed oxidation mechanism for HfO_2 coated ZrB_2 (VA) at 1600°C is presented in Fig. 6.3. Since no short-term experiments for less than 60 min were performed with HfO_2 coated ZrB_2 (VA), the initial behavior is proposed (red frame) according to the observed results after 60 min. As mentioned above, it is expected that the HfCO scale with dissolved Zr will oxidize to m-HfO_2 and/or m-(Hf,Zr)O_2. The thermic energy of the diffusing oxygen molecules increases with the temperature [64, 72]. This would result into increased diffusion processes of oxygen molecules through the dense and protective m-HfO_2. For this reason, the passive oxidation period might be reduced at 1600°C and consequently at 1700°C [137, 149].

In case of extensive oxidation at higher temperatures, more liquid will form beneath the dense scale in a relatively short time and lift the protective scale (Fig. 6.3a). Simultaneously, the enrichment of the ruptured m-HfO_2 by Zr will induce the phase transition to t-(Hf,Zr)O_2 and further destruction of the reaction scale as already hypothesized for 1500°C (Fig. 6.3b). However, the excessive evaporation of B_2O_3 with dissolved ZrO_2 might induce the enhanced precipitation of secondary t-ZrO_2 inside the reaction scale and on top of the surface. As a result, a comprehensive layer of secondary t-ZrO_2 forms. The continuous precipitation of secondary t-ZrO_2 assures the growth of a dense reaction scale at the surface (~83 µm after 240 min (Table 5.8)). It can be assumed that the Knudsen diffusion might be reduced as soon as a comprehensive dense ZrO_2 scale formed uniformly at the surface. Dramatic improvement can be assumed by significantly densification and/or pore diameters smaller than 3 µm, following the observations of Parthasarathy et al. (Fig. 6.3c) [42, 43, 137].

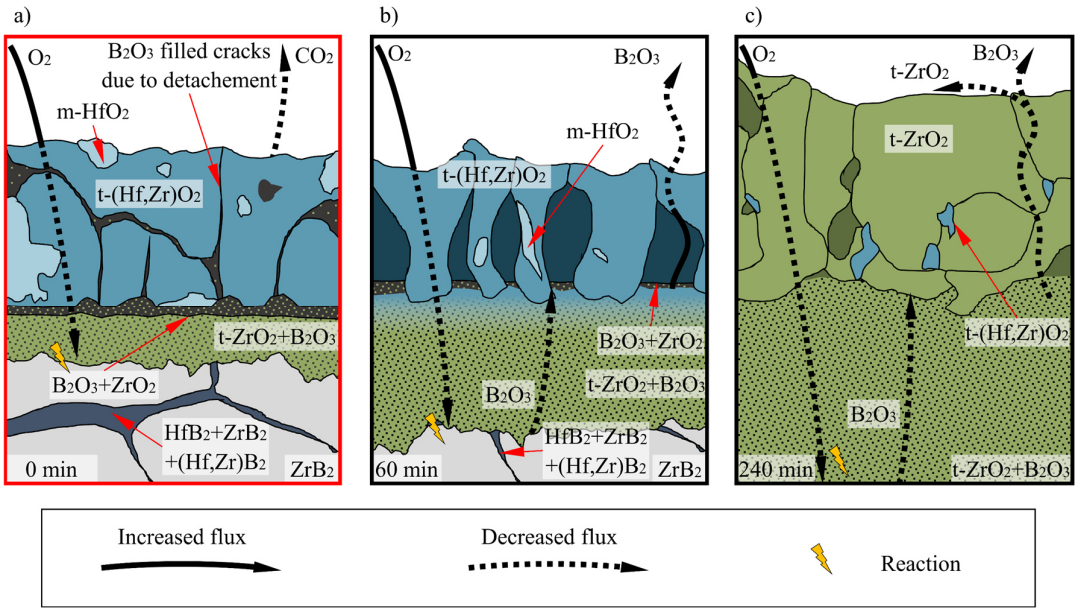

Fig. 6.3: Proposed oxidation mechanisms of HfO_2 coated ZrB_2 (VA) at 1600°C: a) after 0 min of oxidation (extrapolation); b) after 60 min of oxidation; c) after 240 min of oxidation

An identical mechanism is expected for the oxidation temperature of 1700°C but more rapidly. The passive oxidation period is further reduced, ending in a ZrO_2-based reaction scale after 60 min of oxidation (~112 µm thick). The solubility of ZrO_2 in liquid B_2O_3 increases with respect to temperature. In the same time, an enhanced evaporation rate for the B_2O_3 liquid can be observed at 1700°C [58, 59, 137]. This might explain the accelerated formation of a thick and dense ZrO_2 scale as an uppermost layer at 1700°C. The reaction of the Al_2O_3 crucible and the specimen induced the formation of an Al-containing mixed oxide phase ((Al,B)O). This liquid phase was found to fill the pores in the porous t-ZrO_2 (Fig. 5.22, Spec.B24). The effect of the Al-rich oxide phase on the oxidation mechanism at 1700°C can not be estimated. More experiments with HfO_2 coated ZrB_2 (VA) need to be carried out for a detailed statement. Especially short-term experiments need to be considered to understand the oxidation mechanisms and effects of the HfO_2 coating in the initial minutes [137].

6.1.3 Oxidation Kinetics of HfO_2 Coated ZrB_2

The oxide scales of HfO_2 coated ZrB_2 (VA) specimens can be divided into a reaction scale (RS), containing a $(Hf,Zr)O_2$ solid solution with ≥2 at.% Hf, and an underlying porous ZrO_2 scale (PS). Vacuum-annealed HfO_2 coatings had an initial thickness of ~7.5 µm as shown in Fig. 5.9b. An increase in thickness for the HfO_2-containing reaction scale can be observed with increasing exposure time from 60 min to 240 min. However, the increase in the thickness of the reaction scale was found to be relatively small at 1500°C (~12 µm to ~16 µm). A significant increase in the RS thickness was observed at 1600°C (~31 µm to ~83 µm) as well as at 1700°C (~112 µm). Therefore, the growth rate of the RS depends on time and temperature (Fig. 5.23, Table 5.10) [137].

A reduction in the porous oxide scale growth can be observed for HfO_2 coated ZrB_2 (VA) compared to baseline ZrB_2. The scale measurements revealed a reduction of the porous ZrO_2 scale by

~27% after 60 min and ~13% after 240 min at 1500°C. Even at 1600°C, the thickness of the porous oxide scale was found to be reduced by ~15% and ~9% after 60 min and 240 min (compare Table 5.1 and Table 5.10). The reduced oxide scale thickness of HfO_2 coated ZrB_2 (VA) is attributed to the reduced oxygen mobility through the dense HfO_2 scale at the initial time of oxidation. The increased density of the ceramic coating enforces volume diffusion of oxygen molecules to the ZrB_2 substrate, which can be found as the oxidation limiting mechanism (slower diffusion mechanisms than Knudsen diffusion through porous ZrO_2) [72]. As a result, the coating ensures a passive oxidation period with reduced parabolic oxidation rate constants for HfO_2 coated ZrB_2 (VA) compared to baseline ZrB_2 [43, 73, 137, 144].

The activation energy of HfO_2 coated ZrB_2 and baseline ZrB_2 are very similar for an exposure of 60 min and 240 min in a temperature range of 1500°C to 1600°C (Table 5.2, Table 5.11). This indicates similar oxidation mechanisms for both conditions (direct oxidation of ZrB_2, formation of porous ZrO_2 and liquid B_2O_3), once the protective nature of the HfO_2 coating is lost. However, the comparison of the Arrhenius plots for baseline ZrB_2 and HfO_2 coated ZrB_2 reveals a shift to lower oxidation rate constants for the coated ZrB_2 (VA). This is attributed to the passive oxidation period, which is offered by the HfO_2 coating during the initial time of oxidation [137].

A decreasing trend for the activation energy of HfO_2 coated ZrB_2 can be observed in the temperature regime of 1600°C to 1700°C for 60 min of exposure (reduced slope). This might be attributed to the formation of a dense t-ZrO_2 scale at the uppermost section. With respect to time, more secondary t-ZrO_2 will precipitate at the surface at elevated temperatures and form a dense reaction scale. This scale might act similarly to the dense HfO_2 coating in the initial time of oxidation, reducing the Knudsen diffusion of oxygen molecules to the reaction front of ZrB_2. However, the observed (Al,B)O phase might manipulate the results at 1700°C (Fig. 5.22). Therefore, experiments should be repeated to confirm the observations [137].

Based on the parabolic rate constants and the change in the activation energy shown in Fig. 5.24, Table 5.10, and Table 5.11, the following statements can be made:

Oxidation at 1500°C: A limited passive oxidation period with lower parabolic oxidation rate constants is expected due to the pore-free and dense m-HfO_2 scale. However, the scale can not prevent the oxidation of the ZrB_2 substrate for 60 min. Once liquid B_2O_3 accumulates beneath the dense reaction scale, it will lift the protective scale and induce cracking. From this moment, the oxidation kinetics are reaction-controlled and aligns with baseline ZrB_2. The protection is solely attributed to the dense m-HfO_2 scale in the initial time of oxidation, providing volume diffusion mechanisms of oxygen molecules (vacancy diffusion, interstitial diffusion) (<60 min).

Oxidation at 1600°C: Similar oxidation processes are expected as at 1500°C. However, the increased temperature will accelerate the diffusion processes of oxygen molecules through the dense m-HfO_2 scale and the oxidation of ZrB_2. Increased solubility of ZrO_2 in B_2O_3 and enhanced evaporation of B_2O_3 might lead to the precipitation of secondary t-ZrO_2 at the uppermost section of the oxide scale. A certain densification of the uppermost section of the oxide scale would induce limited oxidation protection by reducing the Knudsen diffusion .

Oxidation at 1700°C: Accelerated oxidation of the substrate leads to the loss of the protective coating in the initial time of oxidation. However, the rapid oxidation might induce the dominant

precipitation of secondary ZrO_2 at the uppermost section of the oxide scale. This would enforce the formation of a significantly thick and dense reaction scale.

6.1.4 Conclusions of HfO_2 Coated ZrB_2

- Reactive magnetron sputtering is a successful method to deposit dense m-HfO_2 coatings on ZrB_2 in a reliable and reproducible way.
- Ground ZrB_2 surfaces (10 µm grit size) improve the adhesion of the coating to the substrate due to the mechanical interlocking of the applied HfO_2 coating to the substrate.
- Interdiffusion processes during vacuum-annealing improved the stability of the coating due to the crystallization of the applied coating and the formation of mixed phases such as $Hf(C_{0.84}O_{0.16})$, HfB_2, and $(Hf_{0.5}Zr_{0.5})B_2$.
- Oxidation at elevated temperatures leads to the formation of a dual-layer architecture for the oxide scale, containing an outer m-HfO_2 reaction scale and inner porous t-ZrO_2.
- The accumulation of B_2O_3 beneath the m-HfO_2 scale induces the lift up and the destruction of the protective dense layer with respect to time.
- The enrichment of the m-HfO_2 by Zr and the formation of the solid solution m-$(Hf,Zr)O_2$ reaction scale decreases the transition temperature for the monoclinic to tetragonal phase transition and induces cracks due to the volume reduction.
- Dense m-HfO_2 coating reduces the total oxide scale thickness by ~27% after 60 min and ~13% after 240 min at 1500°C compared to baseline ZrB_2.
- At 1600°C the reaction kinetics are accelerated, limiting the protective period of the dense m-HfO_2 coating for an exposure time <60 min.

On one hand, the performance of the coating could be improved by introducing a diffusion barrier coating (DBC) in between HfO_2 and ZrB_2 against Zr diffusion, which prevents/delays the enrichment of the deposited m-HfO_2 scale by Zr during oxidation. As a result, the transition temperature of the dense m-HfO_2 scale might be unchanged for an extended period. However, it must be considered that the diffusion barrier coatings might have other implications on the oxidation behavior of ZrB_2 and will not prevent spallation due to the formation of B_2O_3 with respect to the oxidation time.

On the other hand, increasing the coating thickness might extend the protective period of the coating. Considering a constant diffusion flux of Zr cations into the m-HfO_2 scale at a specific temperature, a thicker coating (more volume) will decelerate the enrichment of the scale. Consequently, the transition temperature will be higher for extended oxidation and will prolong the protective period of the dense scale. However, it should be considered that increased coating thickness may lead to spallation due to internal stresses after the coating process. In addition,

liquid boria that forms underneath the thick dense coating could again cause cracks and the detachment to the substrate. This will be detrimental for the oxidation resistance.

Therefore, a thick m-HfO_2 coating with a gradient in porosity across the coating thickness might be helpful. i.e. an architecture containing more pores at the coating/substrate and increased density at the coating/atmosphere. This morphology could accommodate the volume expansion due to the liquid boria formation, minimize the stresses, and avoid cracks in the coating for an extended exposure time. Detailed studies on the development of the coating (process parameters, surface roughness, chemical composition, vacuum annealing, porosity, and coating thickness) are required to enable optimal performance.

6.2 Effect of Metallic Niobium Coatings on ZrB_2

This section is based on the published paper of Förster et al. "Oxidation behavior of Nb-coated zirconium diboride" (https://doi.org/10.1016/j.jeurceramsoc.2023.04.029). Content and texts may differ in part from the publication [139].

6.2.1 Processing of Sputtered Nb Coatings on ZrB_2

6.2.1.1 PVD Magnetron Sputtering of Metallic Nb Coatings

Magnetron sputtering was used to apply thin coatings of metallic Nb on ZrB_2. The sputtering behavior of a new Nb target was investigated in different coating runs with given process parameters (Table 5.14). A downward trend in the deposition rate and the resulting coating thickness can be seen and associated with the progressive lifetime of the target [104, 152]. Due to the sputtering mechanism, a trench is created on the planar target surface (compare Fig. 4.5b). With the progressing lifetime of the target the size and depth of the trench increases. Welzel and Ellmer have investigated the effects of target aging to the sputtering process. Various parameters such as the plasma geometry, the ion flux density, and the actively used target surface A_t will change (compare Equ. 2.21). All these factors influence the sputtering process and decrease the deposition rate with respect to the age of the target. Especially for new/"fresh" targets an increased effect can be observed on the deposition rate [152]. Considering these results, a decreasing deposition rate from ~5.6 µm/h to ~5.3 µm/h for the metallic Nb coatings is plausible. However, the coating thickness for the tested specimens was ~9 µm with a deposition rate of ~5.3 µm/h (compare Table 5.12). The columnar grain growth on substrates, which is a characteristic of PVD coatings, manifests in elongated grain boundaries that run from the interface of the coating/substrate to the surface/atmosphere (Fig. 5.25). Defects such as cracks or pores were not observed in the deposited Nb coatings.

6.2.1.2 Vacuum-annealing of Nb Coated ZrB_2 at Elevated Temperatures

Volume expansion during oxidation (compare Table 3.2, ~170 vol%) might lead to internal stresses and the spallation of the coating [153]. The common approach to improve the adhesion of a coating to a substrate and to inducing the crystallization of the magnetron-sputtered coating is annealing in a non-oxidizing atmosphere (e.g. argon or vacuum). Therefore, vacuum-annealing was performed with the Nb-coated ZrB_2 substrates in a graphite furnace. The annealed Nb coating revealed a multilayer system, divided into three distinct sections: an interdiffusion zone (IDZ) near the interface zone of the coating/substrate, an intermediate NbC layer with dissolved Zr and B, as well as an uppermost NbB_2 layer (Fig. 5.28, Spec.C06-C08). Several reactions might occur during the vacuum-annealing at ~1800°C[1] to achieve the observed multilayer system. A schematic, illustrating the hypothesized processes during vacuum-annealing, can be seen in Fig. 6.4.

[1] Compare Fig. 4.6, vacuum-annealing. The process was carried out for 60 min at 1800°C and for 180 min at 1750°C due to a malfunction of the thermocouple

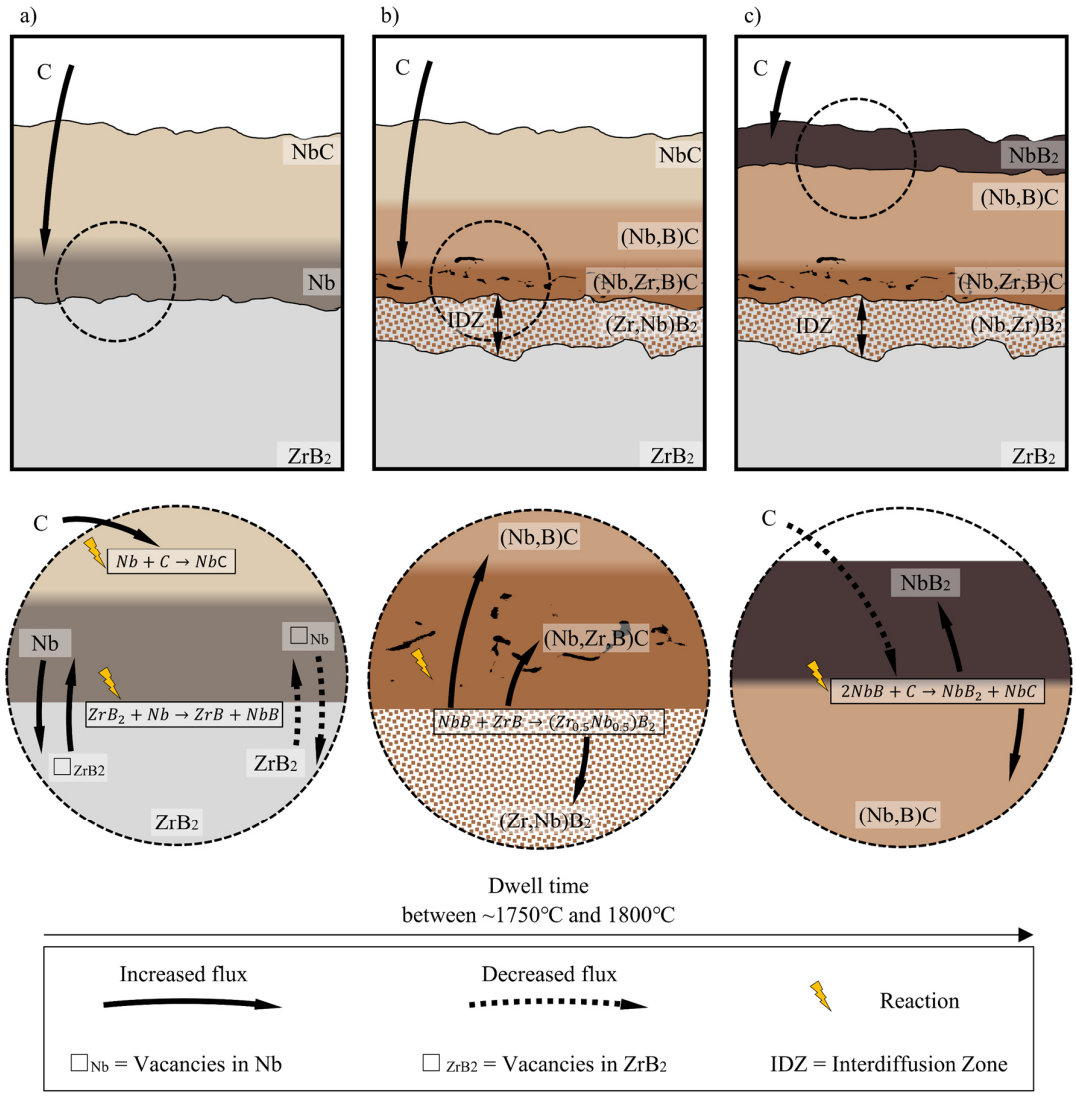

Fig. 6.4: Hypothesized model of interdiffusion and reactions during vacuum-annealing of Nb coated ZrB_2 at ~1800°C with respect to the processing time (compare Fig. 4.6): a) Carburization of metallic Nb and mutual interdiffusion processes at the interface of the coating/substrate in the initial time of the annealing procedure; b) Reaction of metal borides at the interdiffusion zone during the intermediate time of the annealing procedure; c) Reaction of NbB and C at the surface

The formation of NbC during vacuum-annealing has been proven by X-ray diffraction (Fig. 5.27a), electron diffraction (Fig. 5.28), and EDS analysis (Spec.C02, Spec.C05, Spec.C06). Long et al. investigated the sublimation of graphite nanoparticles during vacuum heat treatment in the temperature range of ~1500°C to ~1900°C. The sublimation of graphite induced the formation of gaseous components [154]. Brizes et al. investigated the carburization of metallic niobium in carbon powder during vacuum/argon annealing. A NbC layer of ~10 µm thick formed already after ~25 min at 1800°C [155].

Considering the carburization of metallic Nb and the sublimation of graphite nanoparticles during vacuum-annealing at ~1800°C, the formation of NbC during vacuum-annealing seems plausible. It is proposed, the formation of NbC follows the general reaction in Equ. 6.4 [154-156] (compare Fig. 6.4a).

$$Nb + C \rightarrow NbC \qquad \text{Equ. 6.4}$$

An IDZ of ~2 µm thick formed at the coating/substrate interface during vacuum-annealing (Fig. 5.28c, Spec.C06-C07). The IDZ revealed a chemical composition of ~16 at.% Zr and ~15 at.% Nb (Fig. 5.28c, Spec.C07). Moreover, pores appeared in the former Nb coating near the interface zone of the coating/substrate (Fig. 5.27b). The formation of the porosity could be explained by the mutual diffusion for diffusion couples, based on Fick´s first law of diffusion. The intrinsic diffusion fluxes of two different materials as well as the net flux of vacancies during the mutual diffusion can be described by Equ. 6.5 to Equ. 6.8 [72, 74, 157].

$$\sum J_n = 0 = J_A + J_B + J_{Va} \qquad \text{Equ. 6.5}$$

$$J_{Va} = -J_A - J_B \qquad \text{Equ. 6.6}$$

$$J_{Va} = \left| J_{\square A} + J_{\square B} \right| \qquad \text{Equ. 6.7}$$

$$J_A + J_{\square A} = -J_B - J_{\square B} \qquad \text{Equ. 6.8}$$

with J_A and J_B for the intrinsic diffusion fluxes of the materials, J_{Va} for the net flux of vacancies, and $J_{\square A}$ and $J_{\square B}$ for the vacancy flux of the materials. Porosity will form near the interface zone of the material with increased diffusion flux (e.g. material A; $J_A >> J_B$). The dominant diffusion flux of material A into B will enforce a dominant flux of vacancies from material B to A. Consequently, it leads to the formation of the characteristic Kirkendall porosity near the interface zone of material A [72, 74, 157]. The formation of fine porosity in the former Nb coating near the interface zone can be interpreted as Kirkendall porosity (compare Fig. 5.27and Fig. 5.28). This would indicate a significantly higher diffusion of metallic Nb into the ZrB_2 than Zr cations into the metallic Nb coating. Consequently, the displacement of the transition metal atoms must induce the formation of NbB_2 and ZrC [158]. However, neither ZrC or NbB_2 were observed near the interface zone of the former coating/substrate via TEM electron diffraction, STEM-EDS, or X-ray diffraction. Both reaction products might be dissolved in the NbC layer and the ZrB_2 substrate and formed the observed mixed borides ((Nb,Zr)B) and mixed carbides ((Nb,Zr)C).

Carbon and boron were identified via STEM-EDS (qualitative) across the annealed Nb coating up to the interface zone of the coating/substrate (compare Fig. 5.28, Spec C05, Spec C06). The mutual diffusion of Nb and Zr by itself would not explain the dominant presence of boron across the annealed Nb coating thickness. A mutual diffusion process of boron and carbon seems to be

not plausible since no carbon was detected in the IDZ (compare Fig. 5.28, Spec. C07). Another hypothesis could be the formation of reactive metal borides at annealing temperatures (~1800°C).

Merriles et al. observed the formation of metal borides such as ZrB, NbB and HfB and analysed the electronic structure and the bonding dissociation energies of this composites. This observation proved the possibility of the formation of metal borides [159]. The reaction of Nb and ZrB_2 in the initial time of the annealing process (at ~1800°C, even before the formation of NbC at the former interface zone) could lead to the formation of reactive metal borides, following the proposed reaction of Equ. 6.9 (compare Fig. 6.4a). The recombination of the metal borides during cooling would lead to the mixed diboride-based solid solution (Nb,Zr)B inside the IDZ (no carbon content in the IDZ, compare Fig. 5.28, Spec. C07). The proposed recombination is presented in Equ. 6.10 (compare Fig. 6.4b). Similar reaction could be expected to form mixed carbides in the section of the former Nb coating and would explain the presence of the solid solution of carbon, boron, zirconium and niobium ((Nb,Zr,B)C) near the interface zone of the coating/substrate.

$$ZrB_2 + Nb \rightarrow ZrB + NbB \qquad \text{Equ. 6.9}$$

$$ZrB + NbB \rightarrow (Nb,Zr)B \qquad \text{Equ. 6.10}$$

The phase identification of (Nb,Zr)B in the IDZ via TEM electron diffraction and D-spacing analysis was not possible (compare 5.24c, Diffraction III). The results did not align with the data in several data bases. However, a hexagonal crystal structure was observed, which would support the formation of a diboride-based solid solution. As mentioned above, whereas most of the zirconium was found near the interface zone of the coating/substrate (Fig. 5.28c, Spec.C06-C07), boron was found across the entire thickness of the coating (Fig. 5.28b-c, Spec.C05-C06). The presence of NbB at the coating/substrate would enabled the mobility of boron across the coating during vacuum-annealing, forming NbC with dissolved boron (compare Fig. 6.4b, (Nb,B)C)). BSE micrographs (Fig. 5.27b-c, Fig. 5.28b, Spec.C04) and electron diffraction (Fig. 5.29a, Diffraction I, NbB_2) proved the formation of NbB_2 at the uppermost section of the vacuum-annealed coating. The boron might permeate through the NbC scale to the surface with respect to time. The carburization of the scale by free carbon might induce the reaction of the NbB with C at the uppermost section of the coating, following the proposed Equ. 6.11 (compare Fig. 6.4c). As a result, NbB_2 might form as an uppermost layer.

$$2NbB + C \rightarrow NbB_2 + NbC \qquad \text{Equ. 6.11}$$

As a result, the proposed reactions would explain the formation of NbB_2 at the uppermost section, an intermediate NbC layer with dissolved NbB ((Nb,B)C), a mixed carbide of (Nb,Zr,B)C at the interface zone of the coating/substrate and an IDZ with a mixed boride (Nb,Zr)B solid solution. However, these are hypothetic mechanisms and needs to be investigated in detail for full understanding.

6.2.2 Oxidation Mechanisms of Nb Coated ZrB_2

First, ramped oxidation tests (R/C) were performed with Nb coated ZrB_2 (AC, VA) to investigate the effect of vacuum-annealing on the performance of the coatings. The results pave the way for rapid oxidation testing (P/Q). Depending on the oxidation temperature and the exposure time, a multilayer oxide scale formed on Nb coated ZrB_2 (VA), which contains a reaction scale (RS) and an underlying porous ZrO_2 scale (PS). The oxidation mechanisms for the Nb coated ZrB_2 at different temperatures and exposure times will be discussed in the following

6.2.2.1 Ramped Experiments of Nb Coated ZrB_2 (AC vs. VA) at 1500°C

An effect of the applied Nb coating on the oxidation mechanisms of ZrB_2 can already be observed for Nb coated ZrB_2 (AC) after 60 min at 1500°C. Most of the Nb coating was spalled during the exposure (Fig. 5.32, Fig. 5.33). The spallation of the coating might be induced by the volume expansion during the oxidation from Nb to Nb_2O_5 (Table 3.2), following Equ. 6.12 [139, 153].

$$2Nb + \frac{5}{2}O_2 \rightarrow Nb_2O_5 \qquad \text{Equ. 6.12}$$

The remaining Nb_2O_5 did not prevent the oxidation of the ZrB_2. However, Nb_2O_5 melt at 1500°C (T_M ~1495°C) and modify the B_2O_3 liquid, stabilizing the glassy layer at the surface (Fig. 5.31, Fig. 5.32) as it was observed by Dehdashti et al. [37, 79]. Furthermore, the uppermost section of the ZrO_2 oxide scale got affected by the Nb coating. The reaction of Nb_2O_5 and t-ZrO_2 at 1500°C led to the formation of $Nb_2Zr_6O_{17}$ and engraved crystals at the surface (Fig. 5.31, Spec.C10). Residual Nb_2O_5, containing ~4 at.% Zr (Fig. 5.33b, Spec.C12), was found at the grain boundaries of globular ZrO_2 grains in the uppermost section of the solid oxide scale. The liquid Nb_2O_5 might induce liquid phase sintering [160]. Although, the amount of the Nb_2O_5 liquid did not induce the formation of a comprehensive solid oxide scale and full densification (Fig. 5.32, Fig. 5.33). In comparison with baseline ZrB_2, the Nb coated ZrB_2 (AC) slightly improved the oxidation resistance, reducing the thickness of the porous oxide scale by ~6% (compare Table 5.1 and Table 5.23) [139].

In contrast, Nb coated ZrB_2 (VA) revealed a significant effect of the vacuum-annealing treatment on the oxidation behavior of the underlying substrate. The majority of the oxidized surface was still covered with a ~15 µm thick layer of B_2O_3. Very few zirconia grains were observed at the surface after 60 min at 1500°C (Fig. 5.35a-b). A dense Nb_2O_5 layer was found at the uppermost section of the solid oxide scale as shown in Fig. 5.36. Unlike in the AC case, the comprehensive layer of Nb_2O_5 might indicate less spallation of the deposited coating during oxidation (Fig. 5.36a, Spec.C16). This can be attributed to the formed interdiffusion zone (compare Fig. 5.28c), which formed during vacuum-annealing (chemical bonded) and prevented the coating against spallation (chemically bonded to the substrate) [139]. It is expected that the NbB_2 and NbC layers of the vacuum-annealed Nb scale have a beneficial effect on the oxidation behavior of the system (Fig. 5.27). Even though, all the individual phases would oxidize simultaneously during the ramp-up phase, for the sake of simplicity, mechanisms are explained one by one.

At first, NbB_2 will oxidize to form Nb_2O_5 and B_2O_3 following the proposed reaction in Equ. 6.13. Dokumaci et al. investigated the oxidation of NbB_2 and compared it with metallic Nb. The boronization showed a significant improvement in the case of the oxidation resistance of metallic Nb, forming a liquid solution of Nb_2O_5 and B_2O_3 at the surface during oxidation at 1000°C for 30 min [161]. A similar mechanism is expected for the Nb coated ZrB_2 (VA). The thin layer of NbB_2 at the uppermost section of the annealed coating system will oxidize, following Equ. 6.13 [162].

$$2NbB_2 + \frac{11}{2}O_2 \rightarrow Nb_2O_5 + 2B_2O_3 \qquad \text{Equ. 6.13}$$

The underlying NbC layer subsequently begins to oxidize next. The oxidation of NbC has been studied extensively, forming Nb_2O_5 and CO. The oxidation reaction of NbC is shown in Equ. 6.14 [163]. Since boron is expected to be present in the NbC layer (Table 5.14, Fig. 5.28b-c, Spec.C5, Spec.C6), the equation is extended with NbB to form additional B_2O_3 liquid.

$$2NbC + 2NbB + \frac{15}{2}O_2 \rightarrow 2Nb_2O_5 + B_2O_3 + 2CO\uparrow \qquad \text{Equ. 6.14}$$

While the Nb_2O_5 and B_2O_3 remain on the surface, the gaseous components such as CO would leave the oxide scale. As already mentioned, Nb_2O_5 will form a viscous layer on the surface [80, 81, 114, 119]. Based on the phase diagram for the B_2O_3-Nb_2O_5 system (Fig. 3.4a), the two liquids will mix and form a liquid solution (Nb,B)O at the surface, protecting the underlying substrate [82]. The modification of the B_2O_3 by Nb_2O_5, forming a stable liquid solution was investigated by Dehdashti et al. A significant stabilization of the glass on the surface was achieved due to the addition of ~6 mol% Nb into the ZrB_2 matrix, [37, 79]. However, cross-sections prove there is a distinct layer of free Nb_2O_5 present as an immiscible liquid layer (Fig. 5.36, Spec.C15, Spec,C19, Spec,C20).

Further oxidation proceeds to the layer of (Nb,Zr,B)C. The oxidation will lead to the formation of Nb_2O_5, B_2O_3, CO, and porous t-ZrO_2. Considering the phase diagram of the system Nb_2O_5-ZrO_2 (Fig. 3.4b), the presence of >9 mol% Nb_2O_5 might induce the reaction of a mixed oxide of $Nb_2Zr_6O_{17}$, following Equ. 6.15 [119, 123]. Globular grains with a core-shell structure were found near the former interface zone of the coating/substrate (Fig. 5.37). The core was identified as ZrO_2 and the shell as the mixed oxide scale. Its commensurable complex lattice in combination with the chemical composition enabled the indication as $Nb_2Zr_6O_{17}$ (Fig. 5.38, Fig. 5.37) [139].

$$Nb_2O_5 + 6ZrO_2 \rightarrow Nb_2Zr_6O_{17} \qquad \text{Equ. 6.15}$$

The last layer that undergoes oxidation, is the ~2 µm thick IDZ of the proposed (Nb,Zr)B_2 solid solution at the interface of the coating/substrate. Nb_2O_5, t-ZrO_2 and liquid boria will form as oxidation products. Whereas some Nb_2O_5 liquid might react with the B_2O_3 liquid and migrate to the surface, some of the unreacted Nb_2O_5 liquid will infiltrate the porous t-ZrO_2 network (Fig. 5.35c-d). ZrO_2 might dissolve in the Nb_2O_5 liquid and would explain the Zr content for the residual Nb_2O_5.

The presence of a ZrO_2 containing Nb_2O_5 liquid could enforce liquid phase sintering and might result in the densification of the porous ZrO_2 by forming a solid solution (compare the phase diagram of the system Nb_2O_5-ZrO_2, less than 9 mol% Nb_2O_5 ,Fig. 3.4b) [119, 139, 160].

Finally, the vacuum-annealing process improved the performance of the metallic Nb coating significantly. The prevention of spallation induced the formation of a stabilized (Nb,B)O liquid at the surface, a liquid Nb_2O_5 layer with dissolved ZrO_2, and the densification of the porous ZrO_2 by liquid phase sintering. As a result, the Nb coated ZrB_2 (VA) reduced the porous ZrO_2 layer thickness by ~73% compared to the Nb coated ZrB_2 (AC) (Table 5.23). According to the results of ramped oxidation tests at 1500°C for 60 min, vacuum-annealing for Nb coated ZrB_2 can be considered as a key process step to optimize the performance of the applied metallic Nb coating on ZrB_2 [139].

It needs to be mentioned that the specimen for ramped oxidation revealed a section of extraordinary oxidation protection by forming an intermediate solid layer of NbO (Fig. 5.36, Spec.C16). This layer prevented oxygen mobility and the infiltration of the porous t-ZrO_2 (~18 µm thick) by liquid Nb_2O_5. This oxide scale architecture was increasingly found for the rapid oxidation case and will be discussed elaborately in this section [139].

6.2.2.2 Rapid Oxidation of Nb Coated ZrB_2 (VA) at 1500°C

The hypothesized oxidation mechanisms at 1500°C for an exposure of up to 60 min during rapid oxidation are presented in Fig. 6.5. The initial condition for the oxidation is the vacuum-annealed Nb coating on ZrB_2 (VA) (compare Fig. 6.4c). Similar oxidation processes for the NbB_2, (Nb,B)C, (Nb,Zr,B)C, and (Nb,Zr)B_2 layers are expected as explained in the previous section for the ramped oxidation. However, the thermal shock affects the architecture of the oxide scale differently since there is no oxidation during ramping and cooling.

The oxidized surfaces revealed the formation of a comprehensive liquid layer of (Nb,B)O at the surface due to the glass stabilization of B_2O_3 glass by Nb_2O_5 (Fig. 5.42). Further, a thick liquid layer of Nb_2O_5 (~51 µm) formed during oxidation, considering the melting point of ~1495°C for Nb_2O_5 (Fig. 5.48a-b). The observation of the thick and comprehensive Nb_2O_5 layer along the surface of the specimen enables the assumption that the coating withstand the thermal shock during rapid oxidation (P/Q) at 1500°C. A thin layer of (Nb,Zr)O with the chemical composition for NbO and ≤5 at.% Zr (Fig. 5.48, Spec.C38-39) can be found at the former interface zone of the coating/substrate. X-ray diffraction proved the presence of NbO_2 (Fig. 5.41). A clear phase identification for the (Nb,Zr)O layer was not possible. The layer could have been formed due to the comproportionating of the residual metallic Nb coating beneath the Nb_2O_5 layer and the following layer oxidation of metallic Nb ($NbO \rightarrow NbO_2 \rightarrow Nb_2O_5$) [164]. Another option is the oxidation of the interdiffusion zone to a NbO-based solid solution (IDZ, (Nb,Zr)B_2, see Fig. 6.4c). Nevertheless, the dense and solid layer of NbO and/or NbO_2 will be solid at 1500°C due to the increased melting points of lower stochiometric niobia (compare Table 3.2, melting points of niobium oxides >1700°C). The dense layer could not prevent the oxygen diffusion to the ZrB_2 and did not inhibit the formation of porous ZrO_2 and liquid B_2O_3 (Fig. 5.48a-b). However, it is expected that the dense (Nb,Zr)O layer prevents the migration of the liquid B_2O_3 to the surface and enforces the accumulation of the liquid underneath it.

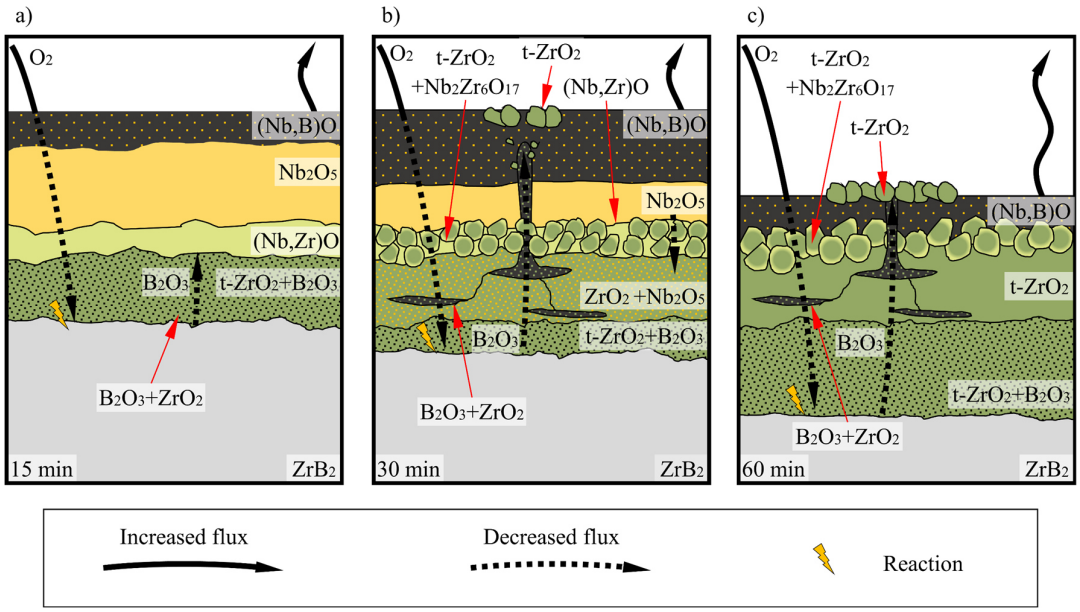

Fig. 6.5: Proposed oxidation mechanisms of Nb coated ZrB_2 (VA) at 1500°C for rapid oxidation with induced thermal shock: a) after 15 min of oxidation; b) after 30 min of oxidation; c) after 60 min of oxidation

Consequently, horizontal crack-type reservoirs form in the porous t-ZrO_2 scale with respect to the oxidation time (between 15 min to 30 min of oxidation) (Fig. 6.5b). Comparable structures were observed by Karlsdottir et al. in ZrB_2-SiC composites, which were defined as convection cells. Reservoirs of borosilicate glass form and widen due to the continuous formation of B_2O_3 liquid. Internal pressure in the reservoirs leads to the breakthrough of the borosilicate liquid through the solid oxide scale, releasing the liquid to the surface with dissolved ZrO_2 [78, 151]. A similar mechanism is expected here for the Nb coated ZrB_2 specimens (VA) during oxidation. The accumulated B_2O_3 liquid breaks through the solid (Nb,Zr)O scale and through the liquid Nb_2O_5 to migrate to the surface (Fig. 5.49). Dissolved ZrO_2 in B_2O_3 liquid will precipitate at the surface and form globular grains of secondary t-ZrO_2 [151]. It is expected that the enhanced migration of liquid B_2O_3 and the stabilization with Nb_2O_5 increase the coverage with protective (Nb,B)O glass. This induces the consumption of the liquified Nb_2O_5 layer with respect to the time. Once the solid (Nb,Zr)O layer get ruptured due to the breakthrough of the convection cells, Nb_2O_5 liquid will infiltrate the underlying porous t-ZrO_2 scale to form an infiltrated layer section of ZrO_2 and Nb_2O_5 (Fig. 6.5b). Simultaneously, Nb_2O_5 readily reacts with the porous zirconia layer (≥10 at.% of Nb_2O_5 is needed) and induces the formation of globular core-shell structured grains with a core of m-ZrO_2 and a shell of a complex mixed oxide phase $Nb_2Zr_6O_{17}$, following Equ. 6.15 (a similar formation can be found in Fig. 5.36).

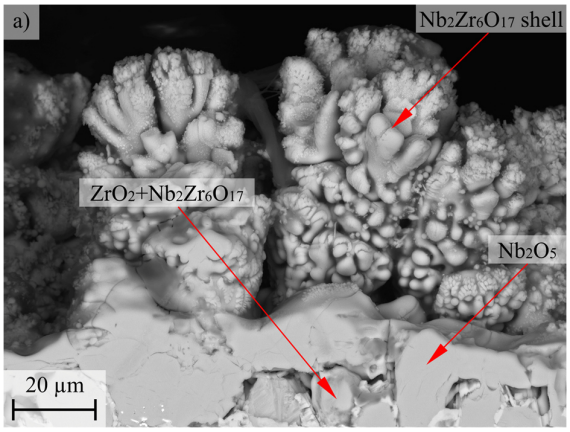

Fig. 6.6: Reacted ZrO_2 grains from the uppermost section of the porous ZrO_2 layer with Nb_2O_5, forming a $Nb_2Zr_6O_{17}$ shell structure, bonded on the residual Nb_2O_5 layer after 60 mins of oxidation at 1500°C

Further oxidation up to 60 min induced the densification of the infiltrated porous ZrO_2 scale (Nb_2O_5+ZrO_2) by means of liquid phase sintering. As a result, an almost dense t-ZrO_2 scale formed (see Fig. 5.48e-f). According to the principle of Knudsen diffusion, the densified t-ZrO_2 scale will slow down the oxygen mobility to the underlying oxidation front of ZrB_2. As a result, the oxidation kinetics will be reduced as the formation of the porous oxide scale and liquid boria. However, the uppermost liquid solution (Nb,B)O keeps on evaporating, resulting in a thinner liquid layer at the surface and the exposition of reacted zirconia grains at the surface. The engraved grains with a cauliflower-shaped structure resemble the situation and are presented in Fig. 6.6. Most of the Nb_2O_5 left the surface after 60 min at 1500°C. It is assumed the Nb_2O_5 liquid is either consumed by the liquid B_2O_3 and leaves the surface due to evaporation or through the infiltration and reaction with the porous t-ZrO_2. In either way, the rate of boria formation at the oxidation front of ZrB_2 must be less than the rate of boria evaporation, which should lead to the recession of the protective glassy layer and less protective nature with respect to the time (Fig. 6.5c).

6.2.2.3 Oxidation of Nb Coated ZrB_2 (VA) at 1600°C

The hypothesized oxidation mechanism at 1600°C is presented in Fig. 6.7. Unlike at 1500°C, no Nb_2O_5 layer, nor a dense (Nb,Zr)O was observed underneath the stabilized liquid solution of (Nb,B)O after 15 min at 1600°C. Rather, globular t-ZrO_2 grains with a $Nb_2Zr_6O_{17}$ outer shell and Nb_2O_5-infiltrated porous ZrO_2 were found after 15 min (see Fig. 5.50a-b). The scale architecture is quite similar to the oxide scale after 60 min at 1500°C, i.e. 100°C rise in the oxidation temperature forces a dramatic increase in the oxidation of the Nb coated ZrB_2 (VA). The formation of liquid B_2O_3 and porous t-ZrO_2 beneath the coating takes place. As no dense (Nb,Zr)O layer was present in the oxide scale, it is expected that the liquid B_2O_3 migrates without inhibition to the surface instead of forming convection cells in the porous t-ZrO_2 (compare the case at 1500°C). This situation is depicted in Fig. 6.7a. The almost dense layer, containing Nb_2O_5-infiltrated ZrO_2 (ZrO_2+Nb_2O_5), and globular ZrO_2 grains with outer $Nb_2Zr_6O_{17}$ separating the distinct layer of liquid (Nb,B)O and the innermost porous t-ZrO_2 scale.

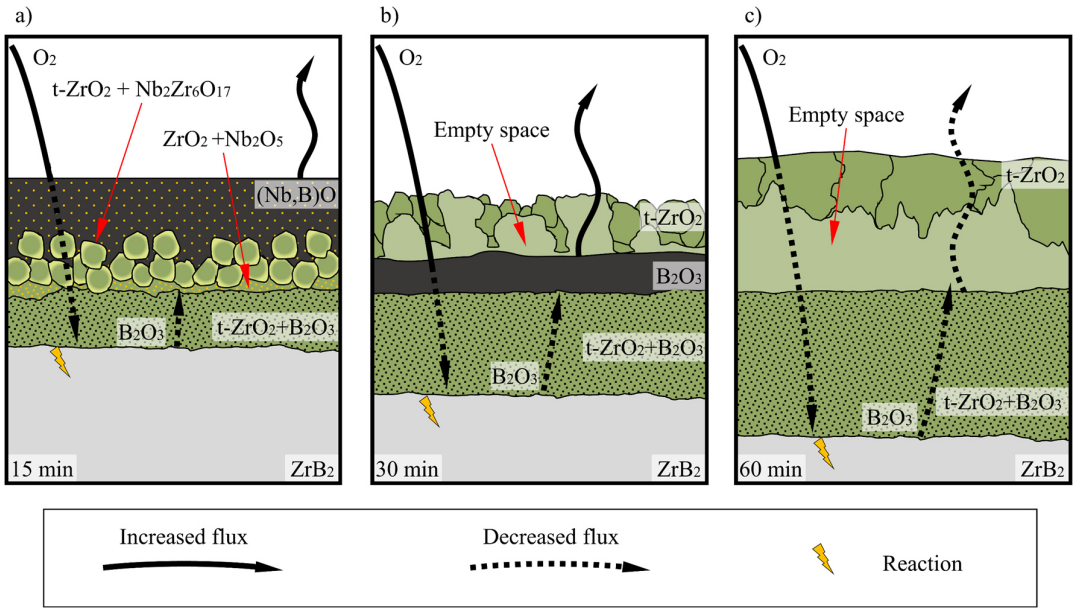

Fig. 6.7: Proposed oxidation mechanisms of Nb coated ZrB_2 (VA) at 1600°C for rapid oxidation with induced thermal shock: a) after 15 min of oxidation; b) after 30 min of oxidation; c) after 60 min of oxidation

Further oxidation induces the densification of the Nb_2O_5-infiltrated ZrO_2 scale (ZrO_2+Nb_2O_5). The evaporation of the protective liquid solution (Nb,B)O at 1600°C leads to the exposure of a quasi-densified ZrO_2 scale at the surface after 30 min of oxidation (see dry surface in Fig. 5.45). As the protective outer liquid layer is missing, the oxidation kinetics will increase, leading to the rapid formation of liquid B_2O_3 and porous t-ZrO_2 beneath the thin and quasi-dense t-ZrO_2 scale. "Fresh" boria forms at the oxidation front of ZrB_2 and might accumulates underneath the quasi-dense ZrO_2 layer. Consequently, the liquid exerts pressure on the quasi-dense t-ZrO_2 scale, forcing its detachment from the porous t-ZrO_2. A B_2O_3 filled gap forms between the reaction scale and the underlying porous t-ZrO_2 (see spalled chunk at the surface, exposing the accumulated glass, Fig. 5.45a). Due to the prior process, the uppermost reaction scale might experience cracks and holes, through which the liquid B_2O_3 migrates to the surface (Fig. 6.7b).

At this moment, no protective mechanisms are active and continuous oxidation of ZrB_2 prevails, forming a thick porous ZrO_2 and liquid boria at the oxidation front. The B_2O_3 glass evaporates and leaves the ruptured reaction scale through holes and cracks. Dissolved ZrO_2 in the boria glass might precipitate at the reaction scale to form secondary t-ZrO_2. As a result, fine cracks and holes, formed during the detachment of the reaction scale, would be sealed by secondary t-ZrO_2 (Fig. 6.7 c). However, the gap between the reaction scale and the porous t-ZrO_2 would never be sealed and could also spall after some time. The spallation of the ruptured reaction scale would lead to catastrophic oxidation since no protection mechanism would protect the underlying substrate against oxidation (Fig. 5.50e-f).

6.2.2.4 Oxidation of Nb Coated ZrB_2 (VA) at 1700°C

The oxidation at 1700°C requires more detailed investigation especially during the initial stages of oxidation, i.e. in steps of 5 min up to 15 min to describe the exact mechanisms. Based on the understood mechanisms at lower temperatures, the following hypothesis is carried out for the oxidation of Nb coated ZrB_2 (VA) at 1700°C.

The multilayer scale, that formed during the vacuum-annealing (Fig.6.4), immediately oxidizes and produces the oxide scale morphology that is proposed in Fig. 6.8a. It is expected, that a liquid solution of (Nb,B)O and a thin Nb_2O_5-infiltrated porous ZrO_2 scale (ZrO_2+Nb_2O_5) will form in the first seconds at 1700°C. The Nb_2O_5-infiltrated ZrO_2 section will densify, forming a solid solution according to the phase diagram (Fig. 3.3b). As a result, it is expected to form a thin quasi-dense t-ZrO_2 scale with several holes immediately at the zeroth minute at 1700°C, enabling the migration and evaporation of fresh B_2O_3, formed at the oxidation front of ZrB_2 (Fig. 6.8a).

Neither boria nor a (Nb,B)O liquid solution was found on top of the surface after 15 mins as shown in Fig. 5.46. Just sparsely distributed crystals of an Nb-rich phase can be found. It implies that as the oxidation progresses (from 0 min to 15 min), the boria reaches the surface through the holes of the quasi-dense reaction scale and evaporates immediately. The precipitation of secondary t-ZrO_2 on the surface enables the formation and growth of a thick and dense t-ZrO_2 scale after 15 min of oxidation. A clear interface is established between the outer dense and inner porous zirconia. A fractured cross-section proved the presence of residual liquid B_2O_3 at the former interface zone of the coating/substrate (Fig. 5.51c-d). Smaller disconnected cavities with B_2O_3 filling could be observed in the outer dense t-ZrO_2 layer. At this stage, boria is expected to use the minor cracks and cavities in the dense layer to reach the surface and finally to evaporate. It is expected, that the rate of boria formation is smaller/equal to the evaporation, preventing the accumulation of an increased amount of liquid B_2O_3 as in the case of 1600°C. Therefore, no detachment of the dense reaction scale might be observed (Fig. 6.8b).

The contamination of tungsten can be explained by the production procedure of the ZrB_2 billets by commercial ZrB_2 powder. The ZrB_2 powder gets ball-milled with WC media to ensure similar particle size and a homogenous distribution of the C powder, which acts as a sintering aid. The ball-milling media might contaminate the ZrB_2 during the milling procedure. The precipitation of WO_3 was also observed for baseline ZrB_2 and other tested ZrB_2 specimens and is not a characteristic of this coating system.

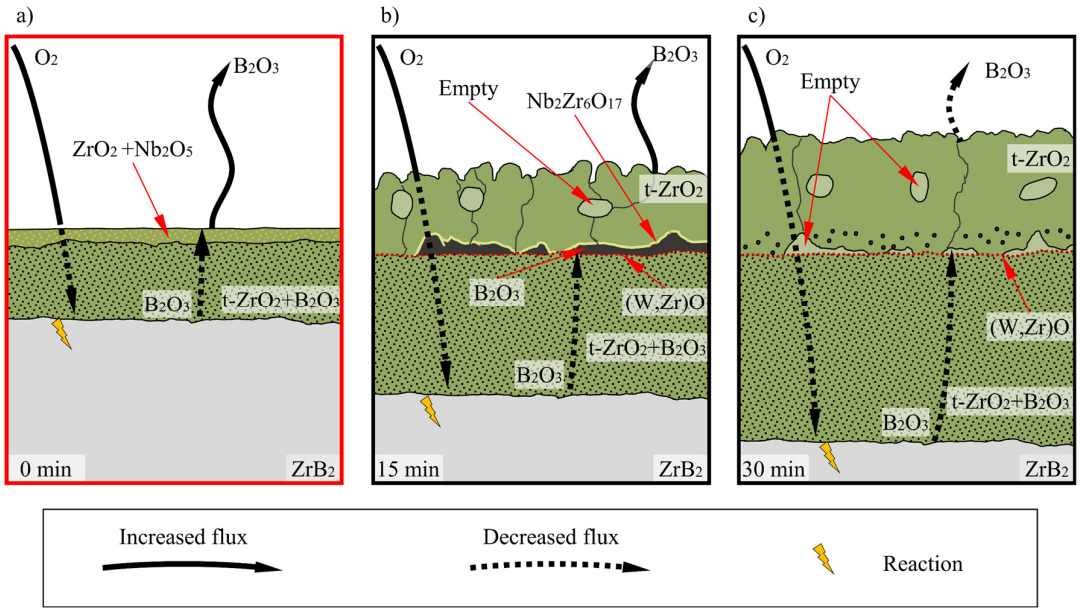

Fig. 6.8: Proposed oxidation mechanisms of Nb coated ZrB_2 (VA) at 1700°C during rapid oxidation with thermal shock: a) after 0 min of oxidation (extrapolation); b) after 15 min of oxidation; c) after 30 min of oxidation

After 30 min of oxidation at 1700°C, the thickness of both, dense and porous ZrO_2, increased significantly (Fig. 5.51e-f, Table 5.23). Further, both layers were found to be sintered together at a few places, ensuring reliable adhesion of the dense t-ZrO_2 scale to the porous ZrO_2 scale. It is hypothesized that the dense reaction scale of secondary t-ZrO_2 will reduce the oxygen mobility to the oxidation front of the ZrB_2 substrate, limiting the oxidation as well as the formation of liquid B_2O_3 and porous t-ZrO_2. No horizontal crack-type reservoirs formed beneath the reaction scale, which might indicate the accumulation of B_2O_3 and the probable loss of the reaction scale. As long as the dense t-ZrO_2 scale is attached to the porous ZrO_2 scale, the equilibrium between the rate of boria formation and evaporation will be maintained and no change in the oxidation mechanism is expected (Fig. 6.8c).

6.2.3 Oxidation Kinetics of Nb Coated ZrB_2

Metallic Nb coatings affect the architecture of the oxide scale that forms on ZrB_2 and improve the oxidation resistance of the substrate compared to baseline ZrB_2. As observed, the oxidation mechanisms change with the oxidation times and temperatures, which influences the corresponding oxidation kinetics and activation energies for the distinct temperature regimes. Comparing the results of baseline ZrB_2 (see Fig. 5.4, Table 5.1) and Nb coated ZrB_2 (VA) (Fig. 5.52, Table 5.23), the Nb coatings reduced the porous t-ZrO_2 scale formation by -55% at 1500°C, -6% at 1600°C, and -55% at 1700°C, each for an exposure time till 30 min. Even for the oxidation up to 60 min a reduction of ~-7% at 1500°C and -12% at 1600°C was achieved due to the deposited coating.

As shown in the Arrhenius plot of Nb coated ZrB_2 (VA) for 15 min (Fig. 5.52b), the activation energies for the temperature regime of 1500°C to 1600°C and 1600°C to 1700°C are almost similar (compare Table 5.24, 688 kJ/mol for 1500°C to 1600°C, 679 kJ/mol for 1600°C to 1700°C).

Consequently, a steady increase in the parabolic oxidation rate constant was observed with respect to the temperature. The protective nature of the specimens for the first 15 min at 1500°C and 1600°C was offered by the liquid solution (Nb,B)O (Fig. 5.36, Fig. 5.48a-b). The liquid layer of (Nb,B)O enforces the permeation of oxygen molecules through the liquid layer and acts similar like the protective B_2O_3 liquid for baseline ZrB_2. The increased protection of the substrate by the (Nb,B)O liquid in the first 15 min at 1500°C and 1600°C can be attributed to the increased stability of the liquid solution compared to B_2O_3 liquid. After 15 min of oxidation at 1700°C, the protective liquid evaporated residue-free and left a dry surface. Form this moment, the protective nature of the specimen can be attributed to the densification of the oxide scale at the uppermost section. The reduced porosity and pore diameters in the densified oxide scale reduce Knudsen diffusion, following the observations of Parthasarathy et al. [42, 43]. Depending on the temperature, the protection of the substrate for 15 min by a liquid layer or densified oxide scale leads to reduced parabolic oxidation kinetics at 1500°C, 1600°C, and 1700°C compared to baseline ZrB_2 (compare $\ln(K_{P(PS)})$ for 15 min from Table 5.1 and Table 5.23).

An impressive effect of the temperature was observed for the oxidation of 30 min. Oxidation rate constants at 1500°C are not changing due to the extended liquid layer protection. The oxidation limiting mechanism is still the permeation of oxygen molecules through the protective liquid. A noticeable difference in the rate constants can be seen at 1600°C. The evaporation of the protective liquid solution (Nb,B)O leads to an almost dry surface after 30 min of oxidation (compare Fig. 5.44 vs. Fig. 5.45). From this moment, the oxidation limiting mechanism can be attributed to the densification of the oxide scale. The evaporation of the protective liquid did not ensure the complete densification of the oxide scale by liquid phase sintering (time-dependent densification process) [160]. Unfortunately, the dense oxide scale can not provide appropriate protection as the liquid layer and leads to an increase of the oxidation rate constant. However, the dense scale still protects the system. This is reflected in the lower oxidation rate constants compared to baseline ZrB_2. Enhanced solubility of ZrO_2 in B_2O_3 at elevated temperatures and the increased evaporation of B_2O_3 liquid might leads to the associated precipitation of secondary t-ZrO_2 at 1700°C (Fig. 5.47e-f). A protective and dense oxide scale formed already after 30 min at 1700°C. The densification and thickening of the reaction scale proceeds with respect to the time (Table 5.23). Consequently, the densified reaction scale will reduce the Knudsen diffusion through the oxide scale and limiting the oxidation progression, following the observations of Parthasarathy et al. [42, 43]. The dense reaction layer assures parabolic oxidation kinetics with reduced rate constants compared to baseline ZrB_2 (compare Table 5.1). The protective nature of the reaction scale shows a lower dependence on temperature as the volatile liquid. This is illustrated in Fig. 5.52b by the significantly decreased activation energy in the temperature range of 1600°C to 1700°C for 30 min of oxidation (activation energy of ~111 kJ/mol). It is expected, further increase in temperature >1700°C might not affect the parabolic oxidation rate constant significantly for the exposure of 30 min since a dense oxide scale would form and control the oxidation.

The long-term oxidation of 60 min led to an increase of the oxidation rate constants at 1500°C and 1600°C (compare orange and blue lines in Fig. 5.52b). The steady evaporation of the protective liquid layer and the densification of the oxide scale induces a transition of the protection mechanism from the protection by the liquid layer to the protection by the dense oxide scale. Finally, after 60 min of oxidation, the protection mechanism at 1500°C and 1600°C can be

attributed to the dense oxide scale, which formed due to the densification of porous t-ZrO_2 and precipitation of secondary t-ZrO_2 at the surface.

Based on the parabolic rate constants and the change in the activation energies shown in Fig. 5.52 and Table 5.24, the following important statements can be made for Nb coated ZrB_2 (VA):

Oxidation at 1500°C: Passive oxidation period at temperature ≤1500°C due to the stabilization of the liquid solution (Nb,B)O at the surface (~30 min). The liquid solution ensures diffusion-controlled oxidation. An increase in the oxidation rate constant can be seen for long-term oxidation between 30 min to 60 min due to the evaporation of the protective liquid.

Oxidation at 1600°C: Limited passive oxidation period (~15 min) with low parabolic rate constants at 1600°C due to the protective liquid layer. Increased evaporation rate of the protective liquid solution (Nb,B)O and the loss of the liquid with respect to the time. Insufficient densification of the oxide scale does not offer protection after 30 min. Steady precipitation and growth of the reaction scale by secondary t-ZrO_2 increases the protection for an exposure >60 min by reducing the Knudsen diffusion of the uppermost section of the oxide scale.

Oxidation at 1700°C: Protective oxidation behavior occurs for an exposure of up to 30 min. The protective nature belongs to the formation of a dense secondary t-ZrO_2 scale at the surface, which reduces the Knudsen diffusion to the oxidation front of ZrB_2.

6.2.4 Conclusions of Nb Coated ZrB_2

- Magnetron sputtering is a successful method to deposit metallic Nb-coatings on polished ZrB_2 substrates (3 µm grit size) in a reliable and reproducible way.

- Vacuum-annealing in a graphite furnace induces the formation of a multilayer system, containing NbB_2 as an overlaying scale, an intermediate layer of carbonized NbC with dissolved boron, and an interdiffusion layer of (Nb,Zr)B_2 at the interface zone of the coating/substrate.

- Vacuum-annealing was found to be a key performance step to ensure improved performance of the metallic Nb coating by enhancing the adhesion of the deposited coating to the substrate.

- The scale architecture of the vacuum-annealed specimen induces the quick formation of a protective liquid solution (Nb,B)O at the surface during the initial time of oxidation and ensures protection.

- The oxidation leads to a multilayer architecture containing a dense reaction scale of t-ZrO_2 and $Nb_2Zr_6O_{17}$, as well as an innermost porous t-ZrO_2 scale with B_2O_3 filled pores.

- The densification of the oxide scale by liquid phase sintering and the coverage with protective liquid (Nb,B)O reduced the oxygen mobility through the oxide scale to the oxidation front of the ZrB_2 substrate.

- Oxidation protection was ensured for the oxidation till 30 min at 1500°C with a reduction of ~55% compared to baseline ZrB_2.

- Limited protection up to 30 min was ensured at 1600°C and 1700°C. However, the dense reaction scale reduces the progression of oxidation compared to baseline ZrB_2.

The protection mechanism of the coating might be improved for temperatures of 1600°C and 1700°C with the deposition of thicker Nb coatings. Instead of ~9 µm, a coating of 15 µm to 20 µm should enhance the passive oxidation period by liquid (Nb,B)O at the surface. Further, a thicker coating might increase the infiltration depth of the porous t-ZrO_2 by liquid Nb_2O_5 and increase the thickness of the dense reaction scale.

Since a dense metallic Nb coating was not found to be a diffusion barrier against oxygen, a high density of the coating is not mandatory for the protection mechanisms. Therefore, an EB-PVD coating with characteristic porosity and increased thickness might improve the oxidation behavior due to an extended period with stabilized B_2O_3 liquid at the surface at higher temperatures for prolonged exposures.

6.3 Effect of Gadolinium Oxide Coatings on ZrB_2

6.3.1 Processing of Reactive Sputtered GdO Coatings on ZrB_2

A multilayer coating experiment was conducted to develop a reliable GdO based coating on ZrB_2 that does not spall during oxidation. In accordance with Berg´s model for reactive sputtering (Fig. 2.18, Equ. 2.21 to Equ. 2.26), the deposition rate decreased with increasing flow of the reaction gas. The high affinity of rare-earths such as gadolinium to react with oxygen and its deoxidation capability for other oxides is well known [165]. Its dominant reactivity with oxygen affects the reactive sputtering process as seen by the data (Table 5.25). A high variation in the deposition rate was observed. This can be attributed to the variation of the partial pressure of oxygen during the sputtering procedure with constant oxygen flux as proven by Särhammer et al. (Fig. 2.19a-b) [105]. A varying partial pressure will affect the reaction at the target surface and might cause target poisoning, forming oxidation products such as Gd_2O_3 with a significantly reduced sputtering rate compared to the metal [103]. The transition from the metallic sputtering process (increased deposition rate, high voltage) to the oxidic sputtering process (reduced deposition rate, low voltage) is not determined by the oxygen flux. Rather, the applied voltage, which indicates the condition at the target, is an appropriate factor. E.g. a voltage of ~400 V ensured a deposition rate of ~7 µm/h (~2.5 sccm, oxygen-doped Gd coatings ($Gd_iO_{(1-i)}$; $[i \in \mathbb{R} \mid 0.5 \leq i \leq 1]$)), and a voltage of ~200 V a deposition rate <1.1 µm/h (~6 sccm, sputtered Gd_2O_3) (compare Table 5.25). However, even voltage-controlled processes can not ensure full process stability for a distinct oxygen-doped Gd coating. A solution might be observing the oxygen partial pressure at the targets during the coating deposition.

The spallation of $Gd_iO_{(1-i)}$ was observed during pre-oxidation at 600°C, whereas sputtered Gd_2O_3 remained at the surface. This can be attributed to the volume expansion of the applied coating during the formation of Gd_2O_3, inducing horizontal cracks (Table 3.3). Sputtered Gd_2O_3 does not experience a significant volume expansion during oxidation since oxygen is already incorporated into the sputtered structure. Considering these observations, a rather unconventional approach was considered to achieve a thicker Gd_2O_3 scale. A ~11 µm thick $Gd_iO_{(1-i)}$ coating was deposited on top of a ~600 nm thick Gd_2O_3 coating (Fig. 5.54c). The pre-oxidation at 600°C revealed the formation of a comprehensive Gd_2O_3 scale with several horizontal cracks (Fig. 5.55b). The crack formation can be assigned to the previously mentioned volume expansion of the $Gd_iO_{(1-i)}$ coating to form crystalline Gd_2O_3. Although, the stresses inside the scale were not high enough to induce the crack propagation and the spallation of the coating. The thin layer of sputtered Gd_2O_3 can be seen as the key solution to ensure the adhesion of the deposited $Gd_iO_{(1-i)}$ coating to the substrate during oxidation. As a result, a reliable two-layer GdO coating system based on volume-stable Gd_2O_3 as a thin first layer and $Gd_iO_{(1-i)}$ with increased deposition rate was successfully developed for ZrB_2, using reactive magnetron sputtering (Fig. 5.54c).

6.3.2 Oxidation Mechanisms of GdO Coated ZrB_2

Ramped oxidation experiments (R/C) with GdO coated ZrB_2 (AC, Pre-oxidized) were performed. Based on these results, rapid oxidation experiments (P/Q) were performed as a next step.

6.3.2.1 Ramped oxidation of GdO Coated ZrB_2 (AC) at 1500°C

The oxidation of the AC and pre-oxidized conditions at 1500°C revealed no significant difference between both conditions, regarding the oxidation protection. The first observation of the specimens revealed a darkish surface with a globular bubble of transparent glass at the center (Fig. 5.56a-b). Analyzed X-ray diffraction patterns prove the presence of m-ZrO_2 at the oxide scale. Some reflections can be assigned to t-ZrO_2 as well. However, Gd-containing phases such as $Gd_2Zr_2O_7$, or Gd_3BO_6 were not detected for both cases (AC and pre-oxidized) (Fig. 5.56c-d). These results indicate the amorphous nature of the translucent Gd-rich glass, which was found on the surface (Fig. 5.56b, Fig. 5.59). Therefore, neither pure Gd_2O_3 (T_M ~2343°C) nor a solid solution of (Gd,Zr)O (T_M ~2300°C) could be identified as the amorphous glass at the surface (compare the phase diagram of Gd_2O_3-ZrO_2, Fig. 3.5b) [129]. In contrast, the binary phase diagram of Gd_2O_3-B_2O_3 shows the reaction product GdB_3O_6 with a melting point <1500°C (Fig. 3.5a) [131]. The EDS analysis of the glass at the surface revealed an excess in oxygen (Fig. 5.57, Spec.D11, ~81 at.%). As already mentioned, boron is not quantifiable by EDS analysis. Only a (Gd,B)O phase such as $GdBO_6$ or GdB_3O_6 might explain the surplus of measured oxygen, concerning the similar effect of an excess of oxygen for B_2O_3 or other boron-containing phases via EDS analysis. Trégouët et al. investigated the crystallization of rare-earth borates such as (Nd,B)O. Their study has revealed the formation of an amorphous metaborate glass due to rapid cooling. Annealing for 10 min at 754°C induces the crystallization of the uppermost section of the surface, whereas the center was still found to be amorphous [166]. This indicates decelerated crystallization kinetics for rare-earth borates, the formation of an amorphous structure during quenching, and would explain the lack of reflections for Gd-containing phases in the X-ray diffraction patterns. The following Equ. 6.16 to Equ. 6.18 might explain the liquid solution formation of GdB_3O_6 at the surface, starting with the oxidation of the GdO coating and the formation of cubic Gd_2O_3 during oxidation at temperatures ≥600°C (compare Equ. 3.5).

$$\frac{4}{i} Gd_i O_{(1-i)} + \frac{(5i-2)}{i} O_2 \rightarrow 2Gd_2O_3 \qquad \text{Equ. 6.16}$$

$$3Gd_2O_3 + (B_2O_3 + ZrO_2) \rightarrow 2Gd_3BO_6 + ZrO_2 \qquad \text{Equ. 6.17}$$

$$Gd_3BO_6 + 4(B_2O_3 + ZrO_2) \rightarrow 3GdB_3O_6 + 4ZrO_2 \qquad \text{Equ. 6.18}$$

with ($Gd_iO_{(1-i)}$; [$i \in \mathbb{R} \mid 0.4 \leq i \leq 1$]), describing the oxidation of Gd_2O_3 (i=0.4), oxygen-doped GdO scales (i>0.4) up to metallic Gd (i=1). The oxidation of ZrB_2 at temperatures >1000°C will lead to the formation of ZrO_2 and liquid B_2O_3. Subsequently, the reaction of Gd_2O_3 and liquid B_2O_3 might undergo the formation of Gd_3BO_6 with a melting point of T_M ~1590 °C (Equ. 6.17). Further enrichment of the composition by B_2O_3 would finally lead to liquid GdB_3O_6 with a melting point of T_M <1275°C (Equ. 6.18).

The pre-oxidation of GdO coated specimens at 600°C was not considered to have a significant effect on the oxidation behavior of ZrB_2. No differences were found via XRD, SEM, and EDS analysis. The GdO coating (AC) will oxidize during the ramp-up phase at temperatures ≥600°C

and form a comprehensive Gd_2O_3 scale before the oxidation process of the ZrB_2 takes place at >1000°C. As a result, the starting conditions for AC and pre-oxidized specimens are the same at 1000°C for ramped oxidation (R/C). The proposed oxidation mechanism of GdO coated ZrB_2 (AC) for the initial oxidation period of ramped oxidation (R/C) at 1500°C is presented in Fig. 6.9.

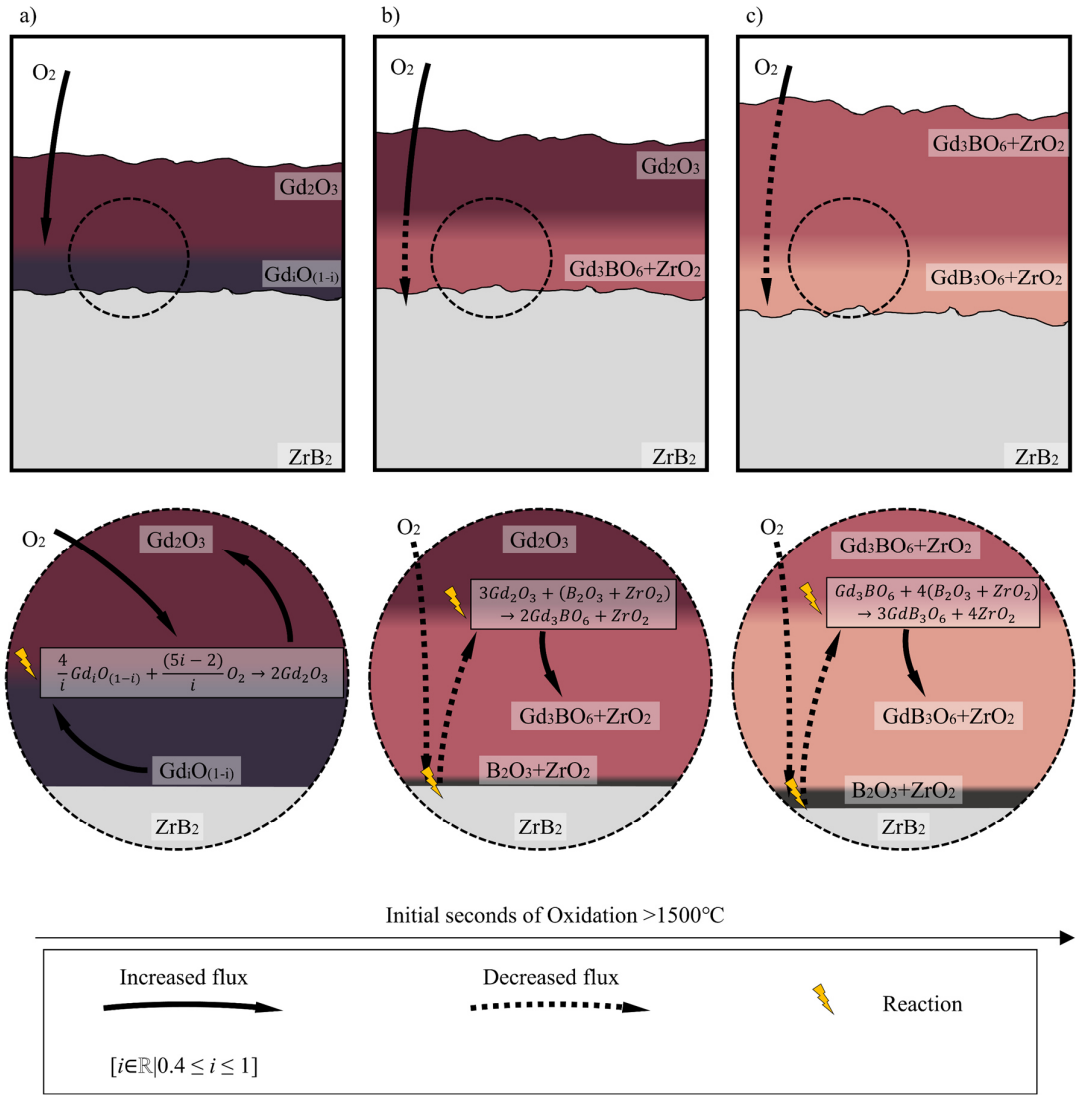

Fig. 6.9: Formation of liquid (Gd,B)O during the initial oxidation of GdO coated ZrB_2 (AC) at ≥1500°C

As mentioned above, the high affinity of GdO to oxygen leads to the formation of crystalline Gd_2O_3 at the surface by consuming enough oxygen during ramping up to 1000°C [167]. The volume expansion of the GdO coating might induce the observed horizontal cracks in the oxidized GdO coating (compare XRD pattern and cross-section in Fig. 5.55, Spec.D04) (Fig. 6.9a). Simultaneously, ZrB_2 may oxidize during ramping (>1000°C) and form ZrO_2 particles, dissolved in the liquid B_2O_3 (Oxidation front very thin and not measurable). The liquid B_2O_3 might react with the Gd_2O_3 as proposed in Equ. 6.17, forming solid Gd_3BO_6 (T_M ~1590°C) (Table 3.3, Fig. 3.5b) [131] (Fig. 6.9b). The continuous formation of B_2O_3 beneath the Gd_3BO_6 scale enriches the scale

and induces the formation of liquid GdB_3O_6 (T_M <1275°C) [131]. As a result, the liquefication of the (Gd,B)O scale will be inevitable with respect to the exposure time. The GdB_3O_6 liquid seems to inhibit the oxygen mobility to the oxidation front of ZrB_2 by enforcing the permeation of oxygen molecules through the liquid layer (Fig. 6.9c). The formation of GdB_3O_6 is assumed to be accelerated near the uncoated edges, since more B_2O_3 will be produced at the uncoated sides in the same time. As a result, liquid GdB_3O_6 forms at the sharp edges and infiltrates the formed oxide scale in the early stages of oxidation (Fig. 5.57d). Cooling enforces the solidification of the liquid solution as an amorphous glass in case of significantly reduced crystallization kinetics [166].

The phase diagram for the system Gd_2O_3-B_2O_3 revealed a limited solubility of B_2O_3 in the (Gd,B)O liquid at temperatures <1300°C [131]. Cooling might lead to the precipitation of B_2O_3 out of the GdB_3O_6 liquid. This would explain the globular bubbles inside the (Gd,B)O phase, which were found to be filled by B_2O_3 and several ZrO_2 dendrites in fractured cross-sections (Fig. 5.58b, Spec.D12). No comprehensive porous ZrO_2 scale has formed at the center of the specimen beneath the (Gd,B)O scale. This demonstrates already the protection of the underlying ZrB_2 by the GdO coating for ramped oxidation at 1500°C.

As a general statement, "GdO coating does not require any intermediate pre-oxidation heat treatment" to improve the oxidation behavior. However, a significant advantage of the pre-oxidized condition compared to AC can be seen in the presence of water (Fig. 5.54d, Fig. 5.55b). It is well known that rare-earths such as samarium (Sm) and gadolinium have a high affinity to water due to their high electropositivity [165, 168]. As a result, metallic gadolinium as well as the oxygen-doped gadolinium coating $Gd_iO_{(1-i)}$ are soluble in water, form hydroxides (compare Equ. 3.6), and get eroded in the presence of water (Fig. 5.54d) [124]. It can be assumed, the presence of water or increased humidity will have a dramatic effect on the oxidation behavior of GdO coated ZrB_2 (AC) and could lead to defects inside the coating or even the spallation of the coating. In contrast, the pre-oxidized GdO scale revealed an inert behavior to water at room temperature (compare Fig. 5.55b). The formation of Gd_2O_3 would ensure the stability of the coating against the exposure of water or moisture during storage. Nevertheless, more investigations are needed to make a clear statement regarding the benefits of pre-oxidation for the reliability of the coating.

6.3.2.2 Rapid oxidation of GdO Coated ZrB_2 (AC) at 1500°C

The Fig.6.10 describes the assumed oxidation mechanisms for rapid oxidation (P/Q) at 1500°C for the oxidation of 15 min, 30 min, and 60 min. As proven via cross-sectional analysis, a significant oxidation of the ZrB_2 substrate has been prevented for up to 15 min by forming a comprehensive and protective (Gd,B)O liquid solution at the surface (Fig. 5.61a). B_2O_3 liquid with dissolved ZrO_2 forms at the oxidation front of ZrB_2 and reacts with the Gd_2O_3 scale, following the proposed Equ. 6.17 and Equ. 6.18. Passive oxidation for the underlying substrate is provided by the decelerated permeation of oxygen molecules through the (Gd,B)O liquid layer to the oxidation front of ZrB_2. The formation of ZrO_2 dendrites can be observed at the oxidation front of ZrB_2. However, a comprehensive porous ZrO_2 did not form. (Fig. 5.67a-b).

Most of the surface is covered by the protective (Gd,B)O liquid after 30 min of oxidation. Surface observation revealed an increased amount of B_2O_3 at the surface (increase of darkish areas in BSE micrographs, Fig. 5.62a). The fractured cross-section proved an increased thickness of the liquid layer from ~226 µm after 15 min to ~322 µm after 30 min of oxidation (average thickness for the

formed glass bubble in the center of the specimen). This behavior can be attributed to the low evaporation rate of the (Gd,B)O liquid solution compared to liquid B_2O_3. Even during passive oxidation period, it is expected to form B_2O_3 liquid and ZrO_2 at the oxidation front of ZrB_2. The stabilization of the liquid B_2O_3 at 1500°C might induce the accumulation of protective liquid at the surface (formation of B_2O_3 >> evaporation of (Gd,B)O) and would increase the liquid layer thickness at the surface. Simultaneously, the growth of ZrO_2 grains inside the (Gd,B)O liquid can be observed at the former interface zone of the coating/substrate (Fig. 5.67c-d). The formation of mixed oxides such as $Gd_2Zr_2O_7$ was not observed (Fig. 5.70b, Spec.D42). However, high contrast BSE micrographs and EDS spot analysis proved the presence of two distinct (Gd,B)O liquids, which were distinguishable by the Zr content. The liquid at the surface/atmosphere contains ~8 at.% Zr. In contrast, the liquid, which encloses the ZrO_2 grains, contains 4 at.% Zr (Fig. 5.68, Spec.D37, Spec.D38). It is assumed that ZrO_2 dendrites formed during oxidation increase in size and form the enlarged grains with respect to time. The driving force might be liquid phase sintering. This mechanism requires, among other parameters, a solubility of the solidifying phase in the liquid solution, a reduced solubility of the liquid phase in the solid, an increased wettability of the solid phase by the liquid solution, and time for the sintering mechanism [160]. Considering the chemical composition of the ZrO_2 grains (Fig. 5.70, Spec.D42, no Gd content) and the surrounding (Gd,B)O phase (Fig. 5.70, Spec.D43, ~4 at.% Zr) the requirements for liquid phase sintering seems to be fulfilled and are consistent with the observations (Fig. 6.10b). Therefore, it is assumed, ZrO_2 will precipitate out of the (Gd,B)O liquid, decrease the amount of dissolved ZrO_2 in the enclosing (Gd,B)O liquid (decreases from ~8 at.% to ~4 at.% Zr), crystalize, and induce the growth of the ZrO_2 grains with respect to time (compare Fig. 6.10b).

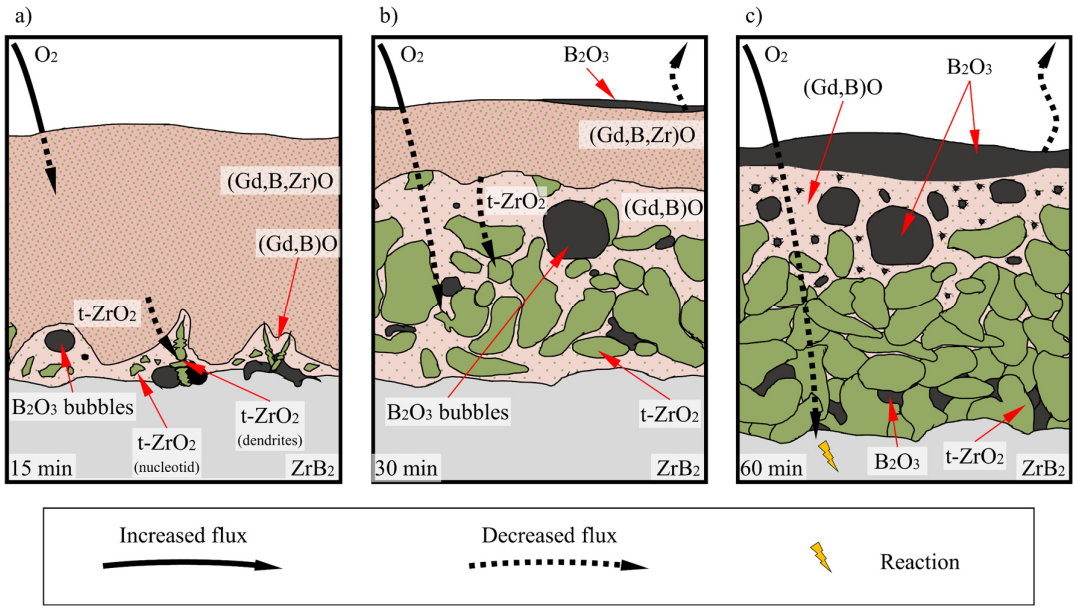

Fig. 6.10: Proposed oxidation mechanisms of GdO coated ZrB_2 at 1500°C for rapid oxidation with induced thermal shock: a) after 15 min of oxidation; b) after 30 min of oxidation; c) after 60 min of oxidation

The reduction of the (Gd,B)O liquid layer thickness was observed after 60 min of oxidation at 1500°C. Considering the phase diagram of Gd_2O_3-B_2O_3, the melting point of the liquid solution decreases with increasing amount of B_2O_3. The continuous enrichment of the (Gd,B)O liquid solution by B_2O_3 might lead to a more "boria-like" liquid solution at the surface, which would readily evaporate at 1500°C (compare Gd_2O_3-B_2O_3 phase diagram (Fig. 3.5b) [42]). The enhanced evaporation rate for the (Gd,B)O liquid solution might exceed the formation rate of B_2O_3 at the oxidation front of ZrB_2 (evaporation of (Gd,B)O >> formation of B_2O_3). Accordingly, the liquid layer thickness would decrease from ~322 µm after 30 min to ~241 µm after 60 min of oxidation (Fig. 5.67c&e). The continuous enrichment of the (Gd,B)O liquid by B_2O_3 is expressed by the formation of a B_2O_3 layer at the surface as well as several B_2O_3-filled bubbles in the residual (Gd,B)O liquid. The excess of B_2O_3 in the liquid solution might precipitate during cooling and form a continuous layer at the surface as well as several B_2O_3-filled bubbles inside the residual (Gd,B)O liquid. The liquid phase sintering of the ZrO_2 grains near the interface zone might continue and lead to the enlarged ZrO_2 grains after 60 min of oxidation (~12 µm in diameter). It can be expected that the grains will sinter together and form a dense oxide scale as the oxidation progresses >60 min (Fig. 6.10c) [160]. However, no comprehensive porous ZrO_2 oxide scale formed during the oxidation at 1500°C. This can be attributed to the protective nature of the (Gd,B)O liquid layer, which enforces the permeation of oxygen molecules even after 60 min of oxidation. The decreased oxidation might be the reason for the grain formation instead of a porous ZrO_2 scale. A decelerates oxidation would enable the full dissolution of the formed ZrO_2 in the (Gd,B)O liquid. With respect to time, single ZrO_2 grains form and induce the precipitation of the dissolved ZrO_2. As a result, dense grains appear instead of a porous ZrO_2 scale.

6.3.2.3 Oxidation of GdO Coated ZrB_2 (AC) at 1600°C

The oxidation at 1600°C affects the formation kinetics of the (Gd,B)O liquid solution, the B_2O_3 liquid, and the ZrO_2 grain growth. The mechanism after 15 min, 30 min , and 60 min of oxidation is presented in Fig. 6.11. The (Gd,B)O scale was found to be ~41 µm thick after 15 min. An increase in the oxidation temperature by 100°C results in an increased evaporation rate of the protective (Gd,B)O liquid solution. Further, the enrichment of the (Gd,B)O liquid by B_2O_3 will decrease the melting point of the liquid and might increase the evaporation rate of the liquid solution in the same time. This would explain the decreased liquid layer thickness at 1600°C. The enrichment of the liquid solution by B_2O_3 after 15 min at 1600°C manifests in the dominant precipitation of B_2O_3 liquid at the surface during cooling (Fig. 5.63). Typically, no continuous layer of B_2O_3 glass forms at the surface during the oxidation at 1600°C as it readily evaporates (compare Fig. 5.3 and Fig. 5.59)[42]. The cross-section of the tested specimen revealed the formation of enlarged ZrO_2 grains enclosed by residual (Gd,B)O liquid with reduced Zr content (Fig. 5.72b, Spec.D44). The enhanced evaporation of the protective (Gd,B)O liquid solution might affect the growth of the single ZrO_2 grains, promoting accelerated precipitation of ZrO_2 out of the liquid. As a result, enlarged grains of ~19 µm formed already after 15 min of oxidation at 1600°C. Furthermore, the accelerated processes enabled the formation of a porous ZrO_2 scale beneath the enlarged ZrO_2 grains with a thickness of ~25 µm. This indicates less protection of the ZrB_2 substrate by the liquid solution at higher temperatures and a more rapid oxidation process compared at 1500°C (not enough time and not enough liquid to dissolve the formed ZrO_2) (Fig. 6.11a).

Throughout the process, B_2O_3 liquid enriches the (Gd,B)O liquid solution with proceeding oxidation at 1600°C, destabilizing the protective liquid layer, and enforces the increased oxidation of the ZrB_2 substrate after 30 min of oxidation (Fig. 6.11b). Consequently, the porous ZrO_2 scale increased to ~33 µm in thickness. In the same time, the ZrO_2 grains sintered together and formed a comprehensive reaction scale of dense ZrO_2 with residual (Gd,B)O liquid solution along the sparsely distributed grain boundaries (Fig. 5.72d, Spec.D46). TEM analysis revealed a similar chemical composition and a monoclinic crystal structure for the porous and dense ZrO_2 at room temperature (Fig. 5.74c-d, Spec.D52-D53; Fig. 5.75b and Fig. 5.76b). HAADF micrographs and Debye-Scherrer diffraction revealed the formation of parallel domains in the dense ZrO_2 with similar crystal orientation (linear-type diffraction pattern, Fig. 5.76a)). This might indicate the formation of twins inside the dense m-ZrO_2 [52, 53, 56]. It is well known that dense t-ZrO_2 undergoes a martensitic transformation during cooling, forming dense m-ZrO_2 below ~1120 °C [46, 54]. The volume expansion of ~7 vol% during the transformation induces stresses and increases the internal energy of the dense m-ZrO_2 [43, 46, 54]. Shearing induces twinning inside the grains and reduces the stresses inside the dense m-ZrO_2 [46, 54, 55]. In contrast, porous m-ZrO_2 revealed arbitrary-shaped crystals with multiple orientations (ring-type diffraction pattern, Fig. 5.75a). The pores in the porous ZrO_2 enable the volume expansion without inducing stresses. Therefore, no twinning was observed in the porous ZrO_2. Finally, this results prove that the grain growth of ZrO_2 must be induced at elevated temperatures via liquid phase sintering of t-ZrO_2 grains and/or the precipitation of t-ZrO_2 out of the (Gd,B)O liquid during the evaporation of the protective liquid. During cooling, the dense t-ZrO_2 scale undergoes martensitic transformation and form dense m-ZrO_2 with twinned crystals as observed [54]. From this it can deduced, the dense t-ZrO_2 as an uppermost layer will reduce the Knudsen diffusion of oxygen molecules to the underlying oxidation front at elevated temperatures, following the observations of Parthasarathy et al. [43, 73, 144] (Fig. 6.11b).

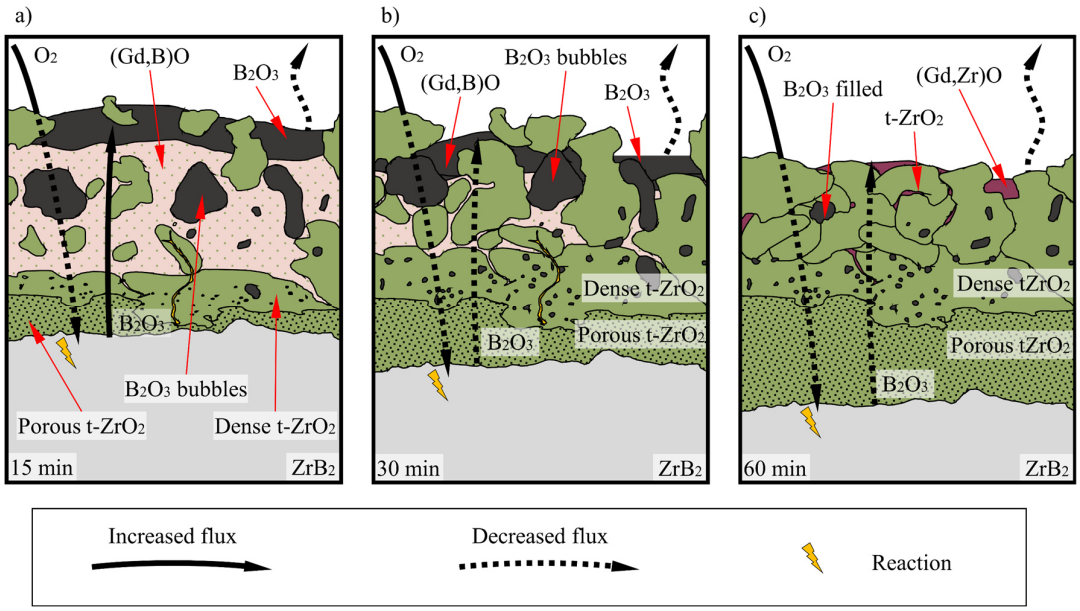

Fig. 6.11: Proposed oxidation mechanisms of GdO coated ZrB_2 at 1600°C for rapid oxidation with induced thermal shock: a) after 15 min of oxidation; b) after 30 min of oxidation; c) after 60 min of oxidation

Further oxidation at 1600°C up to 60 min increases the density of the uppermost section of the oxide scale, forming a dense t-ZrO_2 reaction scale at elevated temperatures with a thickness of ~38 µm. A phase with ~11 at.% Zr, ~19 at.% Gd and ~70 at.% O formed along the residual grain boundaries of the ZrO_2 grains at the uppermost section of the reaction scale (Fig. 5.72f, Spec.D51). Considering the reduced oxygen content for this phase compared to (Gd,B)O liquid (i.e. Fig. 5.67, Spec.D34 with ~82 at.% O), the phase might be assigned as $Gd_2Zr_2O_7$ or Gd_2O_3 with dissolved ZrO_2 ((Gd,Zr)O). The B_2O_3 content in the (Gd,B)O liquid might evaporate and left behind the residuals of the former (Gd,B)O liquid solution. (Gd,Zr)O will be present as a solid phase at 1600°C (compare phase diagram of the Gd_2O_3-ZrO_2 system, T_M~2300°C, Fig. 3.5a) [129]. Therefore, the presence of (Gd,Zr)O in between the sparsely distributed grain boundaries of the dense t-ZrO_2 scale will increase the density of the reaction scale. Further densification due to liquid phase sintering of a (Gd,B)O liquid is not expected after 60 min at 1600°C (Fig. 6.11c).

6.3.2.4 Oxidation of GdO Coated ZrB_2 (AC) at 1700°C

The oxidation at 1700°C requires more detailed investigations for short-term oxidation <15 min to describe the exact processes of the first few minutes. Based on the gained information at lower temperatures, the following hypothesis is carried out for the oxidation of GdO coated ZrB_2 (AC) at 1700°C.

At 1700°C, rapid oxidation of the ZrB_2 substrate proceeds by forming a non-protective porous ZrO_2 scale and liquid B_2O_3 at the oxidation front. The B_2O_3 will react instantaneously with the Gd_2O_3 and form the protective (Gd,B)O liquid solution already in the zeroth minute of oxidation at 1700°C (compare Fig. 6.9). Simultaneously, (Gd,B)O liquid might infiltrate the porous ZrO_2 scale and induce the densification of the uppermost section of the ZrO_2 oxide scale, forming dense t-ZrO_2 (Fig. 6.12a).

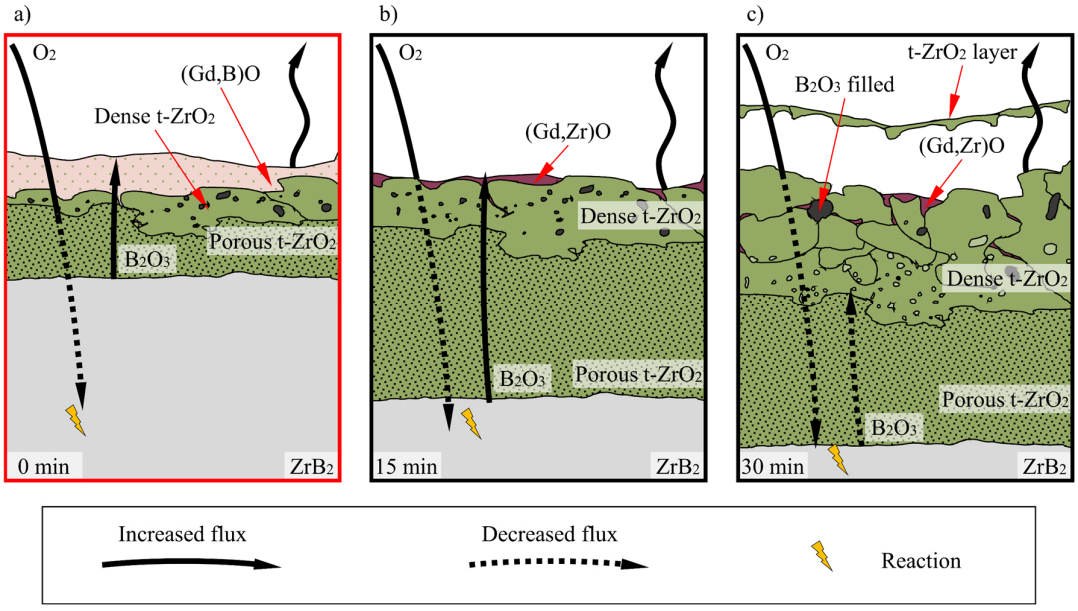

Fig. 6.12: Proposed oxidation mechanisms of GdO coated ZrB_2 at 1700°C for rapid oxidation with induced thermal shock: a) after 0 min of oxidation; b) after 15 min of oxidation; c) after 30 min of oxidation

With progressing oxidation up to 15 min at 1700°C, mostly all liquid B_2O_3 evaporated and exposed the dense ZrO_2 scale with residual grain boundaries. Some boundaries were found to be filled with residual B_2O_3 glass (Fig. 5.65a). It can be assumed that the densified ZrO_2 scale enables the migration of B_2O_3 liquid from the oxidation front of ZrB_2 through the last open channels to the surface. Several engraved crystals cover the surface, revealing a chemical composition of Gd_2O_3 with dissolved ZrO_2 (Fig. 5.65, Spec.D25). X-ray diffraction pattern did not reveal reflections for Gd_2O_3 (Fig. 5.60a). Although, the reflections for Gd_2O_3 could be obscured due to the dominant reflections of m-ZrO_2. Cross-section proved the densification of the uppermost section (Fig. 5.77b) as well as the presence of (Gd,Zr)O along residual grain boundaries of the dense reaction scale. As mentioned above, no further densification by liquid phase sintering is assumed at this stage of oxidation since Gd_2O_3 nor $Gd_2Zr_2O_7$ will melt at temperatures <1700°C (compare Table 3.3) [129] (Fig. 6.12b).

The architecture of the oxide scale does not change at 1700°C by time. An uppermost reaction scale of densified ZrO_2 with residual (Gd,Zr)O along the grain boundaries can be found, which covers a porous ZrO_2 scale (Fig. 5.77c-f). The reaction scale increased by size from ~38 µm after 15 min to ~72 µm after 30 min, even though when liquid phase sintering by (Gd,Zr)O is not expected. B_2O_3-filling of residual porosities in the dense reaction scale as well as in the porous ZrO_2 has been proven (Fig. 5.77e-f). It is expected, B_2O_3 migrates through the residual pores and channels in the densified t-ZrO_2 reaction scale from the oxidation front to the surface and finally evaporate at the surface. As a result, the precipitation of t-ZrO_2 at elevated temperatures can be expected and might induce the growth of the densified oxide scale with respect to time at 1700°C. It should be emphasized, the formation of the thin and detached ZrO_2 layer as an uppermost section of the oxide scale (Fig. 5.77c) could not be understood and must be investigated thoroughly by doing several repetitive experiments (Fig. 6.12c).

6.3.3 Oxidation Kinetics of GdO Coated ZrB_2

Compared to baseline ZrB_2, the reduced parabolic oxidation rate constants for GdO coated ZrB_2 (AC) show clearly that the applied GdO coating has a beneficial effect on improving the oxidation resistance of ZrB_2 (Table 5.1, Table 5.36).

At 1500°C, the protection of the substrate was solely attributed by the presence of the liquid solution (Gd,B)O at the surface. The oxidation of ZrB_2 and the formation of a porous t-ZrO_2 scale has been prevented for an exposure of up to 30 min, providing passive oxidation. The formation and accumulation of a stabilized liquid solution (Gd,B)O at the surface protected the underlying ZrB_2 against oxidation and inhibited the oxygen molecules from reaching the former interface of the coating/substrate. After 60 min of oxidation, several grains of ZrO_2 sintered together, to form a porous structure with residual liquid at the grain boundaries and in the pores. This was counted as a porous oxide scale for to kinetic calculations. As a result, the parabolic oxidation rate constant for the porous ZrO_2 scale increases slightly with respect to the time between 30 min to 60 min at 1500°C (Fig. 5.77a, Table 5.36). The oxidation will be diffusion controlled (permeation of oxygen through the liquid layer), as long as the protective liquid remains as a comprehensive layer at the surface and ensures passive oxidation with significant reduced oxidation rate constants compared to baseline ZrB_2.

The exposure at 1600°C induced the formation of a three-layer architecture, consisting of a thin liquid layer of (Gd,B)O, a dense t-ZrO_2 scale, and a B_2O_3-filled porous t-ZrO_2 scale. The synergy of the protection mechanisms (permeation of oxygen molecules through the liquid layer, reduced Knudsen diffusion through the densified reaction scale) induced the reduction of the porous ZrO_2 scale formation by -70% and -82% after 15 min and after 30 min of oxidation compared to baseline ZrB_2 and provided passive oxidation and significant reduced oxidation rate constants (compare Fig. 5.78a, Table 5.36). However, the increase of the activation energy for the temperature regime of 1500°C to 1600°C for 15 min and 30 min of oxidation can be attributed to the steady loss of the comprehensive liquid solution with increasing temperature (Fig. 5.78b, steep slope between 1500°C to 1600°C). After 60 min at 1600°C, the oxidation rate constant increases and indicates a change of the protection mechanism (Fig. 5.78). The protective liquid evaporates and leaves behind the dense reaction scale. The dense t-ZrO_2 scale reduces the Knudsen diffusion of oxygen molecules through the oxide scale to the oxidation front of ZrB_2 and controls the kinetics during the oxidation of 30 min to 60 min at 1600°C (Equ. 2.16, Equ. 2.17) [43]. The increase of the oxidation rate can be seen as the proof, that the liquid is more protective than the densified ZrO_2 scale. However, the reduction of the porous oxide scale formation (~55%) and the significant reduction of the parabolic oxidation rate constant for GdO coated ZrB_2 confirms the protective nature of the dense t-ZrO_2 scale even after 60 min at 1600°C (compare Table 5.1 and Table 5.36).

At 1700°C the protective nature is solely attributed to the densified reaction scale and residual Gd_2O_3 at the grain boundaries of the reaction scale. Similar oxidation rate constants were calculated for the exposure of 15 min and 30 min. Simultaneously, the applied GdO coating induced a reduction of the porous ZrO_2 scale at 1700°C by -64% after 15 min and -60% after 30 min of exposure compared to baseline ZrB_2 (Table 5.1, Table 5.36). The protection of the system at 1700°C solely based on the dense reaction scale and the reduced Knudsen diffusion of oxygen molecules [43, 73, 144]. In comparison, the oxidation rate constant for the oxidation of 60 min at 1600°C aligns with the rate constants at 1700°C since it based on the similar protection mechanism (no protective liquid, protection solely due to the dense reaction scale). The calculated activation energy for an exposure up to 30 min decreases in the temperature regime of 1600°C to 1700°C (Fig. 5.78b, flatter slope between 1600°C to 1700°C). This again, indicates the loss of the protective liquid, which depends on the temperature, and the transition to a temperature independent protection mechanism. Therefore, controlled oxidation kinetics can be expected even at higher temperatures (activation energy might decrease further with the oxidation temperature). However, this must be proven by experiments.

Overall, the comparison with the baseline ZrB_2 revealed a significant improvement in the oxidation resistance for temperatures up to 1700°C till 30 min, which covers the targeted exposure time for multiple reentries or long-term flight operations (compare Fig. 2.2).

Based on the parabolic rate constants and the activation energies shown in Fig. 5.78 and Table 5.37, the following important statements can be made for GdO coated ZrB_2 (AC):

Oxidation at 1500°C: Passive oxidation period at temperature ≤1500°C due to the stabilization of the liquid solution (Gd,B)O at the surface. The liquid solution ensures diffusion-controlled oxidation for up to 30 min by enforcing the permeation of oxygen molecule through the liquid layer.

A certain increase in the oxidation rate constant can be seen for oxidation between 30 min to 60 min in case of the evaporation of the protective liquid layer.

Oxidation at 1600°C: Limited passive oxidation period with low parabolic rate constants at 1600°C due to the increased evaporation rate of the protective liquid solution (Gd,B)O and the loss of the liquid after 30 min of oxidation. The densification of the oxide scale offers protection by forming a dense reaction scale. The dense reaction scale reduces the Knudsen diffusion through the forced oxide scale and inhibit the presence of oxygen at the oxidation front of ZrB_2.

Oxidation at 1700°C: Oxidation protection occurs for an exposure of up to 30 min. The protective nature belongs to the formation of a dense secondary t-ZrO_2 scale at the surface, which reduces the Knudsen diffusion to the oxidation front of ZrB_2.

6.3.4 Conclusions of GdO Coated ZrB_2

- A GdO coating of ~11 µm in thickness is successfully applied on ZrB_2 by reactive magnetron sputtering, revealing resistance against thermal shocks up to 1700°C.
- The formation of a protective liquid solution (Gd,B)O at the surface inhibits the oxygen mobility and protects the ZrB_2 against oxidation.
- Liquid phase sintering and/or the precipitation of ZrO_2 induces the formation of a dense t-ZrO_2 scale during exposure, which controls the oxygen mobility to the underlying ZrB_2.
- The synergy of the liquid solution (Gd,B)O and the dense t-ZrO_2 scale prevents the oxidation of the ZrB_2 substrate for the exposure of up to 30 min at 1500°C.
- A significant reduction of the formation of a porous ZrO_2 scale by -80% and -61% in thickness can be observed at 1600°C and 1700°C after 30 min of oxidation.
- The oxidation mechanism changes after >30 min of oxidation due to the loss of the protective nature of the liquid solution at 1600°C.
- Steady oxidation conditions can be found at 1700°C, provided by the dense reaction scale at the uppermost section of the oxide scale from the first minute of oxidation up to 30 min.

The applied GdO coating (~11 µm thick) provided a significant improvement of the oxidation resistance of ZrB_2 at temperatures up to 1700°C for an exposure till 30 min. A dense microstructure for the coating is not needed for the protective mechanisms of the GdO coating, since it forms horizontal cracks during oxidation and a comprehensive liquid layer with the B_2O_3. Therefore, the passive oxidation period might be extended for a longer exposure time by increasing the coating thickness. The increased thickness might enhance the thickness of the (Gd,B)O liquid, dissolve more B_2O_3 liquid, and ensure increased stability of the glass. Possible coating methodologies for increased coating thicknesses could be EB-PVD. Therefore, the results encourage further experiments at higher temperatures, longer exposure times, increased coating thickness, and other coatings.

7 Conclusions and Future Aspects

Three different coatings were deposited on ZrB_2 by means of (reactive) magnetron sputtering (HfO_2, metallic Nb, and GdO). As described and discussed in detail, the coatings have affected the oxidation behavior of ZrB_2 by inducing distinct oxidation mechanisms. In the following, the coating performances are compared with each other with respect to the reduction of the porous oxide scale formation (Table 5.1, Table 5.10, Table 5.23, Table 5.36). The results are presented in Fig. 7.1and reveal the beneficial effect of coatings on the oxidation resistance of ZrB_2.

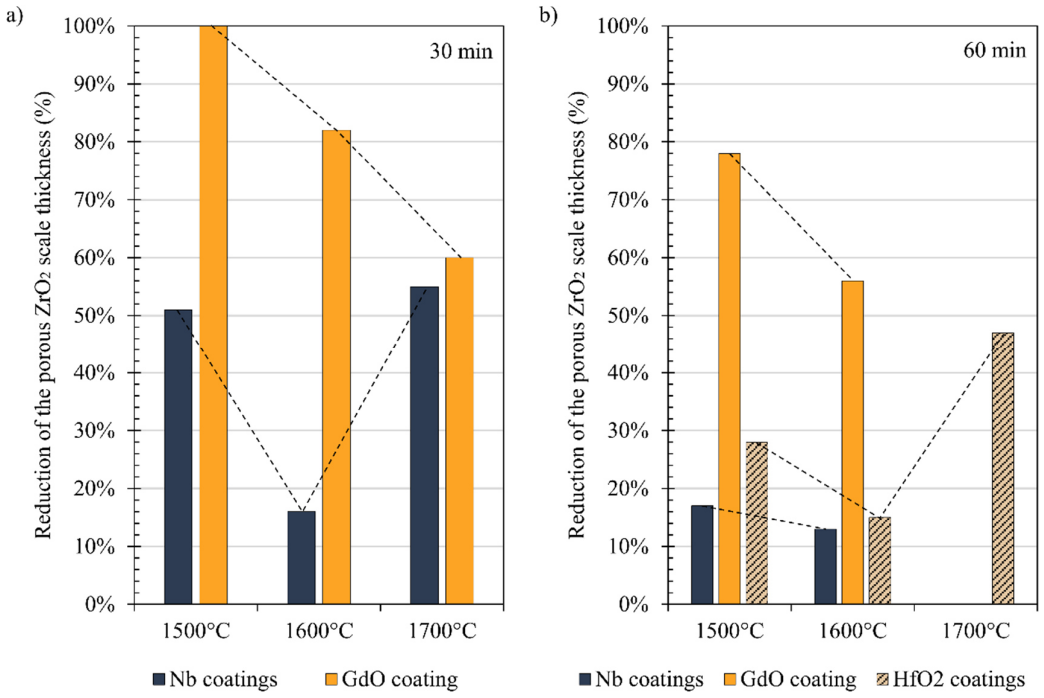

Fig. 7.1: Reduction of the porous oxide scale thickness (PS) compared to baseline ZrB_2 by applied coatings with corresponding trend (dashed line): a) after 30 min of oxidation; b) after 60 min of oxidation

Performance up to 30 min of oxidation: The Arrhenius plots for the coated specimens and baseline ZrB_2 after 30 min of oxidation are presented in Fig. 7.2. Baseline ZrB_2 reveals a steady increase of the oxidation rate constants with respect to temperature with similar activation energies in the temperature regime of 1500°C to 1700°C (straight line for ZrB_2). In contrast, changing slopes/activation energies with respect to temperature of coated specimens reveal the change of protection mechanisms for the substrate (protection by liquid layer at lower temperatures, protection by dense and solid oxide scale at elevated temperatures). The decreased oxidation rate constants compared to baseline ZrB_2 prove the protection of the substrate. Detailed information about the protection mechanisms was discussed in the separate chapters of the discussion (Chapter 6.1.2, 6.2.2, Chapter 6.3.2). Full oxidation protection was provided by GdO coatings for an exposure up to 30 min at 1500°C (-100%). An increase in the oxidation temperature decreases its performance (-82% at 1600°C, -60% at 1700°C). In contrast, the protective nature of Nb coatings decreases significantly between 1500°C (-51%) to 1600°C (-16%). However, a further increase in

temperature to 1700°C enhances the performance of the Nb coating (-55%). The reduction of the porous oxide scale formation of GdO coated and Nb coated ZrB_2 compared to baseline ZrB_2 and the trends of the performance of the coatings (dashed lines) are visualized in Fig. 7.1a.

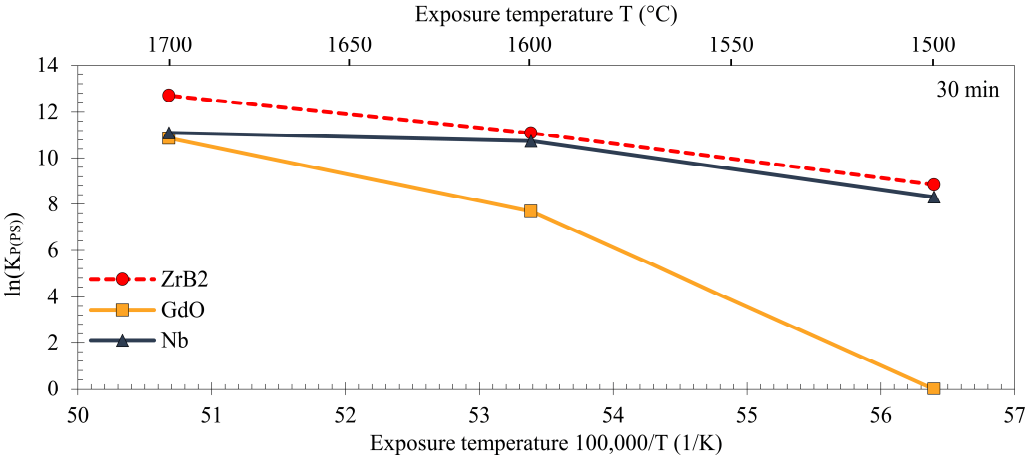

Fig. 7.2: Oxidation rate constants of tested specimens for an exposure of 30 min vs. the inverted oxidation temperature (Arrhenius plot for Nb coated ZrB_2, GdO coated ZrB_2, baseline ZrB_2)

The better performance of the GdO coating compared to Nb coatings for temperatures up to 1600°C is attributed to the more protective (Gd,B)O liquid solution at the surface. The liquid provides a reduced evaporation rate compared to the (Nb,B)O liquid solution or baseline B_2O_3. At 1700°C, both coatings revealed similar protection performance for an exposure of 30 min by forming a dense oxide scale as an uppermost section. The presence of the stabilized liquid induced liquid phase sintering and the densification of the uppermost section of the oxide scale. Further, the evaporation of B_2O_3 glass with dissolved ZrO_2 led to the precipitation of ZrO_2 at the densified oxide scale and increased its protection mechanism with respect to time. In contrast, no densification of the oxide scale was observed for baseline ZrB_2. Consequently, the rate constants increase further at 1700°C.

Performance up to 60 min of oxidation: The Fig. 7.3 presents the Arrhenius plots after 60 min of oxidation for all tested specimens (HfO_2 coated, Nb coated, GdO coated, baseline ZrB_2). An increase in the exposure time from 30 min to 60 min does not affect the oxidation kinetics of baseline ZrB_2. In contrast, the tested coatings revealed protection against oxidation even after 60 min at all test conditions (reduced oxidation rate constants). However, this effect is much more pronounced in the case of GdO coatings and less evident for HfO_2 and Nb coatings. GdO coatings provided a protective nature for up to 60 min at 1500°C (-78%) and 1600°C (-56%) due to the residual liquid at the surface as well as the densification of the solid oxide scale.

The Nb coating and HfO_2 coating provided protection against oxidation. However, compared to the GdO coatings, a reduced protection performance at 1500°C (-16% for Nb, -28% for HfO_2) and 1600°C (-13% for Nb, -15% for HfO_2) can be observed. An interesting highlight, which must be emphasized, is the protection of the HfO_2 coating at 1700°C after 60 min of oxidation. As visible in the Arrhenius plot, the activation energy for the temperature regime of 1600°C to

1700°C for oxidation up to 60 min decreases significantly compared to baseline ZrB_2. This indicates controlled oxidation conditions, independent of temperature. This might be attributed to the densification of the uppermost section of the oxide scale by the precipitation of secondary ZrO_2 (compare Chapter 6.2.1).

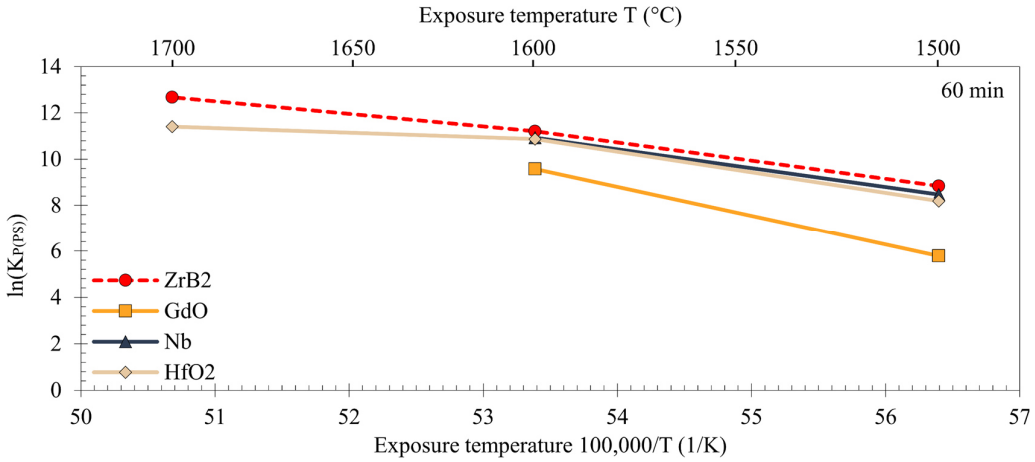

Fig. 7.3: Oxidation rate constants of tested specimens for an exposure of 60 min vs. the inverted oxidation temperature (Arrhenius plot for Nb coated ZrB_2, GdO coated ZrB_2, HfO_2 coated ZrB_2, baseline ZrB_2)

The following final statements can be made:

- Overlay coatings on ZrB_2 decrease the oxidation kinetics at temperatures up to 1700°C for 15 min, 30 min and 60 min. Coatings are potential solutions to improve the oxidation resistance of diboride based UHTC components for hypersonic applications, such as TPS, leading edges, or nose tips.
- Liquid glass stabilization improves the oxidation behavior significantly at temperatures up to 60 min at 1600°C and provides limited protection. The performance depends on the liquid layer thickness, time, and temperature (distinct evaporation rate at specific temperatures).
- Dense overlay coatings provide a certain protection, as long as the coating remains at the surface as a dense scale without defects. The protection is limited and depends on its thickness, oxygen diffusivity, and thermal stability. Once, liquid B_2O_3 forms beneath the coating, the accumulation of the liquid might induce spallation.
- Metal oxide scale densification provides protection and ensures diffusion-controlled oxidation kinetics at elevated temperatures, once the scale is formed. The densification of the uppermost section of the oxide scale depends on time and temperature (precipitation of secondary ZrO_2 and/or liquid phase sintering). Significant densification and improvement can be observed at 1700°C for all tested coating solutions.
- GdO coatings have been proven to be the best performer in this study. Long-term passive oxidation up to 60 min at 1600°C is provided by a protective liquid layer. The densification of the oxide scale induces diffusion-controlled oxidation kinetics at temperatures up to 1700°C for an exposure of up to 30 min.

Till now, in steady atmospheric conditions, glass stabilizers as a coating perform better than dense coatings. Considering hypersonic flights, the enhanced stream of atmospheric molecules will induce shear forces at the surfaces of leading edges and nose tips. A dense oxide scale would withstand the harsh environment, whereas a protective liquid might be blown away. Therefore, the densification of the oxide scale can be seen as the key mechanism to prevent the oxidation of diboride-based UHTCs as hypothesized by Parthasarathy [43] and has been proved in this work. All the applied coatings have served the purpose of scale densification and enhanced protection. However, according to the results of this study, several aspects might be considered for future work in the promising research field of protective overlay coatings for UHTC materials.

First of all, an increased coating thickness might extend the protective nature of the applied coatings. The coating method of (reactive) magnetron sputtering is limited to a coating thickness of up to ~20 µm. An increase in the coating thickness might induce spallation in case of the dense microstructure. To achieve a reliable coating thickness of up to ~100 µm, coating techniques such as EB-PVD might be an appropriate solution. The columnar structured coatings enable the needed volume contraction of the coating and prevent its spallation. A thick coating of metallic Nb or GdO would extend the passive oxidation period by forming a more protective liquid solution at the interface zone of the coating/substrate. The extended period of liquid coverage might improve the densification process of the oxide scale during oxidation (extended time for liquid phase sintering) and would increase the thickness and density of the protective dense oxide scale.

In contrast, the functionality of the HfO_2 coating does not belong to the liquid formation. The dense microstructure of the coating is mandatory for its functionality. A thicker coating would improve the performance. However, the columnar and porous structure of EB-PVD coatings would not ensure the needed protection mechanisms. An opportunity would be a multilayer system with an EB-PVD coating of HfO_2 (columnar structure) as an intermediate layer and a dense magnetron sputtered coating of ~10-15 µm as a protective top layer. The intermediate columnar coating would enable the inevitable volume expansion due to the formation of B_2O_3 liquid at the interface zone and would avoid the spallation of the coating. Simultaneously, the diffusion of Zr cations into the dense HfO_2 top-layer coating would be prevented and would ensure extended stability and density.

Another aspect could be the application of new coatings on diboride-based UHTCs. An appropriate candidate might be the deposition of Al_2O_3 as a protective overlay coating. The long-term oxidation tests of the HfO_2 coatings (1700°C, 60 min of oxidation) revealed the reaction of liquid Boria and the alumina powder/crucible (compare Fig. 5.22c). The cross-section proved the stability of the reaction product at 1700°C for 60 min. Similar to the tested GdO coating, an alumina-based coating might react with the liquid boria at the surface and form a more protective liquid solution compared to baseline B_2O_3. The formation of an aluminum borate layer (e.g. $Al_{18}B_4O_{33}$) at the surface might provide the needed oxidation protection for the underlying ZrB_2 substrate. Further, the liquid solution could infiltrate the porous ZrO_2 scale and might induce the liquid phase sintering mechanisms as observed for the GdO coating and metallic Nb coating (compare Fig.5.48, Fig.5.67) [169, 170].

As already observed, the surface condition of the substrate has an overriding priority for the functionality and adhesion of the coating. Rougher surfaces ensured the adhesion of the HfO_2 coatings

compared to polished surfaces (see Chapter 5.2.1). Specific designed surface conditions (e.g. microstructured, polished, laser-treated, …) could improve the performance of the coatings during oxidation. Furthermore, the surface condition might affect the wettability of the liquid reaction products. Textured or structured surfaces could control the distribution of the liquid at the surface and might avoid the accumulation in the center of the specimens as observed for Nb coatings (compare Fig.5.40) or GdO coatings (compare Fig.5.56, Fig.5.59).

Besides coating and surface engineering, alternative analysis methods must be considered to understand the observed mechanisms such as the densification of glass formation in detail. An important factor is the behavior of the liquid reaction products at the surface (evaporation rate, viscosity, wettability of surfaces, reactivity, …). High-temperature viscosity measurements and thermogravimetric analysis of the liquid reaction products could be used to adjust the properties of the borate glass for improved performance (glass modifier, glass former, glass stabilizer). As mentioned above, the densification of the oxide scale is mandatory for oxidation protection once the protective liquid evaporates. In order to verify the densification of the protective oxide scales (dense coatings or densification due to liquid phase sintering), a detailed analysis by means of the FIB "slice and view" technique or a Nano-CT scan could be carried out.

Finally, the application of the tested coatings of this study should be applied on different diboride UHTC materials. A predestined alternative might be carbon fiber-reinforced UHTCs, also known as UHT ceramic matrix composites (UHTCMCs). Monolithic ZrB_2 applications such as tips of hypersonic vehicles will experience an extremely high thermal shock during operation. Several plasma wind tunnel tests proved that the lack of thermal shock resistance of monolithic ZrB_2 might lead to failure during operation in hypersonic environments. A test-setup for a ZrB_2 nose tip in a plasma wind tunnel can be seen in Fig.8.1. The low thermal shock resistance induced the failure of the nose tip. The high thermal shock resistance of UHTCMCs provokes its usability for such kind of applications. However, its low oxidation resistance must be improved. [162, 163].

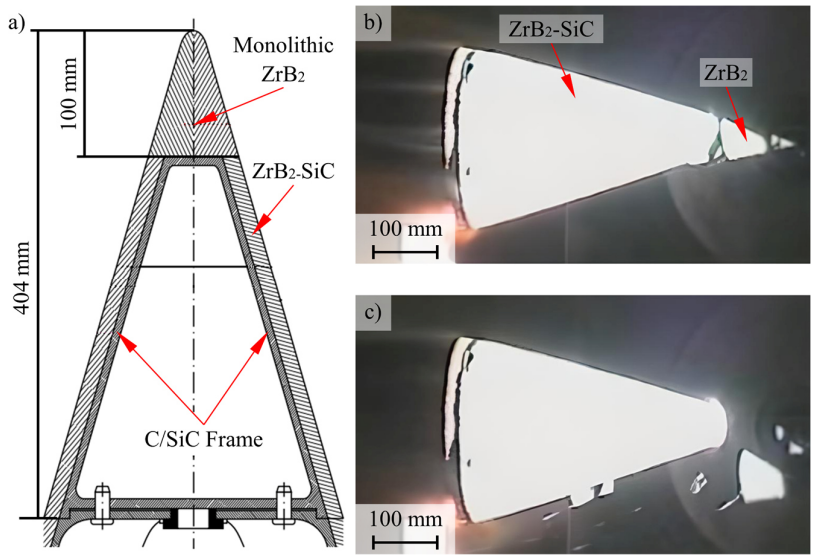

Fig. 7.4: a) Construction of tested nose with monolithic ZrB_2 tip; b-c) Thermal shock induced failure of the nose tip during plasma wind tunnel test [13]

As a ground-breaking step, the tested coatings in this study (HfO_2, metallic Nb, GdO-based coatings) could be applied on UHTCMCs to provide the oxidation protection of the substrate during oxidation. Similar reactions with the matrix, mostly ZrB_2 or ZrB_2-SiC, can be expected as observed in this study with monolithic ZrB_2. The stabilization of the protective liquid at the surface as well as the densification of the oxide scale due to liquid phase sintering might increase the oxidation resistance of the UHTCMCs. New challenges for the tested coatings on UHTCMCs must be considered, such as the rougher surface, the carbon fibers, and the formation of gaseous components such as CO or CO_2 during oxidation. However, the tested coatings in this study might be an appropriate solution to improve the oxidation resistance of the UHTCMC. The thermal shock resistance of UHTCMCs in combination with the oxidation protection by the applied coatings would ensure the reusability of hypersonic applications such as nose tips or leading edges.

Finally, protective overlay coatings for UHTCs represent a completely new research field and have a high potential to be established in the UHTC community. As presented, extensive investigation of different coatings on various UHTC materials such as carbides (TaC, ZrC, HfC) or nitrides (ZrN, HfN, TaN) or UHTCMCs needs to be carried out and new testing methodologies must be considered for detailed analysis to fully exploit the potential of oxidation protective coatings on UHTCs.

List of Publications

Scientific Publications

(1) Förster J.E., Fahrenholtz W.G., Hilmas G.E., Naraparaju R., Journal of the European Ceramic Society, Oxidation behavior of Nb-coated zirconium diboride 43, 5174-82 (2023). https://doi.org/https://doi.org/10.1016/j.jeurceramsoc.2023.04.029

(2) Förster J.E., Fahrenholtz W.G., Hilmas G.E., Naraparaju R., Journal of the European Ceramic Society, Hafnium oxide coating to improve the oxidation behavior of zirconium diboride 44 (2024). https://doi.org/https://doi.org/10.1016/j.jeurceramsoc.2024.116774

(3) Förster J.E., Fahrenholtz W.G., Hilmas G.E., Naraparaju R., Journal of the European Ceramic Society, Oxygen-doped gadolinium coating to improve the oxidation behavior of zirconium diboride (submitted).

(4) Vinci A., Förster J.E., Naraparaju R., Sciti D., Journal of Advanced Ceramics, Oxidation resistance of Nb coated ZrB_2/SiC-based UHTCMCs up to 1700°C (submitted).

(5) Förster J.E., Naraparaju R., Mechnich P., Fahrenholtz W.G., Hilmas G.E., Intention, Oxidation protective coatings for diboride based Ultra-High Temperature Ceramics, based on elemental aluminum and alumina mixtures. Application number: 63/663221, United States of America 2024.

(6) Förster J.E., Naraparaju R., Mechnich P., Fahrenholtz W.G., Hilmas G.E., Intention, Oxidation protective coatings for diboride based Ultra-High Temperature Ceramics, based on elemental aluminum and alumina mixtures. Application number: 10 2024 117 726.8, Germany 2024.

Oral Presentations

(7) 46th International Conference and Expo on Advanced Ceramics & Composites (ICACC22), "Oxidation behavior of Nb coatings on ZrB_2", Daytona Beach, FL, USA, 2022 (Presenter)

(8) Ultra-High Temperature Ceramics: Materials for Extreme Environment Applications V, "Influence of Nb coating on the oxidation behavior of ZrB_2" Snowbird, UT, USA 2022 (Presenter)

(9) 47th International Conference and Expo on Advanced Ceramics & Composites (ICACC22), "Effect of HfO_2 coatings on the oxidation behavior of ZrB_2", Daytona Beach, FL, USA, 2023 (Presenter)

(10) 1st international Workshop for UHTCs and UHTCMCs at DLR, "Protective overlay coatings for UHTCs", Cologne, Germany 2023 (Organizer/Presenter)

(11) 48th International Conference and Expo on Advanced Ceramics & Composites (ICACC22), "Processing of Nb coatings on ZrB_2 and C-ZrB_2/SiC composites", Daytona Beach, FL, USA, 2024 (Presenter)

(12) 48th International Conference and Expo on Advanced Ceramics & Composites (ICACC22), "Oxidation resistance of UHTCMCs up to 1700°C: Influence of Nb coatings", Daytona Beach, FL, USA, 2024 (Co-author)

(13) 48th International Conference and Expo on Advanced Ceramics & Composites (ICACC22), “Effectiveness of YFeSi oxides as a CMAS-resistant layer for EBCs”, Daytona Beach, FL, USA, 2024 (Co-author)

(14) Ultra-High Temperature Ceramics: Materials for Extreme Environment Applications VI, “Influence of GdO coatings the oxidation behavior of zirconium diboride” Giardini Naxos, Messina, Sicily, Italy, 2022 (Presenter)

(15) Ultra-High Temperature Ceramics: Materials for Extreme Environment Applications VI, “Nb-based coatings to improve the oxidation resistance of UHTCMCs at 1700°C” Giardini Naxos, Messina, Sicily, Italy, 2022 (Co-author)

References

1. Dinius, D. *X-15 hypersonic research program*. 2024 [cited 2024 June 28]; Available from: https://www.nasa.gov/reference/x-15/.
2. Dinius, D. *X-43A Hyper-X*. 2024 [cited 2024 June 28]; Available from: https://www.nasa.gov/reference/x-43a/.
3. Huang, A. *Thermal protection materials branch – Reusable materials*. 2023 [cited 2024 June 28]; Available from: https://www.nasa.gov/general/thermal-protection-materials-branch-reusable-materials/.
4. Lockheed, M. *Creating the Blackbird*. 2020 [cited 2024 June 28]; Available from: https://www.lockheedmartin.com/en-us/news/features/history/blackbird.html.
5. Statista, R., Department. *Global turnover of the space economy from 2009 to 2021*. 2022 28.03.2024 [cited 2024 August 14]; Available from: https://www.statista.com/statistics/946341/space-economy-global-turnover/.
6. Padture, N.P., *Advanced structural ceramics in aerospace propulsion.* Nature Materials, 2016. **15**: p. 804-809.
7. Adams, K. *What was project Mercury?* 2008 [cited 2024 August 10]; Adams, Kaitlyn:[Available from: https://www.nasa.gov/learning-resources/for-kids-and-students/what-was-project-mercury-grades-5-8/.
8. Garcia, M.A. *Sierra Space's Dream Chaser New Station Resupply Spacecraft for NASA*. 2023 [cited 2024 August 22]; Available from: https://www.nasa.gov/missions/station/commercial-resupply/sierra-spaces-dream-chaser-new-station-resupply-spacecraft-for-nasa/.
9. Hypersonix. 2024 [cited 2024 July 31]; Available from: https://www.hypersonix.com/technology/visr.
10. Fahrenholtz, W.G. and Hilmas, G.E., *Ultra-high temperature ceramics: Materials for extreme environments.* Scripta Materialia, 2017. **129**: p. 94-99.
11. Lewis, M.J., *Sharp leading edge hypersonic vehicles in the air and beyond.* SAE Transactions, Journal of Aerospace, 1999. **108**(1): p. 841-851.
12. Opeka, M., et al., *Oxidation-based materials selection for 2000°C hypersonic aerosurfaces: Theoretical considerations and histroical experience.* Journal of Materials Science, 2004. **39**: p. 5887-5904.
13. Alfano, D., et al., *UHTC-based hot structures: Characterization, design, and on-ground/in-fight testing*, in *Ultra-High Temperatue Ceramics: Materials for Extreme Environment Applications*, Fahrenholtz, W.G., et al., Editors. 2014, Wiley. p. 416-436.
14. Fahrenholtz, W.G. and Hilmas, G.E., *Oxidation of ultra-high temperature transition metal diboride ceramics.* International Materials Reviews, 2012. **57**(1): p. 61-72.
15. Squire, T.H. and Marshall, J., *Material property requirements for analysis and design of UHTC components in hypersonic applications.* Journal of the European Ceramic Society, 2010. **30**: p. 2239-2251.
16. Zhou, Y., et al., *First-Principles investigation on the chemical bonding and intrinsic elastic properties of transition metal diborides TMB_2 (TM=Zr, Hf, Nb, Ta, and Y)*, in *Ultra-High Temperature Ceramics: Materials for extreme environment applications*, Fahrenholtz, W.G., et al., Editors. 2014, John Wiley & Sons, Inc.: New Jersey. p. 60-82.
17. Le, V.T., et al., *Advanced sandwich structures for thermal protection systems in hypersonic vehicles: A review.* Composites Part B, 2021. **226**: p. 1-44.
18. Bowman, A. *After 15 years, 1000 tests, Orion´s heat shield ready to take the heat*. 2023 [cited 2024 July 28]; Available from: https://www.nasa.gov/humans-in-space/after-15-years-1000-tests-orions-heat-shield-ready-to-take-the-heat/.

19. Suttles, J.T. and Coltrance, L.C., *A study of ballistic reentry trajectories at a velocity of 15240 meters per second*, in *NASA Technical Note*. 1967, National Aeronautics and Space Administration: Washington, D.C., USA. p. 1-86.
20. Miller-Oana, M., et al., *Oxidation behavior of aerospace materials in hight ethalpy flows using an oxyacetylen torch facility.* Journal of The American Ceramic Society, 2015. **98**(4): p. 1300-1307.
21. Schütz, A. *Die Rückkehr des Space Shuttle - Landeprozeduren*. 2008 [cited 2023 May 4]; Available from: https://www.dlr.de/rd/desktopdefault.aspx/tabid-4809/7974_read-11748/7974_page-5/.
22. Fahrenholtz, W.G., *A historical perspective on research related to Ultra-High Temperature Ceramics*, in *Ultra-High Temperature Ceramics: Materials for extreme environment applications*, Fahrenholtz, W.G., et al., Editors. 2014, John Wiley & Sons, Inc.: New Jersey. p. 6-32.
23. Opeka, M., et al., *Mechanical, thermal, and oxidation properties of refractory hafnium and zirconium compounds.* Journal of the European Ceramic Society, 1999. **19**: p. 2405-2414.
24. Van Wie, D.M., et al., *The hypersonic environment: Required operating conditions and design challenges.* Journal of Materials Science, 2004. **39**(19): p. 5915-5924.
25. Balat-Pichelin, M., et al., *Recombination coefficient of atomic oxygen on ceramic materials under earth re-entry conditions by optical emission spectroscopy.* Chemical Physics, 2003. **291**: p. 181-194.
26. Srinivasa Reddy, M. and Amoorthy, K., *Heat flux and surface temperature variations in an unconditioned room of brick masonry construction in a composite climate.* Energy and Buildings, 1989. **13**.
27. Fahrenholtz, W.G., et al., *Introduction*, in *Ultra-High Temperature Ceramics: Materials fo extreme environment applications*, Fahrenholtz, W.G., et al., Editors. 2014, John Wiley & Sons, Inc.: New Jersey. p. 1-5.
28. Inoue, R., et al., *Oxidation of ZrB_2 and its composites: a review.* Journal of Materials Science, 2018. **53**: p. 14885-14906.
29. Zimmermann, J.W., et al., *Thermophysical properties of ZrB_2 and ZrB_2-SiC ceramics.* Journal of The American Ceramic Society, 2008. **91**(5).
30. Neuman, E.W., *Elevated temperature mechanical properties of zirconium dibiride based ceramics*. 2014, Missoury University of Science and Technology.
31. Kaufman, L., et al., *Oxidation characteristics of hafnium and zirconium diboride.* Transactions of the metallurgical society of AIME, 1967. **239**: p. 458-466.
32. Li, H., et al., *Thermodynamic calculation of HfB_2 volatility diagram.* 2011. **32**: p. 422-427.
33. Neuman, E.W., et al., *Processing, microstructure, and mechanical properties of large-grained zirconium diboride ceramics.* Materials Science and Engineering: A, 2016. **670**: p. 196-204.
34. Zhang, G.-J., et al., *Reactive processes for diboride-based ultra-high temperature ceramics*, in *Ultra-High Temperature Ceramics: Materials for extreme environment applications*, Fahrenholtz, W.G., et al., Editors. 2014, John Wiley & Sons, Inc.: New Jersey. p. 33-59.
35. Rezaie, A., et al., *Effect of hot pressing time and temperature on the microstructure ad mechanical properties of ZrB_2-SiC.* Journal of Materials Science, 2007. **42**: p. 2735-2744.
36. Zhang, L., et al., *Thermal and electrical transport properties of spark plasma-sintered HfB_2 and ZrB_2 ceramics.* Journal of The American Ceramic Society, 2011. **94**(8): p. 2562-2570.
37. Dehdashti, M.K., et al., *Effects of transition metals on the oxidation behavior of ZrB_2 ceramics.* Corrosion Science, 2015. **91**: p. 224-231.
38. Shugart, K., et al., *Mechanisms of variability of ZrB_2-30 vol% SiC oxidation kinetics.* Journal of The American Ceramic Society, 2014. **97**(7): p. 2279-2285.

39. Naraparaju, R., et al., *Effect of moisture on the oxidation behaviour of ZrB_2.* Journal of The American Ceramic Society, 2019. **104**(2): p. 1058-1066.
40. Opila, E.J. and Halbig, M.C., *Oxidation of ZrB_2-SiC.* Ceramic Engineering and Science Proceedings, 2001. **22**: p. 221-228.
41. Lin, J., et al., *Analysis of zirconium oxide formed during oxidation at 623 K on Zr-2.5Nb and Zircaloy-4.* Materials Science and Engineering: A, 2004. **381**(1-2): p. 104-112.
42. Parthasarathy, T.A., et al., *A model of the oxidation of ZrB_2, HfB_2 and TiB_2.* Acta Materialia, 2007. **55**: p. 5999-6010.
43. Parthasarathy, T.A., *Effects of phase change and oxygen permeability in oxide scales on oxidation kinetics of ZrB_2 and HfB_2.* Journal of The American Ceramic Society, 2009. **92**: p. 1079-1086.
44. Hassan, R. and Balani, K., *Oxidation kinetics of ZrB_2- and HfB_2-powders and their SiC reinforced composites.* Corrosion Science, 2020. **177**: p. 1-14.
45. Kiemle, T., *Einfluss externer Spannungen auf Phasenumwandlungen in tetragonalem Zirconium Dioxid.* 2017.
46. Jin, X.-J., *Martensitic transformation in zirconia containing ceramics and its applications.* Current Opinion in Solid State and Materials Science, 2005. **9**: p. 313-318.
47. Katz, G., *X-ray diffraction powder pattern of metastable cubic ZrO_2.* Journal of The American Ceramic Society, 1971. **54**(10): p. 531.
48. Bouvier, P., et al., *Low temperature phase transformation of nanocrystalline tetragonal ZrO_2 by neutron and raman scattering studies.* International Journal of Inorganic Materials, 2001. **3**: p. 647-654.
49. Jaffe, J.E., et al., *Low-temperature polymorphs of ZrO_2 and HfO_2: A density-functional theory study.* Physical Review B, 2005. **72**: p. 144107-144115.
50. Reif, M., et al., *An enhanced three-step oxidation process to improve oxide adhesion on zirconium alloys.* Oxidation of metals, 2014. **82**: p. 99-112.
51. Heller, H.J., et al., *Der Einfluss von Martensit auf das Korrosionsverhalten von 18Cr-10Ni-Stahl.* Werkstoffkunde und Korrosion, 1981. **32**: p. 157-167.
52. Baither, D.B., Bernd; Messerschmidt, Ulrich, *Ferroelasticity of t'-zirconia: I, High-voltage electron microscopy studies of the microstructure in polydomain tetragonal zirconia.* Journal of The American Ceramic Society, 1997. **80**(7): p. 1691-1698.
53. Baufeld, B., et al., *Ferroelasticity of t'-zirconia: II, In situ straining in a high-voltage electron microscope.* Journal of The American Ceramic Society, 1997. **80**(7): p. 1699-1705.
54. Kelly, P.M. and Francis Rose, L.R., *The martensitic transformation on ceramics - Its role in transformation toughening.* Progress in Materials Science, 2002. **47**(5): p. 463-557.
55. Chevalier, J., et al., *The tetragonal-monoclinic transformation in zirconia: Lessons learned and future trends.* Journal of The American Ceramic Society, 2009. **92**(9): p. 1901-1920.
56. Simha, N.K., *Twin and habit plane micrstructres due to the tetragonal to monoclinic tranformation of zirconia.* Journal of the Mechanics and Physics of Solids, 1997. **45**(2): p. 261-292.
57. Berger, S.V., *The crystal structure of boron oxide.* Acta Chemica Scandinavica, 1953. **7**(4): p. 611-622.
58. Rizzo, H.F., *Oxidation of boron at temperatures between 400°C an 1300°C in air*, in *Boron synthesis, structure, and properties*, Kohn, J.A., et al., Editors. 1960, Springer: Boston, MA, USA. p. 175-189.
59. Fahrenholtz, W.G., *The ZrB_2 volatility diagram.* Journal of The American Ceramic Society, 2005. **88**(12): p. 3509-3512.
60. Wolfgong, W.J., *Chemical analysis techniques for failure analysis: Part 1, Common instrumental methods*, in *Handbook of materials failure analysis with case studies from*

the aerospace and automotive industries, Hamdy Makhlouf, A.S. and Aliofkhazraei, M., Editors. 2016, Elsevier Ltd. p. 279-307.
61. D'angio', A., *Microwave enhanced chemical vapour infiltration of silicon carbide fibre preforms*, in *College of Engineering and Physical Sciences*. 2018, University of Birmingham.
62. Birks, N., et al., *Introduction to the high-temperatrue oxidation of metals*. 2 ed. 2006, New York: Cambridge University Press.
63. Shugart, K. and Opila, E., *Oxygen diffusion mechanisms during high-temperature oxidation of ZrB_2-SiC.* Journal of The American Ceramic Society, 2017. **101**(4): p. 1765-1779.
64. Young, D.J., *High temperatue oxidation and corrosion of metals*, ed. Burstein, T. Vol. 1. 2008, Netherlads: Elsevier. 576.
65. Kwon, O.H., et al., *Investigation of the electrical conductivity of sintered monoclinic zirconia.* Ceramics International, 2017. **43**(11): p. 8236-8245.
66. Dehdashti, M.K., *Improving the oxidation resistance of diboride-based ceramics*, in *Department of Materials and Engineering*. 2014, Missouri University of Science and Technology: MO, USA.
67. Talmy, I.G., et al., *High-temperature chemistry and oxidation of ZrB_2 ceramics containing SiC, Si_3N_4, Ta_5Si_3 and $TaSi_2$.* Journal of The American Ceramic Society, 2008. **91**(7): p. 22250-2257.
68. Rezaie, A., et al., *Oxidation of zirconium diboride-silicon carbide at 1500°C at a low partial pressure of oxygen.* Journal of The American Ceramic Society, 2006. **89**(10): p. 3240-3245.
69. Cissel, K.S. and Opila, E., *Oxygen diffusion mechanisms during high-temperature oxidation of ZrB_2-SiC.* Journal of The American Ceramic Society, 2018. **101**: p. 1765-1779.
70. Deal, B.E. and Grove, A.S., *General relationship of thermal oxidation of silicon.* Journal of Applied Physics, 1965. **36**: p. 3770-3778.
71. Peleg, M., et al., *The arrhenius equation revisted.* Critical Reviews in Food Science and Nutrition, 2012. **52**(9): p. 830-851.
72. Paul, A., et al., *Thermodynamics, Diffusion and the kirkendall effect in solids*. 1 ed. 2014, Switzerland: Springer International.
73. Teng, W.S., et al., *Revisiting adsorption cooling cycle from mathematical modelling to system development.* Renewable and Sustainable Energy Reviews, 2016. **63**: p. 315-332.
74. Cussler, E.L., *Diffusion, Masstransfer in fluid systems*. 3 ed. 2007: Cambridge University Press.
75. Shugart, K. and Opila, E., *SiC depletion in ZrB_2-30 vol% SiC at ultra-high temperatures.* Journal of The American Ceramic Society, 2015. **98**(5): p. 1673-1683.
76. Shugart, K., et al., *Initial stages of ZrB_2-30 vol% SiC oxidation at 1500°C.* Journal of The American Ceramic Society, 2014. **97**(5): p. 1645-1651.
77. Shugart, K., et al., *Determination of retained B_2O_3 Contet in ZrB_2-30 vol% SiC oxide scales.* Journal of The American Ceramic Society, 2015. **98**(1): p. 287-295.
78. Karlsdottir, S.N., et al., *Convection patterns in liquid oxide films on ZrB_2-SiC composites oxidized at a high temperature.* Journal of The American Ceramic Society, 2007. **90**(9): p. 2863-2867.
79. Dehdashti, M.K., et al., *Oxidation of zirconium diboride with niobium additions.* Journal of the European Ceramic Society, 2013. **33**: p. 1591-1598.
80. Wang, F. and Nothwood, D.O., *Oxides formed between ZrO_2 and Nb_2O_5.* Journal of Materials Science, 1995. **30**: p. 4003-4008.

81. Roth, R.S. and Coughanour, L.W., *Phase equilibrium relations in the systems titania-niobia and zirconia-niobia.* Journal of research of the National Bureau of Standards, 1955. **55**(4): p. 209-213.
82. Levin, E.M., *Phase equilibria in the system iobium pentoxide - Boric acid.* Journal of research of the National Bureau of Standards, 1965. **70A**(1).
83. Dehdashti, M.K., et al., *Effects of temperature and the incorporation of W on the oxidation of ZrB_2 ceramics.* Corrosion Science, 2014. **80**: p. 221-228.
84. Zhang, S.C., et al., *Improved oxidation resistance of zirconium diboride by tungsten carbide additions.* Journal of The American Ceramic Society, 2008. **91**(11): p. 3530-3535.
85. Levin, E.M., *The system WO_3 - B_2O_3.* Journal of The American Ceramic Society, 1965. **48**(9): p. 491-492.
86. Levine, S.R. and Opila, E.J., *Tantalum addition to zirconium diboride for improved oxidation resistance*. 2003, National Aeronautics and Space Administration (NASA). p. 1-18.
87. Talmy, L.G., et al., *Oxidation of ZrB_2 ceramics modified with SiC and goup IV - VI transition metal diborides.* Journal of the Electrochemical Society, 2001. **12**: p. 144-158.
88. Nisar, A., et al., *A perspective on challenges and opportunities in developing high entropy ultra high temperature ceramis.* Ceramics International, 2020. **46**: p. 25845-25853.
89. Drozdz, M., et al., *Chromium-based oxidation-resistant coatings for the protection of engine valves in automotive vehicles.* Materiali in Tehnologije / Materials and Technology, 2017. **51**(4): p. 603-607.
90. Naraparaju, R., *High temperature oxiation behavior of boiler steel with emphasis on shot-peening effects - experimental results and simulation*, in *Lehrstuhl für Materialkunde und Werkstoffprüfung*. 2013, Universität Siegen: Siegen.
91. Lau, H., *Microstructure and morphology of thermally grown oxides of thermal barrier coating systems of turbine blades*, in *Fakultät für Maschinenbau*. 2004, Rheinisch-Westfälische Technische Hochschule Aachen: Aachen.
92. Kaden, U., *Influence of substrate alloy CMSX-4 on the lifetime of an EB-PVD thermal barrier coating system*, in *Fakultät für Maschinenbau*. 2002, Rheinisch-Westfälische Technische Hochschule Aachen: Aachen. p. 154.
93. Naraparaju, R., et al., *EB-PVD alumina (Al_2O_3) as a top coat on 7YSZ TBCs against CMAS/VA infiltration: Deposition and reaction mechanisms.* Journal of the European Ceramic Society, 2018.
94. Laska, N.C., *Lebensdauer und Oxidationsverhalten vn Wärmedämmschicht-Systemen auf Gamma Titanaluminiden*, in *Mathematisch-Naturwissenschaftliche Fakultät*. 2014, Univeristät zu Köln: Köln.
95. Leisner, V., *Neue environmental barrier coatings für SiC/SiC-Faserverbundwerkstoffe durch PVD-Technologien*, in *Fakultät für Maschinenbau*. 2019, Karlsruhe Institut für Technologie (KIT): Karlsruhe. p. 224.
96. Haefer, R.A., *Oberflächen- und Dünnschicht-Technologie*. 1987, Heidelberg: Springer-Verlag.
97. Mattox, D.M., *Handbook of physical vapor deposition (PVD) processing*. Vol. 2. 2010, USA: William Andrew, Elsevier.
98. Dearnley, P.a.L., T., *Vapor deposition coating technologies (CVD, PACVD, PVD, and Hybrid PVD-CVD) and their tribological application*. 2013: Springer, Boston, MA.
99. Braun, M., *Magnetron sputtering technique*, in *Handbook of Manufacturing Engineering and Technology*, Nee, A.Y.C., Editor. 2015, Springer-Verlag: London. p. 2929-2957.
100. Nicolaus, M. and Schäper, M., *Grundlagen der Dünnschichttechnologie*, in *Moderne Beschichtungsverfahren*, Bach, F.-W., et al., Editors. 1992, Wiley-VCH Verlag GmbH & Co. KGaA: Weinheim. p. 35-55.

101. Petrov, I., et al., *Microstructural evolution during film growth.* Journal of Vacuum Science & Technology, 2003. **21**(5): p. 117-128.
102. Ohring, M., *Plasma and ion beam processing of thin films*, in *Materials Science of Thin Films: Deposition and Structure*. 2002. p. 203-275.
103. Berg, S., et al., *Upgrading the "Berg-modle" for reactive sputtering process.* Thin Solid Films, 2014. **565**: p. 186-192.
104. Berg, S. and Nyberg, T., *Fundamental understanding and modeling of reactive sputtering processes.* Thin Solid Films, 2005. **476**: p. 215-230.
105. Särhammar, E. and Berg, S., *Applying "the upgraded Berg modle" to predict hysteresis free reactive sputtering.* Surface & Coatings Technology, 2015. **279**: p. 39-43.
106. Dickson, R.J. and Lepoutre, P., *Mechanical interlocking in coating adhesion to paper.* Tappi Journal, 1997. **80**(11): p. 149-157.
107. Barna, P.B. and Adamik, M., *Fundamental structure forming phenomena of polycrystalline films and the structure zone modles.* Thin Solid Films, 1998. **317**: p. 27-33.
108. Sciti, D., et al., *Sintering and mechanicla properties of ZrB_2-$TaSi_2$ and HfB_2-$ZaSi_2$ ceramic composites.* Journal of The American Ceramic Society, 2008. **91**(10): p. 3285-3291.
109. Ruh, R., et al., *The system zirconia-hafnia.* Journal of The American Ceramic Society, 1968. **51**(1): p. 23-27.
110. Johnson, B. and Jones, J.L., *Structures, phase equilibria, and properties of HfO_2.* Woodhead Publishing Series in Electronic and Optical Materials, 2019: p. 25-45.
111. Wyckoff, R.W.G., *Crystal structures*. Vol. 1. 1963, New York: Interscience Publisher.
112. Delheusy, M., *X-ray investigation of Nb/O interfaces*. 2008: Paris. p. 191.
113. Nico, C., et al., *NbO/Nb_2O_5 core-shells by thermal oxidation.* Journal of the European Ceramic Society, 2013. **33**: p. 3077-3083.
114. Nico, C., et al., *Niobium oxides and niobates physical properties: Review and prospects.* Progress in Materials Science, 2016. **80**: p. 1-37.
115. Tupin, M., et al., *Oxidation kinetics of ZrNbO in steam: Differences between the pre- and post-transition stages.* Journal of Nuclear Materials, 2005. **342**: p. 108-118.
116. Lindau, I. and Spicer, W.E., *Oxidation of Nb as studied by the uv-photoemission technique.* Journal of Applied Physics, 1974. **45**(9): p. 3720-3725.
117. Arbuzov, M.P. and Chuprina, V.G., *The oxidation of niobium and the structure of niobium oxides*. 1965. p. 129-133.
118. Bouillet, C., et al., *Oxidation of niobium sheets at high temperature.* Solid State Ionics, 1997: p. 819-824.
119. Mestres, L., et al., *Phase diagram at low temperature of the system ZrO_2/Nb_2O_5.* Zeitschrift für anorganische und allgemeine Chemie, 2000(627): p. 294-298.
120. Adadurov, G.A., et al., *Phase transition of shock-compressed T-Nb_2O_5 and H-Nb_2O_5.* 1971.
121. Vishwanadh, B., et al., *A study on the oxidation behavior of Nb alloy (Nb-1 pct Zr-0.1 pct C) and silicide-coated Nb alloys.* The Minerals, Metals & Materials Society, 2012. **44A**: p. 2258-2269.
122. Manning, W.R., et al., *Thermal Expansion of Nb_2O_5.* Journal of The American Ceramic Society, 1972. **55**(7): p. 342-347.
123. Galy, J. and Roth, R.S., *The crystal structure of $Nb_2Zr_6O_{17}$.* Journal of Solid State Chemistry, 1973. **7**: p. 277-285.
124. Winter, M.J. *Gadolinium - Reaction of elements*. 2024 [cited 2024 May 15]; Available from: https://www.webelements.com/gadolinium/chemistry.html.
125. Garg, A.B., et al., *Role of GdO addition in the structural stability of cubic Gd_2O^3 at high pressure: Determination of the equation of states of GdO and Gd_2O_3.* Materialia, 2024. **34**: p. 1-11.

126. Norman, M., et al., *The lattice spacing of thorium-rich solid solutions with praseodymium, samarium, gadolinium and erbium.* Journal of the Less-Common Metals, 1966. **11**: p. 395-402.
127. Adachi, G.-Y. and Imanaka, N., *The binary rare earth oxides.* American Chemical Society, 1998. **98**: p. 1479-1514.
128. Jamnezhad, H. and Jafari, M., *Structure of Gd_2O_3 nanoparticles at high temperature.* Journal of Magnetism and Magnetic Materials, 2016. **408**: p. 164-167.
129. Lakiza, S.N., et al., *Phase diagram of the ZrO_2-Gd_2O_3-Al_2O_3 system.* Journal of the European Ceramic Society, 2006. **26**: p. 233-246.
130. Dudnik, E.V., et al., *The $Gd_2Zr_2O_7$-based materials for thermal barriere coatings.* Powder Metallurgy and Metal Ceramics, 2018. **57**(5-6): p. 301-315.
131. Cohen-Adad, M.T., et al., *Gadolinium and yttrium borates: Thermal behavior and structural consideration.* Journal of Solid State Chemistry, 2000. **154**: p. 204-213.
132. Madshal, M., et al., *Structural studies and physical properties of Gd_2O_3-doped borate glass.* Journal of Materials Science: Materials in Electronics, 2021. **32**: p. 14642-14653.
133. Sindlhauser, M. *Materialien, Targets aus allen Metallen*. 2024 [cited 2022 August 10]; Available from: https://www.sindlhauser.de/metalle-edelmetalle.html.
134. Zhu, S., *Densification, microstructure, and mechanical properties of zirconium diboride based ultra-high temperature ceramics*, in *Department of Materials Science and Engineering*. 2008, Missouri University of Science ad Technology: MO, USA.
135. S.A.S., S., *Safety data sheet, Epofix resin*. 2020: Denmark. p. 1-18.
136. S.A.S., S., *Safety data sheet, Epofix hardener*. 2020: Denmark. p. 1-17.
137. Förster, J.E., et al., *Hafnium oxide coating to improve the oxidation behavior of zirconium diboride.* Journal of the European Ceramic Society, 2024. **44**(15).
138. Liu, Z. and Gao, W., *A numerical model to predict the kinetics of anisothermal oxidation of metals.* High Temperature Materals and Processes, 1997. **17**(4): p. 231-236.
139. Förster, J.E., et al., *Oxidation behavior of Nb-coated zirconium diboride.* Journal of the European Ceramic Society, 2023. **43**(12): p. 5174-5182.
140. Tan, A.J., et al., *Hydration of gadolinium oxide (GdOx) and its effect on voltage-induced Co oxidation in a Pt/Co/GdOx/Au heterostructure.* Physical Review Materials, 2019. **3**(064408): p. 1-8.
141. Santucci, S., et al., *Oxygen loss and recovering induced by ultrahigh vacuum and oxygen annealing on WO_3 thin film surfaces: Influences on the gas response properties.* Journal of Vacuum Science & Technology A, 2001. **19**: p. 1467-1473.
142. Rodenbücher, C., et al., *Hafnium carbide formation in oxygen deficient hafnium oxide thin films.* Applied Physics Letters, 2016. **108**: p. 1-6.
143. Pan, Y., et al., *Thermodynamic assessment of the ternary B-Hf-ZrsSystem with refined B-Hf description.* Journal of Phase Equilibria and Diffusion, 2021. **42**: p. 864-878.
144. Gilron, J. and Soffer, A., *Knudsen diffusion in microporous carbon membranes with moleclar sieving character.* Journal of Membrane Science, 2002. **209**: p. 339-352.
145. Bargeron, C.B., et al., *Oxdation of hafnium carbide in the temperature range 1400°C to 2060°C.* Journal of The American Ceramic Society, 1993. **76**(4): p. 1040-1046.
146. Shimada, S. and Inagaki, M., *Oxidation kinetics of hafnium caride in the temperature range of 480°C- 600°C.* Journal of The American Ceramic Society, 1992. **75**(10): p. 2671-2678.
147. Ikeda, M., et al., *Theoretical analysis of oxygen diffusion in monoclinic HfO_2.* Materials Research Society Symposium Proceedings, 2004. **786**: p. 1-6.
148. Patil, R.N. and Subbarao, E.C., *Axial thermal expansion of ZrO_2 and HfO_2 in the range room temperature to 1400°C.* Journal of Applied Crystallography, 1969. **2**: p. 281-288.
149. Bargeron, C.B., et al., *Oxidation mechanisms of hafnium carbide and hafnium diboride in the temperature range 1400°C to 2100°C.* Johns Hopkins APL Technical Digest, 1993. **14**(1): p. 29-36.

150. Shimada, S. and Yunazar, F., *Oxidation of hafnium carbide and titanium carbide single crystals with the formation of carbon at high temperatures and low oxygen pressures.* Journal of The American Ceramic Society, 2000. **83**(4): p. 721-728.
151. Karlsdottir, S.N. and Halloran, J.W., *Zirconia transport by liquid convection during oxidation of zirconium diboride-silicon carbide.* Journal of The American Ceramic Society, 2008. **91**(1): p. 272-277.
152. Welzel, T. and Ellmer, K., *The influence of the target age on laterally resolved ion distributions in reactive planar magnetron sputtering.* Surface & Coatings Technology, 2011. **205**: p. 294-298.
153. Borowski, T., et al., *Effect of oxidation temperature on the properties of niobium in view of its biomedical applications.* Surface & Coatings Technology, 2023. **473**: p. 1-11.
154. Long, B.A., et al., *Sublimation kinetics of individual graphite and grephene nano-particel (NPs): NP-to-NP variations and evolving structure-kinetics and structure-emissivity relationships.* Journal of The American Ceramic Society, 2020. **142**(33): p. 1-70.
155. Brizes, W.F., et al., *Carbon diffusion in the carbides of niobium.* Journal of Nuclear Materials, 1966. **20**: p. 57-67.
156. Zhao, N., et al., *Thermal kinetic study of the formation mechanism of NbC-Fe composite layer on the surface of GCr15 prepared by hot pressure diffusion.* Materials Research Express, 2023. **10**: p. 1-12.
157. Strandlund, H. and Larsson, H., *Prediction of kirkendall shift and porosity in binary and ternary diffusion couples.* Acta Materialia, 2004. **52**: p. 4695-4703.
158. Rapp, R.A., et al., *Displacement reactions in the solid state.* Metallurgical Transactions, 1973. **4**: p. 1283-1292.
159. Merriles, D.M., et al., *Chemical bonding and electronic structure of early transition metal borides: ScB, TiB, VB, YB, ZrB, NbB, LaB, HfB, TaB, and WB.* The Journal of the Physical Chemistry A, 2021. **125**(20): p. 4420-4432.
160. German, R.M., et al., *Review: Liquid phase sintering.* Journal of Materials Science, 2009. **44**: p. 1-39.
161. Dokumaci, E., et al., *Effect of boronizing on the oxidation of niobium.* Journal of Refractory Metals and Hard Materials, 2013. **41**: p. 276-281.
162. Swadźba, R., *High temperature oxidation behavior of C103 alloy with boronized and siliconized coatings during 1000h at 1100°C in air.* Surface & Coatings Technology, 2019. **370**: p. 331-339.
163. Shimada, S. and Inakaki, M., *I kinetic study on oxidation of niobium caride.* Solid State Ionics, 1993. **63-65**: p. 312-317.
164. Reed, T.B., et al., *Niobium monoxide*, in *Inorganic syntheses*, Murphy, D.W. and Interrante, L.V., Editors. 1995, John Wiley & Son Inc.
165. Okabe, T.H., et al., *Thermodynamic considerations of direct oxygen removal from titanium by utilizing the deoxidation capability of rear earth metals.* Metallurgical and Materials Transcribtions B, 2018. **49**: p. 1056-1066.
166. Trégouet, H., et al., *Spectroscopic investigation and christalization study of rare earth metaborate glasses.* Procedia Materials Science, 2014. **7**: p. 131-137.
167. San Andrés, E., et al., *Growth of gadolinium oxide by thermal oxidation of thin metallic gadolinium layers*, in *11th International Conference on Ultimate Integration on Silicon*. 2010: Glasgow, Scotland. p. 1-4.
168. Johannesson, K.H., et al., *The solubility control of rare earth elements in natural terrestrial waters and the significance of PO und CO in limiting dissolved rare earth concentrations: A review of recent information.* Aquatic Geochemistry, 1995. **1**: p. 157-173.
169. Förster, J.E., et al., *Oxidation protective coatings for diboride-based ultra-high temperature ceramics, based on elemental aluminum and alumina mixtures*. 2024: Germany.

170. Förster, J.E., et al., *Oxidation protective coatings for diboride-based ultra-high temperature ceramics, based on elemental aluminum and alumina mixtures*. 2024: United States of America.